ESCOLA DE DOUTORAMENTO
INTERNACIONAL DA USC

Julián
Lomba Castro

Tese de doutoramento

Lepton Universality measurements in semileptonic decays of b-quark hadrons in the LHCb experiment at CERN

Santiago de Compostela, 2023

Programa de Doutoramento en Física Nuclear e de Partículas

TESE DE DOUTORAMENTO

LEPTON UNIVERSALITY MEASUREMENTS IN SEMILEPTONIC DECAYS OF *B*-QUARK HADRONS IN THE LHCB EXPERIMENT AT CERN

Julián Lomba Castro

ESCOLA DE DOUTORAMENTO INTERNACIONAL DA UNIVERSIDADE DE SANTIAGO DE COMPOSTELA

PROGRAMA DE DOUTORAMENTO EN FÍSICA NUCLEAR E DE PARTÍCULAS

SANTIAGO DE COMPOSTELA

ANO 2023

DECLARACIÓN DO AUTOR/A DA TESE

D./Dna. **Julián Lomba Castro**

Título da tese: **Lepton Universality measurements in semileptonic decays of b-quark hadrons in the LHCb experiment at CERN**

Presento a miña tese, seguindo o procedemento axeitado ao Regulamento, e declaro que:

1) A tese abarca os resultados da elaboración do meu traballo.
2) De ser o caso, na tese faise referencia ás colaboracións que tivo este traballo.
3) Confirmo que a tese non incorre en ningún tipo de plaxio doutros autores nin de traballos presentados por min para a obtención doutros títulos.
4) A tese é a versión definitiva presentada para a súa defensa e coincide a versión impresa coa presentada en formato electrónico

E comprométome a presentar o Compromiso Documental de Supervisión no caso de que o orixinal non estea na Escola.

En **Santiago de Compostela**, **22 de marzo do 2023**.

Sinatura electrónica

AUTORIZACIÓN DO DIRECTOR/TITOR DA TESE

D./Dna. **Juan José Saborido Silva**

En condición de: **Titor/a e director/a**

Título da tese: **Lepton Universality measurements in semileptonic decays of b-quark hadrons in the LHCb experiment at CERN**

INFORMA:

Que a presente tese, correspóndese co traballo realizado por D/Dna Julián Lomba Castro, baixo a miña dirección/titorización, e autorizo a súa presentación, considerando que reúne os requisitos esixidos no Regulamento de Estudos de Doutoramento da USC, e que como director/titor desta non incorre nas causas de abstención establecidas na Lei 40/2015.

En **Santiago de Compostela**, **22 de Marzo de 2023**

Sinatura electrónica

« Sir Isaac Newton is said to have avowed that he felt like a child picking up shells beside the great and unexplored ocean of truth. »

– Frankenstein (Mary Shelley)

« You miss 100% of the shots you don't take. – Wayne Gretzky »

– Michael Scott

« la cencia no se ace sola ahi que acerla »

– @cientefico

Acknowledgements

First, I would like to thank IGFAE's LFU group, specially Juan, for his care during my studentship; Toño, for his helpfulness and clarity; and Abraham, for looking after all PhD students. Of course, also my office mates Alessandra and Óscar, who made my day-to-day life much more easy and fun, and also María, whose tips and tricks were essential even after all these years. Also the other members like Arnau, Cibrán, and Ricci, whose comments were always helpful.

Then, I also must thank a lot of people from LHCb, including Marcello, Mark, Michel, and Donal, who were conveners of the Semileptonic WG during my PhD, as well as many people from similar $R(X_c)$ analyses, namely Guy, Olivier, and Resmi, among others; all of their insight and comments were essential for the work of this thesis. Also Adam (Morris), who helped me learn many things during the beginning of my time as MC liaison, and Biljana, who accompanied me during that time and in countless meetings, making the task much more bearable. Of course, also Adam (Davis), Gloria, and Michal, who led the simulation meetings during that time and always were kind to help.

I must also acknowledge the various fundings received by the IGFAE, Xunta de Galicia (*Axuda de apoio á etapa predoutoral*), and Ministerio de Universidades (*Formación del Profesorado Universitario*), which provided the financial support for my PhD studentship and my stay at CERN.

No ámbito máis persoal, agradecer (outra vez) a Ale, Óscar, e Vero pola súa compañía nas alegrías e nos dramas todos estes anos; aos amigos de "covfefe" Adrián, Alexandre, Fidel, Gabi, e Gonzalo, cos que me levo divertindo e estando forísima dende a carreira, xunto con Carlos e Saúl máis recentemente; e a Efrén por facer a estadía en Saint Genis máis levadeira.

Xa fóra do traballo, agradecer a Carol polo seu apoio neste último ano, a Guerre por sempre estar aí para o que sexa, a Cos por sempre escoitar e apoiar, ás miñas amizades da Guarda, Aroa e Dave, coas que sempre puiden desconectar de todo isto, e á miña familia (meus pais e meu irmán), que sempre estiveron apoíandome e axudando.

– Julián

Abstract

Lepton Flavour Universality (LFU) is an assumed symmetry within the Standard Model (SM) that implies that the coupling between gauge bosons and the different leptons does not depend on the flavour (family) of the lepton. In particular, the so-called LFU ratios such as $R(D^{(*)}) \equiv \frac{B\to D^{(*)}\tau^-\overline{\nu}_\tau}{B\to D^{(*)}\mu^-\overline{\nu}_\mu}$ are being thoroughly measured by different experiments, finding tensions with the SM predictions up to the 3σ range.

In this thesis, a preliminary simultaneous measurement of the $B^- \to D^{(*)0}\tau^-\overline{\nu}_\tau$ branching fractions and the $R(D^{(*)0})$ LFU ratios is reported, with the decay channels

$$\begin{aligned} D^{*0} &\to D^0\{\pi^0,\gamma\}, \\ D^0 &\to K^-\pi^+, \\ \tau^- &\to \pi^-\pi^+\pi^-(\pi^0)\nu_\tau. \end{aligned}$$

This work is done with LHCb Run 2 data corresponding to pp collisions at a centre-of-mass energy of 13 TeV from the years 2016–2018, with an integrated luminosity of 5.4 fb^{-1}. The obtained results, with blinded values, are

$$\begin{aligned} \mathcal{B}(B^- \to D^0\tau^-\overline{\nu}_\tau) &= (\text{xxx} \pm 0.13\ (\text{stat.}) \pm 0.22\ (\text{syst.}) \pm 0.07\ (\text{ext.})) \times 10^{-2}\ , \\ \mathcal{B}(B^- \to D^{*0}\tau^-\overline{\nu}_\tau) &= (\text{xxx} \pm 0.11\ (\text{stat.})\ ^{+0.15}_{-0.14}\ (\text{syst.}) \pm 0.15\ (\text{ext.})) \times 10^{-2}\ , \end{aligned}$$

for the branching fractions, and

$$\begin{aligned} R(D^0) &= \text{xxx} \pm 0.056\ (\text{stat.}) \pm 0.096\ (\text{syst.}) \pm 0.034\ (\text{ext.})\ , \\ R(D^{*0}) &= \text{xxx} \pm 0.020\ (\text{stat.}) \pm 0.026\ (\text{syst.}) \pm 0.029\ (\text{ext.})\ , \end{aligned}$$

for the LFU ratios.

In addition, the base work for a complementary and analogous measurement of the $R(D^{(*)-})$ ratios and $B^0 \to D^{(*)-}\tau^+\nu_\tau$ branching fractions, with $\tau^- \to \pi^-\pi^+\pi^-\nu_\tau$ and $D^- \to K^-\pi^+\pi^+$, is laid out, including the production of simulation samples, the selection of events, and the study of the relevant control samples.

INDEX

1

Introduction

The Standard Model is a theoretical framework that describes the fundamental particles and their interactions through three fundamental forces: electromagnetic, weak, and strong nuclear forces. It has been extremely successful in predicting and explaining a wide range of experimental results in particle physics, including the discovery of the Higgs boson in 2012 at the Large Hadron Collider (LHC), one of the most important and recent validations of the Standard Model, which represented the culmination of decades of theoretical and experimental work. However, it is known that the Standard Model is incomplete, as it does not incorporate gravity and does not account for dark matter, which is believed to make up a significant portion of the universe's mass. Therefore, current research in particle physics is focused on testing the Standard Model's predictions and exploring new physics beyond it, in order to better understand the universe at the smallest scales.

The LHC is currently the largest and most powerful particle accelerator in the world, located at CERN near Geneva, Switzerland. The LHC is a key tool in the study of particle physics and is central to ongoing efforts to test and validate the predictions of the Standard Model, namely the behaviour of particles and fundamental forces at very high energies and the search for new particles beyond the Standard Model, including the search for dark matter. This collider is used to accelerate two beams of protons to very high energies before colliding them head-on. These collisions produce a wide variety of subatomic particles, which can be detected and analyzed by sophisticated detectors surrounding the collision points. The LHCb is one of the main experiments located at the LHC and provides the experimental framework for this thesis.

This thesis contains my work in two current analyses from the LHCb experiment

which aim to shed light onto recent tensions between the Standard Model and experimental results regarding the property called Lepton Flavour Universality (LFU). Multiple experiments, including BaBar and Belle along with LHCb, have worked and are working on testing the validity of LFU and, within the last decade, the tension between experiments and theory has remained approximately around 2–3 standard deviations on multiple measured quantities, suggesting the existence of new physics effects. These "anomalies" have motivated the particle physics community to closely study their possible explanations and to accurately measure them, in hopes of finding a breakthrough in the Standard Model.

The analyses presented within this thesis are two of the same nature. The main one —from now on referred to as the $R(D^{(*)0})$ analysis— aims to simultaneously measure the $R(D^0)$ and $R(D^{*0})$ quantities, ratios of branching fractions defined as $R(D^{(*)0}) = \mathcal{B}(B^- \to D^{(*)0}\tau^-\overline{\nu}_\tau)/\mathcal{B}(B^- \to D^{(*)0}\ell^-\bar{\nu}_\ell)$, where ℓ is either an electron or a muon. This measurement is done in the hadronic channel $\tau^- \to \pi^-\pi^+\pi^-(\pi^0)\nu_\tau$, and would be the first measurement of $R(D)$ with this channel done by the LHCb experiment. The second analysis studies the $R(D^{(*)-})$ ratio, defined in an analogous way and with the same goal, thus both analyses providing independent and complementary results. Due to the immense similarity between the two analyses, the developed algorithms and methods of one of them can be re-purposed for the other one. This is why the second one, $(R(D^{(*)-}))$, is at a much earlier stage and will be discussed just briefly and partially throughout this thesis.

The objectives of this thesis are detailed in section 1.1. An overview of the theoretical foundations and experimental precedents of this work is detailed in chapter 2, including the strategy and methodology followed by these particular analyses in section 2.5. A rundown of the technical set-up and inner workings of the LHCb experiment is presented in chapter 3. Chapter 4 contains a summary of the selection and the preparation of the real and simulated data which is analysed. A study of certain control samples to improve the quality and understanding of the simulated data is presented in chapter 5. The determination of the desired branching fractions and ratios of the $R(D^{(*)0})$ analysis is detailed in chapter 6. Chapter 7 contains a study of the possible systematic effects and errors affecting those results, with their consequential corrections and adjustments. Finally, the preliminary results of the analysis are presented and discussed in chapter 8, along with the conclusions of this thesis.

1.1 Objectives

The main goal of this thesis is the measurement of the $R(D^{(*)0})$ ratios of branching fractions, defined as

$$R(D^{(*)0}) = \frac{\mathcal{B}(B^- \to D^{(*)0}\tau^-\overline{\nu}_\tau)}{\mathcal{B}(B^- \to D^{(*)0}\ell^-\bar{\nu}_\ell)}, \tag{1.1}$$

where ℓ^- can be either a muon or an electron. This measurement is to be done with data taken by the LHCb experiment between 2016 and 2018 and with the decay mode $\tau^- \to \pi^-\pi^+\pi^-(\pi^0)\nu_\tau$.

For this measurement, the denominator $\mathcal{B}(B^- \to D^{(*)0}\ell^-\bar{\nu}_\ell)$ is taken from an external source, so the measurement of the branching fractions $\mathcal{B}$ $(B^- \to D^{(*)0}\tau^-\overline{\nu}_\tau)$ are needed to perform the main measurement, and therefore are another objective of this thesis.

Finally, a secondary objective of this thesis is the preparation of the measurement of the $R(D^{(*)-})$ ratios, defined analogously as

$$R(D^{(*)-}) = \frac{\mathcal{B}(B^0 \to D^{(*)-}\tau^+\nu_\tau)}{\mathcal{B}(B^0 \to D^{(*)-}\ell^+\nu_\ell)} \tag{1.2}$$

and performed in the same conditions as the previous $R(D^{(*)0})$ measurement. This second measurement is expected to be performed after the previous one is completed and, as such, its completion is not within the scope of this thesis. As a consequence, the goal for this measurement is the preparation of algorithms and studies that will facilitate this future measurement and serve as its base.

2

Theoretical foundations and precedents

Contents

In this chapter, an overview of the foundations of this thesis is presented. In the first place, an introduction to the Standard Model of particle physics; secondly, a summary of Lepton Flavour Universality, both theoretical and experimental; then, a collection of physical principles which are relevant to particle colliders; and lastly, a summary of the measurements that precede and motivate this thesis, along with the strategy followed in the data analysis.

2.1 The Standard Model

The Standard Model (SM) [1] is a particle physics theory that describes fundamental interactions (the electromagnetic, weak, and strong interactions) and has so far successfully described the phenomena observed by particle physics experiments.

The SM is a renormalisable quantum field theory based on the local symmetry of twelve conserved currents: eight "colour" charges (corresponding to the strong interaction) and four electroweak charges (corresponding to the electroweak interaction), including the electric charge; forming together the $SU(3)\otimes SU(2)\otimes U(1)$ algebra of the SM. The SM also classifies the fundamental particles, distinguishing between fundamental fermions (matter particles) and fundamental bosons (force carriers and the Higgs boson).

The fundamental fermions all have spin 1/2 and are classified in quarks and leptons. Quarks have both colour and electroweak charges, and are what all hadrons (such as protons and neutrons) are composed of. The leptons are the electron (e^-), the muon (μ^-), the tauon (τ^-), and their three associated neutrinos (ν_e, ν_μ, and ν_τ). Leptons have electroweak charge but no colour. Fermions are grouped in weakly charged doublets and in three "generations" or "families" which have identical quantum numbers but different masses, forming the pattern

$$\begin{bmatrix} u & \nu_e \\ d & e \end{bmatrix}, \begin{bmatrix} c & \nu_\mu \\ s & \mu \end{bmatrix}, \begin{bmatrix} t & \nu_\tau \\ b & \tau \end{bmatrix};$$

where brackets separate each family, and each column is an electroweak doublet. At the same time, each quark can come in three different colour variants. There is no known explanation for this three-family structure.

On the other hand, the fundamental force carriers all have spin 1 and are the photon (γ, carrier of the electromagnetic interaction), the W and Z bosons (W^+, W^-, and Z^0, carriers of the weak interaction), and the gluons (g, carriers of the strong interaction). The photon and the gluons have zero mass due to the invariance of their local gauge symmetries, which also causes the conservation of the electric charge and of the colour charges. The W and Z bosons, on the contrary, have been measured to have mass ($m_W \approx 80.4$ GeV/c^2, $m_Z \approx 91.2$ GeV/c^2 [2]), implying that the electroweak gauge symmetry is broken, and explaining the short range of the weak interaction. An additional particle, the Higgs boson (H^0, with spin 0), is what produces the breaking of the electroweak symmetry in the SM, giving mass to the fermions and W and Z bosons in the process.

The Higgs boson was successfully detected for the first time at the Large Hadron Collider in 2012, with a mass of $m_H \approx 125$ GeV/c^2 [2–4].

2.1.1 Flavour-mixing matrices

As a consequence of the electroweak symmetry breaking, the mass eigenstates of fermions (the states which propagate freely through space) do not have to match with their weak eigenstates (the states which interact with the W and Z bosons). This property is famously responsible for phenomena such as neutrino oscillation and particle-antiparticle oscillations ($K^0 \rightleftharpoons \overline{K}^0$, $B^0 \rightleftharpoons \overline{B}^0$, etc.). Mathematically, mass eigenstates can be expressed as a quantum mixture of the weak eigenstates, forming two different eigenbases, making both sets of states related through a rotation matrix. These flavour-mixing matrices are key for describing flavour-changing processes within the SM.

The CKM matrix

The Cabibbo-Kobayashi-Maskawa (CKM) matrix [5, 6] is a transformation matrix that relates the mass eigenstates of quarks with their weak eigenstates:

$$\begin{pmatrix} d' \\ s' \\ b' \end{pmatrix} = \begin{pmatrix} V_{ud} & V_{us} & V_{ub} \\ V_{cd} & V_{cs} & V_{cb} \\ V_{td} & V_{ts} & V_{tb} \end{pmatrix} \begin{pmatrix} d \\ s \\ b \end{pmatrix}, \tag{2.1}$$

where d', s', and b' denote the quarks' weak eigenstates, while d, s, and b, their mass eigenstates, thus $|V_{ij}|$ representing the $q_i \to q_j W^{\pm}$ transition amplitude. This concept was first used by Cabibbo for two quark families and, later, Kobayashi and Maskawa extended it for three quark families. In the SM with three quark families, the CKM matrix must be unitary, thus providing a powerful way of testing its validity by measuring the CKM matrix elements, since any deviation from unitarity would indicate the presence of new physics (NP). The measured values are so far consistent with unitarity and are, as averaged by [2],

$$|V_{CKM}| \approx \begin{pmatrix} 0.974 & 0.224 & 0.004 \\ 0.221 & 0.975 & 0.041 \\ 0.008 & 0.039 & 1.014 \end{pmatrix}. \tag{2.2}$$

The PMNS matrix

In an analogous way to the CKM matrix, the Pontecorvo-Maki-Nakagawa-Sakata (PMNS) matrix [7, 8] relates the weak and mass eigenstates of the three known families of leptons, and was originally developed to describe neutrino oscillations:

$$\begin{pmatrix} \nu_e \\ \nu_\mu \\ \nu_\tau \end{pmatrix} = \begin{pmatrix} U_{e1} & U_{e2} & U_{e3} \\ U_{\mu 1} & U_{\mu 2} & U_{\mu 3} \\ U_{\tau 1} & U_{\tau 2} & U_{\tau 3} \end{pmatrix} \begin{pmatrix} \nu_1 \\ \nu_2 \\ \nu_3 \end{pmatrix}, \tag{2.3}$$

where ν_l and ν_i denote the leptons' weak and mass eigenstates, respectively. In the SM, this matrix must also be unitary.

There is, however, a key difference in the use of the PMNS matrix compared to the CKM matrix: the flavour of the quarks present in a certain decay can be easily determined, providing the knowledge of which CKM terms contribute to the amplitude of the decay, and express them in terms of a leading term, thanks to the hierarchical nature of the CKM matrix (as seen in eq. 2.2). For leptons, one cannot determine which neutrino mass eigenstates are present in a decay, due to their small mass differences and to the fact that they are not directly detected in experiments. Thus, in a $W^- \to l^- \bar{\nu}_l$ vertex, the neutrino will be produced in a superposition of its mass eigenstates, adding a factor $\sum_i |U_{li}|^2$ to the decay amplitude which, if the unitarity of the PMNS matrix is true, is 1 by definition, making the PMNS matrix not play a role at all in leptonic and semileptonic decays within the SM [9].

2.2 Lepton Flavour Universality

Lepton Flavour Universality (LFU) is a property of the SM which implies that the coupling between gauge bosons and leptons is independent of the lepton family (flavour). This property is often called "accidental", in the sense that there are no fundamental principles that cause it, rather arising mathematically due to the assumed symmetries within the SM.

If this property is true, then the branching fractions of decays with leptons in the final state should be independent of the lepton flavour, and only differ due to the different masses of each lepton. This property can be tested to verify the validity of the SM, since a violation of LFU would be a sign of new physics beyond the SM, requiring new particles that contribute to these decays [10].

2.2.1 Status of LFU tests

In the past decade, experiments such as LHCb, BaBar, and Belle have shown some tensions between their experimental results and the SM predictions regarding ratios of branching fractions of leptonic and semileptonic decays, hinting at a possible violation of LFU. These tensions are mainly found in semileptonic b-quark decays via neutral currents ($b \to s l^+ l^-$) and via charged currents ($b \to c l^- \bar{\nu}_l$).

BaBar and Belle are the so-called "B-factory" experiments, electron-positron colliders designed to produce $\Upsilon(4S)$ resonances (formed by a $b\bar{b}$ pair), which decay mainly (more than 96% of times [2]) to B^+B^- or $B^0\overline{B}^0$, hence their name. On the other hand, LHCb

is a forward spectrometer designed to study the b quarks produced from pp collisions in the LHC, and will be described thoroughly in section 3.2.

Rare semileptonic b-hadron decays

Neutral current $b \to s l^+ l^-$ decays cannot happen at tree level in the SM, which makes them strongly suppressed and a powerful probe in the search of NP, since their branching fractions are very sensitive to the contributions of potential new particles. Several small deviations from the SM have also been observed in measurements of angular distributions [11–13] and of single branching fractions [14–16] on this kind of decays.

LFU tests with rare decays are usually done by measuring the ratio of the muonic and electronic branching fractions in a given region of the squared di-lepton mass (q^2) distribution,

$$R(\mathcal{H}_s)[q^2_{min}, q^2_{max}] \equiv \frac{\int_{q^2_{min}}^{q^2_{max}} \frac{\mathrm{d}\Gamma(\mathcal{H}_b \to \mathcal{H}_s \mu^+ \mu^-)}{\mathrm{d}q^2} \mathrm{d}q^2}{\int_{q^2_{min}}^{q^2_{max}} \frac{\mathrm{d}\Gamma(\mathcal{H}_b \to \mathcal{H}_s e^+ e^-)}{\mathrm{d}q^2} \mathrm{d}q^2}, \tag{2.4}$$

where $\mathcal{H}_b$ and $\mathcal{H}_s$ are a b hadron and a s hadron, respectively. The theoretical predictions for these ratios have very small uncertainties and are very close to unity [17].

LFU has been notably tested on rare semileptonic decays with measurements of the quantities $R(K)$ [18–20], $R(K^*)$ [20–23], $R(K^0_S)$ [23], and $R(pK)$ [24]. The results of these tests are summarised in table 2.1. The older results seemed to show a consistent trend of deviations, pointing to a possible excess of electronic decays over muonic decays, thus offering an interesting opportunity in the search for NP, combined with angular observables and branching fraction measurements. However, the newer measurements by Belle and LHCb tend to agree with the Standard Model.

Tree-level semileptonic b-hadron decays

Charged-current semileptonic b decays ($b \to c l^- \bar{\nu}_l$) happen at tree level in the SM and have a larger branching fraction than $b \to s l^+ l^-$ decays, making it easier to measure their semitauonic modes. This allows LFU tests to be usually performed by comparing the semitauonic and semimuonic (or semielectronic) branching fractions,

$$R(\mathcal{H}_c) \equiv \frac{\mathcal{B}(\mathcal{H}_b \to \mathcal{H}_c \tau^- \overline{\nu}_\tau)}{\mathcal{B}(\mathcal{H}_b \to \mathcal{H}_c \ell^- \bar{\nu}_\ell)}, \tag{2.5}$$

where $\mathcal{H}_c$ is a c hadron and ℓ either a muon or an electron. LHCb uses the muonic mode because of its detector design, which provides higher detection efficiency and momentum resolution for muons compared to electrons, while the B-factories use the electronic mode as the denominator.

LFU tests done with these decays include $R(D)$ [26–28], $R(D^*)$ [26–31], $R(J/\psi)$ [32], and $R(\Lambda_c)$ [33]. The results of these tests are also showing deviations from the SM,

and are summarised on table 2.2. In particular, the global average of $R(D)$ and $R(D^*)$ measurements –which are the quantities studied in this thesis– is currently at 3.2 standard deviations (3.2σ) from the SM predictions [34], as shown on fig. 2.1. Measurements of angular observables will be key to be able to distinguish between different NP scenarios [35].

Tests on other sectors

Apart from the tests on b-hadron decays, there are other sectors in which LFU can be tested. Purely leptonic decays, like $Z^0 \to l^+ l^-$ and $W^- \to l^- \bar{\nu}_l$ are precisely measured in multiple experiments and, so far, they have mostly shown good agreement with LFU. The Z relative branching fractions have been measured to be [42]

$$\frac{\mathcal{B}(Z \to \mu^+ \mu^-)}{\mathcal{B}(Z \to e^+ e^-)} = 1.0009 \pm 0.0028, \tag{2.6}$$

$$\frac{\mathcal{B}(Z \to \tau^+ \tau^-)}{\mathcal{B}(Z \to e^+ e^-)} = 1.0019 \pm 0.0032, \tag{2.7}$$

all within a 1σ agreement with unity, while the W relative branching fractions are [43]

$$\frac{\mathcal{B}(W^- \to \mu^- \overline{\nu}_\mu)}{\mathcal{B}(W^- \to e^- \overline{\nu}_e)} = 0.993 \pm 0.019, \tag{2.8}$$

$$\frac{\mathcal{B}(W^- \to \tau^- \overline{\nu}_\tau)}{\mathcal{B}(W^- \to e^- \overline{\nu}_e)} = 1.063 \pm 0.027, \tag{2.9}$$

$$\frac{\mathcal{B}(W^- \to \tau^- \overline{\nu}_\tau)}{\mathcal{B}(W^- \to \mu^- \overline{\nu}_\mu)} = 1.070 \pm 0.026, \tag{2.10}$$

where 2.3σ and 2.6σ tensions can be seen between tauonic decays and electronic and muonic decays, respectively, while electron-muon universality holds within 1σ.

More LFU tests have been performed on other sectors, like on $\tau^- \to \ell^- \bar{\nu}_\ell \nu_\tau$ decays [44] or on the (semi)leptonic decays of other mesons, such as J/ψ [45], $K^\pm$ [46], or $D^\pm_{(s)}$ [47]; but none of them have found tensions higher than 2σ with the SM as to date.

2.2.2 SM predictions for $R(D^{(*)})$

$b \to c l^- \bar{\nu}_l$ decays can be described through an effective Hamiltonian, separating the amplitude into a leptonic tensor and a hadronic tensor, which can be parameterised in terms of form factors.

For $B \to D \tau^- \overline{\nu}_\tau$ decays, this hadronic tensor is parameterised with two form factors ($f_{+,0}$), allowing its differential rate to be written as [48]

Table 2.1: List of latest $R(\mathcal{H}_s)$ published results by the LHCb, Belle, and BaBar collaborations, for similar q^2 ranges. To be compared with the SM prediction of $R(\mathcal{H}_s) \approx 1$ [17].

Observable	q^2 range $[\mathrm{GeV}^2/c^4]$	Result	Source
$R(K)$	$(0.10, 8.12)$	$0.74^{+0.40}_{-0.31} \pm 0.06$	BaBar (2012) [20]
	$(1.1, 6.0)$	$0.846^{+0.042+0.013}_{-0.039-0.012}$	LHCb (2021) [18]
	$(1.0, 6.0)$	$1.03^{+0.28}_{-0.24} \pm 0.01$	Belle (2021) [19]
	$(0.045, 1.0)$	$0.994^{+0.090+0.029}_{-0.082-0.027}$	LHCb (2022) [25]
	$(1.0, 6.0)$	$0.949^{+0.042}_{-0.041} \pm 0.022$	LHCb (2022) [25]
$R(K^*)$	$(0.10, 8.12)$	$1.06^{+0.48}_{-0.33} \pm 0.08$	BaBar (2012) [20]
	$(1.1, 6.0)$	$0.69^{+0.11}_{-0.07} \pm 0.03$	LHCb (2017) [21]
	$(1.1, 6.0)$	$0.96^{+0.45}_{-0.29} \pm 0.11$	Belle (2021) [22]
	$(0.045, 6.0)$	$0.70^{+0.18+0.03}_{-0.13-0.04}$	LHCb (2022) [23]
	$(0.045, 1.0)$	$0.927^{+0.093+0.036}_{-0.087-0.035}$	LHCb (2022) [25]
	$(1.0, 6.0)$	$1.027^{+0.072+0.027}_{-0.068-0.026}$	LHCb (2022) [25]
$R(pK)$	$(0.1, 6.0)$	$0.86^{+0.14}_{-0.11} \pm 0.05$	LHCb (2019) [24]
$R(K^0_S)$	$(1.1, 6.0)$	$0.66^{+0.20+0.02}_{-0.14-0.04}$	LHCb (2022) [23]

Table 2.2: List of latest $R(\mathcal{H}_c)$ published results by the LHCb, Belle, and BaBar collaborations. To be compared with the SM predictions on the right-most column.

Observable	Result	Source	SM prediction
$R(D)$	$0.440 \pm 0.058 \pm 0.042$	BaBar (2013) [26, 27]	0.298 ± 0.004 [34]
	$0.307 \pm 0.037 \pm 0.016$	Belle (2020) [28]	
	$0.441 \pm 0.060 \pm 0.066$	LHCb (2022) [36]	
$R(D^*)$	$0.332 \pm 0.024 \pm 0.018$	BaBar (2013) [26, 27]	0.254 ± 0.005 [34]
	$0.336 \pm 0.027 \pm 0.030$	LHCb (2015) [29]	
	$0.283 \pm 0.019 \pm 0.029$	LHCb (2018) [30, 31]	
	$0.283 \pm 0.018 \pm 0.014$	Belle (2020) [28]	
	$0.281 \pm 0.018 \pm 0.024$	LHCb (2022) [36]	
$R(J/\psi)$	$0.71 \pm 0.17 \pm 0.18$	LHCb (2018) [32]	$[0.25, 0.28]$ [37–40]
$R(\Lambda_c)$	$0.242 \pm 0.026 \pm 0.040 \pm 0.059$	LHCb (2022) [33]	0.324 ± 0.004 [41]

$$\frac{\mathrm{d}\Gamma(B \to D\tau^-\overline{\nu}_\tau)}{\mathrm{d}q^2} = \frac{G_F^2|V_{cb}|^2|\vec{\mathbf{p}}_D|q^2}{96\pi^3 m_B^2}\left(1-\frac{m_\tau^2}{q^2}\right)^2\left[|H_0|^2\left(1+\frac{m_\tau^2}{2q^2}\right)+\frac{3m_\tau^2}{2q^2}|H_t|^2\right], \quad (2.11)$$

where $q^2 \equiv (p_D - p_B)^2$ and $H_{0,t}$ are the helicity amplitudes, which are related to the form factors through

$$H_0(q^2) = \frac{2m_B|\vec{\mathbf{p}}_D|}{q^2}f_+(q^2), \quad (2.12)$$

$$H_t(q^2) = \frac{m_B^2 - m_D^2}{\sqrt{q^2}}f_0(q^2). \quad (2.13)$$

For $B \to D^*\tau^-\overline{\nu}_\tau$ decays, four form factors are needed $(g, f, \mathcal{F}_1, \mathcal{F}_2)$, and the decay rate can be written as

$$\frac{\mathrm{d}\Gamma(B \to D^*\tau^-\overline{\nu}_\tau)}{\mathrm{d}q^2} = \frac{G_F^2|V_{cb}|^2|\vec{\mathbf{p}}_{D^*}|q^2}{96\pi^3 m_B^2}\left(1-\frac{m_\tau^2}{q^2}\right)^2 \times \\ \times\left[(|H_{++}|^2+|H_{--}|^2+|H_{00}|^2)\left(1+\frac{m_\tau^2}{2q^2}\right)+\frac{3m_\tau^2}{2q^2}|H_{0t}|^2\right], \quad (2.14)$$

with the helicity amplitudes again related to the form factors by

$$H_{\pm\pm}(w) = f(w) \mp m_B m_{D^*}\sqrt{w^2-1}g(w), \quad (2.15)$$

$$H_{00}(w) = \mathcal{F}_1(w)/\sqrt{q^2}, \quad (2.16)$$

$$H_{0t} = \frac{m_{D^*}\sqrt{w^2-1}}{\sqrt{1+r^2-2rw}}\mathcal{F}_2(w), \quad (2.17)$$

where $r \equiv m_{D^*}/m_B$ and $w \equiv (m_B^2 + m_D^2 - q^2)/(2m_B m_D)$.

With these expressions and their equivalents for $B \to D^{(*)}\ell^-\bar{\nu}_\ell$ decays, the desired branching fraction ratios can be expressed in terms of the form factors with

$$R(D^{(*)}) = \frac{\mathrm{d}\Gamma(B \to D^{(*)}\tau^-\overline{\nu}_\tau)/\mathrm{d}q^2}{\mathrm{d}\Gamma(B \to D^{(*)}\ell^-\bar{\nu}_\ell)/\mathrm{d}q^2}, \quad (2.18)$$

allowing to compute their predicted SM values from form factor calculations.

BGL parameterisation

In order to compute form factors, several parameterisations can be used. The Boyd-Grinstein-Lebed (BGL) parameterisation [49–51] is the form factor parameterisation that is used for the analyses contained in this thesis, it parameterises a generic form factor $f_{(i)}$ as

$$f_{(i)}(z) = \frac{1}{P_{(i)}(z)\,\Phi_{(i)}(z,\mathcal{N})} \sum_{n=0}^{\infty} a_n^{(i)} z^n(w,\mathcal{N}) \tag{2.19}$$

where $z(q^2, t_0)$ is a parametric function that maps the q^2 plane on a unit disk, $P_{(i)}(z)$ and $\Phi_{(i)}(z,\mathcal{N})$ are the Blaschke factors and outer functions[1], respectively; and $\mathcal{N} \equiv (t_+ - t_0)/(t_+ - t_-)$, with $t_\pm \equiv (m_B \pm m_D)^2$ and $t_0 < t_+$ being a free parameter which determines the point of the q^2 plane mapped onto the origin of the z plane. The parameters $a_n^{(i)}$ are constrained by the condition

$$\sum_{n=0}^{\infty} (a_n^{(i)})^2 < 1. \tag{2.20}$$

In practice, the sum in equation 2.19 is truncated at a certain low number N (in this thesis, $N = 2$ is used). The BGL parameters can be estimated from lattice-QCD calculations and from experimental data.

Status of SM predictions

Predicted values for $R(D)$ and $R(D^*)$ were derived by several collaborations, mainly using fits to lattice-QCD calculations and experimental data. Their results are listed on table 2.3. The averages of these predictions, as computed by [34], are

$$R(D)_{\text{SM}} = 0.298 \pm 0.004 \tag{2.21}$$

and

$$R(D^*)_{\text{SM}} = 0.254 \pm 0.005, \tag{2.22}$$

both predictions being below the current average of experimental results by 2.16σ and 2.26σ, respectively. Taking into account the correlation between both experimental quantities, the difference with these predictions sums up to 3.2σ. This comparison between experimental results and theoretical predictions are graphically represented on figure 2.1.

2.2.3 Theoretical implications of LFU violation

If a violation of lepton flavour universality in B mesons decaying into tauons was to be confirmed, it would imply that there are NP contributions to these decays (new interacting particles) which are not flavour universal. Some of these NP possibilities are discussed here. Note that everything that is discussed here is only what pertains to $b \to c l^- \bar{\nu}_l$ decays, due to their relevance to this thesis, but similar and equally interesting discussions exist for $b \to s l^+ l^-$ decays, some theoretical approaches even simultaneously covering both types of decays.

[1] Blaschke factors and outer functions are mathematical products used in complex analysis, constructed to deal with poles in functions and, applied to this case, depend on the spin and parity (J^P) of each form factor and its corresponding B_c resonances [50, 51].

Table 2.3: List of currently published SM predictions for $R(D)$ and $R(D^*)$.

Source	$R(D)_{\mathrm{SM}}$	$R(D^*)_{\mathrm{SM}}$
Fermilab Lattice, MILC collaborations (2015) [52]	0.299 ± 0.011	–
HPQCD collaboration (2015) [53]	0.300 ± 0.008	–
D. Bigi, P. Gambino (2016) [54]	0.299 ± 0.003	–
F. Bernlochner *et al.* (2017) [55]	0.299 ± 0.003	0.257 ± 0.003
S. Jaiswal, S. Nandi, S.K. Patra (2017) [56]	0.299 ± 0.004	0.257 ± 0.005
D. Bigi, P. Gambino, S. Schacht (2017) [57]	–	0.260 ± 0.008
P. Gambino, M. Jung, S. Schacht (2019) [58]	–	$0.254^{+0.007}_{-0.006}$
BaBar collaboration (2019) [59]	–	0.253 ± 0.005
M. Bordone, M. Jung, D. van Dyk (2020) [60]	0.298 ± 0.003	0.247 ± 0.006
M. Bordone, M. Jung, D. van Dyk (2020) [60]	0.297 ± 0.003	0.250 ± 0.003
Fermilab Lattice, MILC collaborations (2021) [61]	–	0.265 ± 0.013
G. Martinelli, S. Simula, L. Vittorio (2022) [62]	0.296 ± 0.008	0.261 ± 0.020

Effective Field Theory studies

One way to explore the possible contributions of NP is by using the effective Hamiltonian:

$$\mathcal{H}_{\mathrm{eff}}(b \to c l^- \bar{\nu}_l) = \frac{4G_F}{\sqrt{2}} V_{cb} \sum_i \mathcal{C}_i \mathcal{O}_i, \tag{2.23}$$

where $\mathcal{O}_i$ are 4-fermion operators which encode the different processes by which the decay may occur; $\mathcal{C}_i$ are Wilson coefficients, which indicate the relative coupling strength of each one of the possible processes, and i is an index that runs over all the 4-fermion operators. In the standard model, the Wilson coefficients should have the same value for all three lepton families, due to LFU.

Since the Wilson coefficients can be computed from experimental data, and different theoretical scenarios beyond the SM (BSM) give different values to them, it is useful to express Wilson coefficients as $\mathcal{C}_i = \mathcal{C}_i^{\mathrm{SM}} + \mathcal{C}_i^{\mathrm{NP}}$, where $\mathcal{C}_i^{\mathrm{SM}}$ is the value expected from the SM and $\mathcal{C}_i^{\mathrm{NP}}$ is a hypothetical NP contribution. Within this framework, data can be used to constrain the value of each $\mathcal{C}_i^{\mathrm{NP}}$, and thus constraining or discarding possible NP scenarios [63].

Proposed models

Some of the BSM models which are most commonly used to describe the hypothetical breaking of LFU on $b \to c l^- \bar{\nu}_l$ decays and that can fit with the existing Wilson coefficient measurements are:

- A new vector boson, $W'^{\pm}$ which couples differently to the τ lepton, some models also including its coupling to a right-handed neutrino [64–69].

- The existence of a charged Higgs boson, $H^{\pm}$, in what is called a two-Higgs doublet model (2HDM) which would also mediate weak interactions with different couplings to each lepton [48, 70–76].
- Leptoquarks (LQ), hypothetical bosons with strong and electroweak charge which allow quarks to turn into leptons and *vice versa* [77–81].

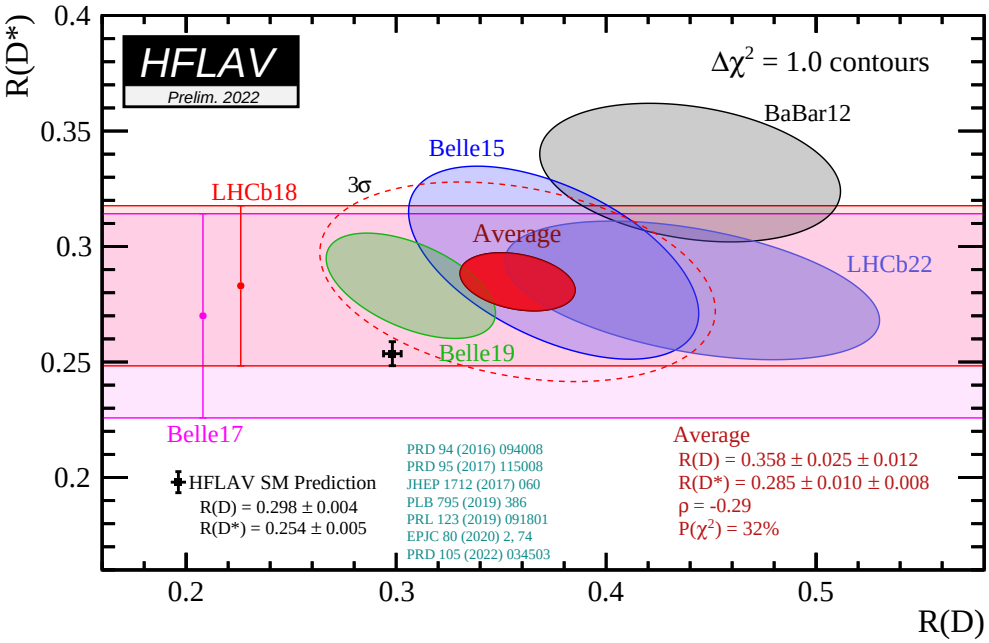

Figure 2.1: Experimental results and theoretical predictions comparison for $R(D)$ and $R(D^*)$ as of 2022. Plot extracted from [34].

2.3 Theory of pp collisions

Since the data analysed in this thesis comes from proton-proton collisions at the LHC (see section 3.1), it is interesting to briefly introduce some theory concepts behind such collisions.

2.3.1 Rapidity and pseudorapidity

We define the concept of a particle's *rapidity* (y) as

$$y \equiv \frac{1}{2} \ln \frac{E + p_z c}{E - p_z c}, \tag{2.24}$$

where $E = \gamma mc^2$ is the energy of the particle and p_z is the component of its momentum along the beam axis (the direction in which the protons travel and collide). Rapidity measures the magnitude of the relativistic boost of the particle in the beam direction with respect to the laboratory frame of reference. Thus $y = 0$ is a particle that travels perpendicularly to the colliding protons and $y = \pm\infty$ is a particle that travels in the same direction as the protons. Another useful property of rapidity is that rapidity differences (Δy) are Lorentz-invariant under boosts in the beam direction.

An alternative to rapidity, commonly used in experimental particle physics, is *pseudo-rapidity* (η), defined as

$$\eta \equiv \frac{1}{2} \ln \frac{p + p_z}{p - p_z} = -\ln \left[\tan \frac{\theta}{2} \right], \tag{2.25}$$

where p is the magnitude of the particle's 3-momentum and θ is the angle between the trajectory of the particle and that of the colliding protons. This quantity has the advantage of not requiring the mass/energy of the particle, while being equivalent to rapidity for massless particles and being approximately equal to rapidity for particles with $p_T \gg m$. Since pseudorapidity can be determined only with the particle's angle, it is useful in particle colliders, where the expressions 'low-rapidity' or 'high-rapidity regions' are often used to refer to the detector regions perpendicular or close to the beam axis direction, respectively.

Pseudorapidity is also used to define the angular separation between two particles,

$$\Delta R \equiv \sqrt{\Delta\eta^2 + \Delta\phi^2}\ , \tag{2.26}$$

where $\Delta\eta$ and $\Delta\phi$ are, respectively, the differences in pseudorapidity and azimuthal angle between the two particles. Like $\Delta\eta$, the quantity ΔR is also Lorentz-invariant in the massless limit.

2.3.2 Centre-of-mass energy ($\sqrt{s}$)

The centre-of-mass energy of two colliding particles is denoted by

$$\sqrt{s} = \sqrt{(p_a + p_b)^2}c, \tag{2.27}$$

where p_a and p_b are the four-momenta of each particle. In the case of pp collisions in the LHC, with two symmetrically colliding particles, the centre-of-mass energy is equivalent to the energy in the laboratory frame of reference. It is important to note, though, that the particles produced in these collisions often come from parton-parton collisions within the colliding protons, which are not symmetrical in the laboratory frame [82].

The notation "$\sqrt{s}$" comes from the so-called Mandelstam variables, quantities which are defined in a two-particle scattering process of the form $a + b \to c + d$ as

$$\begin{aligned} s &\equiv (p_a + p_b)^2 c^2, \\ t &\equiv (p_a - p_c)^2 c^2, \\ u &\equiv (p_a - p_d)^2 c^2. \end{aligned} \tag{2.28}$$

These quantities are all Lorentz-invariant, thus their usefulness in high-energy physics.

2.3.3 Proton-proton collision types

Proton collisions can be categorized in two types: elastic and inelastic. Elastic interactions do not produce new particles, the two protons simply altering their trajectories upon interacting. On the other hand, inelastic interactions do produce new particles, either with one or both protons surviving, or none of them. The inelastic cross-section of pp interactions at a centre-of-mass energy of $\sqrt{s} = 13$ TeV is $\sigma_{\text{inel}} = 75.4 \pm 5.4$ mb [83].

Inelastic interactions are at the same time categorized in diffractive and non-diffractive. Diffractive inelastic interactions can be:

- Single diffractive scattering: one of the protons remains while the other dissociates and hadronises, resulting in a highly boosted set of particles.
- Double diffractive scattering: both protons dissociate and hadronise, resulting in two opposite highly boosted set of particles.
- Central diffractive scattering: both protons remain in the final state, but a set of particles is produced in the low-rapidity region.

The particle systems produced in a diffractive interaction remain with the same internal quantum numbers of the proton that produced them. On the other hand, in non-diffractive interactions, colour charge is exchanged between both protons, resulting in producing a larger number of particles, which are distributed more or less uniformly in the whole rapidity range. Non-diffractive interactions account for roughly ∼60% of all proton-proton interactions at LHC energies [84]. Fig. 2.2 illustrates the different types of inelastic pp interactions.

2.3.4 b quark production

The production of $b\bar{b}$ pairs from inelastic pp collisions is the main interest of the LHCb experiment and it is a widely exploited feature by its analyses, including the ones presented within this thesis.

The $pp \to b\bar{b}X$ reaction is produced mainly from gluon-gluon and quark-quark interactions within the colliding protons. Since the momenta of these interacting partons tend to be highly asymmetrical in the laboratory frame [82], the produced $b\bar{b}$ pairs are emitted at very high rapidities, close to the direction of the proton beam. This feature is exploited by the LHCb detector's configuration, as will be shown on section 3.2. The $b\bar{b}$ pair production angular distribution is shown on fig. 2.3.

The $b\bar{b}$ pair production cross-section at $\sqrt{s} = 13$ TeV is measured to be $\sigma(pp \to b\bar{b}X) \approx 560$ μb [87], or $\sigma = 144 \pm 21$ μb if restricted to the LHCb acceptance range ($2 < \eta < 5$).

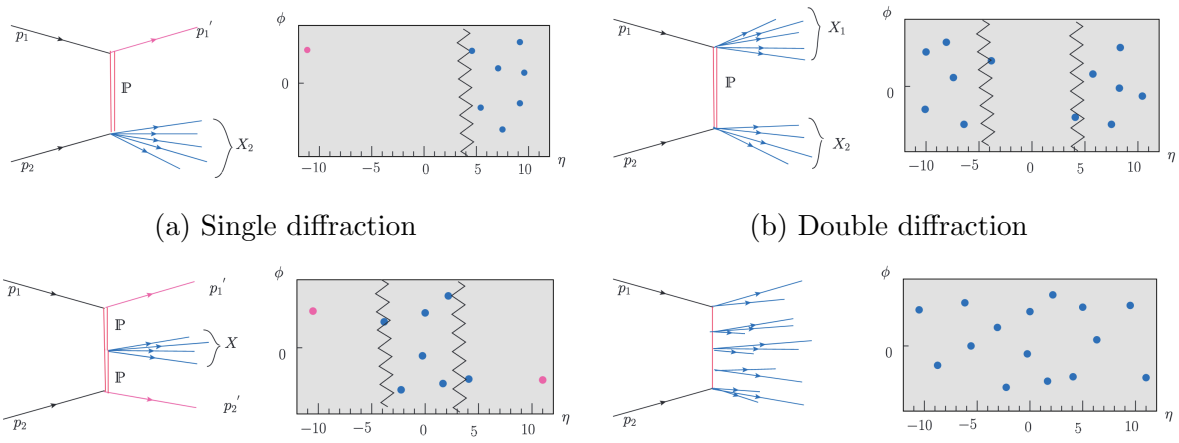

(a) Single diffraction

(b) Double diffraction

(c) Central diffraction

(d) Non-diffractive process

Figure 2.2: Feynman diagrams and angular distributions of different types of pp inelastic interactions. Figures extracted from [85].

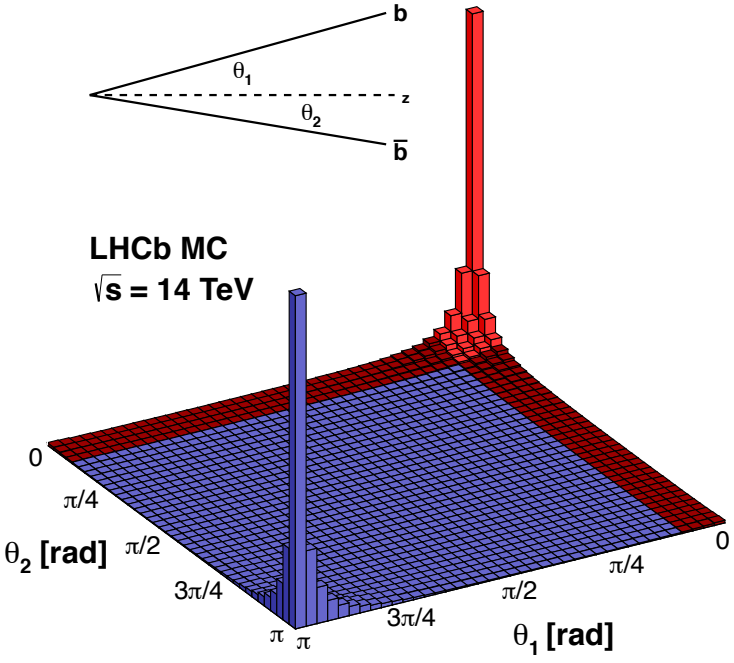

Figure 2.3: $b\bar{b}$ pair production angular distribution. The LHCb acceptance is represented in red. Figure extracted from [86].

2.4 $R(D^{(*)})$ measurements at LHCb

As mentioned in section 2.2.1, the LHCb experiment is one of the main contributors to the current LFU tests scene. Due to the relevance for the topic of this thesis, it is worth reviewing the current status, techniques, and prospects of the $R(D^{(*)})$ measurements at LHCb.

As explained earlier, LHCb tests LFU on semitauonic decays by measuring the ratio $R(\mathcal{H}_c)$ (eq. 2.5) between the tauonic and muonic modes, which for $R(D^{(*)})$ takes the form:

$$R(D^{(*)}) = \frac{\mathcal{B}(B \to D^{(*)}\tau^-\overline{\nu}_\tau)}{\mathcal{B}(B \to D^{(*)}\mu^-\overline{\nu}_\mu)}, \tag{2.29}$$

where the B meson will either be a B^+ or a B^0 depending on the sign of the $D^{(*)}$. Since the τ lepton decays inside the detector, a decay channel needs to be chosen, the two common choices at LHCb being:

- $\tau^- \to \mu^-\overline{\nu}_\mu\nu_\tau$ (muonic channel): provides the advantage of having the same charged final-state particles in both sides of the ratio, thus reducing systematic uncertainties. It suffers from the presence of background from inclusive $B \to D^{(*)}\mu^-\overline{\nu}_\mu(X)$ decays.
- $\tau^- \to \pi^-\pi^+\pi^-\nu_\tau(\pi^0)\nu_\tau$ (hadronic or "three-prong" channel): offers better momentum reconstruction, thanks to only having one neutrino and having three charged tracks, which allow the reconstruction of the τ decay vertex.

Muonic measurements

At the present time, there is only one published result of $R(D^*)$ by LHCb using the muonic channel [29], which was done with Run 1 data. LHCb is currently working on new $R(D^{(*)})$ and $R(D_s^*)$ analyses with data from Run 2. The strategy behind the existing result is explained below, while the analyses that are underway follow an almost identical strategy.

Due to the presence of two neutrinos in the final state, the B momentum is approximated by assuming that the z-momentum of the B meson is the same as that of the $D^*\mu$ system. Both the tauonic and the muonic channels are selected in the same sample using multivariate analysis techniques to reduce background contributions. A three-dimensional fit in the energy of the muon, the squared missing mass ($m^2_{\text{miss}} = (p_B - p_{D^*} - p_\mu)^2$), and q^2 is used to extract the yields of both signal channels. The result, as shown previously on table 2.2, was $R(D^*) = 0.336 \pm 0.027(\text{stat}) \pm 0.030(\text{syst})$, which is 2.1σ above the SM prediction.

Hadronic measurements

The only currently published result of $R(D^{(*)})$ by LHCb using the hadronic channel is $R(D^{*-})$ [30, 31], done with Run 1 data. There are other hadronic analyses by LHCb

(including the ones presented in this thesis) working to measure $R(D^{(*)})$, $R(D_s^{(*)})$ and $R(D^{**})$, using Run 2 data. All current analyses follow a similar strategy to the published one, explained below.

The measurement using the hadronic channel is made by measuring the ratio of the tauonic decay channel with respect to the prompt decay channel,

$$\mathcal{K}(D^{*-}) \equiv \frac{\mathcal{B}(B^0 \to D^{*-}\tau^+\nu_\tau)}{\mathcal{B}(B^0 \to D^{*-}\pi^+\pi^-\pi^+)}. \tag{2.30}$$

This is done to minimize the systematic uncertainties in the ratio, by having the same final-state particles in both sides. A different normalisation channel may be chosen instead of the prompt channel, depending on the requirements of the analysis.

Then, the known values of the branching fractions of the muonic and normalisation channels are used as external inputs to determine the value of the desired observable,

$$R(D^*) = \frac{\mathcal{B}(B^0 \to D^{*-}\pi^+\pi^-\pi^+)}{\mathcal{B}(B^0 \to D^{*-}\mu^+\nu_\mu)}\mathcal{K}(D^{*-}). \tag{2.31}$$

The ability to reconstruct the τ vertex is exploited to separate signal and normalisation channels, and a boosted decision tree (BDT) is used to suppress background. The yield of the signal is obtained through a three-dimensional fit in q^2, τ decay time, and the output of the BDT, and the normalisation yield is obtained by fitting the invariant mass of the $D^*3\pi$ system. The result of this measurement, as shown previously on table 2.2, was $R(D^*) = 0.291 \pm 0.019(\text{stat}) \pm 0.029(\text{syst})$, 1.1σ above the SM prediction.

2.4.1 Prospects

New measurements with smaller uncertainties are essential in order to clarify the current tensions with the SM predictions, which are currently at 3.2σ, as discussed on section 2.2.1. Since all previous analyses by LHCb were done with just Run 1 data, LHCb is at a prime position to improve its contribution by adding the data from Run 2, which contains approximately double the integrated luminosity and four times as many $b\bar{b}$ events compared to Run 1, thus expecting a significant reduction in statistical uncertainty. Regarding systematic uncertainties, they are expected to improve as well [35,88]. Fig. 2.4 shows an estimation of the possible uncertainties of future LHCb $R(\mathcal{H}_c)$ measurements.

The main source of systematic uncertainty in these measurements is the limited size of the simulated samples. These samples are essential for these analyses because of the nature of the decays involving multiple neutrinos: since they are undetected, the reconstructed kinematic variables have broad distributions, difficult to be described analytically, thus relying on simulated samples to model the different contributions. Furthermore, these samples need to be significantly large due to the use of multiple fitting dimensions, reducing the amount of data per bin. This situation is going to improve along with the development of better simulation techniques, notably fast simulation, which will allow to

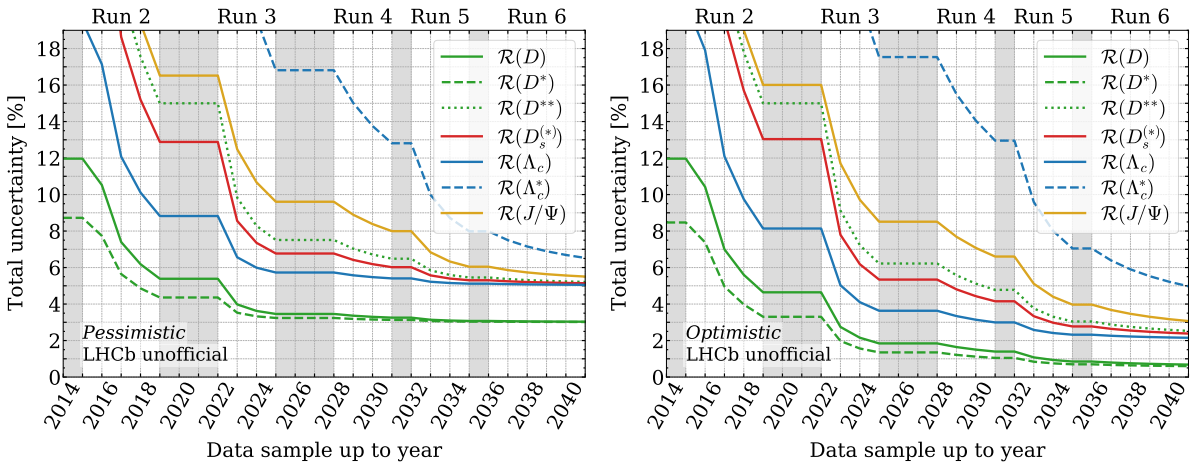

Figure 2.4: Expected total uncertainty for different $R(\mathcal{H}_c)$ measurements by LHCb, by data-taking years. Left: systematic uncertainty capped at 3% for $R(D^{(*)})$ and 5% for other ratios. Right: systematic uncertainty capped at 0.5% for $R(D^{(*)})$ and 2% for other ratios. Figure extracted from [35].

produce larger samples in less time. Other important sources of systematic uncertainty are the modeling of background channels and the external uncertainties. Both are expected to improve with new measurements, improving both the knowledge of background channels and the uncertainty of the measurements.

2.5 Analysis strategy

This section details the strategy followed to measure $R(D^{(*)0})$ and $R(D^{(*)-})$ within these analyses.

$R(D^{(*)0})$ measurement

As discussed previously, the main goal of this analysis is the measurement of the $R(D^0)$ and $R(D^{*0})$ quantities.

$$R(D^{(*)0}) = \frac{\mathcal{B}(B^- \to D^{(*)0}\tau^-\overline{\nu}_\tau)}{\mathcal{B}(B^- \to D^{(*)0}\mu^-\overline{\nu}_\mu)} \,, \tag{2.32}$$

with LHCb's Run 2 data from 2016–2018, and with the following decay modes:

$$\begin{aligned} D^{*0} &\to D^0\{\pi^0, \gamma\}, \\ D^0 &\to K^-\pi^+, \\ \tau^- &\to \pi^-\pi^+\pi^-(\pi^0)\nu_\tau. \end{aligned}$$

As such, the approach taken is very similar to the previous hadronic-tau measurement from LHCb [30,31] shown in section 2.4; the main difference being that this analysis aims to measure both $R(D^0)$ and $R(D^{*0})$ simultaneously, while the previous analysis only measured $R(D^*)$. This is possible thanks to the increased statistics available with Run 2 data compared to Run 1.

The denominator in eq. 2.32, $\mathcal{B}(B^- \to D^{(*)0}\mu^-\overline{\nu}_\mu)$, will be taken from an external source, while the numerator, $\mathcal{B}(B^- \to D^{(*)0}\tau^-\overline{\nu}_\tau)$, will be computed from our measurement as

$$\mathcal{B}(B^- \to D^{(*)0}\tau^-\overline{\nu}_\tau) = \frac{N_{B^-\to D^{(*)0}\tau^-\overline{\nu}_\tau}}{N_{B^+\to\overline{D}^0 D_s^+}} \times \mathcal{B}(B^+ \to \overline{D}^0 D_s^+)\times \\ \times \frac{\varepsilon_{B^+\to\overline{D}^0 D_s^+}\mathcal{B}(D_s^+ \to \pi^+\pi^-\pi^+)}{\varepsilon^{\tau\to 3\pi\nu_\tau}_{B^-\to D^{(*)0}\tau^-\overline{\nu}_\tau}\mathcal{B}(\tau^- \to \pi^-\pi^+\pi^-\nu_\tau) + \varepsilon^{\tau\to 3\pi\pi^0\nu_\tau}_{B^-\to D^{(*)0}\tau^-\overline{\nu}_\tau}\mathcal{B}(\tau^- \to \pi^-\pi^+\pi^-\pi^0\nu_\tau)}, \quad (2.33)$$

where N are the measured yields of each decay channel and ε, their efficiencies. The yields are the actual quantities which are measured from data, while the efficiencies are estimated from simulation samples. All the other branching fractions are external inputs. This is done, as in the Run 1 analysis, to minimize systematic uncertainties by computing the ratio of two decay channels with the same visible final states and topology ($B^- \to D^{(*)0}\tau^-\overline{\nu}_\tau$ with $\tau^- \to \pi^-\pi^+\pi^-(\pi^0)\nu_\tau$ and $B^+ \to \overline{D}^0 D_s^+$ with $D_s^+ \to \pi^+\pi^-\pi^+$, and both with $D^0 \to K^-\pi^+$). $B^+ \to \overline{D}^0 D_s^+$ was chosen as a normalisation channel because of the precision with which it is measured [2] compared to other possible candidates such as $B^- \to D^0\pi^-\pi^+\pi^-$:

$$\begin{aligned} \mathcal{B}(B^+ \to \overline{D}^0 D_s^+) &= 0.0090 \pm 0.0009\ , \\ \mathcal{B}(D_s^+ \to \pi^+\pi^-\pi^+) &= 0.0108 \pm 0.0004\ , \\ \mathcal{B}(B^- \to D^0\pi^-\pi^+\pi^-) &= 0.0056 \pm 0.0021\ . \end{aligned} \quad (2.34)$$

A general rundown of the strategy, which will be expanded upon throughout this thesis, is presented below.

1. **Generation of simulation samples** (section 4.2): multiple simulation samples are produced, containing the main signal and background decays. These are mainly used for efficiency computation and background description.

2. **Data selection** (section 4.3): inclusive $B \to D^0\pi^-\pi^+\pi^-(X)$ events, with $D^0 \to K^-\pi^+$, are selected from the available 2016–2018 data and from the generated simulation samples. In summary: three charged pions are required to form a good vertex (the τ vertex) and the three pions and the D^0 are also required to form a good vertex (the B vertex), and these two vertices are required to be well differentiated in order to reduce background contributions. A Boosted Decision Tree (BDT)

is implemented to discriminate the main remaining backgrounds. Two different selections are applied: one for the signal channel ($B^- \to D^{(*)0}\tau^-\overline{\nu}_\tau$) and another for the normalisation channel ($B^+ \to \overline{D}^0 D_s^+$).

3. **Optimisation of the simulation samples** (section 4.5): a set of corrections is applied to the simulation samples in order to improve their description of the data. These include the re-weighting of particle identification (PID) variables, B kinematics, event multiplicity, trigger efficiency, form factors, and a correction on the resolution of the B and 3π vertices.

4. **Computation of efficiencies** (section 4.6): the simulated samples are used to compute the reconstruction efficiencies of each channel.

5. **Study of control samples** (chapter 5): a set of complementary selections is used to obtain samples enriched with the main background events, which are used to determine further corrections to the simulation samples in those particular background channels. Particularly, the main double-charm backgrounds ($B \to \overline{D}^0 D_s^+(X)$, $B \to \overline{D}^0 D^+(X)$, and $B \to \overline{D}^0 D^0(X)$) and the prompt $B \to D^0 3\pi(X)$ background are studied.

6. **Determination of the signal yields** (section 6.1): the yields of the $B^- \to D^{(*)0}\tau^-\overline{\nu}_\tau$ signal channels are obtained from a three-dimensional template fit on the q^2, the τ decay time, and the output of the BDT.

7. **Determination of the normalisation yield** (section 6.2): the yield of the $B^+ \to \overline{D}^0 D_s^+$ normalisation mode is obtained from a fit to the invariant mass $m(\overline{D}^0 D_s^+)$ peak.

8. **Study of systematic effects and uncertainties** (chapter 7): the different possible sources of systematic effects, errors, and uncertainties in the measured yields are studied, and the resulting corrections are applied.

9. **Measurement of the $B^- \to D^{(*)0}\tau^-\overline{\nu}_\tau$ branching fractions, $R(D^0)$, and $R(D^{*0})$** (chapter 8): the desired branching fractions and LFU ratios are computed using eqs. 2.32 and 2.33 with the measured yields, the computed efficiencies, and the needed external inputs.

$R(D^{(*)-})$ measurement

A second analysis, aiming to measure the $R(D^-)$ and $R(D^{*-})$ quantities, will also be partially discussed throughout this thesis, in parallel to the previous one. This analysis follows practically the same general strategy and workflow of $R(D^{(*)0})$, the only main differences being the used signal channel, which is $B^0 \to D^{(*)-}\tau^+\nu_\tau$ with the decay modes

$$
\begin{aligned}
D^{*-} &\to D^{-}\{\pi^0, \gamma\}, \\
D^{-} &\to K^{+}\pi^{-}\pi^{-}, \\
\tau^{+} &\to \pi^{+}\pi^{-}\pi^{+}(\pi^0)\overline{\nu}_{\tau};
\end{aligned}
$$

and the data selection procedure, which needs to select D^- mesons with $D^- \to K^+\pi^-\pi^-$ instead of $D^0 \to K^-\pi^+$.

Because of the big similarity between the two analyses, this one was left in a second plane, with the intention of first perfecting the $R(D^{(*)0})$ measurement procedure and then directly transferring the developed and optimised algorithms to this $R(D^{(*)-})$ analysis, thus minimising the needed effort and parallel work. As a result, only a handful of steps —in a preliminary status— are presented in this thesis: the generation of simulation samples (section 4.2), the data selection (section 4.3), and the study of control samples (chapter 5).

3

The LHCb experiment at the LHC

Contents

In this chapter, an overview of the experimental setup used for this thesis is presented. Namely, the Large Hadron Collider and the layout and characteristics of the LHCb detector, along with a summary of the relevant software used within the LHCb experiment.

3.1 The Large Hadron Collider

The Large Hadron Collider (LHC) [89] is a hadron accelerator and collider composed of two rings installed in a 26.7 km tunnel between the French and Swiss border near

Geneva, between 45 m and 170 m depth, originally used for the Large Electron-Positron collider (LEP). The LHC was built at CERN, with its accelerator complex acting as particle injector for the collider.

The LHC was designed to operate at centre-of-mass energies up to 14 TeV, accelerating two proton beams rotating in opposite directions inside its two rings. These beams are kept in their circular trajectory by LHC's superconducting magnets, which are kept at a temperature of 1.9 K using superfluid helium to ensure their performance, with fields above 8 T.

The protons in the LHC are obtained from ionised hydrogen and injected into LHC through a series of accelerators composed of: Linear Accelerator 2 (Linac2), Proton Synchrotron Booster (PSB), Proton Synchroton (PS), and Super Proton Synchrotron (SPS).

The hadron beams at the LHC are composed of "bunches", small groups of hadrons which are distributed along the LHC rings. In the proton-proton configuration, bunches might be down to 25 ns apart, resulting in a crossing frequency of up to 40 MHz.

LHC was also designed to collide heavy ions. The heavy-ion collisions produced so far include p-Pb, Pb-Pb, and Xe-Xe. These collisions take place on dedicated separate runs from the regular pp runs.

The LHC has four main experiments located at large caverns along the tunnel, these being: ALICE (A Large Ion Collider Experiment), ATLAS (A Toroidal LHC Apparatus), CMS (Compact Muon Solenoid), and LHCb (Large Hadron Collider beauty). The beams are slightly deviated at these four points of the tunnel in order to induce the collisions inside the detectors of these experiments. The location of these experiments within the LHC, as well as the rest of the CERN accelerator complex layout, is shown on fig. 3.1.

ALICE [91] is a heavy-ion detector which focuses on QCD, operating mainly with heavy-ion collisions, thus being designed to deal with the high particle multiplicities which are expected of heavy-ion collisions.

ATLAS [92] and CMS [93] are general-purpose detectors with similar configurations and scientific goals. Their main achievement has been the discovery of the Higgs boson in 2012 [3, 4], and they mainly research the properties of the Higgs boson and the existence of particles beyond the Standard Model.

LHCb [94] was designed to study B physics, and will be explained in detail in the following section.

At the time of writing this thesis, the LHC has had two full operational runs: Run 1, from 2009 to 2013, with a pp collision centre-of-mass energy of 7–8 TeV, and Run2, from 2015 to 2018, with a centre-of-mass energy of 13 TeV. The LHC is currently on its third operational run (Run 3), which began on July 2022 and is planned to end on 2026, running at a centre-of-mass energy of 13.6 TeV.

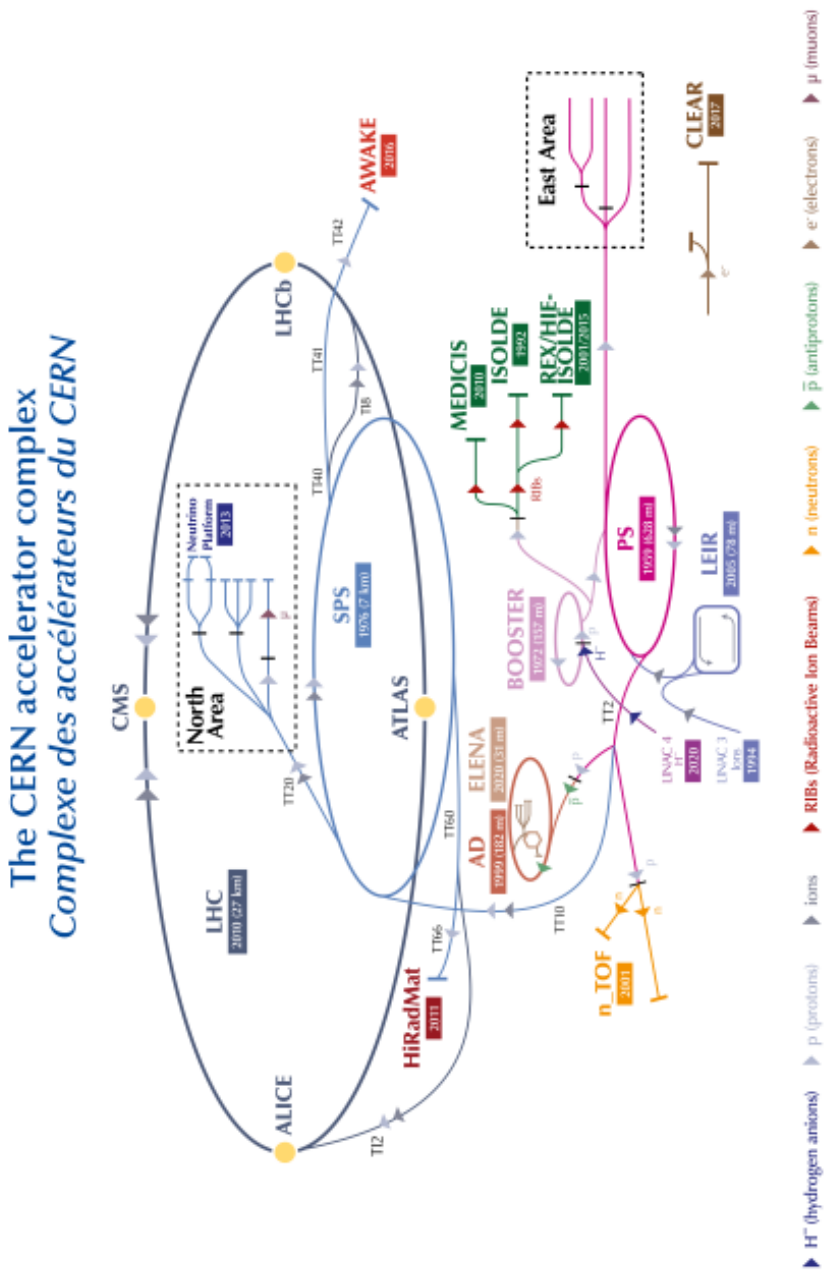

Figure 3.1: Layout of the CERN accelerator complex as of 2022. Image extracted from [90].

3.2 The LHCb detector

The LHCb experiment is located at point 8 of the LHC, reusing the cavern where DELPHI (Detector with Lepton, Photon and Hadron Identification) [95] operated in times of the LEP. LHCb's focus is the search for physics beyond the Standard Model, mainly through CP violation and rare decays in beauty and charm decays.

The LHCb detector is a single-arm spectrometer with an acceptance of $1.6 \leq \eta \leq 4.9$ [94] (where η is the pseudorapidity, as defined on section 2.3.1), which corresponds to an angular acceptance of 10 mrad $\leq \theta \leq$ 300 mrad. This forward configuration is the main distinguishing characteristic of LHCb compared to the other three main LHC experiments, its reason being the optimization to cover the produced b hadrons which are highly boosted at the LHC energies in proton-proton collisions, and thus predominantly produced in a low-angle cone in the beam direction, as seen on fig. 2.3.

LHCb was designed to run at an instantaneous luminosity of around $2\text{–}4\times10^{32}/\text{cm}^2/\text{s}$, lower than the LHC in general ($\sim10^{34}/\text{cm}^2/\text{s}$). This is achieved by tuning the beam focus at its interaction point. This lower luminosity provides multiple advantages for LHCb, namely: an average of 1–2 pp collisions per bunch crossing [96] (less background due to multiple collisions, compared to the $\sim$20 collisions per crossing that the LHC provides), a lower occupancy in the detector, and reduced radiation damage. By taking into account the $b\bar{b}$-production cross-section (section 2.3.4), this instantaneous luminosity provides an estimated number of $\sim4\times10^4$ $b\bar{b}$ pairs per second within the LHCb acceptance, at $\sqrt{s} = 13$ TeV.

LHCb has so far recorded data corresponding to a total integrated luminosity of 8.7 fb^{-1}, with 3.0 fb^{-1} on Run 1 and 5.7 fb^{-1} on Run 2. A graphical representation of LHCb's data-taking runs is shown on fig. 3.2.

An essential key of most LHCb analyses is being able to separate the B decay vertex (often called secondary vertex or SV) from the pp collision vertex (primary vertex or PV). This allows the identification of background decays that originate directly from the pp collision. This is achieved thanks to the low multiplicity of events, the large flight distance of b hadrons ($\sim$7 mm [82]), and the excellent vertex resolution of the detector.

Another important characteristic of LHCb is its trigger system, which needs to be able to deal with the large number of b hadrons that are generated and the many different final states which are studied at LHCb.

The LHCb detector is composed of several subdetectors which will be detailed in the following subsections. Their general layout is shown on figure 3.3.

The LHCb experiment uses a specific coordinate system which will be used throughout this thesis: the pp interaction point is set as the origin, with the z axis running along the beam axis towards the rest of the detector system. The y axis is the upwards vertical direction, as defined by gravity, and the direction of the x axis is chosen as to keep the "right-handedness" of the system ($\hat{x} \times \hat{y} = \hat{z}$), resulting in it running horizontally towards the left of the detector, when looking at it from the negative-z side. The "transverse momentum" (p_T) of a particle is also commonly used, defined within this coordinate

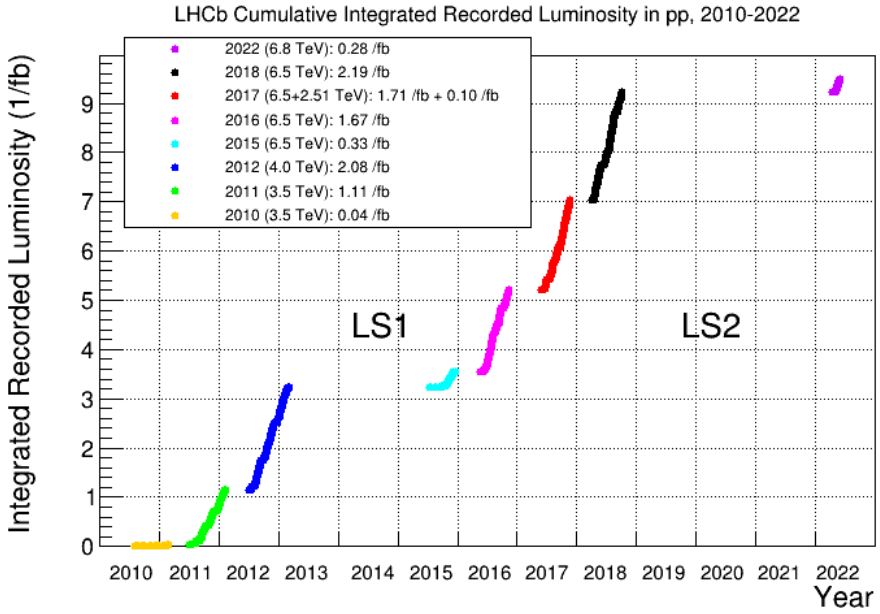

Figure 3.2: LHCb recorded integrated luminosity in pp collisions from 2010 to 2022. Plot extracted from [97].

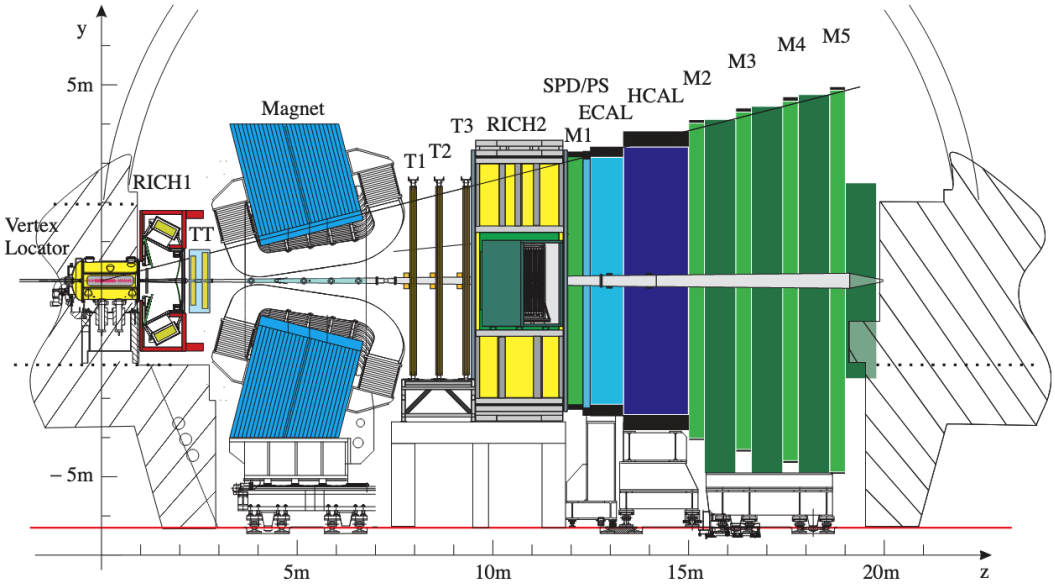

Figure 3.3: LHCb detector layout. Image extracted from [98].

system as $p_T = \sqrt{p_x^2 + p_y^2}$.

It is important to note that the LHCb detector which was used for the analyses in this thesis and which is described here has been replaced by an upgraded detector [99]

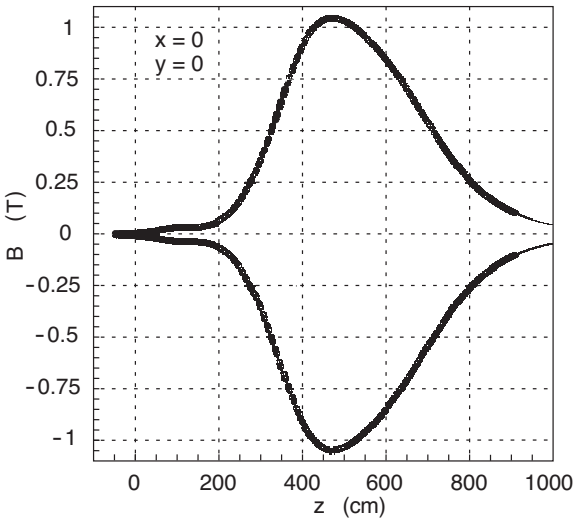

Figure 3.4: Measured vertical component of the dipole magnet's field along the z axis, for both polarities. Plot extracted from [94].

during the LHC's 2nd long shutdown (LS2), which started on December 2018. The new detector has already started taking data on the LHC Run 3 beginning in July 2022. The main goal of this upgrade is to allow data-taking at a higher instantaneous luminosity of around $2 \times 10^{33}/\text{cm}^2/\text{s}$, for which the trigger system has been changed to be fully software, and the tracking equipment has been replaced entirely.

3.2.1 Magnet

A dipole magnet with saddle-shaped coils creates a magnetic field in the vertical direction in the central region of the detector. This field deflects charged particles in the horizontal plane, allowing for the measurement of their momentum. Its design aims to maximise the field in the region between the vertex locator and the Trigger Tracker station, while minimising its effect on the RICH detectors. The integrated magnetic field or bending power is 4 Tm, integrated over the first 10 m from the interaction point in the beam direction [100]. The direction of the magnetic field (up or down) is changed periodically in order to take into account possible systematic effects.

The magnetic field needs to be precisely measured in order to achieve the needed relative momentum resolution for charged particles of about 0.4%. For this, the field has been mapped in the volumes inside the magnet, the VELO region, the tracking stations, and inside the magnetic shielding for the RICH detectors. The result of this measurement along the z axis is shown on fig. 3.4; its relative precision was 4×10^{-4} [94].

The presence of the LHCb dipole magnet affects the trajectory of the beams circulating in the LHC, so three compensator magnets are placed around the detector to counter this effect [89].

3.2.2 Tracking system

The tracking system of LHCb is composed of the VELO, placed around the interaction point, the TT, upstream of the magnet, and the T-stations, downstream of the magnet. Together, these subdetectors provide the necessary data to reconstruct the trajectory of the particles that traverse the detector, as will be detailed on section 3.3.

VELO

The Vertex Locator (VELO) is the closest subdetector to the interaction point, providing precise measurements of tracks near the primary vertex and thus allowing to identify and locate the primary and secondary vertices, essential feature of b and c-hadron decays.

The VELO consists of 42 modules of silicon strip sensors (300 μm thick), each module with one part that measures the radial coordinate (R-sensor) and another which measures the azimuthal angle (ϕ-sensor). The readouts are placed in the outer part of the modules. The use of this coordinate system ($r\phi$) was chosen to allow a fast track reconstruction in the software trigger.

The sensors are maintained in a vacuum which is separated from the LHC vacuum by a thin walled corrugated aluminum sheet. The geometry is designed as to allow the two halves of the VELO to overlap when it is fully closed, and it minimises the material traversed by a charged particle from the interaction point to the sensors. Schematics of the VELO are shown on fig. 3.5.

The two halves of the VELO detector are designed to be retractable, in order to accommodate the increased aperture that is required by the LHC during injection, during which the VELO halves retract by 3 cm. This feature also allows the fine adjustment of

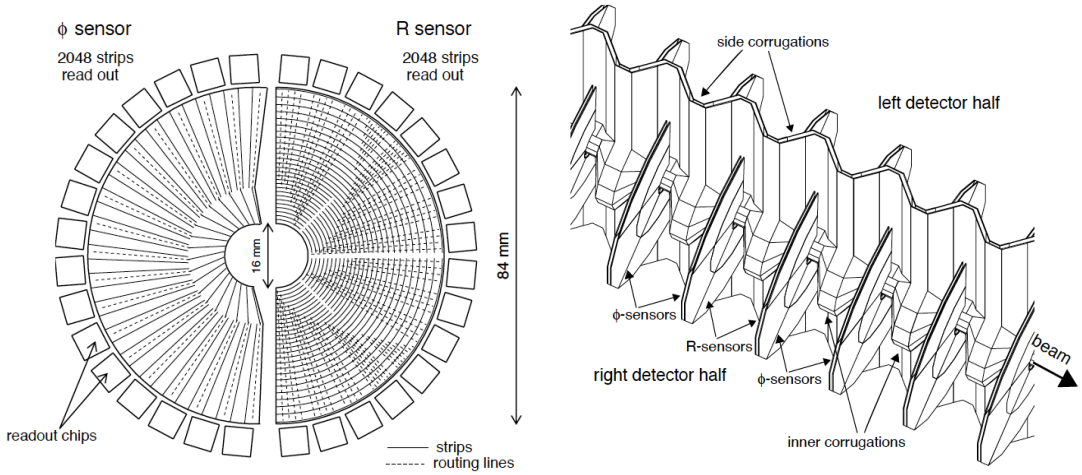

Figure 3.5: Left: schematic of the front view of a VELO module. Right: schematic showing the corrugated sheet that separates the VELO from the beam vacuum, and how it fits with the modules. Images extracted from [101].

the position of the detector in the xy plane with an accuracy of $\sim$10 µm, being able to adapt to possible displacements of the beam ($\pm$5 mm). When there is a stable beam and the VELO is fully closed, the inner part of the sensors are at a 7 mm distance from the beam axis.

As mentioned before, the measurements provided by VELO are used to reconstruct primary and secondary vertices of b and c-hadron decays, they also provide a precise measurement of their lifetimes and of the impact parameter of particles used to tag their flavour. The detached vertices of these hadrons are essential for the LHCb experiment, they are used in the trigger in order to optimize the content of the recorded data, and they are also used in the off-line analyses. For this purpose, the VELO needs a very high resolution in particle trajectory reconstruction. Its primary vertex spatial resolution is 71 µm in the z direction and 13 µm in the transverse plane, for 25-track vertices [102]; its IP resolution is better than 25 µm for tracks with $p_T < 1$ GeV/c, and its decay time and decay length resolutions are, respectively, around 50 fs and 230 µm. The VELO's average signal-to-noise ratio is around 20:1, and it has a track reconstruction efficiency of 98% or higher in data.

Silicon tracker

The Silicon Tracker (ST) is composed of two different detectors: the Tracker Turicensis (TT) and the Inner Tracker (IT), both silicon microstrip detectors.

All ST stations have four detection layers in a "x–u–v–x" arrangement [94], meaning the first and last layers being made of vertical strips, while the second and third layers are rotated by $-5°$ and $+5°$ respectively.

The TT [103] consists of a single station which is located upstream of the dipole magnet and downstream of the RICH1. The TT is composed of four planar detection layers of silicon sensors and covers the full acceptance of LHCb. The four detection layers of the station are separated in two pairs (x–u and v–x), the first one at $z = 2.35$ m and the second at $z = 2.62$ m, this separation of 27 cm being designed to optimize the track reconstruction algorithm. Each layer consists of two horizontally retractable layers, one on each side of the beam pipe. The layers use 150 cm long silicon modules, with readout electronics on both ends, on the outside of the LHCb acceptance. The first two layers have 14 full modules, 7 on each side of the beam pipe, while two half-modules are situated on the center, one above and the other below the pipe. The last two layers have 16 full modules and two half-modules.

The half-module is the basic construction unit of the TT layers, consisting of seven silicon sensors plus the readout electronics at its end. The seven sensors are segmented either on a 4–2–1 readout grouping, for the ones situated around the beam pipe, or a 4–3 grouping, for the other modules. The sensors are 500 µm thick. The full modules described above are composed of two half-modules. Adjacent modules within a layer are staggered by $\sim$1 cm in z and overlap by a few millimeters in x, to avoid acceptance gaps.

The IT [104] has three stations, located downstream of the magnet. Each station

consists of four detector boxes arranged around the beam pipe, two on each side of the pipe, and the other two above and below it. The boxes are horizontally retractable. Each one of the boxes contains four detection layers, each layer consisting of seven detector modules. Adjacent modules within a layer are staggered by 4 mm in z and overlap by 3 mm in x. The modules on the top and bottom boxes contain a single 320 μm thick silicon sensor, while the ones in the side boxes contain two 410 μm thick sensors. These thicknesses were chosen to optimize the signal-to-noise ratio while minimising the material of the detector.

The spatial resolution of the ST modules is around 50 μm, while the hit efficiency was measured to be greater than 99.7% and 99.8% for the TT and the IT, respectively [96].

Outer tracker

The Outer Tracker (OT) [105] is a drift-time detector located downstream of the magnet, along with the IT. While the IT covers the region closest to the beam pipe, the OT complements it, covering the rest of the LHCb acceptance. A diagram of this arrangement is shown on fig. 3.6. This design decision is justified by the higher density of particles produced at low angles, making the resolution, occupancy, and radiation hardness requirements looser in the outer region. The OT and the IT stations are often treated as part of the same stations, called T-stations and labelled T1, T2, and T3.

The OT consists of three stations, each one composed of arrays of straw-tube modules, and each module containing two staggered layers of 64 tubes each, with 5 mm of inner diameter. A mixture of 70% Argon and 30% CO_2 is chosen in the tubes to ensure a drift time below 50 ns.

Each station consists of four layers arranged in a x–u–v–x configuration, with the first and last layers having the tubes oriented vertically, while the second and third layers have them angled by $+5°$ and $-5°$, respectively. The stations are also divided in two horizontally retractable halves.

The OT single hit resolution is 205 μm [96], and the efficiency of the straw tubes is 97%.

3.2.3 Particle identification

Particle identification (PID) is the process of assigning a particle type to each reconstructed track, and it is a fundamental requirement for LHCb, due to the importance and difficulty on distinguishing between particles that leave similar signals on the detector, such as kaons and pions, or photons and electrons.

The PID detector system of LHCb is composed of the RICH detectors, one upstream and another one downstream of the magnet, the calorimeters and the muon stations, these last two being, in that order, the subdetectors which are farther away from the interaction point.

RICH detectors

The Ring Imaging Cherenkov (RICH) detectors fulfill a fundamental role in particle identification. There are two of them: RICH 1, between the VELO and the TT, and RICH 2, between T3 and the muon detector.

RICH detectors use Cherenkov radiation emitted by charged particles to identify them, since the opening angle of this radiation is dependent on the particle velocity. The mass of the particle is measured by combining this velocity measurement with the reconstructed momentum.

In both detectors, Cherenkov light is focused with a combination of mirrors to reflect it out of the LHCb acceptance, where they use Hybrid Photon Detectors (HPDs) to detect the Cherenkov photons in the wavelength range 200–600 nm, these HPDs are shielded by iron boxes that attenuate the magnetic field from the dipole magnet to allow for their correct performance.

RICH 1 is designed to detect low momentum particles, covering the range ∼1–60 GeV/c and the full LHCb acceptance. It uses aerogel and C_4F_{10} gas radiators. RICH 1 is located in the $990 < z < 2165$ mm region of LHCb.

On the other hand, RICH 2 is designed to cover the region where high momentum particles are generated, thus having a small acceptance of ∼±15 mrad to ±120 mrad in the horizontal plane and to ±100 mrad in the vertical plane. It detects particles with momentum from ∼15 GeV/c to ≤ 100 GeV/c and uses a CF_4 radiator. RICH 2 is located in the $9500 < z < 11832$ mm region of LHCb.

The fluorocarbon gases used on each RICH detector were chosen so their refractive

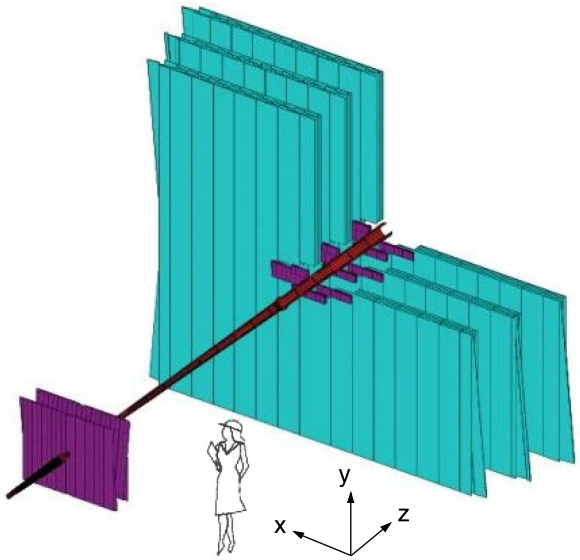

Figure 3.6: Diagram of the ST and OT stations. The ST is shown in purple, while the OT is represented in cyan. Image extracted from [94].

indices match with the momentum spectrum expected from the particles studied at LHCb. The Cherenkov angular resolutions of RICH 1 and RICH 2 are, respectively, 1.618 mrad and 0.68 mrad [106]. The PID performance provided by the RICH detectors depends on the type of particle and the used criteria; for example, for kaon-pion separation, the kaon ID efficiency can be estimated to be ∼95% with a pion misidentification ratio of ∼10%.

Calorimeters

The purpose of the LHCb calorimeters [107] is mainly the measurement of the energies and positions of electrons, photons, and hadrons. There are two main calorimeters, placed between the muon stations M1 and M2: the Electromagnetic Calorimeter (ECAL) and the Hadron Calorimeter (HCAL). Each one consists of alternating layers of scintillating and absorbing material.

The ECAL is located at $z = 12.5$ m and covers the almost-full LHCb acceptance except for $\theta < 25$ mrad due to the high radiation level around the beam pipe. The calorimeter is divided in three sections (inner, middle, and outer), each with a different cell size, to accommodate the dependence of the hit density with the distance to the pipe. The ECAL uses lead as absorber, having 66 layers with a thickness of 2 mm each, alternated with paper and scintillating tile layers, adding to a total of 42 cm of depth in the beam direction. The ECAL was measured to have an energy resolution of $\sim 9\%/\sqrt{E/\mathrm{GeV}} \oplus 0.8\%$.

The HCAL is divided in two sections (inner and outer). It uses iron as absorber, using steel plates alternated with the scintillator tiles, placed parallel to the beam axis, and has a depth of 1286 mm in the beam direction. The HCAL was measured to have an energy resolution of $\sim 69\%/\sqrt{E/\mathrm{GeV}} \oplus 9\%$.

In order to distinguish electrons from neutral and charged pions, another calorimeter system is placed in front of the ECAL, composed of the Preshower Detector (PS) and the Scintillator Pad Detector (SPD). The PS distinguishes charged particles from neutrals, then, a single 15 mm thick lead sheet is placed between the PS and the SPD, which causes electrons and photons to shower, while the heavier hadrons are more likely to pass due to their longer interaction length; then, the SPD detects the electromagnetic showers. This system, along with the information from the ECAL, allows rapid electron identification for the trigger system.

Muon stations

The muon system [108] consists of five rectangular stations, receiving the names M1–M5, covering an angular acceptance from 20 (16) mrad to 306 (258) mrad in the bending (non-bending) plane. The muon system is used in the L0 trigger to select high-p_T muons, as well as in offline reconstruction, to identify muons.

The stations M2–M5, placed downstream of the calorimeters, are separated by 80 cm thick iron absorbers to select the most penetrating muons. Each station is divided in four concentric regions with different segmentation, allowing the particle flux and channel

occupancy to be similar through the four regions. Since practically all electromagnetically or strongly-interacting particles decay in one of the calorimeters, muons are virtually the only particles to be detected at these stations.

The muon stations use multi-wire proportional chambers, except in the inner region of M1, where triple gas electron multiplier (triple-GEM) detectors are used due to the expected high particle rate. The hit efficiency was measured to be around 99% or greater for all regions of all stations [96].

3.2.4 Trigger system

The crossing frequency with visible interactions in LHCb is ∼10 MHz, thanks to its lower luminosity compared to the LHC, but the rate at which events are written to storage is ∼2 kHz. At LHCb's luminosity, ∼100 kHz of $b\bar{b}$ pairs are expected, but only 15% of those pairs will produce at least one B meson with all its decay products in the detector acceptance. In addition, the branching fractions of typical decays studied at LHCb are lower than 10^{-3}. The trigger system [109] tries to select events which are of interest to LHCb analyses while discarding the ones that aren't, achieving this way the needed reduction in write-to-storage frequency. There are two trigger levels: the Level-0 (L0) and the High Level Trigger (HLT).

The L0 uses custom electronics on the detectors to select events with the highest transversal energy particles (in the calorimeters and in the muon system), it also uses pile-up information from the VELO in order to reject events with many primary interactions. This reduces the event rate to ∼1 MHz, enough to read the full event data.

The HLT consists of a software application (running on a dedicated computing farm) to select the events of physical interest. Since it is software-based, it can be adjusted for changes in running conditions or in physics goals. The HLT is further divided in two stages: HLT1 and HLT2. HLT1 uses the tracking system to reconstruct the particles corresponding to the L0 output, confirming or discarding its decision, and reducing the rate to ∼30 kHz, which is low enough to run offline track reconstruction on HLT2. HLT2 reconstructs composite particle candidates ($K^* \to K^+\pi^-$, $\Phi \to K^+K^-$, $J/\psi \to \mu^+\mu^-$...) and uses cuts on the properties of the reconstructed particles, such as the invariant mass or the B momentum, to further reduce the rate to the desired ∼2 kHz.

3.3 Track reconstruction at LHCb

Track reconstruction (or tracking) is the process of forming particle trajectories from the information (hits) that the tracker detectors collect. At LHCb, tracks are classified in five categories [94, 96] according to where their hits are, as shown on fig. 3.7:

- **Long tracks** have hits on the VELO and on the T stations (and optionally, the TT). These tracks provide the best momentum measurements, thanks to having information from virtually the full magnetic field range.

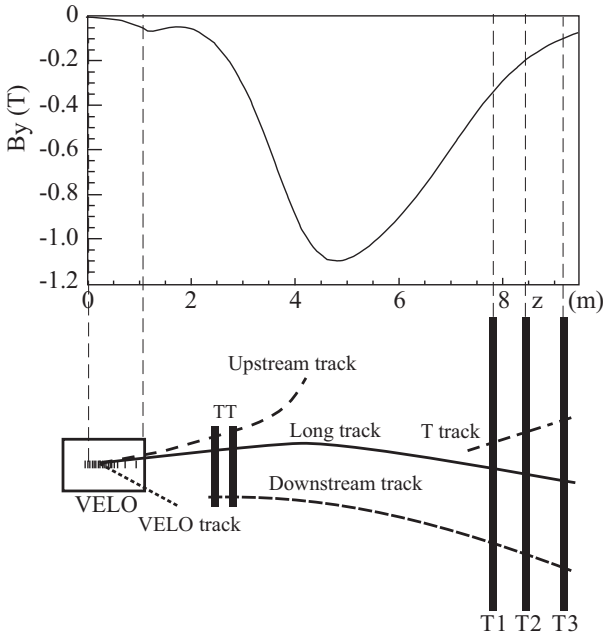

Figure 3.7: Diagram of the LHCb track types, compared to the vertical component of the magnetic field on top. Image extracted from [94].

- **Upstream tracks** have hits only on the VELO and TT stations. They generally correspond to particles with low momentum that are pushed out of the detector acceptance by the magnetic field.
- **Downstream tracks** have hits only on the TT and T stations. These are typical on long-lived particles that decay outside of the VELO.
- **VELO tracks** have hits only on the VELO, corresponding primarily to very low or negative rapidities. They are used for primary vertex reconstruction.
- **T tracks** have hits only on the T stations, and are typical from particles produced in secondary interactions.

The LHCb tracking algorithm for long tracks first starts by searching for track candidates or "seeds" in the VELO and T stations: first, VELO hits that are compatible with a straight line trajectory are combined into a VELO track. Then, the "forward tracking" algorithm combines the VELO track with the information from the T stations, searching for the best possible combination of hits that define a track. After that, the "track matching" algorithm, matches these tracks with T tracks which are reconstructed independently. TT hits are the last to be combined with the already formed long track, by extrapolating its position to the TT stations.

Downstream and upstream tracks are found by extrapolating T or VELO tracks, respectively, to the TT position, searching for compatible TT hits.

Track candidates are then fitted with a Kalman filter, which takes into account multiple scattering and energy loss. The momentum resolution of the tracking algorithm is found to be between ∼0.35% at lower momenta and ∼0.55% at higher momenta (100–140 GeV/c).

The tracking algorithm often suffers from so-called "ghost" tracks: reconstructed tracks that do not correspond to a real particle. These are usually due to a wrong match of VELO and T hits. A neural network classifier is used to significantly reduce the misreconstruction rate.

The track-finding efficiency (probability of the trajectory of a particle passing through the full tracking system being reconstructed) has been found to be consistently above 96% for the whole momentum and pseudorapidity ranges, only falling lower than that on high-multiplicity events with more than 200 tracks.

In addition, LHCb's PID system assigns numerical variables that represent the probability of a reconstructed track being of a certain kind of particle. The two kinds of variables recorded by LHCb are:

- PID_X: the log-likelihood difference between the X and pion hypotheses ($\mathrm{PID}_X = \log \mathcal{L}_X - \log \mathcal{L}_\pi$), as determined by the calorimeters and the RICH and muon detectors.

- $P_{\mathrm{NN}}(X)$: the Bayesian posterior probability of a particle being of the type X. This quantity is determined using a neural network which takes the PID information as input and is trained separately for each type of particle.

3.4 Simulation of data samples

Simulated data samples are an essential part of high-energy physics, specially for data analysis. Important steps like the optimization of the signal selection or the description of the background channels tend to highly rely on the analysis of simulated samples.

LHCb's simulation framework is called Gauss [110]. Gauss manages the creation of simulated events, interfacing with multiple external applications in the following steps:

1. A production tool (most commonly Pythia [111], which is the one used for the simulated samples on this thesis) generates events with the required signal particle.

2. The decay tool known as EvtGen [112] simulates the decay of the particle. Usually, the desired decay chain and final state(s) of the decay are specified by the analysts and imposed by EvtGen.

3. The signal particle and its decay products may be required to pass generator level cuts, also specified by the analysts and very important to optimize CPU and disk usage.

4. The generated particles are transported through the detector simulation. GEANT4 [113] is the tool that simulates the interaction of the particles with the detector. The detector geometry and data-taking conditions (such as the magnet polarity) are also specified by the analysts to fit with the data-taking period they intend to simulate.

After this procedure, the output is transformed to an analogous format to real data via another framework called BOOLE [114], which digitises the simulated data, simulating the experiment electronics and data acquisition system. The rest of the data processing (from the trigger onwards) is practically the same as with real data, the main difference being that in simulated samples there can be more information about the event which in real data would be impossible to know, such as the true identity of the particles or the information about their full decay chain.

Due to the great size of simulated data required by LHCb analyses, a variety of "fast simulation" options were developed and implemented in the workflow, with the objective of reducing the computing workload. The main fast simulation techniques used at LHCb are:

- **ReDecay** [115]: a technique that reuses the non-signal parts of an event for multiple simulations of the signal part.
- **Detector reduction**: certain parts of the subdetectors might be switched off in the simulation in order to speed up the process.
- **Particle gun**: a technique that directly generates a signal particle with a certain kinematic distribution, instead of generating a full event.

4

Description of the datasets

Contents

In this chapter, the data and simulation samples used for the $R(D^{(*)0})$ and $R(D^{(*)-})$ analyses are described, as well as the selection and correction procedures applied to them.

4.1 Data samples

The data used in this thesis were taken during LHCb's Run 2 in the years 2016, 2017, and 2018; therefore corresponding to proton-proton collisions at a centre-of-mass energy of 13 TeV, with an integrated luminosity of 5.4 fb^{-1}.

4.2 Simulation samples

Several simulation samples are used to model the different signal and background channels which are present in the data. All the simulation samples used in the $R(D^{(*)0})$ and $R(D^{(*)-})$ analyses were generated with 2016 data-taking conditions and both magnet polarities, with corrections applied to account for small differences with 2017 and 2018 data (section 4.5.2). Filtered productions[1] were used for all samples, meaning that the generated events are filtered before being written to disk, in order to save space. For the samples with a larger number of events, ReDecay [115] was also used to speed up the production. The full list of simulation samples, along with their size and other details, are listed in table 4.1.

In general, the generated samples for both analyses correspond to the following categories:

- **Signal samples**: samples with $B \to D^{(*)}\tau^-\overline{\nu}_\tau$ and $\tau^- \to \pi^-\pi^+\pi^-(\pi^0)\nu_\tau$, used to model the signal components.
- D^{**} **samples**: samples with $B \to D^{**}\tau^-\overline{\nu}_\tau$ and $\tau^- \to \pi^-\pi^+\pi^-(\pi^0)\nu_\tau$, used to model the D^{**} feeddown component in the signal fit.
- **Normalisation samples**: used to study and model the normalisation channel.
- **Double-charm samples**: samples with $B \to DD(X)$, used to study the double-charm control samples and model their respective components in the signal fit.
- **Prompt samples**: samples with $B \to D\pi^-\pi^+\pi^-(X)$, used to study the prompt control samples and model their respective components in the signal fit.
- **Combinatorial background samples**: samples where the D and the 3π are not from the same B, used to model the combinatorial background component in the fit.

[1] The filtering conditions imposed on the simulation samples are just the stripping selection conditions explained in section 4.3.1.

Decay(s)	Simulation options	N_{disk} (Magnet Up / Down)	Used in
$B^- \to D^0\tau^-(\to \pi^-\pi^+\pi^-\nu_\tau)\overline{\nu}_\tau$	Sim09i filtered	1001755 / 10121572	$R(D^{(*)0})$
$B^- \to D^0\tau^-(\to \pi^-\pi^+\pi^-\pi^0\nu_\tau)\overline{\nu}_\tau$	Sim09i filtered	754189 / 773537	$R(D^{(*)0})$
$B^0 \to D^-\tau^+(\to \pi^+\pi^-\pi^+\overline{\nu}_\tau)\overline{\nu}_\tau$	Sim09i filtered	1007018 / 1013919	$R(D^{(*)-})$
$B^0 \to D^-\tau^+(\to \pi^+\pi^-\pi^+\pi^0\overline{\nu}_\tau)\overline{\nu}_\tau$	Sim09i filtered	767843 / 757454	$R(D^{(*)-})$
$B^- \to D^{*0}\tau^-(\to \pi^-\pi^+\pi^-\nu_\tau)\overline{\nu}_\tau$	Sim09i filtered	1001245 / 1007497	$R(D^{(*)0})$
$B^- \to D^{*0}\tau^-(\to \pi^-\pi^+\pi^-\pi^0\nu_\tau)\overline{\nu}_\tau$	Sim09i filtered	756863 / 759234	$R(D^{(*)0})$
$B^0 \to D^{*-}\tau^+(\to \pi^+\pi^-\pi^+\overline{\nu}_\tau)\nu_\tau$	Sim09e ReDecay filtered	680071 / 687279	Both
$B^0 \to D^{*-}\tau^+(\to \pi^-\pi^+\pi^-\pi^0\overline{\nu}_\tau)\nu_\tau$	Sim09c ReDecay	20107962 / 20039288	Both
$B^- \to D^{**}\tau\nu_\tau$	Sim09k ReDecay filtered	286712 / 288831	Both
$\overline{B}^0 \to D^{**}\tau\nu$	Sim09k ReDecay filtered	255781 / 250003	Both
$B_s^0 \to D^{**}\tau\nu$	Sim09k ReDecay filtered	288831 / 286712	Both
$B^- \to D^0D_s^-(\to \pi^-\pi^+\pi^-)$	Sim09i filtered	520804 / 520972	$R(D^{(*)0})$
$B^0 \to D^-D_s^+(\to \pi^+\pi^-\pi^+)$	Sim09i filtered	503923 / 522840	$R(D^{(*)0})$
$B^- \to D^0X_cX'$	Sim09h ReDecay filtered	1288010 / 1853494	$R(D^{(*)0})$
$\overline{B}^0 \to D^0X_cX'$	Sim09h ReDecay filtered	10754686 / 11004407	$R(D^{(*)0})$
$B_s^0 \to D^0X_cX'$	Sim09h ReDecay filtered	2429723 / 3501039	$R(D^{(*)0})$
$B^0 \to D^-X_cX'$	Sim09h ReDecay filtered	10113090 / 9663985	$R(D^{(*)-})$
$B^+ \to D^-X_cX'$	Sim09h ReDecay filtered	3584626 / 3549315	$R(D^{(*)-})$
$B_s^0 \to D^-X_cX'$	Sim09h ReDecay filtered	3596604 / 3138401	$R(D^{(*)-})$
$B^- \to D^0\pi^-\pi^+\pi^-$	Sim09i filtered	284698 / 262503	$R(D^{(*)0})$
$B^0 \to D^-\pi^+\pi^-\pi^+$	Sim09i filtered	253892 / 254360	$R(D^{(*)-})$
$B^- \to D^0\pi^-\pi^+\pi^-(X)$	Sim09i ReDecay filtered	14240203 / 14230745	$R(D^{(*)0})$
$B^- \to D^-\pi^+\pi^-\pi^+X$	Sim09l ReDecay filtered	8918131 / 9003685	$R(D^{(*)-})$
$\overline{B}^0 \to D^0\pi^-\pi^+\pi^-X$	Sim09i ReDecay filtered	17818266 / 17890479	$R(D^{(*)0})$
$\overline{B}^0 \to D^-\pi^+\pi^-\pi^+(X)$	Sim09l ReDecay filtered	25661634 / 25878336	$R(D^{(*)-})$
$B_s^0 \to D^0\pi^-\pi^+\pi^-X$	Sim09i ReDecay filtered	1813758 / 1823421	$R(D^{(*)0})$
D^0 and 3π not from same B	Sim09i ReDecay filtered	12592113 / 12503618	$R(D^{(*)0})$
D^- and 3π not from same B	Sim09l ReDecay filtered	12504140 / 12520970	$R(D^{(*)-})$

Table 4.1: Simulation samples used in the $R(D^{(*)0})$ and $R(D^{(*)-})$ analyses. D^{**} represents any of the $D_2^*(2460)$, $D_1(2420)$, $D_1'(2430)$, $D_0^*(2300)$, $D_{s1}(2536)^+$ or $D_{s2}^*(2573)^+$ mesons, 'Sim09x' is the version of LHCb's simulation framework that was used, and N_{disk} is the number of events saved on disk.

4.3 Selection of events

Selection requirements (or "cuts") are used to discard as many background events as possible, while improving the signal-to-noise ratio. All the selection cuts explained in this section were applied to both data and simulation samples, and in both the $R(D^{(*)0})$ and $R(D^{(*)-})$ analyses, unless stated otherwise.

4.3.1 Preselection

The following set of cuts is applied at the beginning of the selection process:

- **Stripping selection:** all events were required to pass the `StrippingBu2D0TauNuForB2XTauNuAllLines` stripping line, for the $R(D^{(*)0})$ analysis; or the `StrippingB0d2DTauNuForB2XTauNuAllLines` stripping line, for the $R(D^{(*)-})$ analysis. The requirements applied by each of these lines are shown in tables 4.2 and 4.3.

- **Cleaning cuts:** a set of cleaning selection cuts are applied after the stripping selection, in order to suppress background events. These cuts require the B and 3π vertices to be displaced from the PV, the impact parameter χ^2 of the pions that form the τ vertex to be incompatible with being produced at the PV, and the PV of the D and τ candidates to be compatible.

- **PIDCalib synchronisation:** a loose requirement on the momentum and pseudorapidity of the candidate tracks is also applied to synchronise the selection with the `PIDCalib` requirements (section 4.5.1).

A detailed list of the preselection cuts after the stripping selection is shown in table 4.4.

4.3.2 Trigger selection

Selected events are required to pass conditions on all three trigger levels:

- At the hardware L0 level, events are required to be either triggered on signal (TOS) by the L0 hadronic line (`L0HadronDecision_TOS`) or triggered independently of signal (TIS) globally (`L0Global_TIS`).

- At the HLT1 level, events are required to pass the `B_Hlt1TrackMVADecision_TOS` line.

- At the HLT2 level, they are required to pass at least one of the 2-, 3-, or 4-body topological lines [116].

The "TIS" and "TOS" trigger categories [117] are defined based on whether the signal candidate was enough to trigger the decision ("triggered on signal") or if the trigger

Target particles	Variable	Requirement
Cuts on the B^+	$m(D^0 3\pi)$	$\in [2.7, 5.6\ \text{GeV}/c^2]$
	DOCA	< 0.15 mm
	cos(DIRA)	> 0.995
Cuts on the D^0	$\lvert m(K\pi) - m(D^0)_{\text{PDG}} \rvert$	$< 40\ \text{MeV}/c^2$
	Vertex χ^2/DOF	< 10
	cos(DIRA)	> 0.995
	PV distance χ^2	> 36
	p_T	$> 1.2\ \text{GeV}/c$
	Min. χ^2_{IP}(PV)	> 10
	$\text{DOCA}_{K\pi}$	< 0.5 mm
	$\text{DOCA}_{K\pi}$ χ^2	< 15
Cuts on the τ	cos(DIRA)	> 0.99
	$m(3\pi)$	$\in [0.4, 3.5\ \text{GeV}/c^2]$
	Max. DOCA	< 0.15 mm
	$\min[m(\pi^+\pi^-)]$	$< 1.67\ \text{GeV}/c^2$
	At least two pions p_T	$> 0.3\ \text{GeV}/c^2$
	Vertex χ^2	< 25
	At least two pions with χ^2_{IP}(PV)	> 5
Cuts on the D^0 daughters	p	$> 2\ \text{GeV}/c$
	Ghost probability	< 0.4
	Track prob. χ^2	$> 10^{-8}$
	Min. χ^2_{IP}(PV)	> 10
	$p_T(K)$	$> 1.5\ \text{GeV}/c$
	$p_T(\pi)$	$> 0.25\ \text{GeV}/c$
	K track χ^2/DOF	< 30
	π track χ^2/DOF	< 3
	K PID_K	> 3
	π PID_K	< 50
Cuts on the τ daughter pions	p_T	$> 0.25\ \text{GeV}/c$
	χ^2_{IP}(PV)	> 4
	χ^2/DOF	< 4
	PID_K	< 8
	Ghost probability	< 0.4

Table 4.2: List of selection cuts applied by the `StrippingBu2D0TauNuForB2XTauNu-AllLines` stripping line, for the $R(D^{(*)0})$ analysis.

Target particles	Variable	Requirement
Cuts on the B^0	$m(D^-3\pi)$	$\in [2.7, 5.6\ \text{GeV}/c^2]$
	DOCA	< 0.15 mm
	cos(DIRA)	> 0.995
Cuts on the D^-	$\lvert m(K2\pi) - m(D^-)_{\text{PDG}}\rvert$	$< 40\ \text{MeV}/c^2$
	Vertex χ^2/DOF	< 10
	cos(DIRA)	> 0.995
	PV distance χ^2	> 50
	p_T	$> 1.6\ \text{GeV}/c$
	Min. χ^2_{IP}(PV)	> 10
	$\text{DOCA}_{K2\pi}$	< 0.5 mm
	$\text{DOCA}_{K2\pi}$ χ^2	< 15
Cuts on the τ	cos(DIRA)	> 0.99
	$m(3\pi)$	$\in [0.4, 3.5\ \text{GeV}/c^2]$
	Max. DOCA	< 0.15 mm
	$\min[m(\pi^+\pi^-)]$	$< 1.67\ \text{GeV}/c^2$
	At least two pions p_T	$> 0.3\ \text{GeV}/c^2$
	Vertex χ^2	< 25
	At least two pions with χ^2_{IP}(PV)	> 5
Cuts on the D^- daughters	p	$> 2\ \text{GeV}/c$
	Ghost probability	< 0.4
	Track prob. χ^2	$> 10^{-8}$
	Min. χ^2_{IP}(PV)	> 10
	$p_T(K)$	$> 1.5\ \text{GeV}/c$
	$p_T(\pi)$	$> 0.25\ \text{GeV}/c$
	K track χ^2/DOF	< 30
	π track χ^2/DOF	< 3
	K PID_K	> 3
	π PID_K	< 50
Cuts on the τ daughter pions	p_T	$> 0.25\ \text{GeV}/c$
	χ^2_{IP}(PV)	> 4
	χ^2/DOF	< 4
	PID_K	< 8
	Ghost probability	< 0.4

Table 4.3: List of selection cuts applied by the `StrippingB0d2DTauNuForB2XTauNuAllLines` stripping line, for the $R(D^{(*)-})$ analysis.

Variable	Requirement
3π vertex transverse distance to PV	> 0.2 mm
B vertex transverse distance to PV	> 0.6 mm
τ vertex χ^2	< 16
τ daughter pions' $\chi^2_{\text{IP}}(\text{PV})$	> 15
τ daughter pions' $P_{\text{NN}}(\pi)$	> 0.2
D daughter kaon's $P_{\text{NN}}(K)$	> 0.4
D daughter pion(s)' $P_{\text{NN}}(\pi)$	> 0.4
$\lvert z_{\text{PV}}(D) - z_{\text{PV}}(3\pi)\rvert$	< 0.0001 mm
All tracks p	$\in [2, 200\ \text{GeV}/c]$
All tracks η	$\in [1.5, 5]$
Number of SPD hits	≤ 450

Table 4.4: List of cuts applied in the preselection of events after the stripping phase in both the $R(D^{(*)0})$ and the $R(D^{(*)-})$ analyses.

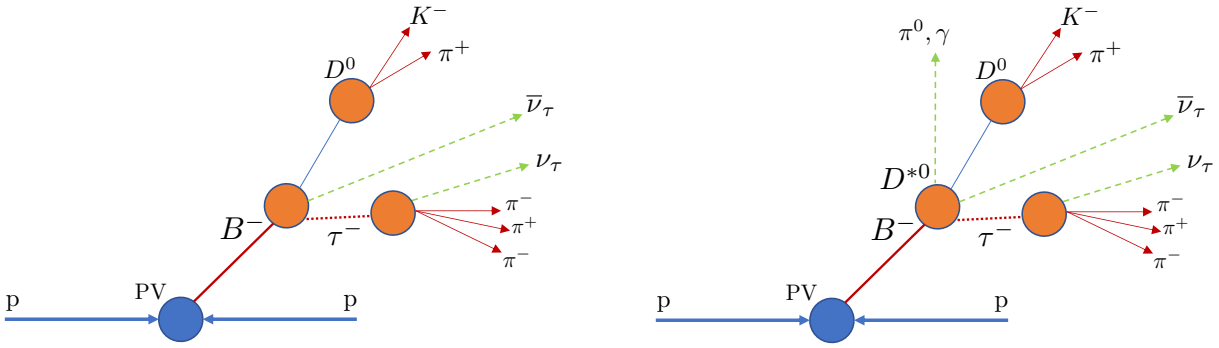

Figure 4.1: Topology of the signal decays corresponding to the $B^- \to D^0\tau^-\overline{\nu}_\tau$ (left) and $B^- \to D^{*0}\tau^-\overline{\nu}_\tau$ (right) decay chains.

decision was made with only the rest of the event, not including the signal ("triggered independently of signal"). An event can be assigned to both categories if it triggers both decisions: this overlapping category is called "TISTOS". This separation in TIS and TOS categories at the L0 level may produce discrepancies between data and simulation samples. This is addressed and corrected accordingly in section 4.5.3.

4.3.3 Distance detachment criterion

The final state of the signal decays consist of a D meson and three charged pions. The topology of these decays is shown in figs. 4.1 and 4.2. The largest background contribution is, by far, from "prompt" $B \to D\,\pi^-\pi^+\pi^- X$ decays. Thanks to the VELO's excellent resolution, the distance between vertices can be used to distinguish between events where the three pions' vertex is "detached" from the B vertex, suggesting an

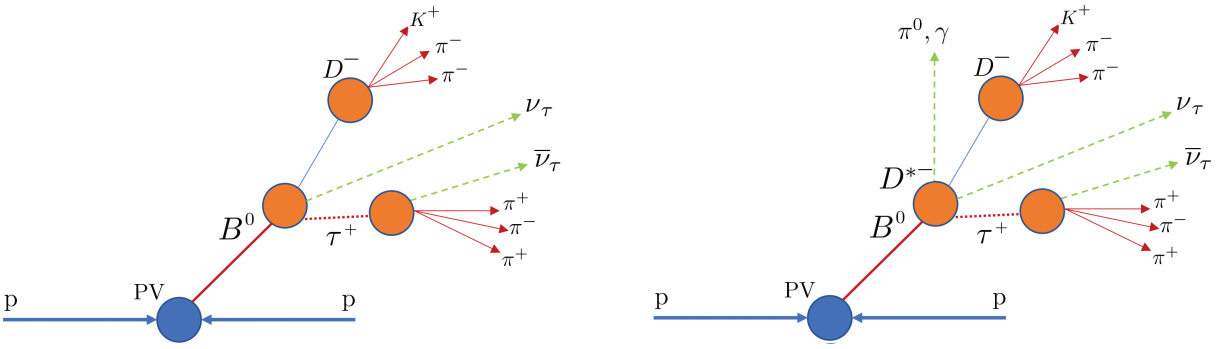

Figure 4.2: Topology of the signal decays corresponding to the $B^0 \to D^- \tau^+ \nu_\tau$ (left) and $B^0 \to D^{*-} \tau^+ \nu_\tau$ (right) decay chains.

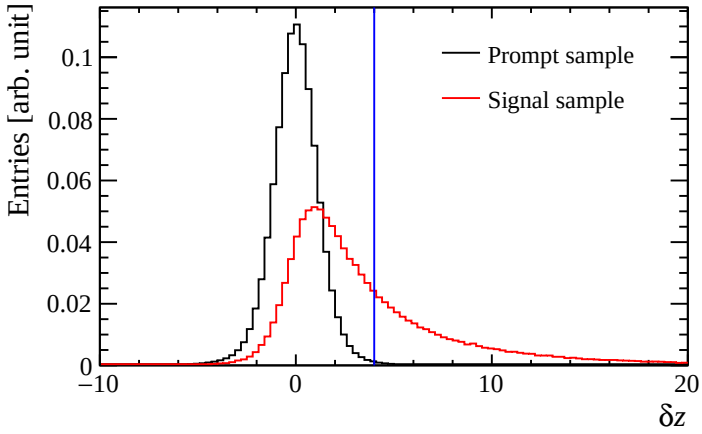

Figure 4.3: Distance between the τ and B vertices along the beam direction (z) divided by its uncertainty for the inclusive prompt $B^- \to D^0 \pi^- \pi^+ \pi^- (X)$ simulation sample (black) and the signal $B^- \to D^0 \tau^- \overline{\nu}_\tau$ with $\tau^- \to \pi^- \pi^+ \pi^- \nu_\tau$ simulation sample (red). The blue vertical line indicates the $\delta z > 4$ criterion applied in this analysis. The distributions are normalised to the same area.

intermediate particle such as the τ, and events where the three pions' vertex is compatible with the B vertex, and thus compatible with a prompt decay. This criterion uses the distance in the z axis between both vertices divided by its uncertainty, which we shall define as

$$\delta z \equiv \frac{z_{3\pi} - z_B}{\sqrt{\sigma(z_{3\pi}) + \sigma(z_B)}}, \tag{4.1}$$

where $z_{3\pi}$ and z_B are the z coordinates of the three pions and B vertices, respectively, and σ their uncertainties. Fig. 4.3 shows the distribution of this δz variable for prompt and signal simulated decays.

This analysis uses the requirement $\delta z > 4$ to select signal candidates, the same

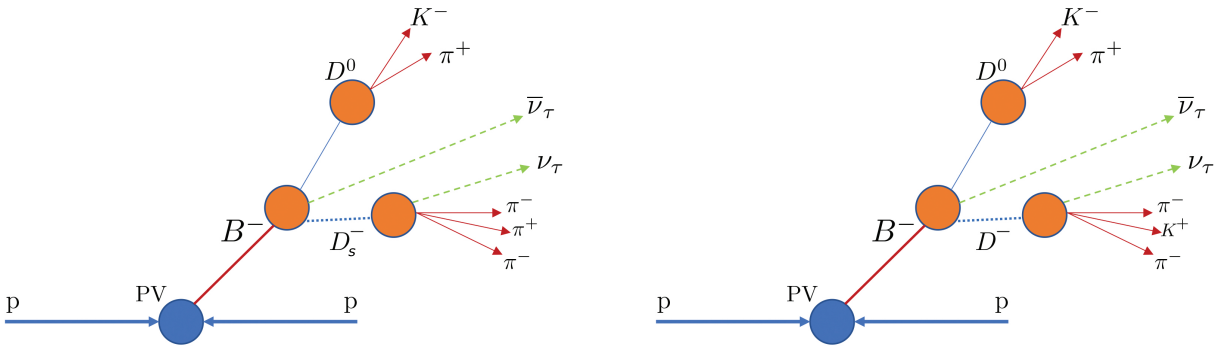

Figure 4.4: Topology of two of the most common double-charm background decays in the $R(D^{(*)0})$ analysis: $B^- \to D^0 D_s^-$ (left) and $B^- \to D^0 D^-$ (right), where the kaon from $D^- \to K^+ 2\pi^-$ is misidentified as a pion. Compare with the signal topology in fig. 4.1.

criterion that was used in the previous Run 1 hadronic $R(D^*)$ measurement [31]. The main background contributions after this detachment selection are due to double-charm decays ($B \to DDX$) where the second D meson can also produce a three-prong decay, thus producing a very similar topology to the signal decay, which is not possible to distinguish via this criterion.

A complementary criterion, $\delta z \in [-3, 0]$, is also used to select a "prompt-enriched" sample for the prompt control sample studies of section 5.1.

4.3.4 Vertex isolation

There are a number of other B decays that produce a similar topology to signal decays, but with more charged tracks associated to their vertices. $B \to DDX$ decays are an example of such background decays, since D mesons can decay into 4 or 5-prong final states, such as $D_s^- \to \pi^-\pi^+\pi^-\pi^+\pi^- X$ or $\overline{D}^0 \to K^+\pi^-\pi^+\pi^- X$, possibly generating fake $\tau^- \to \pi^-\pi^+\pi^-\nu_\tau$ vertices. Decays where extra charged tracks point to the B vertex also exist, such as $B \to DDK^\pm$ or $B \to DD\pi^\pm$. In order to avoid mistakenly selecting these decays as signal, the following vertex isolation requirements are used.

Extra tracks can be identified by their impact parameter χ^2 with respect to the corresponding vertex. This quantity, $\chi^2_{\text{IP}}(V)$, is defined as the difference between the χ^2 of a vertex V built with and without the considered track, thus acting as a measurement of how likely it is that the extra track comes from the same vertex as the other tracks, with higher values implying less likelihood.

Then, the quantities $N_{\text{iso}}(V)$ are defined as the number of additional tracks with $p_T > 250$ MeV/c, $\chi^2_{\text{IP}}(\text{PV}) > 4$, and $\chi^2_{\text{IP}}(V) < 25$. As such, $N_{\text{iso}}(V)$ is a measurement of how many additional tracks a vertex V has, compared to the expected tracks from a signal decay. The distribution of the isolation variables $N_{\text{iso}}(\tau)$ and $N_{\text{iso}}(B)$ is shown in fig. 4.5 for $B^- \to D^0\tau^-\overline{\nu}_\tau$ signal and for $B^0 \to \overline{D}^0 D_s^+ X$ background simulated events.

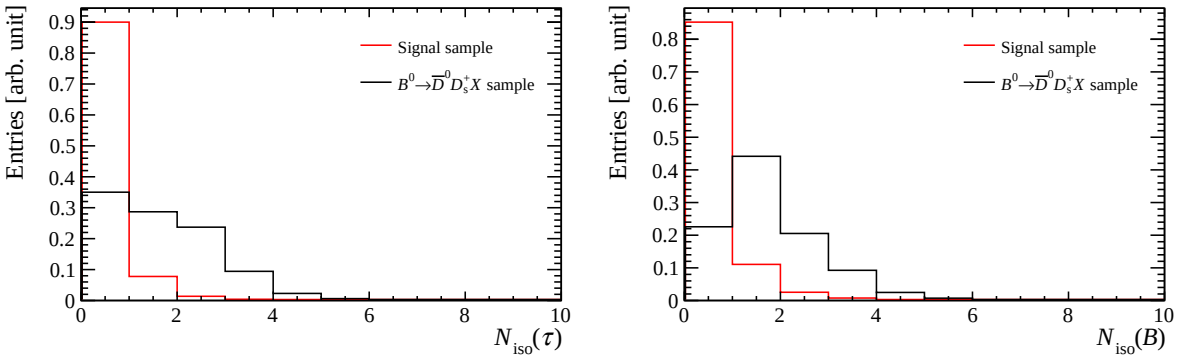

Figure 4.5: Distributions of the isolation variables $N_{\text{iso}}(\tau)$ (left) and $N_{\text{iso}}(B)$ (right) for signal $B^- \to D^0 \tau^- \overline{\nu}_\tau$, with $\tau^- \to \pi^-\pi^+\pi^-\nu_\tau$ (red), and background $B^0 \to \overline{D}^0 D_s^+ X$ (black) simulated events.

This method, also used by the Run 1 $R(D^*)$ analysis [31], imposes the requirement

$$N_{\text{iso}}(\tau) = 0 \ \wedge \ N_{\text{iso}}(B) = 0, \tag{4.2}$$

discarding events with any additional tracks.

However, the $R(D^{(*)0})$ analysis needs to take one more possibility into account: a D^0 candidate can come from a $D^{*+} \to D^0\pi^+$ decay, with this slow pion being able to escape the previous vertex isolation requirements. To counter this effect, tracks with $\chi^2_{\text{IP}}(B) < 25$ and with a charge compatible with being the pion from a D^{*+} decay are used to detect and suppress these events: by adding the slow pion track to the D^0 candidate, selected events are required to have an invariant mass of the $D^0\pi^+$ system incompatible with a D^{*+}, by imposing the condition

$$m(D^0\pi^+) - m(D^0) \notin [143, 148 \text{ MeV}/c^2] \tag{4.3}$$

in order to discard events with a $D^{*+} \to D^0\pi^+$ decay. This condition is justified by the observed invariant mass distribution, shown in fig. 4.6. The reverse condition is also used to obtain D^{*+}-enriched samples, used for the control sample studies shown in chapter 5.

4.3.5 Signal and normalisation selections

Along with the previously discussed preselection and vertex detachment and isolation conditions, a final set of requirements is imposed on the signal and normalisation samples, in order to isolate as much as possible the desired decay modes. The q^2 is required to be positive, the τ decay time smaller than 2 ns, the mass of the reconstructed D meson must be within 20 MeV/c^2 of its known mass, and a PID requirement is imposed on the opposite-signed π^+ from the τ decay, to suppress misidentified kaons from $D^+ \to K^-\pi^+\pi^+(X)$ decays.

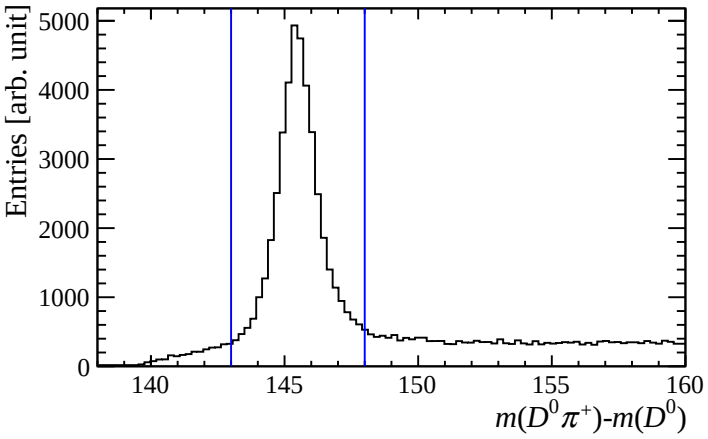

Figure 4.6: Invariant mass distribution $m(D^0\pi^+) - m(D^0)$ from data obtained by adding a track compatible with the pion of a $D^{*+} \to D^0\pi^+$ decay. These events have already passed the isolation requirements of eq. 4.2. The applied D^{*+} veto is shown by the two vertical blue lines.

Additionally, the D daughters are required to not come from the τ candidate by requiring $\chi^2_{\text{IP}}(\tau) > 5$. This suppresses decays such as $\overline{D}^0 \to \pi^+\pi^-\pi^+\pi^-$, where the charged pions may form a fake τ vertex, along with the D vertex with the remaining pion.

These requirements are summarised in table 4.5.

4.3.6 The BDT

As discussed previously, double-charm decays, and specially $B \to DD_s^+(X)$ decays, are the main source of background after selection, due to the similarity of their topology with signal decays. In order to model and suppress this contribution, a Gradient Boosted Decision Tree (BDT), created using the TMVA toolkit [118], is implemented to aid in the discrimination of this background. The output of this BDT is used as one of the three dimensions in the signal fit (section 6.1.1).

For the training of the BDT, the $B^- \to D^0\tau^-\overline{\nu}_\tau$ simulation sample is used as signal, and the $B \to \overline{D}^0 D_s^+(X)$ simulation sample as background. Both samples are passed through all the signal selection requirements before being input into the BDT.

The input variables for the BDT are chosen avoiding those which are too correlated with the other two fit variables (q^2, t_τ). This criterion results in a high presence of variables related to the 3π system, since the dynamics of the pions coming from a τ^- decay is very different to that of the pions coming from a D_s^+ decay. Notably, the presence of decays with intermediate resonant states such as $\rho^0 \to \pi^+\pi^-$ is very different from one particle to the other, thus, the mass distributions of pairs of pions which may have come from a resonance can be very discriminating variables.

Variable	Requirement (signal sample)	Requirement (normalisation sample)
q^2	> 0 GeV$^2/c^4$	> 0 GeV$^2/c^4$
t_τ	< 2 ns	< 2 ns
Oppositely charged pion's $P_{\mathrm{NN}}(K)$	< 0.1	< 0.1
$\lvert m(D) - m(D)_{\mathrm{PDG}}\rvert$	< 20 MeV$/c^2$	< 20 MeV$/c^2$
D daughters' $\chi^2_{\mathrm{IP}}(\tau)$	> 5	> 5
$m(3\pi)$	< 1600 MeV$/c^2$	–
BDT	> -0.4	–
$\lvert m(3\pi) - m(D_s^+)_{\mathrm{PDG}}\rvert$	–	< 30 MeV$/c^2$
$\lvert m(D3\pi) - m(B)_{\mathrm{PDG}}\rvert$	–	< 60 MeV$/c^2$

Table 4.5: Final selection cuts applied to the signal and normalisation samples. The BDT variable is defined in section 4.3.6. The "PDG" subscript indicates that the mass value is taken from [2].

In addition, since $D_s^+ \to 3\pi X$ decays often produce extra neutral particles, neutral isolation variables are also added as an input to the BDT. This neutral isolation consists on searching for neutral particles which deposited energy in the electromagnetic calorimeter with an angular separation (as defined in eq. 2.26) of $\Delta R \leq 0.4$ with respect to the 3π direction.

The chosen input variables used for the BDT training are listed below, where the three pions from the τ decay are identified with a number as $\tau^- \to \pi_0^-\pi_1^+\pi_2^-\nu_\tau$:

- $\min[m(\pi_0^-\pi_1^+), m(\pi_2^-\pi_1^+)]$, the minimum mass of the pairs of oppositely charged pions.
- $\max[m(\pi_0^-\pi_1^+), m(\pi_2^-\pi_1^+)]$, the maximum mass of the pairs of oppositely charged pions.
- $m(\pi_0^-\pi_2^-)$, the mass of the pair of same-sign pions: .
- $\dfrac{p_T(\Delta R_{3\pi} < 0.4)}{p_T(3\pi) + p_T(\Delta R_{3\pi} < 0.4)}$, where $p_T(3\pi)$ is the transverse momentum of the 3π system and $p_T(\Delta R_{3\pi} < 0.4)$ is the transverse momentum of the photons detected in the electromagnetic calorimeter with $\Delta R \leq 0.4$ with respect to the 3π direction.
- $N(\Delta R_{3\pi} < 0.4)$, the number of photons detected in the electromagnetic calorimeter with $\Delta R \leq 0.4$ with respect to the 3π direction.

The distributions of these five variables are shown in fig. 4.7, and the output of the BDT is shown in fig. 4.8.

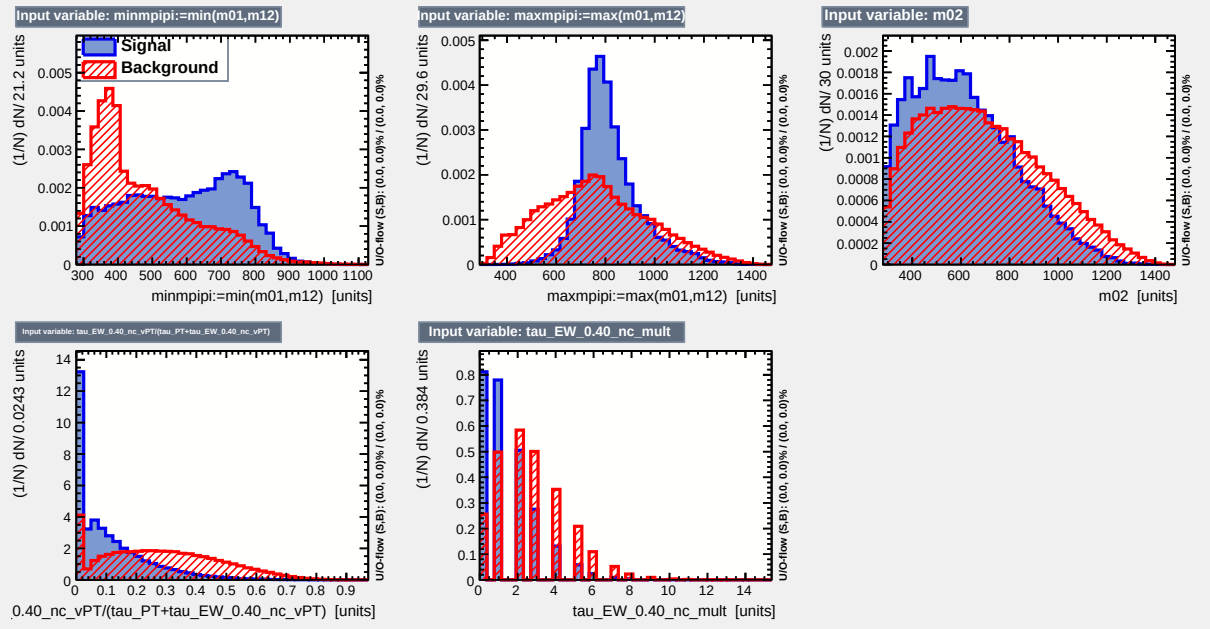

Figure 4.7: Distribution of the input variables of the BDT for signal (blue) and background (red).

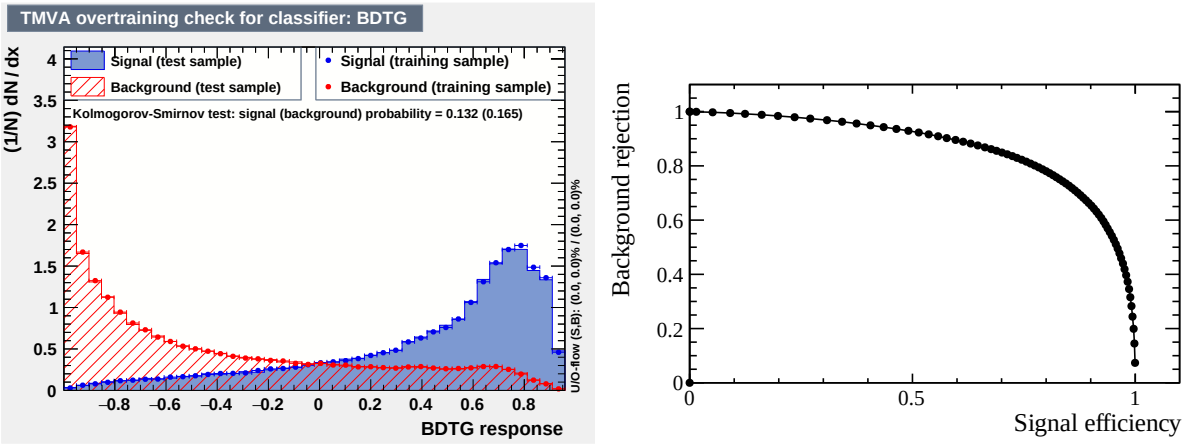

Figure 4.8: Left: distribution of the BDT output variable for signal and background. Right: background rejection rate as a function of the signal efficiency.

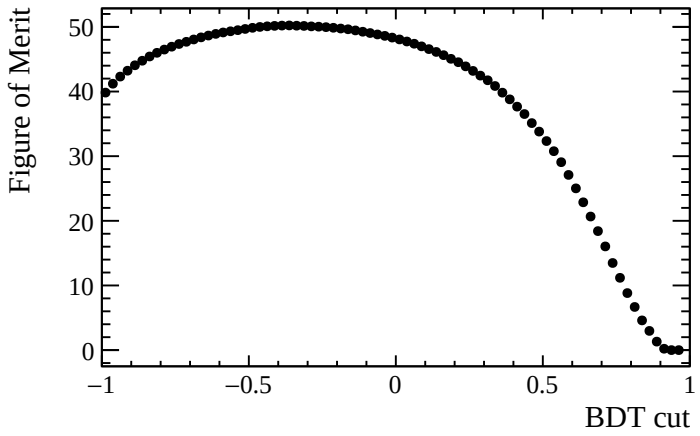

Figure 4.9: Distribution of the BDT figure of merit (eq. 4.4) as a function of the BDT output value chosen for the selection cut.

Since the BDT output is used as one of the dimensions in the 3D signal fit (section 6.1.1), it is not optimal to use the significance, $\frac{S}{\sqrt{S+B}}$, as a figure of merit to select the events that go into the fit, since this approach significantly reduces the size of the signal sample (therefore harming the effectiveness of the fit) and optimal background rejection is not the main goal of this cut, since the fit needs a significant amount of background events in order to properly model their distribution. A compromise between high signal efficiency and high background rejection is needed.

To accomplish this, the figure of merit is chosen to be the significance multiplied by the signal efficiency,

$$\text{FoM} = \frac{S}{\sqrt{S+B}}\,\varepsilon_S, \tag{4.4}$$

where ε_S is the signal efficiency of the BDT requirement and S and B are, respectively, the number of signal and background events selected by the BDT requirement.

The BDT requirement found by maximising this figure of merit is BDT > -0.4 (as shown in fig. 4.9), which provides a signal efficiency of 90% and a background rejection of 65%. This cut is applied to the signal samples after all the previous selection requirements.

4.4 Reconstruction of signal events

The decay chains of the signal decays, $B \to D^{(*)}\tau^-\overline{\nu}_\tau$, contain two unreconstructible neutrinos, one from the τ vertex and another from the B vertex. This causes each of the vertices to be reconstructible only up to a two-fold ambiguity, leaving us with a challenging scenario for momentum reconstruction. The strategy used in these analyses and described in this section is the same that was used in the Run 1 $R(D^*)$ hadronic analysis [31], which proved to perform well.

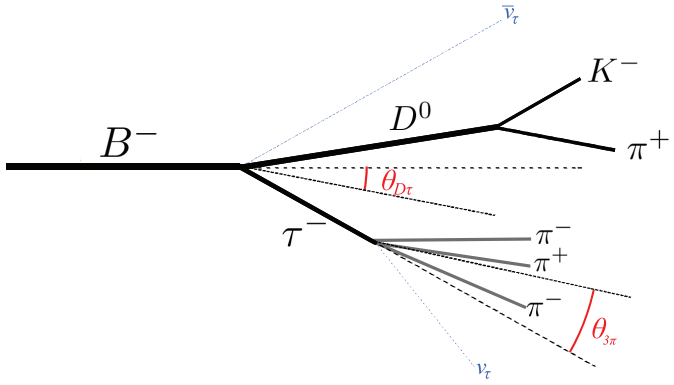

Figure 4.10: Angles used in the reconstruction of $B^- \to D^0\tau^-\overline{\nu}_\tau$ decays. $\theta_{D\tau}$ is the angle between the directions of the $D\tau^-$ system and the B^-, and $\theta_{3\pi}$ is the angle between the 3π system and the direction of the τ^-. The undetectability of the neutrinos limits the available information for the reconstruction of this kind of decay.

Reconstruction of the τ

In signal events, the τ is reconstructed under the $\tau^- \to \pi^-\pi^+\pi^-\nu_\tau$ decay hypothesis. The tracks of the three charged pions are used to reconstruct the τ decay vertex, and the line which connects this vertex with the B decay vertex provides the direction of the τ momentum. Due to the unknowability of the neutrino's momentum, the τ momentum is given by

$$|\vec{p}_\tau| = \frac{(m_{3\pi}^2 + m_\tau^2)|\vec{p}_{3\pi}|\cos\theta_{3\pi} \pm E_{3\pi}\sqrt{(m_\tau^2 - m_{3\pi}^2)^2 - 4m_\tau^2|\vec{p}_{3\pi}|^2\sin^2\theta_{3\pi}}}{2(E_{3\pi}^2 - |\vec{p}_{3\pi}|^2\cos^2\theta_{3\pi})}, \tag{4.5}$$

where every variable is expressed in natural units ($c = 1$), $m_{3\pi}$, $\vec{p}_{3\pi}$, and $E_{3\pi}$ are, respectively, the mass, 3-momentum, and energy of the 3π system, and $\theta_{3\pi}$ is the angle between the directions of the τ momentum and of the 3π system.

In order to rid us of the quadratic ambiguity in eq. 4.5, we approximate $\theta_{3\pi}$ as its maximum allowed value

$$\theta_{3\pi}^{(\max)} \equiv \arcsin\left(\frac{m_\tau^2 - m_{3\pi}^2}{2m_\tau|\vec{p}_{3\pi}|}\right), \tag{4.6}$$

which makes the second term of eq. 4.5 vanish. With this approximation, the τ momentum can be estimated as

$$|\vec{p}_\tau| \approx \frac{(m_{3\pi}^2 + m_\tau^2)|\vec{p}_{3\pi}|\cos\theta_{3\pi}^{(\max)}}{2(E_{3\pi}^2 - |\vec{p}_{3\pi}|^2\cos^2\theta_{3\pi}^{(\max)})}. \tag{4.7}$$

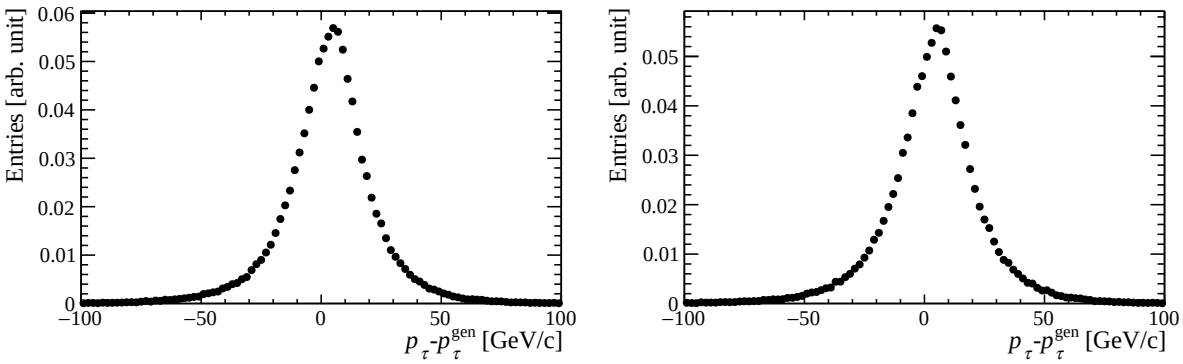

Figure 4.11: Distribution of the τ momentum resolution (difference between reconstructed and true momentum) for the $B^- \to D^0\tau^-\overline{\nu}_\tau$ (left) and $B^- \to D^{*0}\tau^-\overline{\nu}_\tau$ (right) simulated samples.

A comparison of this reconstructed τ momentum with the corresponding generated momentum is shown in fig. 4.11.

Reconstruction of the B

For the B meson, the direction of its momentum is taken from the line that connects the PV to the B decay vertex. Then, since there is also one neutrino coming from the B, the magnitude of its momentum also suffers a quadratic ambiguity in the form

$$|\vec{p}_B| = \frac{(m_{D\tau}^2 + m_B^2)|\vec{p}_{D\tau}|\cos\theta_{D\tau} \pm E_{D\tau}\sqrt{(m_B^2 - m_{D\tau}^2)^2 - 4m_B^2|\vec{p}_{D\tau}|^2\sin^2\theta_{D\tau}}}{2(E_{D\tau}^2 - |\vec{p}_{D\tau}|^2\cos^2\theta_{D\tau})}. \tag{4.8}$$

where every variable is expressed in natural units ($c = 1$), $m_{D\tau}$, $\vec{p}_{D\tau}$, and $E_{D\tau}$ are, respectively, the mass, 3-momentum, and energy of the $D\tau$ system, and $\theta_{D\tau}$ is the angle between the directions of the B momentum and of the $D\tau$ system. All of these quantities are computed using the tau momentum approximation discussed previously.

In the same fashion as with the τ momentum, the angle $\theta_{D\tau}$ is approximated to its maximum value,

$$\theta_{D\tau}^{(\max)} \equiv \arcsin\left(\frac{m_B^2 - m_{D\tau}^2}{2m_B|\vec{P}_{D\tau}|}\right), \tag{4.9}$$

and the B momentum is approximated as

$$|\vec{p}_B| \approx \frac{(m_{D\tau}^2 + m_B^2)|\vec{p}_{D\tau}|\cos\theta_{D\tau}^{(\max)}}{2(E_{D\tau}^2 - |\vec{p}_{D\tau}|^2\cos^2\theta_{D\tau}^{(\max)})}. \tag{4.10}$$

A comparison of this reconstructed B momentum with the corresponding generated momentum is shown in fig. 4.12.

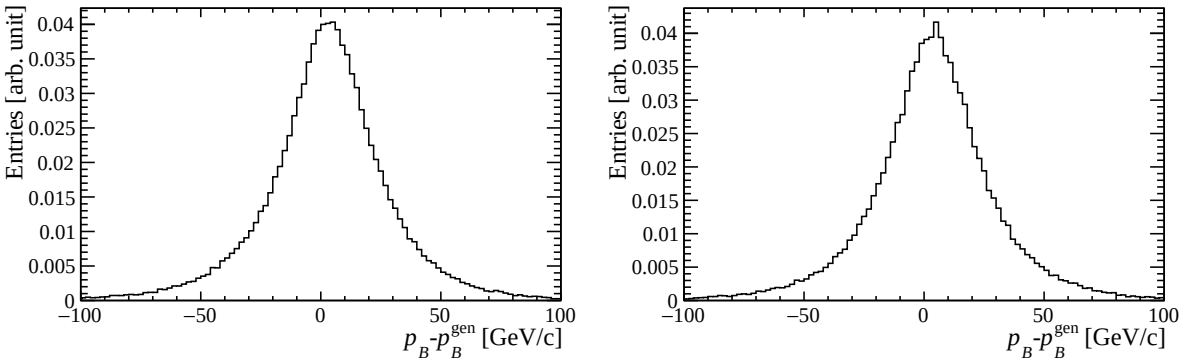

Figure 4.12: Distribution of the B^- momentum resolution (difference between reconstructed and true momentum) for the $B^- \to D^0\tau^-\overline{\nu}_\tau$ (left) and $B^- \to D^{*0}\tau^-\overline{\nu}_\tau$ (right) simulated samples.

Transferred momentum and decay time

Using the approximations discussed above, the 4-momenta of the B and the τ can be estimated as

$$p_\tau = (m_\tau, \vec{p}_\tau) \tag{4.11}$$

and

$$p_B = (m_B, \vec{p}_B), \tag{4.12}$$

providing us with a measurement of the squared transferred momentum, $q^2 = (p_B - p_D)^2$, and of the τ decay time,

$$t_\tau = \frac{m_\tau L_\tau}{|\vec{p}_\tau|}, \tag{4.13}$$

where L_τ is the τ flight distance, measured as the length of the segment that connects the B and τ decay vertices.

These two quantities will be used, together with the output of a boosted decision tree, as the three dimensions on which the signal yield fit is performed (section 6.1.1). A comparison of these estimations with their corresponding generated values are shown in figs. 4.13 and 4.14.

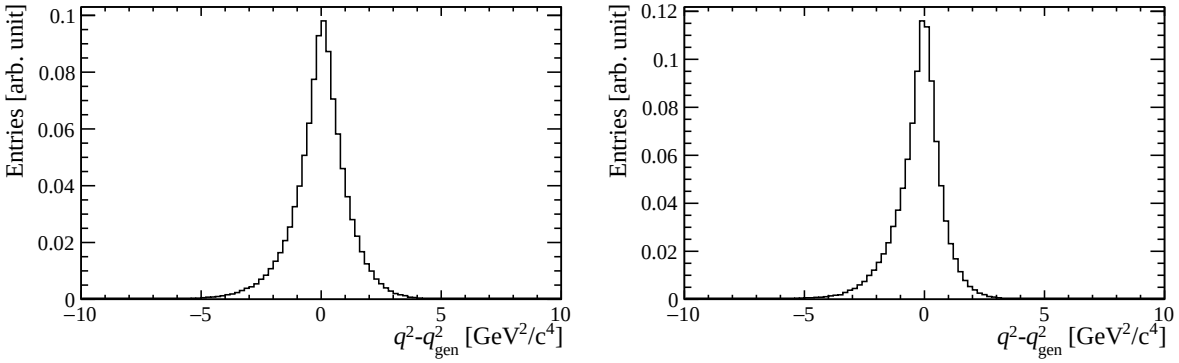

Figure 4.13: Distribution of the q^2 resolution (difference between reconstructed and true value) for the $B^- \to D^0\tau^-\overline{\nu}_\tau$ (left) and $B^- \to D^{*0}\tau^-\overline{\nu}_\tau$ (right) simulated samples.

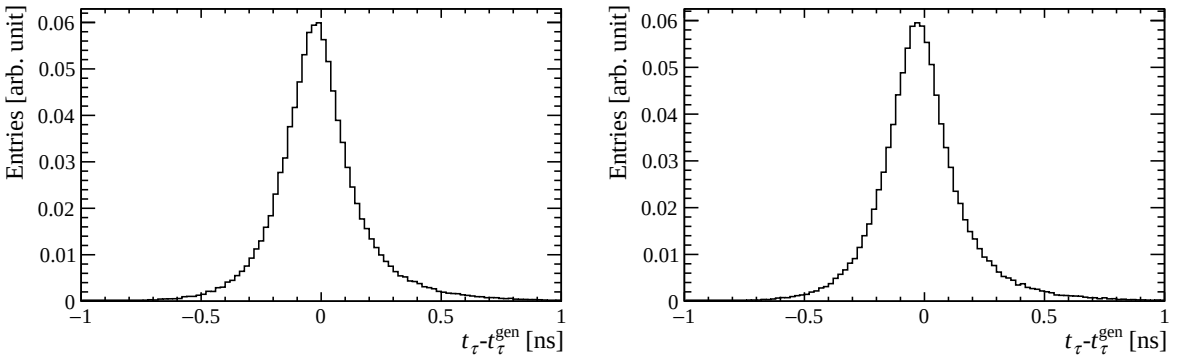

Figure 4.14: Distribution of the τ decay time resolution (difference between reconstructed and true value) for the $B^- \to D^0\tau^-\overline{\nu}_\tau$ (left) and $B^- \to D^{*0}\tau^-\overline{\nu}_\tau$ (right) simulated samples.

4.5 Corrections on the simulation samples

The simulation samples are known to not describe real data accurately in some variables. These are: charged-particle identification, vertex resolution, B kinematics, event multiplicity, trigger response, and form factors for the signal decays. The corrections applied to these categories are discussed in the following sections.

4.5.1 Corrections on charged-particle identification

The `PIDCalib` tool [119] is used to correct the simulation to match the particle identification (PID) performance observed in data.

`PIDCalib` uses template calibration samples of pions and kaons to compute a weight for each simulated event, taking into consideration the binning on track momentum, pseudo-rapidity, and the number of tracks in the event, together with the PID requirements applied to the selected events. In order to include tracks with momentum in the range $[2, 200]$ MeV/c, the default `PIDCalib` binning scheme was extended.

The applied requirements on the PID variables (see section 3.3 for their definition) are:

- $\text{PID}_K > 3$ and $P_{\text{NN}}(K) > 0.4$ for the kaon coming from the D,
- $\text{PID}_K < 50$ and $P_{\text{NN}}(\pi) > 0.4$ for the pion(s) coming from the D,
- $\text{PID}_K < 8$ and $P_{\text{NN}}(\pi) > 0.2$ for the three pions coming from the τ candidate,
- $P_{\text{NN}}(K) < 0.1$ for the oppositely charged pion coming from the τ.

All these cuts are applied at the preselection stage (section 4.3.1), except the last one, which is applied in the signal and normalisation selections (section 4.3.5).

`PIDCalib` takes as input the simulation samples before cutting on the PID variables, compares them to the calibration samples, and determines the efficiency of a given PID requirement for each individual track. A weight is computed for each decay candidate, consisting on the product of the individual efficiencies of each track. These weights are used to calibrate the simulation samples.

4.5.2 Corrections on vertex resolution

Before applying the vertex detachment cut $\delta z > 4$ (see section 4.3.3), the largest background contribution to the data sample comes from prompt events ($B \to D3\pi(X)$). Since the three pions from these events come directly from the B vertex, the width of the Δz distribution is due only to vertex resolution effects, while the width of the δz distribution also depends on the uncertainties of the z-positions of the B and 3π vertices ($\sigma(z_{3\pi})$ and $\sigma(z_B)$).

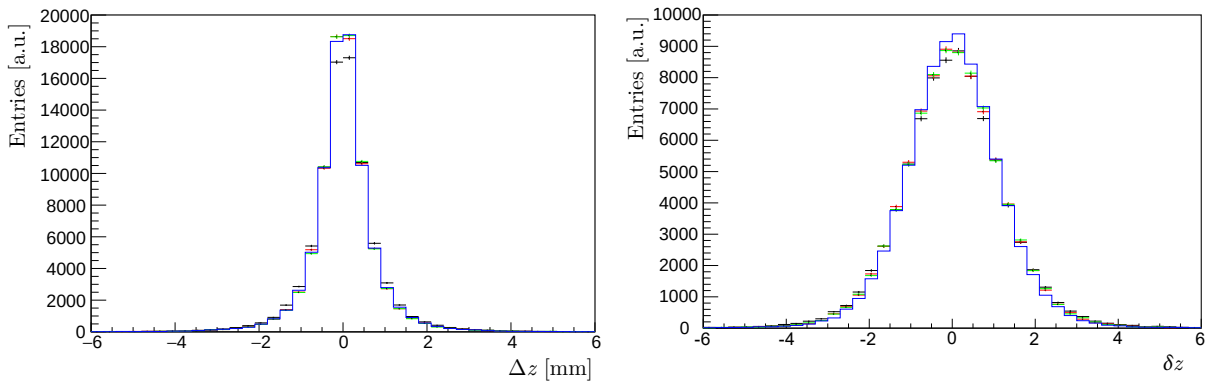

Figure 4.15: Δz (left) and δz (right) distributions for 2016 (black), 2017 (red), 2018 (green) data and simulation (blue) for exclusive $B \to D^0 3\pi$ events. The widths of the distributions are due to vertex-resolution effects (both Δz and δz) and the values of the z-position uncertainties (δz). The resolution in 2016 data is worse than in 2017 and 2018. The simulation (2016 only) is in agreement with 2017 and 2018 data in the Δz distribution (left), but disagrees in δz (right). The simulation disagrees with 2016 data in both distributions.

These distributions are shown in fig. 4.15 for exclusive $B \to D^0 3\pi$ decays, where the differences between the data and simulation samples can be observed. The following procedure is applied to the simulation samples, in order to match the data from the different data-taking periods:

- A scaling factor is applied to each one of the z-position uncertainties ($\sigma(z_{3\pi})$ and $\sigma(z_B)$).
- A smearing factor is applied to the δz distribution. As shown below, this smearing is only needed to describe 2016 data.

These corrections are computed with the prompt control sample (see section 5.1) and are tested in the exclusive $B \to D^0 3\pi$ peak.

The uncertainties $\sigma(z_{3\pi})$ and $\sigma(z_B)$ depend on the invariant mass distributions of the tracks that form their vertices: $m(3\pi)$ and $m(D^0 3\pi)$, respectively. The dependence between the mean $\sigma(z)$ uncertainties and their correspondent invariant mass is shown in fig. 4.16, along with the ratios with 2016 data.

The values of the $\sigma(z_{3\pi})$ and $\sigma(z_B)$ uncertainties in the simulation samples are corrected by applying first-order polynomials depending on the $m(3\pi)$ and $m(D^0 3\pi)$ invariant masses,

$$\begin{aligned} \sigma(z_{3\pi})' &= (\alpha_0^{(3\pi)} + \alpha_1^{(3\pi)}\, m(3\pi))\ \sigma(z_{3\pi}), \\ \sigma(z_B)' &= (\alpha_0^{(B)} + \alpha_1^{(B)}\, m(D^0 3\pi))\ \sigma(z_B), \end{aligned} \tag{4.14}$$

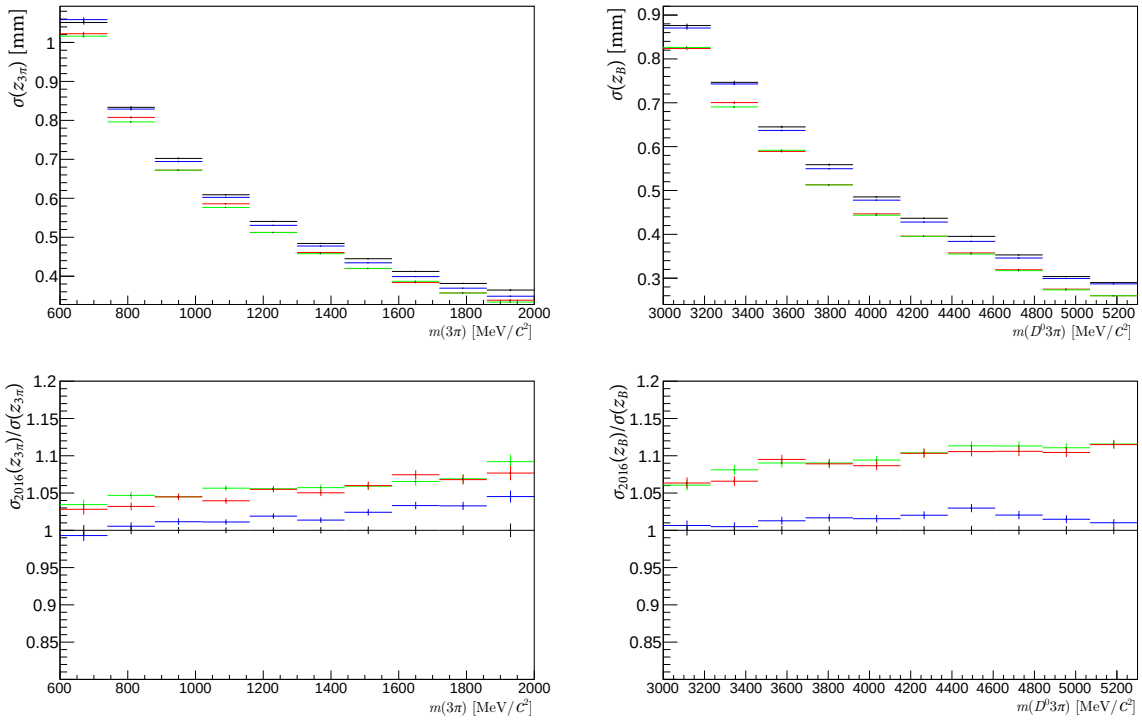

Figure 4.16: Top: mean of the $\sigma(z_{3\pi})$ (left) and $\sigma(z_B)$ (right) distributions as a function of $m(3\pi)$ and $m(D^0 3\pi)$, respectively. 2016, 2017 and 2018 data are shown in black, red and green, and simulation in blue. Bottom: the corresponding ratios 2016/2017, 2016/2018 and 2016/simulation.

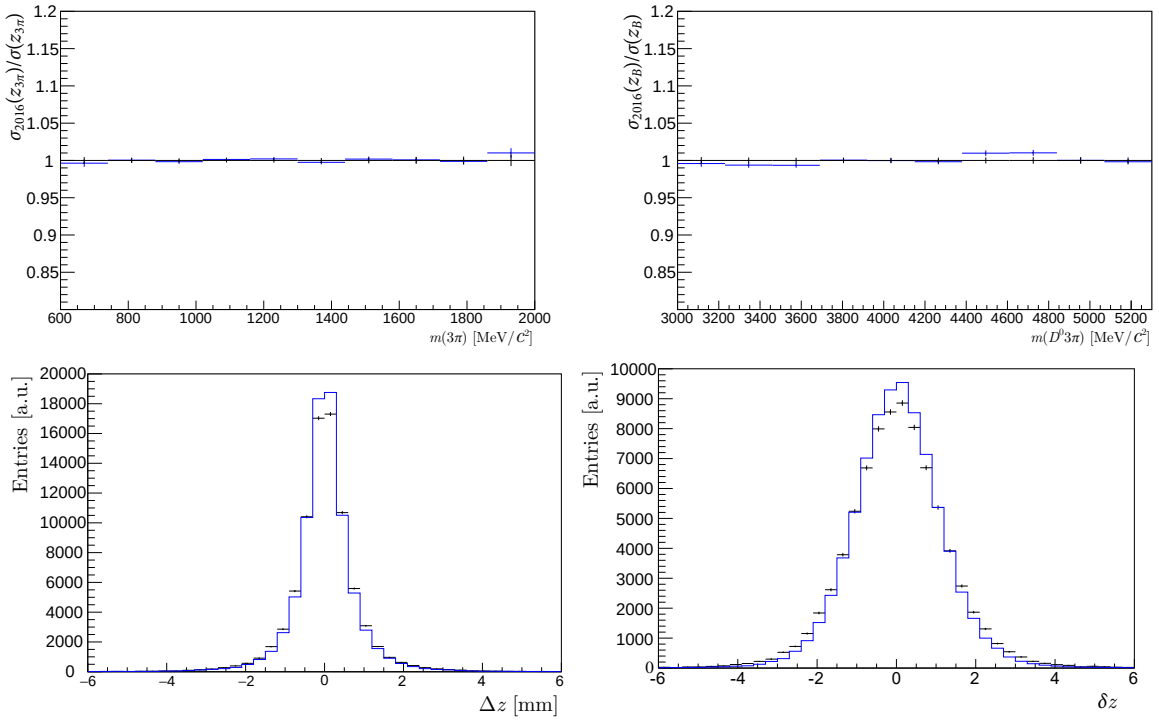

Figure 4.17: Top: ratio data(2016)/simulation for the mean of the $\sigma(z_{3\pi})$ (left) and $\sigma(z_B)$ (right) as a function of $m(3\pi)$ and $m(D^0 3\pi)$ after the vertex-uncertainty scaling correction. Bottom: Δz (left) and δz (right) distributions for 2016 data (black) and simulation (blue) after the correction.

where $\sigma(z)'$ is the corrected value of the uncertainty, and α_i are the polynomial coefficients, which are determined from a fit to data. The results of these corrections are shown in fig. 4.17 for 2016 data, and figs. 4.20 and 4.21 for 2017 and 2018 data.

The previous correction correctly matches simulation and data for the 2017 and 2018 periods. However, for 2016 data, the simulation sample still needs an additional vertex resolution smearing. This smearing is modelled as a double-Gaussian distribution,

$$f_{\text{smear.}}(\beta, \Delta\sigma_1, \Delta\sigma_2) \equiv \beta\ \text{Gauss}(0, \Delta\sigma_1) + (1-\beta)\ \text{Gauss}(0, \Delta\sigma_2), \tag{4.15}$$

where β, $\Delta\sigma_1$, and $\Delta\sigma_2$ are free parameters to be fitted to the data distribution. A simultaneous fit to simulation and 2016 data in the δz distribution is performed using the following PDFs:

$$\begin{aligned} \text{PDF}_{\text{MC}} \equiv\ & \alpha_1 \times \text{Gaus}(\mu, \sigma_1) + (1-\alpha_1) \times \alpha_2 \times \text{Gaus}(\mu, \sigma_2) + \\ & + (1-\alpha_1) \times (1-\alpha_2) \times \text{Gaus}(\mu, \sigma_3), \\ \text{PDF}_{\text{data}} \equiv\ & \text{PDF}_{\text{MC}} \circledast f_{\text{smear.}}(\beta, \Delta\sigma_1, \Delta\sigma_2), \end{aligned} \tag{4.16}$$

where μ, α_1, α_2, σ_1, σ_2, σ_3, β, $\Delta\sigma_1$, and $\Delta\sigma_2$ are the free parameters of the fit and the

Parameter	Value
α_1	0.43 ± 0.10
α_2	0.942 ± 0.009
σ_1	0.82 ± 0.04
σ_2	1.21 ± 0.05
σ_3	2.83 ± 0.28
μ	0.023 ± 0.003
β	0.90 ± 0.03
$\Delta\sigma_1$	0.25 ± 0.05
$\Delta\sigma_2$	1.51 ± 0.14

Table 4.6: Results of the simultaneous fit to simulation and 2016 data in the δz distribution. The used models are described in eq. 4.16.

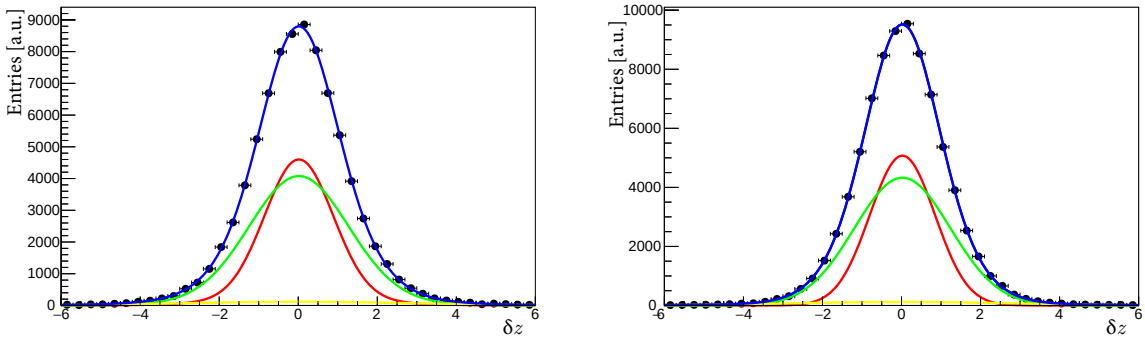

Figure 4.18: Projections of the simultaneous fit to 2016 data (left) and simulation (right) after the vertex-uncertainty correction. The used models are described in eq. 4.16.

symbol "⊛" represents the convolution of two functions. The fit results are shown in table 4.6 and the corresponding projections, in fig. 4.18. The resulting smearing function is used to correct the simulation sample for 2016 data.

Since these corrections are different for each data-taking year, and all the simulation samples are produced with 2016 conditions, they are applied separately to three portions of each simulation sample, following the same proportion of total events as data-taking years (31%/32%/37% for 2016/2017/2018). The portion corresponding to 2016 corrections is applied both the $\sigma(z)$ scaling and the δz smearing factors, while the portions corresponding to 2017 and 2018 are only corrected with the $\sigma(z)$ scaling factor.

The comparisons of the Δz and δz distributions before and after all this correction procedure are shown in figs. 4.19, 4.20 and 4.21 for 2016, 2017 and 2018 data. These corrections are applied to all simulation samples.

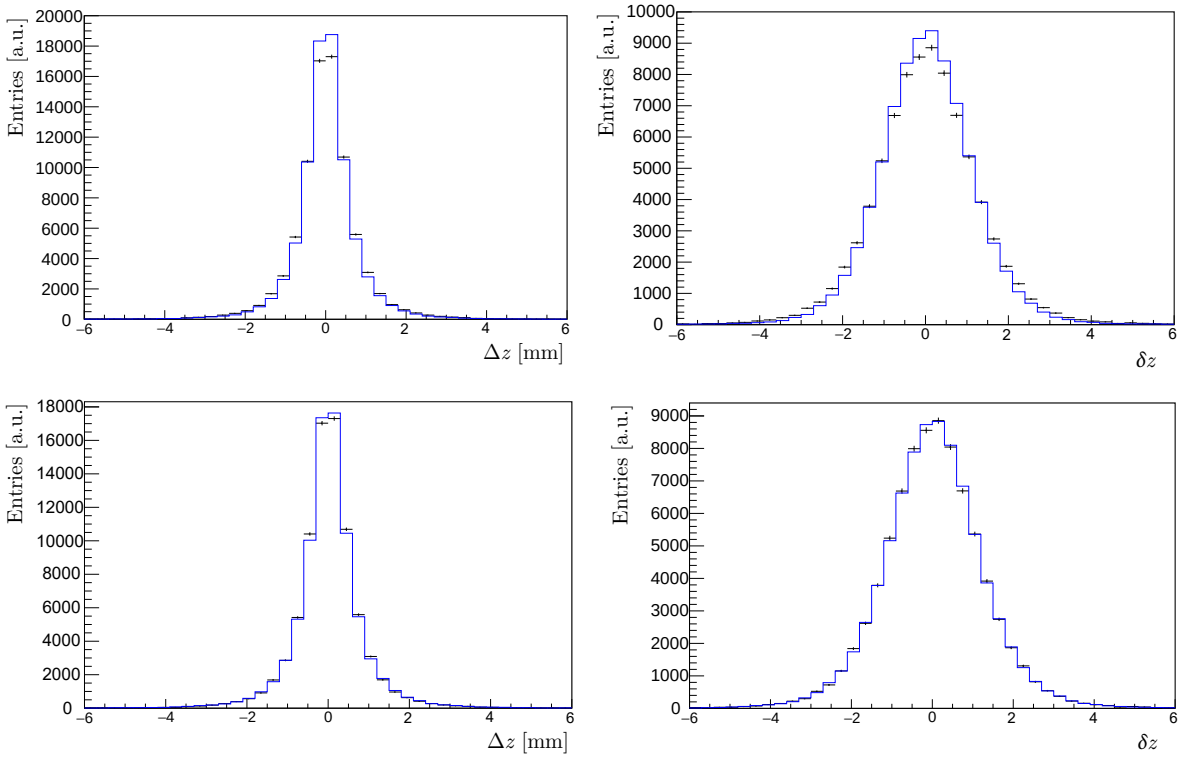

Figure 4.19: Comparison of the Δz (left) and δz (right) distributions before (top) and after (bottom) the 2016-data corrections for vertex uncertainty and resolution. Black points correspond to 2016 data and the blue histograms, to simulation.

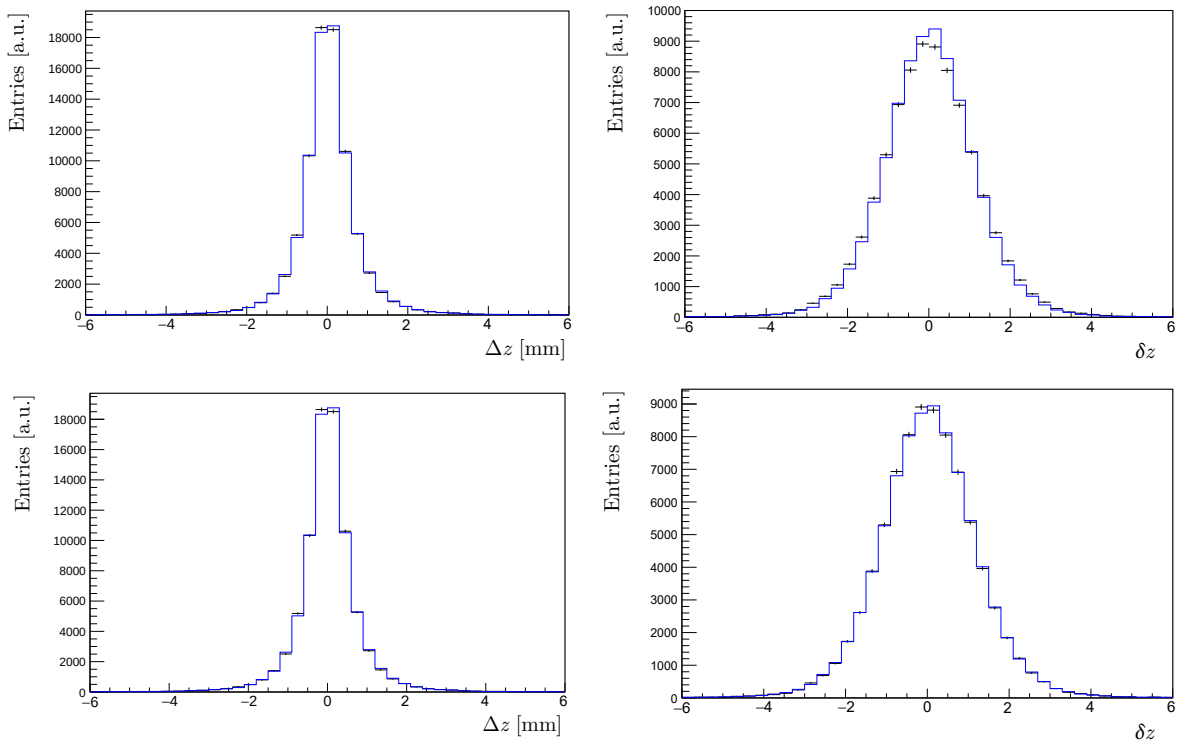

Figure 4.20: Comparison of the Δz (left) and δz (right) distributions before (top) and after (bottom) the 2017-data corrections for vertex uncertainty. Black points correspond to 2017 data and the blue histograms, to simulation.

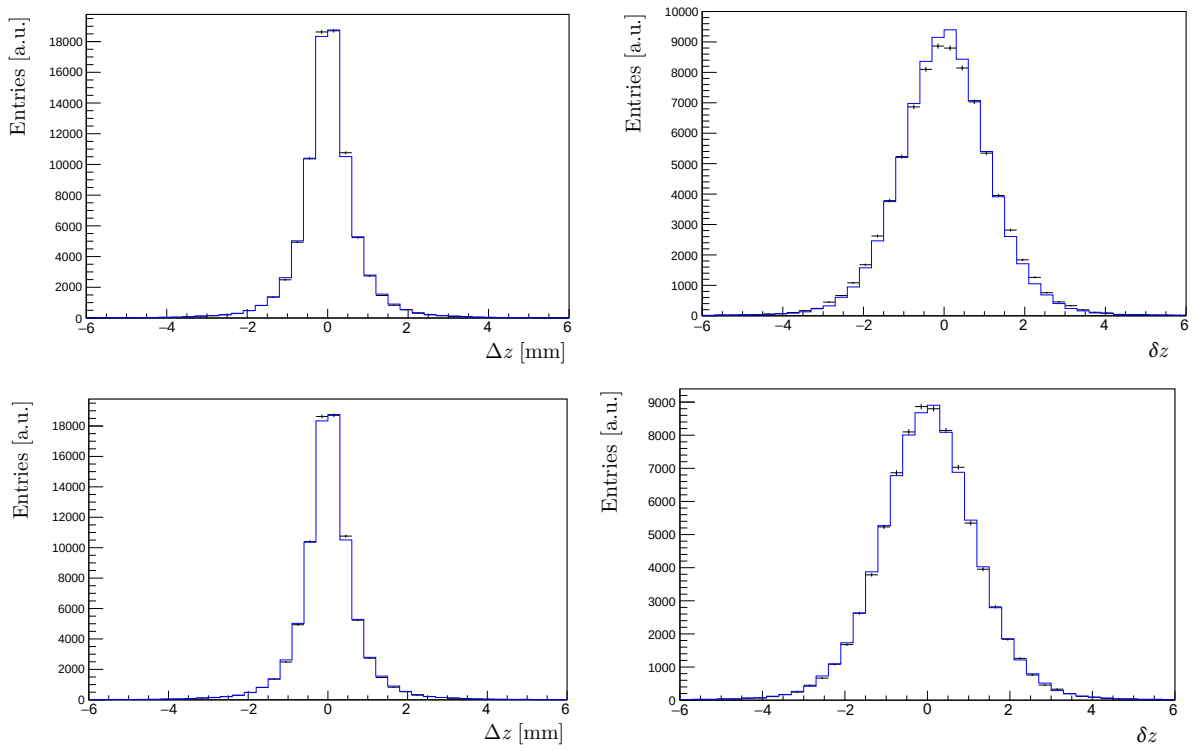

Figure 4.21: Comparison of the Δz (left) and δz (right) distributions before (top) and after (bottom) the 2018-data corrections for vertex uncertainty. Black points correspond to 2018 data and the blue histograms, to simulation.

4.5.3 Corrections on event multiplicity, B kinematics, and trigger category

The event multiplicity and B kinematics play an important role in the analysis, the former affecting the trigger selection and the later the whole selection procedure. The simulation samples show disagreement with real data when comparing variables related to these properties. A sequential 2D re-weighting is performed using the exclusive $B \to D^0 3\pi$ invariant mass peak in order to correct these discrepancies in the simulation samples.

First, the re-weighting is done on the total number of tracks of the event, N_{tracks}, and the number of degrees of freedom of the B's PV, $N_{\text{DoF}}^{(\text{PV})}$, variables which are related to the event multiplicity, affecting the trigger selection.

This reweighting consists on constructing a 2D histogram with the mentioned variables as axes and applying a weight to each bin of the histogram, according to the ratio of real data over simulated data in that bin. After this step, the same procedure is applied again on the transverse momentum and pseudorapidity of the B ($p_T(B)$ and $\eta(B)$).

This 2D re-weighting is done independently in three exclusive trigger categories, based on which trigger categories they were selected in (see section 4.3.2), which are

- Events that *do not* pass the `B_L0Global_TIS` requirements.
- Events that *do not* pass the `B_L0HadronDecision_TOS` requirements.
- Events that pass both the `B_L0Global_TIS` and `B_L0HadronDecision_TOS` requirements.

After the 2D re-weighting, a 1D re-weighting in the trigger variables is performed in order to make the TISTOS efficiencies in simulation and data match. "TISTOS efficiencies" refer to the TIS and TOS trigger efficiencies, defined respectively as

$$\varepsilon_{\text{TIS}} \equiv N_{\text{TISTOS}}/N_{\text{TOS}} \quad \text{and} \quad \varepsilon_{\text{TOS}} \equiv N_{\text{TISTOS}}/N_{\text{TIS}}, \tag{4.17}$$

where "TIS" and "TOS" refer to the two L0-trigger lines used in this analysis, and "TISTOS" refers to the events belonging to both categories, as shown in section 4.3.2. Since events can belong to both trigger categories simultaneously, these weights take a non-trivial form and modify the number of events in each category as

$$\begin{aligned} N'_{\text{TIS}} &= w_{\text{TIS}}(N_{\text{TIS}} - N_{\text{TISTOS}}) + w_{\text{TIS}} w_{\text{TOS}} N_{\text{TISTOS}}, \\ N'_{\text{TOS}} &= w_{\text{TOS}}(N_{\text{TOS}} - N_{\text{TISTOS}}) + w_{\text{TIS}} w_{\text{TOS}} N_{\text{TISTOS}}, \\ N'_{\text{TISTOS}} &= w_{\text{TIS}} w_{\text{TOS}} N_{\text{TISTOS}}, \end{aligned} \tag{4.18}$$

where N' are the number of events after re-weighting, and w_{TIS} and w_{TOS} are the weights applied, respectively, to events in the TIS and TOS categories (applying both weights in the events that belong to both categories). Using these expressions along with imposing the condition that the TISTOS efficiencies from eq. 4.17 in data and simulation match, the weights can be computed as

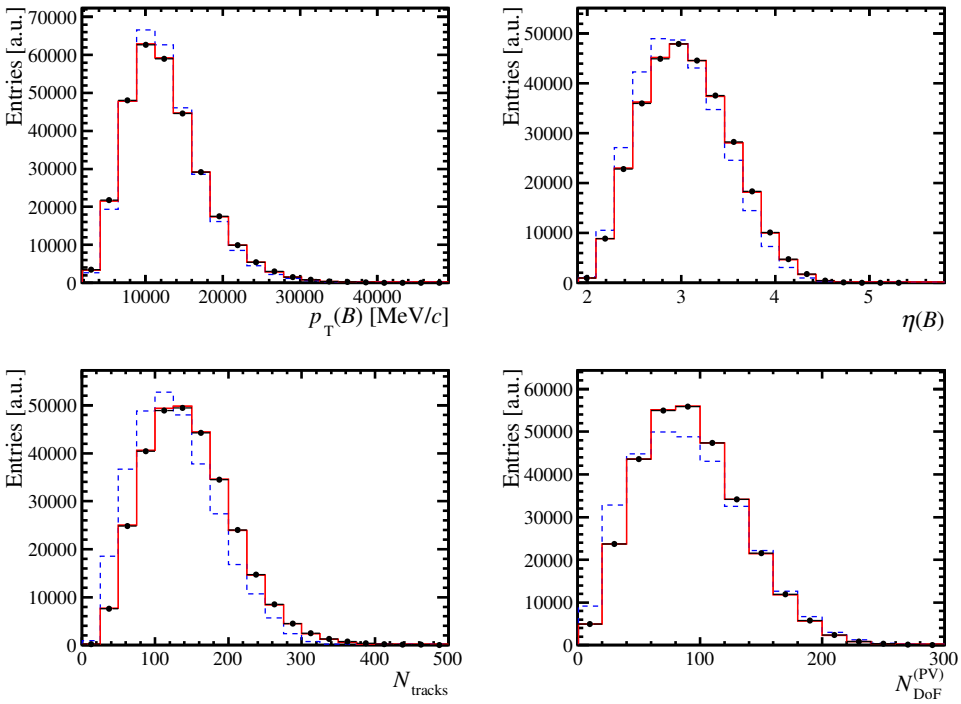

Figure 4.22: Comparison between data (black), simulation before re-weighting (dashed blue), and after re-weighting (red) of the B-kinematics and occupancy variables. The selected events correspond to exclusive $B \to D^0 3\pi$ decays.

$$
\begin{aligned}
w_{\text{TIS}} &= \frac{\varepsilon^{(\text{data})}_{\text{TIS}}}{1-\varepsilon^{(\text{data})}_{\text{TIS}}} \frac{N_{\text{TOS}} - N_{\text{TISTOS}}}{N_{\text{TISTOS}}}, \\
w_{\text{TOS}} &= \frac{\varepsilon^{(\text{data})}_{\text{TOS}}}{1-\varepsilon^{(\text{data})}_{\text{TOS}}} \frac{N_{\text{TIS}} - N_{\text{TISTOS}}}{N_{\text{TISTOS}}},
\end{aligned}
\tag{4.19}
$$

where $\varepsilon^{(\text{data})}$ are the TISTOS efficiencies as computed from data, and N (as before) are the number of events in each category before applying these weights.

To compute these weights, the exclusive $B^- \to D^0\pi^-\pi^+\pi^-$ and the inclusive $B^- \to D^0\pi^-\pi^+\pi^-(X)$ simulation samples are used together, to maximize the statistics in the exclusive peak. Prior to the 2D re-weighting, these samples are re-weighted in the $m(3\pi)$ distribution, so their kinematics match with the data. The results of these steps are shown in fig. 4.22.

To make sure that the re-weighting procedure is working properly, a cross-check is made by computing the weights using only the exclusive $B \to D^0 3\pi$ sample, and then applying them to the inclusive $B \to D^0 3\pi(X)$ sample. The result of this check is shown on fig. 4.23.

The weights obtained from this method are applied to all the simulated samples using

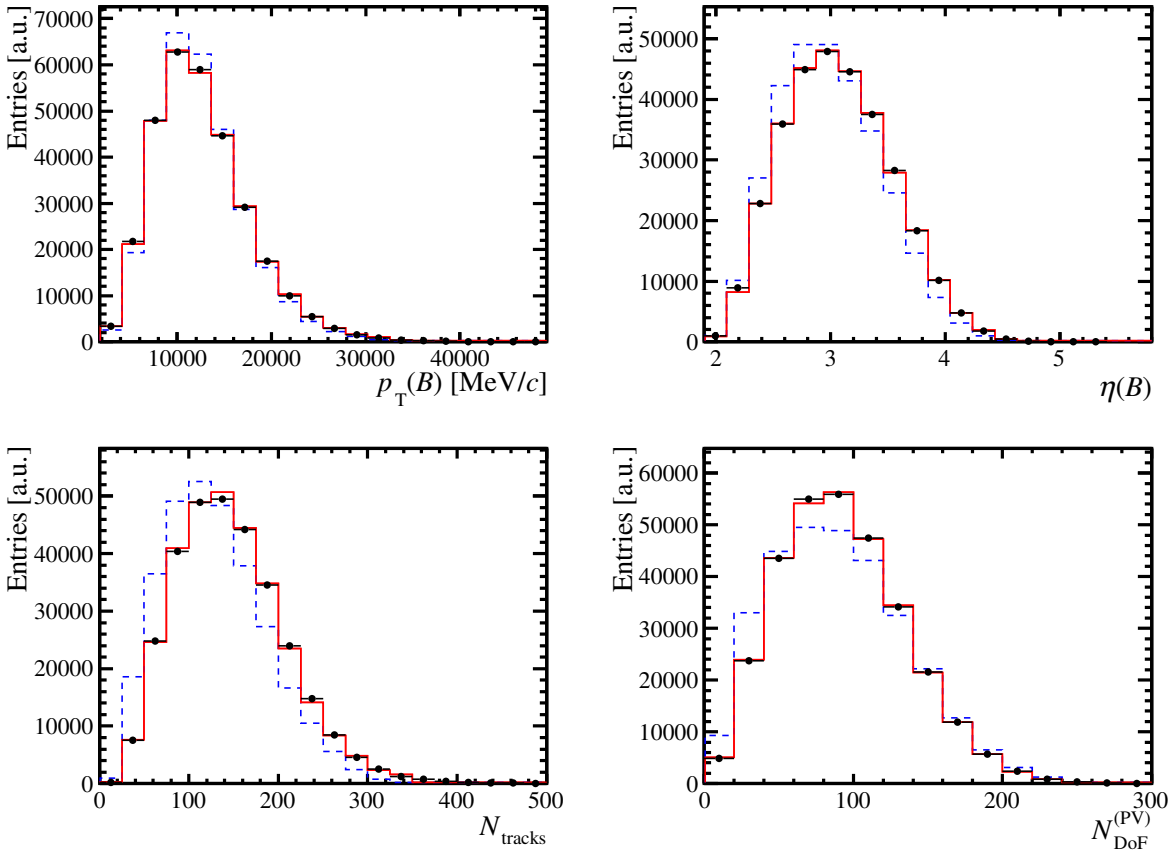

Figure 4.23: Comparison between data (black), simulation before re-weighting (dashed blue), and after re-weighting (red) of the B-kinematics and occupancy variables. The selected events correspond to exclusive $B \to D^0 3\pi$ decays. The weights used in this re-weighting were computed using only the exclusive $B \to D^0 3\pi$ simulated sample, and then applying them to the inclusive $B^- \to D^0\pi^-\pi^+\pi^-(X)$ sample as a cross-check of the re-weighting procedure.

Parameter	Value
a_0^+	0.01566 ± 0.00011
a_1^+	-0.0342 ± 0.0031
a_2^+	-0.090 ± 0.022
a_0^0	0.07935 ± 0.00058
a_1^0	-0.205 ± 0.014
a_2^0	-0.23 ± 0.10

Table 4.7: BGL parameters and their uncertainties for $B \to D\tau^-\overline{\nu}_\tau$, as estimated in [54] through a global fit to lattice and experimental data for $N = 2$.

	a_0^+	a_1^+	a_2^+	a_1^0	a_2^0
a_0^+	1	0.304	−0.294	0.212	0.161
a_1^+	0.304	1	0.422	0.747	0.190
a_2^+	−0.294	−0.422	1	−0.034	0.148
a_1^0	0.212	0.747	−0.034	1	−0.210
a_2^0	0.161	0.190	0.148	−0.210	1

Table 4.8: Correlation matrix of the $B \to D\tau^-\overline{\nu}_\tau$ BGL parameters for the $N = 2$ fit in [54].

the variables N_{tracks}, $N_{\text{DoF}}^{(\text{PV})}$, $p_T(B)$, $\eta(B)$, and the L0 trigger response.

4.5.4 Form-factor re-weighting

The underlying theoretical models used in the generation of simulation samples might cause sizable effects that make them differ from real data. In order to reduce these effects, the approach taken in these analyses is the reweighting of the simulated samples using the software tool HAMMER (Helicity Amplitude Module for Matrix Element Re-weighting) [120], which effectively transforms simulated samples from the theoretical framework in which they were generated to another desired model. HAMMER was developed for the analysis of $b \to c\tau^-\overline{\nu}_\tau$ processes with different form-factor parameterisations, as is our case.

As shown in section 2.2.2, the BGL form-factor parameterisation is used for these analyses. Following equation 2.19 and considering that we are truncating the equation at $N = 2$, six free parameters are needed for $B \to D\tau^-\overline{\nu}_\tau$ decays (a_n^+ and a_n^0, with $n \in [0, 2]$), and twelve for $B \to D^*\tau^-\overline{\nu}_\tau$ decays ($a_n^{\mathcal{F}_1}$, $a_n^{\mathcal{F}_2}$, a_n^f, and a_n^g).

For this parameterisation, the relevant factors, free parameters (table 4.7), and their correlation matrix (table 4.8) are estimated in [54] for $B \to D\tau^-\overline{\nu}_\tau$ decays with $N = 2$ (which is the reason why we truncate the series at the same value) using lattice QCD calculations from the HPQCD and FNAL/MILC collaborations and experimental data from BaBar and Belle.

Parameter	Value
a_0^g	$0.0299^{+0.0053}_{-0.0035}$
a_1^g	$0.04^{+0.07}_{-0.20}$
a_2^g	$-0.9^{+1.8}_{-0.0}$
a_0^f	0.01218 ± 0.00016
a_1^f	$-0.029^{+0.021}_{-0.013}$
a_2^f	$0.5^{+0.0}_{-0.3}$
$a_0^{\mathcal{F}_1}$	$0.1675 a_0^f$
$a_1^{\mathcal{F}_1}$	$-0.0051^{+0.0049}_{-0.0013}$
$a_2^{\mathcal{F}_1}$	$0.065^{+0.009}_{-0.089}$
$a_0^{\mathcal{F}_2}$	0.0595 ± 0.0093
$a_1^{\mathcal{F}_2}$	$-0.318 \pm 0.170 - 0.056 a_2^{\mathcal{F}_2}$
$a_2^{\mathcal{F}_2}$	$\lvert a_2^{\mathcal{F}_2} \rvert < 1$

Table 4.9: BGL parameters and their uncertainties for $B \to D^* \tau^- \overline{\nu}_\tau$, as estimated in [122] through a global fit to lattice and experimental data for $N = 2$. The parameter $a_2^{\mathcal{F}_2}$ can take any value in the range $[-1, 1]$ and is fixed to zero. Its possible variation will be later considered when computing the systematic uncertainties.

For $B \to D^* \tau^- \overline{\nu}_\tau$ decays, ref. [121] shows that the twelve parameters can be reduced down to ten by using the relation

$$\mathcal{F}_1(0) = (m_b - m_{D^*}) f(0), \tag{4.20}$$

which generates a constraint between the parameters $a_0^{\mathcal{F}_1}$ and a_0^f; and the relation between $\mathcal{F}_1$ and $\mathcal{F}_2$ shown in [122] which allows to ignore one of the $a_n^{\mathcal{F}_i}$ parameters ($a_2^{\mathcal{F}_2}$ is chosen). The estimation of these parameters, as computed by [122] using QCD lattice data and Belle experimental data, is shown in table 4.9.

The $B \to D^{(*)} \tau^- \overline{\nu}_\tau$ simulated events used in this thesis were generated following the ISGW2 model [123]. They are re-weighted to the BGL parameterisation using HAMMER, inputting the previous parameters and correlations. A comparison of the q^2 distribution before and after this re-weighting is shown in fig. 4.24.

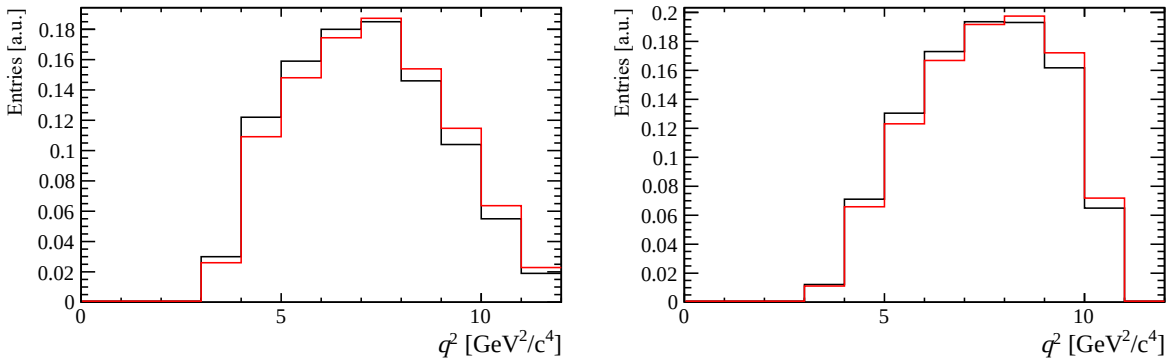

Figure 4.24: True q^2 distribution for simulated $B^- \to D^0\tau^-\overline{\nu}_\tau$ (left) and $B^- \to D^{*0}\tau^-\overline{\nu}_\tau$ (right) events as generated with the ISGW2 model (black line) and after the HAMMER re-weighting to the BGL parameterisation (red).

4.6 Efficiencies

The efficiencies of the signal and normalisation channels are needed to measure the LFU ratios, as seen in section 2.5.

Efficiencies are measured in three different stages:

1. Generation efficiency: the number of events accepted in the generation phase over the total number of events that were generated.

2. Filtering efficiency: the number of events that were selected by the filtering script (see section 4.2) over the number of events that passed the previous stage.

3. Selection efficiency: the number of events that pass the selection cuts described in section 4.3 (depending on the sample, either signal or normalisation selection cuts) over the number of events that passed the previous stage. This efficiency is computed after all corrections from section 4.5 are applied.

Then, the total efficiency for each sample is the product of the three efficiencies above. The resulting efficiencies for the simulated signal and normalisation samples are shown in table 4.10.

In addition, several other parameters are used as input for the signal fit model (section 6.1.1), which are

- $f_{3\pi}^{D^0}$, $f_{3\pi}^{D^{*0}}$, and $f_{3\pi}^{D^{*+}}$, defined as the ratio of events with $\tau^- \to \pi^-\pi^+\pi^-\nu_\tau$ over the number of events with $\tau^- \to \pi^-\pi^+\pi^-(\pi^0)\nu_\tau$ of the corresponding decay, and

Decay	Generation eff.	Filtering eff.	Selection eff.	Total eff.
$B^- \to D^0\tau^-\overline{\nu}_\tau$, $\tau^- \to \pi^-\pi^+\pi^-\nu_\tau$	$(4.182 \pm 0.008)\%$	$(5.0063 \pm 0.0034)\%$	$(4.648 \pm 0.015)\%$	$(9.73 \pm 0.04) \times 10^{-5}$
$B^- \to D^0\tau^-\overline{\nu}_\tau$, $\tau^- \to \pi^-\pi^+\pi^-\pi^0\nu_\tau$	$(3.713 \pm 0.007)\%$	$(4.936 \pm 0.004)\%$	$(2.093 \pm 0.012)\%$	$(3.837 \pm 0.023) \times 10^{-5}$
$B^- \to D^{*0}\tau^-\overline{\nu}_\tau$, $\tau^- \to \pi^-\pi^+\pi^-\nu_\tau$	$(4.018 \pm 0.007)\%$	$(4.9301 \pm 0.0034)\%$	$(4.240 \pm 0.014)\%$	$(8.398 \pm 0.033) \times 10^{-5}$
$B^- \to D^{*0}\tau^-\overline{\nu}_\tau$, $\tau^- \to \pi^-\pi^+\pi^-\pi^0\nu_\tau$	$(3.606 \pm 0.007)\%$	$(4.881 \pm 0.004)\%$	$(1.775 \pm 0.011)\%$	$(3.123 \pm 0.020) \times 10^{-5}$
$\overline{B}^0 \to D^{*+}\tau^-\overline{\nu}_\tau$, $\tau^- \to \pi^-\pi^+\pi^-\nu_\tau$	$(15.97 \pm 0.16)\%$	$(2.2727 \pm 0.0019)\%$	$(0.490 \pm 0.006)\%$	$(1.778 \pm 0.028) \times 10^{-5}$
$\overline{B}^0 \to D^{*+}\tau^-\overline{\nu}_\tau$, $\tau^- \to \pi^-\pi^+\pi^-\pi^0\nu_\tau$	$(15.68 \pm 0.15)\%$	1 ± 0	$(3.93 \pm 0.10) \times 10^{-5}$	$(0.616 \pm 0.017) \times 10^{-5}$
$B^+ \to \overline{D}^0 D_s^+$, $D_s^+ \to \pi^+\pi^-\pi^+$	$(5.986 \pm 0.011)\%$	$(6.137 \pm 0.006)\%$	$(10.37 \pm 0.03)\%$	$(38.09 \pm 0.13) \times 10^{-5}$

Table 4.10: Generation, filtering, selection, and total efficiencies for all signals and the normalisation mode.

computed as

$$f_{3\pi}^X \equiv \frac{N(B \to X\tau^-(\to 3\pi)\overline{\nu}_\tau)}{N(B \to X\tau^-(\to 3\pi(\pi^0))\overline{\nu}_\tau)} = \\ = \frac{\mathcal{B}(\tau \to 3\pi)\varepsilon^{(\tau\to 3\pi)}_{B\to X\tau^-\overline{\nu}_\tau}}{\mathcal{B}(\tau \to 3\pi)\varepsilon^{(\tau\to 3\pi)}_{B\to X\tau^-\overline{\nu}_\tau} + \mathcal{B}(\tau \to 3\pi\pi^0)\varepsilon^{(\tau\to 3\pi\pi^0)}_{B\to X\tau^-\overline{\nu}_\tau}}\ , \quad (4.21)$$

where $\tau \to 3\pi$ is short for $\tau^- \to \pi^-\pi^+\pi^-\nu_\tau$.

- $f_{D^{*+}/D^{*0}}$, defined as the ratio of $\overline{B}^0 \to D^{*+}\tau^-\overline{\nu}_\tau$ events over $B^- \to D^{*0}\tau^-\overline{\nu}_\tau$ events, computed as

$$f_{D^{*+}/D^{*0}} \equiv \frac{N(B \to D^{*+}\tau^-(\to 3\pi(\pi^0))\overline{\nu}_\tau)}{N(B \to D^{*0}\tau^-(\to 3\pi(\pi^0))\overline{\nu}_\tau)} = \\ = \frac{\mathcal{B}(D^{*+} \to D^0X)}{\mathcal{B}(D^{*0} \to D^0X)}\frac{f_d}{f_u}\frac{\mathcal{B}(\overline{B}^0 \to D^{*+}\tau^-\overline{\nu}_\tau)}{\mathcal{B}(B^- \to D^{*0}\tau^-\overline{\nu}_\tau)}\times \\ \times \frac{\mathcal{B}(\tau \to 3\pi)\varepsilon^{(\tau\to 3\pi)}_{\overline{B}^0\to D^{*+}\tau^-\overline{\nu}_\tau} + \mathcal{B}(\tau \to 3\pi\pi^0)\varepsilon^{(\tau\to 3\pi\pi^0)}_{\overline{B}^0\to D^{*+}\tau^-\overline{\nu}_\tau}}{\mathcal{B}(\tau \to 3\pi)\varepsilon^{(\tau\to 3\pi)}_{B^-\to D^{*0}\tau^-\overline{\nu}_\tau} + \mathcal{B}(\tau \to 3\pi\pi^0)\varepsilon^{(\tau\to 3\pi\pi^0)}_{B^-\to D^{*0}\tau^-\overline{\nu}_\tau}}, \quad (4.22)$$

where f_u and f_d are the B^+ and B^0 mesons production fractions, assumed to be equal; the branching fractions $\mathcal{B}(B^- \to D^{*0}\tau^-\overline{\nu}_\tau)$ and $\mathcal{B}(\overline{B}^0 \to D^{*+}\tau^-\overline{\nu}_\tau)$ are also assumed to be equal, based on isospin symmetry, and the ratio $\mathcal{B}(D^{*+} \to D^0X)/\mathcal{B}(D^{*0} \to D^0X)$ is set to 0.677, following [2].

The results for these f parameters are shown in table 4.11.

Parameter	Value
$f_{3\pi}^{D^0}$	0.8363 ± 0.0019
$f_{3\pi}^{D^{*0}}$	0.8442 ± 0.0019
$f_{3\pi}^{D^{*+}}$	0.853 ± 0.004
$f_{D^{*+}/D^{*0}}$	0.1418 ± 0.0020

Table 4.11: Values of the efficiency parameters needed for the input of the signal fit model.

5

Study of control samples

Contents

In this chapter, several independent data samples which contain decays that are important to model correctly in the final fit (the main background channels) are studied. These are known as control samples, and they are selected specifically to isolate as much as possible the desired decay channels. Their study is essential to understand their contribution to the final fit and correct the used simulation samples accordingly.

5.1 The "prompt" control sample

A small fraction of $B \to D3\pi(X)$ decays, where the three pions are produced directly at the B vertex (without the presence of a hadron with non-negligible lifetime), referred to as "prompt", pass the distance-detachment requirement, thus being present in the signal-selection sample. They sit at the low-lifetime region, as is the case of signal events. Therefore, it is important to produce a control sample to improve the modelling of this component in the signal fit.

To obtain the control sample for prompt $B \to D3\pi(X)$ decays, a cut in the z-coordinate distance between the B and the 3π vertices divided by its uncertainty (same δz quantity used in the vertex detachment criterion of section 4.3.3) is applied. In this case, events in the range $\delta z \in [-3, 0]$ are selected. The lower cut suppresses combinatorial background, while the upper cut also suppresses contributions from decays that have the 3π vertex displaced from the B vertex. This sample is further reduced by using the decay vertex of the reconstructed D meson to satisfy $z_D - z_B > 0$, further suppressing combinatorial background.

$R(D^{(*)0})$ analysis: prompt $B \to D^0 3\pi(X)$ decays

For the $R(D^{(*)0})$ analysis, the $B \to D^0\pi^-\pi^+\pi^-(X)$ simulation samples are used to perform the following study.

As seen in fig. 5.1, the simulation sample does not correctly reproduce the data. To correct for this discrepancy, a 2D histogram in the BDT and q^2 variables is used, with the same binning as the one used in the signal fit, and weights are computed for each bin, according to the data/simulation fraction. Fig. 5.1 also shows the result of applying these weights to the used simulation sample. These weights are then applied to the prompt $B \to D^0 3\pi(X)$ component of the signal fit (section 6.1.1). The uncertainties of these weights are not used in the fit; the systematic uncertainty derived from this decision is studied in section 7.1.3.

$R(D^{(*)-})$ analysis: prompt $B \to D^+ 3\pi(X)$ decays

In an analogous way, for the $R(D^{(*)-})$ analysis, the $B \to D^+\pi^-\pi^+\pi^-(X)$ simulation samples are studied. The weights to correct the simulation sample are computed in the same way as in the $R(D^{(*)0})$ case. Fig. 5.2 shows the BDT and q^2 simulation distributions before and after the correction, compared to the data distributions.

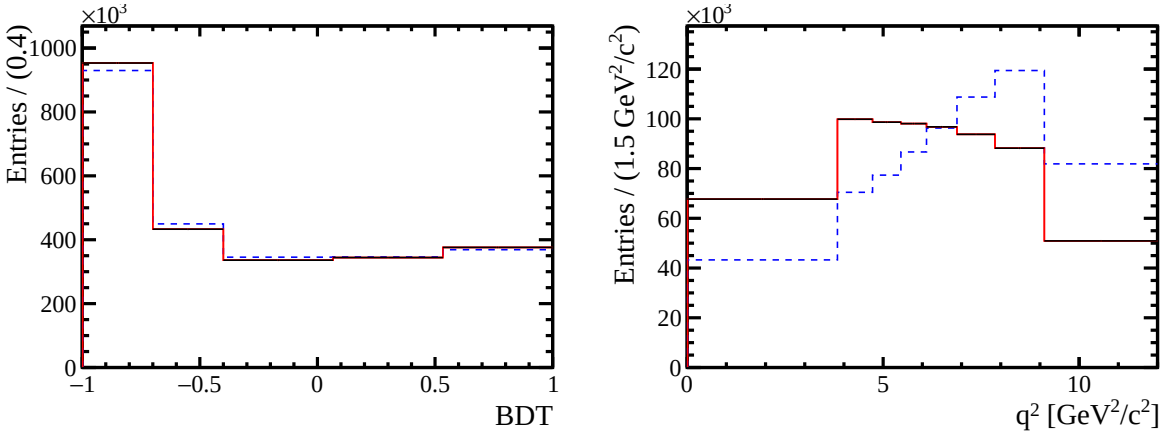

Figure 5.1: BDT output and q^2 distributions for the $B \to D^0 3\pi(X)$ prompt control sample. The dashed blue line represents the original simulation sample, while the red line is the same simulation sample after re-weighting in these variables. Data is shown in black. The distributions are normalised to the number of events in data.

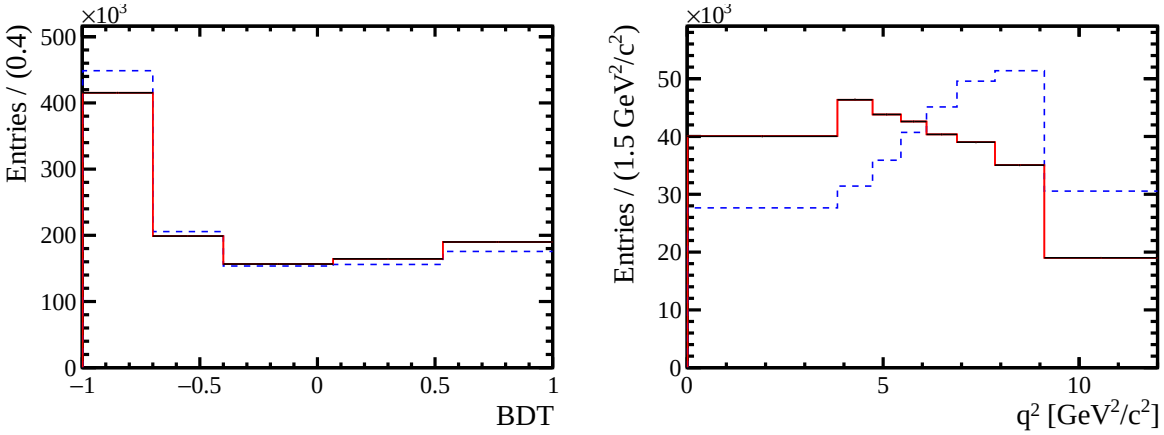

Figure 5.2: BDT output and q^2 distributions for the $B \to D^+ 3\pi(X)$ prompt control sample. The dashed blue line represents the original simulation sample, while the red line is the same simulation sample after re-weighting in these variables. Data is shown in black. The distributions are normalised to the number of events in data.

5.2 The double-charm control samples

5.2.1 $B \to \overline{D}^0 D_s^+(X)$ control sample

To obtain the $B \to \overline{D}^0 D_s^+(X)$ control sample, data candidates within a ± 30 MeV/c^2 mass window around the known D_s^+ mass (from [2]) are selected. The resulting D_s^+-enriched sample is then split into the following two subsamples:

- $\overline{D}^0 D_s^+$ subsample, obtained by applying the same cuts as in the normalisation selection (section 4.3.5), except the requirement on the $m(D^0 3\pi)$ invariant mass.
- $D^{*-} D_s^+$ subsample, obtained by finding an additional track compatible with a pion with the right charge giving an invariant mass difference $m(\overline{D}^0\pi^-) - m(\overline{D}^0)$ in the range $[143, 148]$ MeV/c^2. In this sample, when the isolation variables are calculated, the extra pion is not taken into account. This subsample is thus composed of events with a D^{*-} candidate whose reconstructed mass is in the correct window and with no extra charged particles coming from the B and τ vertices.

In order to characterise the different components in these subsamples, simulation samples have been generated. Histograms from this samples are scaled by the factor

$$\frac{N_{\mathrm{RS}}^{(\overline{D}^0 D_s^+)} - N_{\mathrm{WS}}^{(\overline{D}^0 D_s^+)}}{N_{\mathrm{sim.}}^{(\overline{D}^0 D_s^+)}},$$

where $N_{\mathrm{RS}}^{(\overline{D}^0 D_s^+)}$, $N_{\mathrm{WS}}^{(\overline{D}^0 D_s^+)}$ and $N_{\mathrm{sim.}}^{(\overline{D}^0 D_s^+)}$ indicate the number of events in the right-sign, the wrong-sign and the simulation samples, respectively. The wrong-sign sample is composed of $D^0 D_s^+$ combinations instead of the right-sign combination $\overline{D}^0 D_s^+$. These wrong-sing combinations are used to describe the combinatorial background.

The simulation sample is divided into multiple components and a one-dimensional simultaneous fit is performed to the $m'_{\overline{D}^0 D_s^+}$ distribution of the $\overline{D}^0 D_s^+$ subsample and the $m'_{D^{*-} D_s^+}$ distribution of the $D^{*-} D_s^+$ subsample. Here, $m'_{\overline{D}^0 D_s^+}$ ($m'_{D^{*-} D_s^+}$) is the invariant mass obtained by adding the reconstructed momenta of the $\overline{D}^0$ (D^{*-}) and of the D_s^+ candidates and then deconvoluting it by subtracting the reconstructed masses of the $\overline{D}^0$ (or D^{*-}) and of the D_s^+ mesons and adding their respective known masses from [2]:

$$m'_{\overline{D}^0 D_s^+} \equiv m_{\mathrm{meas.}}(\overline{D}^0 D_s^+) - m_{\mathrm{meas.}}(\overline{D}^0) - m_{\mathrm{meas.}}(D_s^+) + m_{\mathrm{PDG}}(\overline{D}^0) + m_{\mathrm{PDG}}(D_s^+), \quad (5.1)$$

$$m'_{D^{*-} D_s^+} \equiv m_{\mathrm{meas.}}(D^{*-} D_s^+) - m_{\mathrm{meas.}}(D^{*-}) - m_{\mathrm{meas.}}(D_s^+) + m_{\mathrm{PDG}}(D^{*-}) + m_{\mathrm{PDG}}(D_s^+). \quad (5.2)$$

The components used to describe the data are:

- $B^+ \to \overline{D}^0 D_s^+$,

- $B^+ \to \overline{D}^{*0} D_s^+$,
- $B^+ \to \overline{D}^0 D_s^{*+}$,
- $B^+ \to \overline{D}^{*0} D_s^{*+}$,
- $B^+ \to \overline{D}^0 D_{s1}(2460)^+$,
- $B^+ \to \overline{D}^{*0} D_{s1}(2460)^+$,
- $B^+|B_s^0 \to \overline{D}^0 D_s^+ X$,
- $B^0 \to \overline{D}^0 D_s^+ X$,
- $B^0 \to D^{*-} D_s^+$,
- $B^0 \to D^{*-} D_s^{*+}$,
- $B^0 \to D^{*-} D_{s0}^*(2317)^+$,
- $B^0 \to D^{*-} D_{s1}(2460)^+$,
- Combinatorial background (from "wrong-sign" data).

In the previous list, the component $B^+|B_s^0 \to \overline{D}^0 D_s^+ X$ contains decays originated from a B^+ or a B_s^0 which are not included in any of the other components. Similarly, the component $B^0 \to \overline{D}^0 D_s^+ X$ contains B^0 decays to $\overline{D}^0 D_s^+ X$ which are not included in any other component.

In order to explain the fit procedure, we shall first define the following parameters:

- The relative yield of a component i with respect to the $B^+ \to \overline{D}^0 D_s^+$ component in the $\overline{D}^0 D_s^+$ sample,

$$F_i \equiv \frac{N_i^{(\overline{D}^0 D_s^+)}}{N_{B^+ \to \overline{D}^0 D_s^+}^{(\overline{D}^0 D_s^+)}}. \tag{5.3}$$

  In the yields in this ratio, and in everything that follows, the subsample is indicated as super-index and the component as a sub-index.

- The relative yield of a component i with respect to the $B^0 \to D^{*-} D_s^+$ component in the $\overline{D}^0 D_s^+$ sample,

$$F_i^* \equiv \frac{N_i^{(\overline{D}^0 D_s^+)}}{N_{B^0 \to D^{*-} D_s^+}^{(\overline{D}^0 D_s^+)}}. \tag{5.4}$$

  From the definitions, it follows that the F_i and F_i^* parameters are related through the expression

$$F_i = F_{B^0 \to D^{*-} D_s^+} F_i^*. \tag{5.5}$$

- The relative efficiency of a component i between the two subsamples,

$$\epsilon_i \equiv \frac{N_i^{(D^{*-}D_s^+)}}{N_i^{(\overline{D}^0 D_s^+)}} \ . \tag{5.6}$$

The free parameters of the fit are chosen to be $N_{D_s^+}^{(\overline{D}^0 D_s^+)}$, the total number of signal events in the $\overline{D}^0 D_s^+$ subsample (events which are not background), and then either a F_i or a F_i^* parameter for each component other than $B^+ \to \overline{D}^0 D_s^+$. The F_i^* parameters are assigned only to three of the main components in the $D^{*-}D_s^+$ subsample ($B^0 \to D^{*-}D_s^{*+}$, $B^0 \to D^{*-}D_{s0}^*(2317)^+$ and $B^0 \to D^{*-}D_{s1}(2460)^+$), while a F_i free parameter is used for every other component.

The probability density function (PDF) used to fit the $\overline{D}^0 D_s^+$ data subsample is

$$\begin{aligned}&\mathrm{PDF}^{(\overline{D}^0 D_s^+)}(m'_{\overline{D}^0 D_s^+}) \\ &\qquad = N_{\mathrm{WS}}^{(\overline{D}^0 D_s^+)} \mathrm{PDF}_{\mathrm{WS}}^{(\overline{D}^0 D_s^+)}(m'_{\overline{D}^0 D_s^+}) + \sum_i N_i^{(\overline{D}^0 D_s^+)} \mathrm{PDF}_i^{(\overline{D}^0 D_s^+)}(m'_{\overline{D}^0 D_s^+}),\end{aligned} \tag{5.7}$$

while the PDF to fit the $D^{*-}D_s^+$ data subsample is

$$\begin{aligned}&\mathrm{PDF}^{(D^{*-}D_s^+)}(m'_{D^{*-}D_s^+}) \\ &\qquad = N_{\mathrm{WS}}^{(D^{*-}D_s^+)} \mathrm{PDF}_{\mathrm{WS}}^{(D^{*-}D_s^+)}(m'_{D^{*-}D_s^+}) + \sum_i N_i^{(D^{*-}D_s^+)} \mathrm{PDF}_i^{(D^{*-}D_s^+)}(m'_{D^{*-}D_s^+}).\end{aligned} \tag{5.8}$$

In these expressions, $\mathrm{PDF}_{\mathrm{WS}}^{(\overline{D}^0 D_s^+)}(m'_{\overline{D}^0 D_s^+})$ and $\mathrm{PDF}_{\mathrm{WS}}^{(D^{*-}D_s^+)}(m'_{D^{*-}D_s^+})$ are the $m'_{\overline{D}^0 D_s^+}$ and $m'_{D^{*-}D_s^+}$ PDFs, taken from the wrong-sign data sample, and $\mathrm{PDF}_i^{(\overline{D}^0 D_s^+)}(m'_{\overline{D}^0 D_s^+})$ and $\mathrm{PDF}_i^{(D^{*-}D_s^+)}(m'_{D^{*-}D_s^+})$ are the $m'_{\overline{D}^0 D_s^+}$ PDFs for the i^{th} simulation component, taken from simulation. The superscripts indicate to which subsample these quantities are referring to. The yields of each component in each subsample can be expressed uniquely in terms of the free parameters of the fit and the relative efficiencies as

$$N_i^{(\overline{D}^0 D_s^+)} = N_{D_s^+}^{(\overline{D}^0 D_s^+)} \frac{F_i}{\sum_j F_j} \ , \tag{5.9}$$

and

$$N_i^{(D^{*-}D_s^+)} = N_{D_s^+}^{(\overline{D}^0 D_s^+)} \cdot \epsilon_i \cdot \frac{F_i}{\sum_j F_j} \ , \tag{5.10}$$

where the relative efficiencies are calculated with eq. 5.6 using simulation and are fixed parameters in the fit. The components of each PDF are shown in tables 5.1 and 5.2 for the $\overline{D}^0 D_s^+$ and $D^{*-}D_s^+$ subsamples, respectively. In those tables, the sum of the F_i parameters is defined as:

Component	Yield
$B^+ \to \overline{D}^0 D_s^+$	$N_{D_s^+}^{(\overline{D}^0 D_s^+)} \cdot F_{B^+\to\overline{D}^0 D_s^+} / \sum_i F_i$
$B^+ \to \overline{D}^{*0} D_s^+$	$N_{D_s^+}^{(\overline{D}^0 D_s^+)} \cdot F_{B^+\to\overline{D}^{*0} D_s^+} / \sum_i F_i$
$B^+ \to \overline{D}^0 D_s^{*+}$	$N_{D_s^+}^{(\overline{D}^0 D_s^+)} \cdot F_{B^+\to\overline{D}^0 D_s^{*+}} / \sum_i F_i$
$B^+ \to \overline{D}^{*0} D_s^{*+}$	$N_{D_s^+}^{(\overline{D}^0 D_s^+)} \cdot F_{B^+\to\overline{D}^{*0} D_s^{*+}} / \sum_i F_i$
$B^+ \to \overline{D}^0 D_{s1}(2460)^+$	$N_{D_s^+}^{(\overline{D}^0 D_s^+)} \cdot F_{B^+\to\overline{D}^0 D_{s1}(2460)^+} / \sum_i F_i$
$B^+ \to \overline{D}^{*0} D_{s1}(2460)^+$	$N_{D_s^+}^{(\overline{D}^0 D_s^+)} \cdot F_{B^+\to\overline{D}^{*0} D_{s1}(2460)^+} / \sum_i F_i$
$B^+ \vert B_s^0 \to \overline{D}^0 D_s^+ X$	$N_{D_s^+}^{(\overline{D}^0 D_s^+)} \cdot F_{B^+\vert B_s^0\to\overline{D}^0 D_s^+ X} / \sum_i F_i$
$B^0 \to \overline{D}^0 D_s^+ X$	$N_{D_s^+}^{(\overline{D}^0 D_s^+)} \cdot F_{B^0\to\overline{D}^0 D_s^+ X} / \sum_i F_i$
$B^0 \to D^{*-} D_s^+$	$N_{D_s^+}^{(\overline{D}^0 D_s^+)} \cdot F_{B^0\to D^{*-} D_s^+} / \sum_i F_i$
$B^0 \to D^{*-} D_s^{*+}$	$N_{D_s^+}^{(\overline{D}^0 D_s^+)} \cdot F_{B^0\to D^{*-} D_s^+} \cdot F^*_{B^0\to D^{*-} D_s^{*+}} / \sum_i F_i$
$B^0 \to D^{*-} D_{s0}^*(2317)^+$	$N_{D_s^+}^{(\overline{D}^0 D_s^+)} \cdot F_{B^0\to D^{*-} D_s^+} \cdot F^*_{B^0\to D^{*-} D_{s0}^*(2317)^+} / \sum_i F_i$
$B^0 \to D^{*-} D_{s1}(2460)^+$	$N_{D_s^+}^{(\overline{D}^0 D_s^+)} \cdot F_{B^0\to D^{*-} D_s^+} \cdot F^*_{B^0\to D^{*-} D_{s1}(2460)^+} / \sum_i F_i$
Comb. background	$N_{\mathrm{WS}}^{(\overline{D}^0 D_s^+)}$

Table 5.1: Yields for each component of $\mathrm{PDF}^{(\overline{D}^0 D_s^+)}(m'_{\overline{D}^0 D_s^+})$, the probability density function used to fit the $\overline{D}^0 D_s^+$ control sample.

$$
\begin{aligned}
\sum_i F_i \;=\;& F_{B^+\to\overline{D}^0 D_s^+} + F_{B^+\to\overline{D}^{*0} D_s^+} + F_{B^+\to\overline{D}^0 D_s^{*+}} + F_{B^+\to\overline{D}^{*0} D_s^{*+}} \\
&+ F_{B^+\to\overline{D}^0 D_{s1}(2460)^+} + F_{B^+\to\overline{D}^{*0} D_{s1}(2460)^+} + F_{B^+\vert B_s^0\to\overline{D}^0 D_s^+ X} \\
&+ F_{B^0\to\overline{D}^0 D_s^+ X} + F_{B^0\to D^{*-} D_s^+} + F_{B^0\to D^{*-} D_s^+} \cdot F^*_{B^0\to D^{*-} D_s^{*+}} \\
&+ F_{B^0\to D^{*-} D_s^+} \cdot F^*_{B^0\to D^{*-} D_{s0}^*(2317)^+} \\
&+ F_{B^0\to D^{*-} D_s^+} \cdot F^*_{B^0\to D^{*-} D_{s1}(2460)^+}
\end{aligned}
\tag{5.11}
$$

where, by definition, $F_{B^+\to\overline{D}^0 D_s^+} = 1$.

A simultaneous fit is done using these two PDFs, where the background yields $N_{\mathrm{WS}}^{(\overline{D}^0 D_s^+)}$ and $N_{\mathrm{WS}}^{(D^{*-} D_s^+)}$ are fixed to the number of events in the wrong-sign $D^0 D_s^+$ and $D^{*-} D_s^+$ samples, respectively. The results are shown in table 5.3 and figs. 5.3 and 5.4 and will be used to model the $B \to \overline{D}^0 D_s^+(X)$ component in the signal fit (section 6.1.1).

Component	Yield
$B^+ \to \overline{D}^0 D_s^+$	$N_{D_s^+}^{(\overline{D}^0 D_s^+)} \cdot \epsilon_{B^+ \to \overline{D}^0 D_s^+} \cdot F_{B^+ \to \overline{D}^0 D_s^+} / \sum_i F_i$
$B^+ \to \overline{D}^{*0} D_s^+$	$N_{D_s^+}^{(\overline{D}^0 D_s^+)} \cdot \epsilon_{B^+ \to \overline{D}^{*0} D_s^+} \cdot F_{B^+ \to \overline{D}^{*0} D_s^+} / \sum_i F_i$
$B^+ \to \overline{D}^0 D_s^{*+}$	$N_{D_s^+}^{(\overline{D}^0 D_s^+)} \cdot \epsilon_{B^+ \to \overline{D}^0 D_s^{*+}} \cdot F_{B^+ \to \overline{D}^0 D_s^{*+}} / \sum_i F_i$
$B^+ \to \overline{D}^{*0} D_s^{*+}$	$N_{D_s^+}^{(\overline{D}^0 D_s^+)} \cdot \epsilon_{B^+ \to \overline{D}^{*0} D_s^{*+}} \cdot F_{B^+ \to \overline{D}^{*0} D_s^{*+}} / \sum_i F_i$
$B^+ \to \overline{D}^0 D_{s1}(2460)^+$	$N_{D_s^+}^{(\overline{D}^0 D_s^+)} \cdot \epsilon_{B^+ \to \overline{D}^0 D_{s1}(2460)^+} \cdot F_{B^+ \to \overline{D}^0 D_{s1}(2460)^+} / \sum_i F_i$
$B^+ \to \overline{D}^{*0} D_{s1}(2460)^+$	$N_{D_s^+}^{(\overline{D}^0 D_s^+)} \cdot \epsilon_{B^+ \to \overline{D}^{*0} D_{s1}(2460)^+} \cdot F_{B^+ \to \overline{D}^{*0} D_{s1}(2460)^+} / \sum_i F_i$
$B^+ \vert B_s^0 \to \overline{D}^0 D_s^+ X$	$N_{D_s^+}^{(\overline{D}^0 D_s^+)} \cdot \epsilon_{B^+ \vert B_s^0 \to \overline{D}^0 D_s^+ X} \cdot F_{B^+ \vert B_s^0 \to \overline{D}^0 D_s^+ X} / \sum_i F_i$
$B^0 \to \overline{D}^0 D_s^+ X$	$N_{D_s^+}^{(\overline{D}^0 D_s^+)} \cdot \epsilon_{B^0 \to \overline{D}^0 D_s^+ X} \cdot F_{B^0 \to \overline{D}^0 D_s^+ X} / \sum_i F_i$
$B^0 \to D^{*-} D_s^+$	$N_{D_s^+}^{(\overline{D}^0 D_s^+)} \cdot \epsilon_{B^0 \to D^{*-} D_s^+} \cdot F_{B^0 \to D^{*-} D_s^+} / \sum_i F_i$
$B^0 \to D^{*-} D_s^{*+}$	$N_{D_s^+}^{(\overline{D}^0 D_s^+)} \cdot \epsilon_{B^0 \to D^{*-} D_s^{*+}} \cdot F_{B^0 \to D^{*-} D_s^+} \cdot F^*_{B^0 \to D^{*-} D_s^{*+}} / \sum_i F_i$
$B^0 \to D^{*-} D_{s0}^*(2317)^+$	$N_{D_s^+}^{(\overline{D}^0 D_s^+)} \cdot \epsilon_{B^0 \to D^{*-} D_{s0}^*(2317)^+} \cdot F_{B^0 \to D^{*-} D_s^+} \cdot F^*_{B^0 \to D^{*-} D_{s0}^*(2317)^+} / \sum_i F_i$
$B^0 \to D^{*-} D_{s1}(2460)^+$	$N_{D_s^+}^{(\overline{D}^0 D_s^+)} \cdot \epsilon_{B^0 \to D^{*-} D_{s1}(2460)^+} \cdot F_{B^0 \to D^{*-} D_s^+} \cdot F^*_{B^0 \to D^{*-} D_{s1}(2460)^+} / \sum_i F_i$
Comb. background	$N_{\mathrm{WS}}^{(D^{*-} D_s^+)}$

Table 5.2: Yields for each component of $\mathrm{PDF}^{(D^{*-} D_s^+)}(m'_{D^{*-} D_s^+})$, the probability density function used to fit the $D^{*-} D_s^+$ control sample.

Parameter	Normalised	Fit result
$N_{D_s^+}^{(\overline{D}^0 D_s^+)}$	21513	21520 ± 150
$F_{B^+ \to \overline{D}^{*0} D_s^+}$	0.845274	0.915 ± 0.054
$F_{B^+ \to \overline{D}^0 D_s^{*+}}$	0.76273	0.935 ± 0.056
$F_{B^+ \to \overline{D}^{*0} D_s^{*+}}$	1.58996	1.828 ± 0.047
$F_{B^+ \to \overline{D}^0 D_{s1}(2460)^+}$	0.246918	0.332 ± 0.038
$F_{B^+ \to \overline{D}^{*0} D_{s1}(2460)^+}$	0.584063	0.710 ± 0.040
$F_{B^+ \vert B_s^0 \to \overline{D}^0 D_s^+ X}$	1.35287	0.817 ± 0.037
$F_{B^0 \to \overline{D}^0 D_s^+ X}$	0.32178	0.0990 ± 0.0092
$F_{B^0 \to D^{*-} D_s^+}$	0.13668	0.1205 ± 0.0041
$F^*_{B^0 \to D^{*-} D_s^{*+}}$	1.92549	1.705 ± 0.062
$F^*_{B^0 \to D^{*-} D_{s0}^*(2317)^+}$	0.120261	0.146 ± 0.036
$F^*_{B^0 \to D^{*-} D_{s1}(2460)^+}$	0.745098	0.398 ± 0.048

Table 5.3: Free parameters of the simultaneous fit, with their values before ("normalised") and after the fit ("fit result").

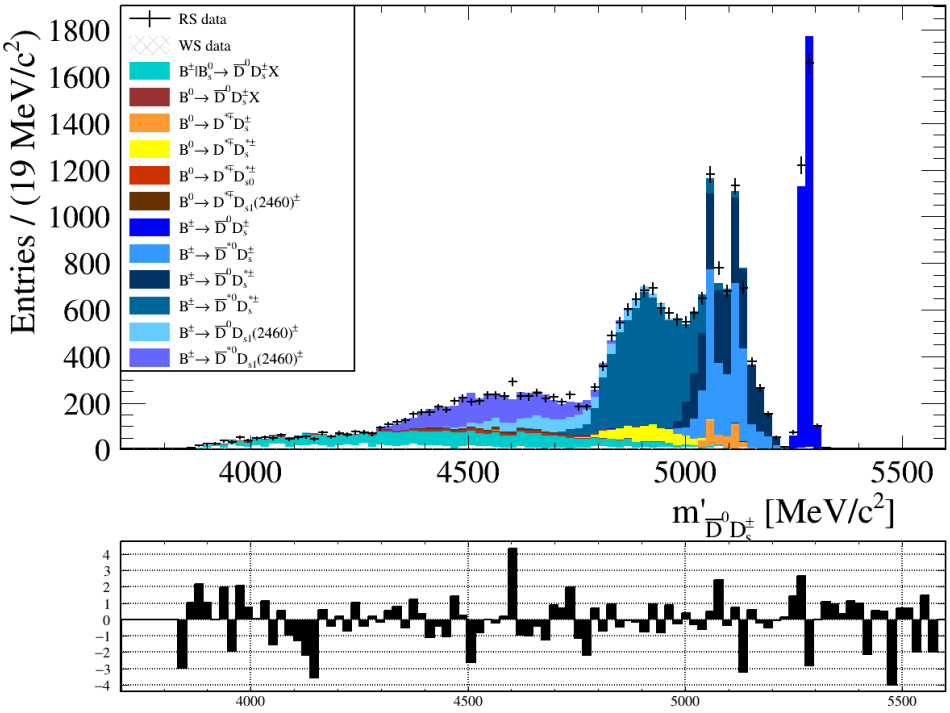

Figure 5.3: Invariant mass data and PDF of the $\overline{D}^0 D_s^+$ subsample after fitting (top) and its pull (bottom).

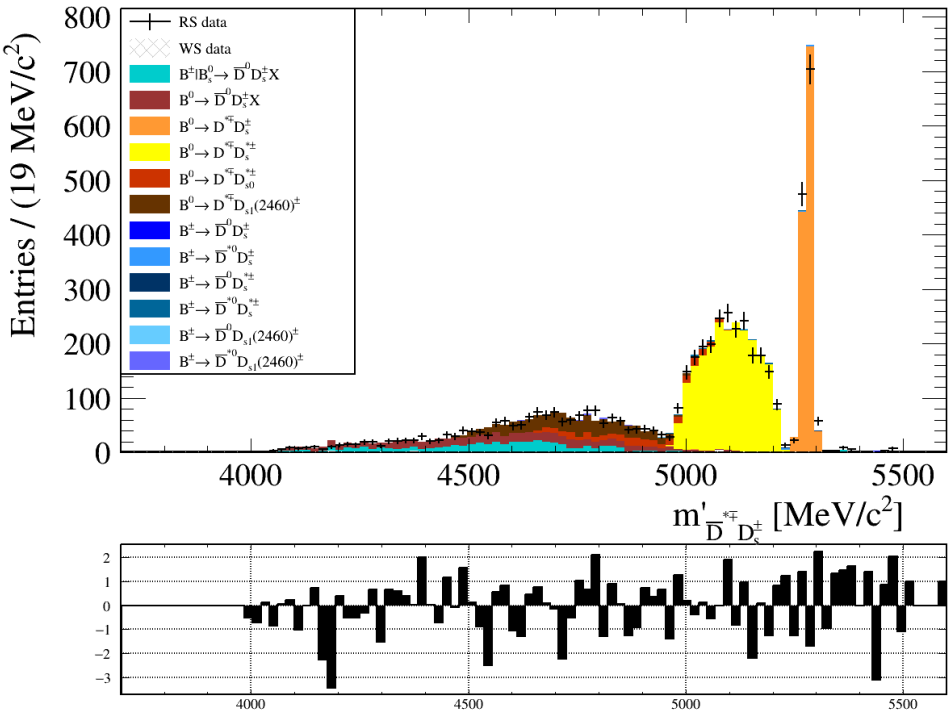

Figure 5.4: Invariant mass data and PDF of the $D^{*-}D_s^+$ subsample after fitting (top) and its pull (bottom).

5.2.2 $B \to \overline{D}^0 D^0(X)$ control sample

To obtain the $B \to \overline{D}^0 D^0(X)$ control sample, charged tracks which come from the same vertex as the three pions and that are compatible with being a kaon[1] are used to reconstruct the exclusive $D^0 \to K^-\pi^+\pi^-\pi^+$ decay. Events are selected if their $m(K^-\pi^+\pi^-\pi^+)$ invariant mass is in a ± 30 MeV/c^2 mass window around the known D^0 mass (from [2]). To take into account this extra kaon, the requirements $N_{\text{iso}}(\tau) = 1$, and $N_{\text{iso}}(B \vee \tau) = 1$[2] are applied instead of the cuts on $N_{\text{iso}}(\tau)$ and $N_{\text{iso}}(B)$ which are used in the nominal selection (section 4.3.4).

First, as in the previous control sample, the simulation histograms are scaled by a factor of $(N_{\text{RS}} - N_{\text{WS}})/N_{\text{sim.}}$. Then, the simulation sample is divided into multiple components and a one-dimensional fit is performed to the $m'_{\overline{D}^0 D^0}$ invariant mass distribution. Following a similar procedure as before, the $m'_{\overline{D}^0 D^0}$ distribution is obtained by adding the reconstructed momenta of the $\overline{D}^0$ and of the D^0 (the sum of the kaon and the three pions) and then deconvoluting it by subtracting the reconstructed masses of the $\overline{D}^0$ and of the D^0 and adding their respective known masses:

$$m'_{\overline{D}^0 D^0} \equiv m_{\text{meas.}}(\overline{D}^0 D^0) - m_{\text{meas.}}(\overline{D}^0) - m_{\text{meas.}}(D^0) + m_{\text{PDG}}(\overline{D}^0) + m_{\text{PDG}}(D^0). \quad (5.12)$$

The components used to describe the data are

- $B^- \to D^{*-} D^0$,
- $B^{+,0} \to D^{*0,-} D^{*+}$,
- $B \to \overline{D}^0 D^0 X$, which contains every decay not contained in any other component,
- Combinatorial background (from "wrong-sign" data).

The free parameters of the fit are chosen to be N_{D^0} (the total number of events in the control sample), and a F_i^* parameter for each component other than $B^- \to D^{*-} D^0$, where F_i^* is the relative yield of the component i with respect to the $B^- \to D^{*-} D^0$ component,

$$F_i^* \equiv \frac{N_i}{N_{B^- \to D^{*-} D^0}}. \quad (5.13)$$

The PDF used for the fit is

$$\text{PDF}(m'_{\overline{D}^0 D^0}) = \text{PDF}_{\text{WS}}(m'_{\overline{D}^0 D^0}) + \sum_i N_i \, \text{PDF}_i(m'_{\overline{D}^0 D^0}), \quad (5.14)$$

[1] The used criteria are: $\text{PID}_K > 1$, $\chi^2_{\text{IP}}(\tau) < 5$, and $\chi^2_{\text{IP}}(\text{PV}) > 4$

[2] Sometimes, a track can be compatible with both the B and the τ vertices, so it is possible that when imposing $N_{\text{iso}}(\tau) = 1$, $N_{\text{iso}}(B)$ is also 1 due to counting the same track. The quantity $N_{\text{iso}}(B \vee \tau)$ is defined to take this effect into account: it counts the number of tracks that fulfill the isolation conditions for both the B and τ vertices, without double-counting them.

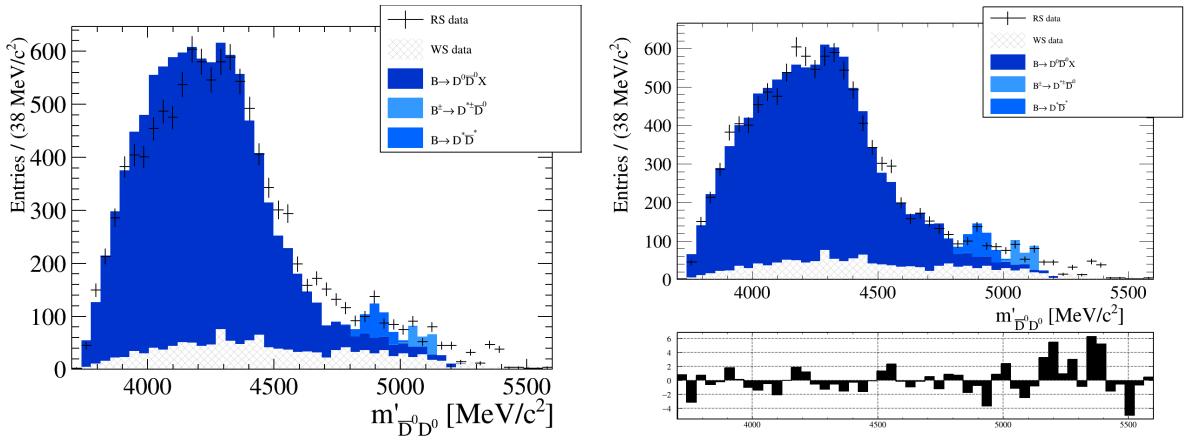

Figure 5.5: Invariant mass distribution of the $B \to \overline{D}^0 D^0(X)$ control sample of data and PDF before (left) and after (right) the fit procedure.

Parameter	Normalised	Fit result
N_{D^0}	9669	9663 ± 98
$F^*_{B^{+,0} \to D^{*0,-} D^{*+}}$	1.86857	1.57 ± 0.21
$F^*_{B \to \overline{D}^0 D^0 X}$	91.8171	56.8 ± 5.5

Table 5.4: Free parameters of the $B \to \overline{D}^0 D^0(X)$ control sample fit, with their values as they are before ("normalised") and after the fit ("fit result").

where $\mathrm{PDF}_{\mathrm{WS}}(m'_{\overline{D}^0 D^0})$ is the $m'_{\overline{D}^0 D^0}$ distribution of the wrong-sign data sample and $\mathrm{PDF}_i(m'_{\overline{D}^0 D^0})$ is the $m'_{\overline{D}^0 D^0}$ distribution of the i^{th} simulation component (with its integral normalised to 1). The yield of each component (N_i) can be expressed uniquely in terms of the free parameters of the fit as

$$N_i = N_{D^0} \frac{F^*_i}{\sum_j F^*_j}. \tag{5.15}$$

After this initial fit, to improve the description of data, the $B \to \overline{D}^0 D^0 X$ component is re-weighted with the sum of a 4^{th}-order polynomial and a Gaussian distribution (to compensate the lack of simulated events seen around 4700 MeV/c^2 in fig. 5.5), which is fitted to the ratio between the data (with wrong-sign data substracted) and simulation sample distributions. After this re-weighting, the fit is repeated, obtaining the results shown in table 5.4 and in fig. 5.5.

5.2.3 $B \to \overline{D}^0 D^+(X)$ control sample

To obtain the $B \to \overline{D}^0 D^+(X)$ control sample, exclusive $D^+ \to K^+\pi^-\pi^+$ events are selected in a ± 30 MeV/c^2 mass window around the known D^+ mass (from [2]). For this,

events where the opposite-signed reconstructed pion passes the $P_{\mathrm{NN}}(K) > 0.2$ cut are selected, treating it as a misreconstructed kaon. The other two pions are required to pass their correspondent cut with $P_{\mathrm{NN}}(K) < 0.1$.

The subsequent strategy is analogous to the one used for the $B \to \overline{D}^0 D^0(X)$ control sample, and will follow the same notation.

First, the simulation histograms are scaled by a factor of $(N_{\mathrm{RS}} - N_{\mathrm{WS}})/N_{\mathrm{sim.}}$. Then, the simulation sample is divided into multiple components and a one-dimensional fit is performed to the $m'_{\overline{D}^0 D^+}$ distribution. $m'_{\overline{D}^0 D^+}$ is the invariant mass obtained by adding the reconstructed momenta of the $\overline{D}^0$ and of the D^+ (the sum of the kaon and the two pions) and then deconvoluting it by subtracting the reconstructed masses of the $\overline{D}^0$ and of the D^+ and adding their respective known masses:

$$m'_{\overline{D}^0 D^+} \equiv m_{\mathrm{meas.}}(\overline{D}^0 D^+) - m_{\mathrm{meas.}}(\overline{D}^0) - m_{\mathrm{meas.}}(D^+) + m_{\mathrm{PDG}}(\overline{D}^0) + m_{\mathrm{PDG}}(D^+). \quad (5.16)$$

The components used to describe the data are

- $B^+ \to \overline{D}^0 D^+$,
- $B \to \overline{D}^0 D^+ \pi$, which contains the decays: $B^+ \to \overline{D}^0 D^{*+}$, $B^+ \to \overline{D}^{*0} D^+$, and $B^0 \to D^{*-} D^+$.
- $B^{+,0} \to D^{*0,-} D^{*+}$,
- $B \to \overline{D}^0 D^+ X$, which contains any decay not included in any of the other components,
- Combinatorial background (from "wrong-sign" data).

The free parameters of the fit are chosen to be N_{D^+} (the total number of events in the control sample), and then a F_i parameter for each component other than $B^+ \to \overline{D}^0 D^+$, F_i being the relative yield of a component i with respect to the $B^+ \to \overline{D}^0 D^+$ component,

$$F_i \equiv \frac{N_i}{N_{B^+ \to \overline{D}^0 D^+}}. \quad (5.17)$$

The PDF used for the fit is

$$\mathrm{PDF}(m'_{\overline{D}^0 D^+}) = \mathrm{PDF}_{\mathrm{WS}}(m'_{\overline{D}^0 D^+}) + \sum_i N_i \ \mathrm{PDF}_i(m'_{\overline{D}^0 D^+}), \quad (5.18)$$

where $\mathrm{PDF}_{\mathrm{WS}}(m'_{\overline{D}^0 D^+})$ is the $m'_{\overline{D}^0 D^+}$ distribution of the wrong-sign data sample and $\mathrm{PDF}_i(m'_{\overline{D}^0 D^+})$ is the $m'_{\overline{D}^0 D^+}$ distribution of the i^{th} simulation component (with its integral normalised to 1). The yield of each component (N_i) can be expressed uniquely in terms of the free parameters of the fit as

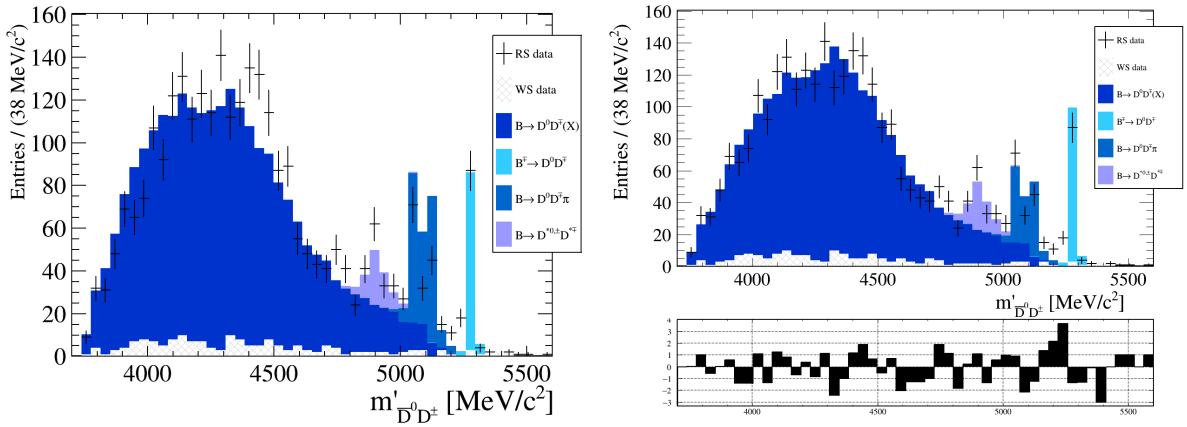

Figure 5.6: Invariant mass distribution of the $B \to \overline{D}^0 D^+(X)$ control sample of data and PDF before (left) and after (right) the fit procedure.

Parameter	Normalised	Fit result
N_{MC}	2670	2670 ± 52
$F_{B\to\overline{D}^0 D^+\pi}$	2.23883	1.32 ± 0.18
$F_{B^{+,0}\to D^{*0,-}D^{*+}}$	0.762452	0.77 ± 0.15
$F_{B\to\overline{D}^0 D^+ X}$	25.4828	22 ± 2.2

Table 5.5: Free parameters of the $B \to \overline{D}^0 D^+(X)$ control sample fit, with their values as they are before ("normalised") and after the fit ("fit result").

$$N_i = N_{D^+} \frac{F_i}{\sum_j F_j}. \tag{5.19}$$

After this initial fit, to improve the description of data, the $B \to \overline{D}^0 D^+ X$ component is re-weighted with a 4^{th}-order polynomial, which is fitted to the ratio between the data (with wrong-sign data substracted) and simulation distributions. After this re-weighting, the fit is repeated, obtaining the results shown in table 5.5 and in fig. 5.6.

5.2.4 Control samples for $R(D^{(*)-})$

For the equivalent control samples in the $R(D^{(*)-})$ analysis there is a key difference to take into account: in $R(D^{(*)0})$, the D^{*-} mesons are reconstructed in the $D^{*-} \to D^0\pi^-$ channel, which allows us to veto the D^{*-} and, in the case of the $B \to \overline{D}^0 D_s^+(X)$ control sample, divide the samples in two subsamples, one with D^{*-} and another one without D^{*-}. However, in the $R(D^{(*)-})$ analysis, the D^{*-} decay which feeds into the final state, $D^{*-} \to D^-\pi^0$, is not reconstructed due to the difficulty in reconstructing a neutral pion compatible with this decay. As a result, these control samples do not have any mass

requirement on the D^{*-} and are not divided in subsamples, while everything else in the procedure is analogous to the $R(D^{(*)0})$ control samples.

Since the signal fit procedure is still not developed for this analysis, these control samples are not yet optimised, with many more components present than in their $R(D^{(*)0})$ counterparts and with only a basic fit performed, without further corrections applied.

$B \to D^- D_s^+(X)$ control sample

The same strategy as with the $B \to \overline{D}^0 D_s^+(X)$ control sample (section 5.2.1) is followed, except for the sample splitting. The resulting control sample has all the cuts of the signal selection (section 4.3.5), except the requirement on the $m(D^-3\pi)$ invariant mass, and in addition to a ± 30 MeV/c^2 mass-window cut around the known D_s^+ mass (from [2]).

A one-dimensional fit is performed in the $m'_{D^-D_s^+}$ distribution, with

$$m'_{D^-D_s^+} \equiv m_{\text{meas.}}(D^- D_s^+) - m_{\text{meas.}}(D^-) - m_{\text{meas.}}(D_s^+) + m_{\text{PDG}}(D^-) + m_{\text{PDG}}(D_s^+). \quad (5.20)$$

The components used to describe the data are:

- $B^0 \to D^- D_s^+$,
- $B^0 \to D^{*-} D_s^+$,
- $B^0 \to D^- D_s^{*+}$,
- $B^0 \to D^{*-} D_s^{*+}$,
- $B^0 \to D^- D_{s0}^*(2317)^+$,
- $B^0 \to D^{*-} D_{s0}^*(2317)^+$,
- $B^0 \to D^- D_{s1}(2460)^+$,
- $B^0 \to D^{*-} D_{s1}(2460)^+$,
- $B_s^0 \to D^- D_s^+$,
- $B_s^0 \to D^{(*)-} D_s^{(*)+}$, containing the decays $B_s^0 \to D^{*-} D_s^+$, $B_s^0 \to D^- D_s^{*+}$, and $B_s^0 \to D^{*-} D_s^{*+}$,
- $B^0 | B_s^0 \to D^- D_s^+(X)$, containing the decays originated from a B^0 or a B_s^0 which are not included in the previous components,
- $B^- \to D^- D_s^+ X$, containing the decays originated from a B^- which are not included in the previous components,

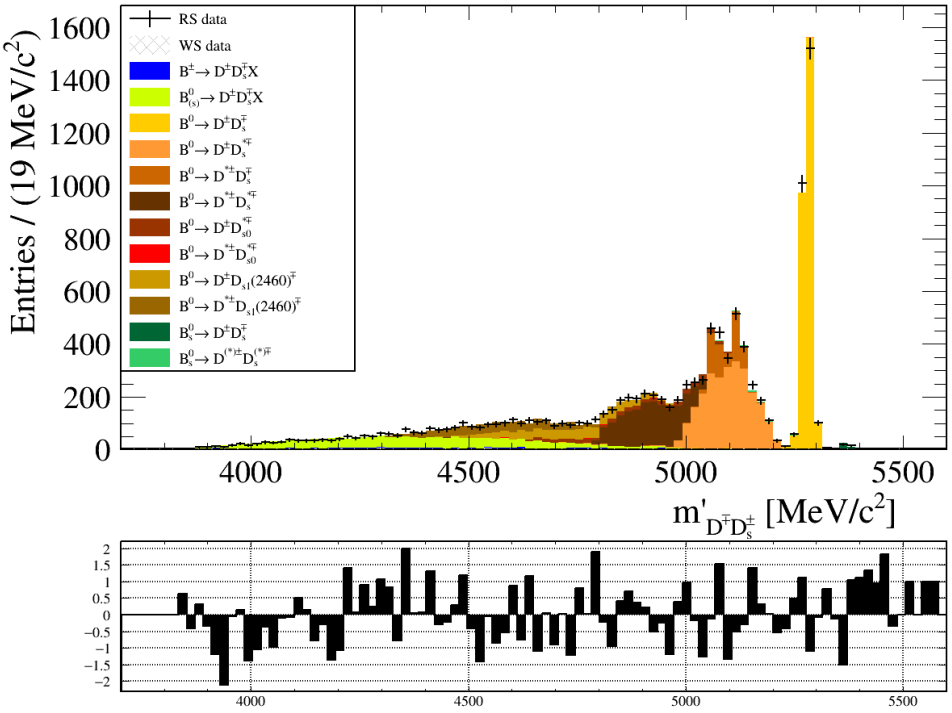

Figure 5.7: Invariant mass data and PDF of the $B \to D^- D_s^+(X)$ control sample subsample after fitting (top) and its pull (bottom).

- Combinatorial background (from "wrong-sign" data).

The fit is done following the same strategy as in the $B \to \overline{D}^0 D_s^+(X)$ control sample, but without the complication of having two subsamples, and with the F parameters defined as

$$F_i \equiv \frac{N_i}{N_{B^0 \to D^- D_s^+}}, \tag{5.21}$$

where N_i is the yield of the i-th component. The used PDF is

$$\mathrm{PDF}(m'_{D^- D_s^+}) = N_{\mathrm{WS}} \mathrm{PDF}_{\mathrm{WS}}(m'_{D^- D_s^+}) + \sum_i N_i \mathrm{PDF}_i(m'_{D^- D_s^+}), \tag{5.22}$$

where N_{WS} is the yield of the wrong-sign component, which is fixed to the value obtained from data. The free parameters of the fit are the total yield ($N_{D_s^+}$) and the F parameters of every component except the wrong-sign and $B^0 \to D^- D_s^+$ components. The results of this fit are shown in table 5.6 and in fig. 5.7

Parameter	Normalised	Fit result
$N_{D_s^+}$	10987	10990 ± 100
$F_{B^0 \to D^{*-} D_s^+}$	0.321612	0.236 ± 0.028
$F_{B^0 \to D^- D_s^{*+}}$	0.927875	0.926 ± 0.043
$F_{B^0 \to D^{*-} D_s^{*+}}$	0.61807	0.571 ± 0.030
$F_{B^0 \to D^- D_{s0}^*(2317)^+}$	0.11807	0.119 ± 0.054
$F_{B^0 \to D^{*-} D_{s0}^*(2317)^+}$	0.0419661	0.006 ± 0.033
$F_{B^0 \to D^- D_{s1}(2460)^+}$	0.329954	0.264 ± 0.069
$F_{B^0 \to D^{*-} D_{s1}(2460)^+}$	0.24076	0.254 ± 0.033
$F_{B_s^0 \to D^- D_s^+}$	0.108316	0.0145 ± 0.0024
$F_{B_s^0 \to D^{(*)-} D_s^{(*)+}}$	0.154132	0.013 ± 0.013
$F_{B^0 \mid B_s^0 \to D^- D_s^+(X)}$	2.16183	0.564 ± 0.075
$F_{B^- \to D^- D_s^+ X}$	0.251925	0.075 ± 0.091

Table 5.6: Free parameters of the $B \to D^- D_s^+(X)$ control sample fit, with their values before ("normalised") and after the fit ("fit result").

$B \to D^- D^0(X)$ control sample

The same strategy as in the previous control sample is used, except for the sample selection. The same set of criteria as in the $B \to \overline{D}^0 D^0(X)$ control sample (section 5.2.2) is used to select D^0 mesons with $D^0 \to K^- \pi^+ \pi^- \pi^+$. The rest of the selection is the same as in the nominal selection, except for the requirement on the $m(D^- 3\pi)$ invariant mass.

A one-dimensional fit is performed in the $m'_{D^- D^0}$ distribution, with

$$m'_{D^- D^0} \equiv m_{\text{meas.}}(D^- D^0) - m_{\text{meas.}}(D^-) - m_{\text{meas.}}(D^0) + m_{\text{PDG}}(D^-) + m_{\text{PDG}}(D^0). \quad (5.23)$$

The components used to describe the data are:

- $B^- \to D^- D^0$,
- $B^- \to D^{*-} D^0$,
- $B^- \to D^- D^{*0}$,
- $B^- \to D^{*-} D^{*0}$,
- $B^0 \to D^- D^{*+}$,
- $B^0 \to D^{*-} D^{*+}$,
- $B^0 \to D^- D_{s1}(2460)^+$,
- $B^0 \to D^{*-} D_{s1}(2460)^+$,

Parameter	Normalised	Fit result
N_{D^0}	5662	5652 ± 75
$F_{B^- \to D^{*-} D^0}$	0.280212	0 ± 0.00013
$F_{B^- \to D^- D^{*0}}$	1.34661	1.04 ± 0.16
$F_{B^- \to D^{*-} D^{*0}}$	0.443559	0 ± 0.00017
$F_{B^0 \to D^- D^{*+}}$	0.432935	0.30 ± 0.13
$F_{B^0 \to D^{*-} D^{*+}}$	0.203187	0.219 ± 0.059
$F_{B^0 \to D^- D_{s1}(2460)^+}$	0.163347	0.84 ± 0.16
$F_{B^0 \to D^{*-} D_{s1}(2460)^+}$	0.112882	0.94 ± 0.17
$F_{B^0 \to D^- D^0(X)}$	3.8672	6.17 ± 0.59
$F_{B_s^0 \to D^- D^0(X)}$	0.857902	2.38 ± 0.57
$F_{B^- \to D^- D^0(X)}$	11.5485	7.98 ± 0.98

Table 5.7: Free parameters of the $B \to D^- D^0(X)$ control sample fit, with their values before ("normalised") and after the fit ("fit result").

- $B^0 \to D^- D_s^+(X)$, containing the decays originated from a B^0 which are not included in the previous components,
- $B_s^0 \to D^- D_s^+(X)$, containing the decays originated from a B_s^0 which are not included in the previous components,
- $B^- \to D^- D_s^+ X$, containing the decays originated from a B^- which are not included in the previous components,
- Combinatorial background (from "wrong-sign" data).

The F parameters in this control sample are defined as

$$F_i \equiv \frac{N_i}{N_{B^- \to D^- D^0}}, \tag{5.24}$$

where N_i is the yield of the i-th component. The used PDF is

$$\mathrm{PDF}(m'_{D^- D^0}) = N_{\mathrm{WS}} \mathrm{PDF}_{\mathrm{WS}}(m'_{D^- D^0}) + \sum_i N_i \mathrm{PDF}_i(m'_{D^- D^0}), \tag{5.25}$$

where N_{WS} is the yield of the wrong-sign component, which is fixed to the value obtained from data. The free parameters of the fit are the total yield (N_{D^0}) and the F parameters of every component except the wrong-sign and $B^- \to D^- D^0$ components. The results of this fit are shown in table 5.7 and in fig. 5.8

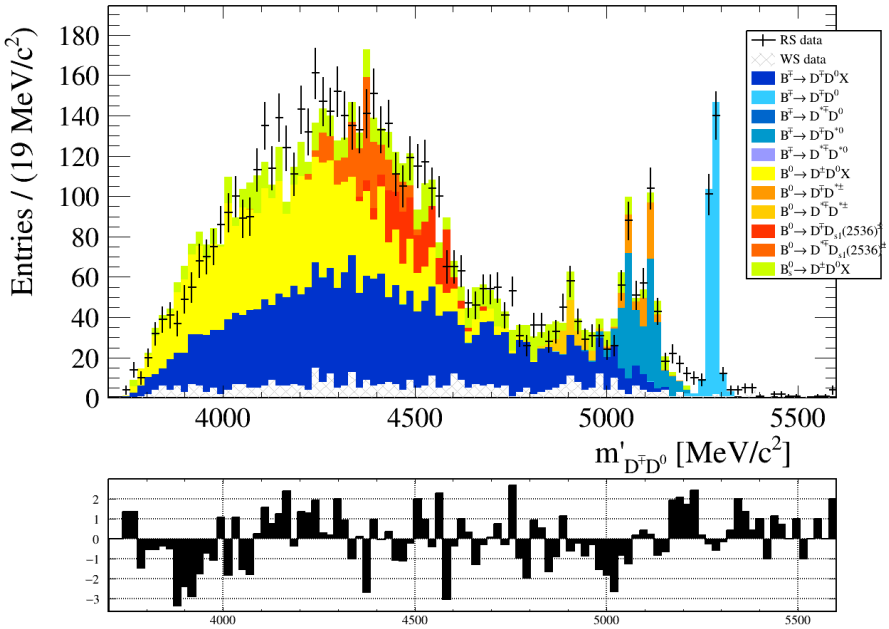

Figure 5.8: Invariant mass data and PDF of the $B \to D^- D^0(X)$ control sample subsample after fitting (top) and its pull (bottom).

$B \to D^- D^+(X)$ control sample

The same strategy as in the previous control sample is used, except for the sample selection. The same set of criteria as in the $B \to \overline{D}^0 D^+(X)$ control sample (section 5.2.3) is used to select D^+ mesons with $D^+ \to K^+\pi^-\pi^+$. The rest of the selection is the same as in the nominal selection, except for the requirement on the $m(D^-3\pi)$ invariant mass.

A one-dimensional fit is performed in the $m'_{D^-D^+}$ distribution, with

$$m'_{D^-D^+} \equiv m_{\text{meas.}}(D^-D^+) - m_{\text{meas.}}(D^-) - m_{\text{meas.}}(D^+) + m_{\text{PDG}}(D^-) + m_{\text{PDG}}(D^+). \quad (5.26)$$

The components used to describe the data are:

- $B^0 \to D^- D^+$,
- $B^0 \to D^- D^{*+}$,
- $B^0 \to D^{*-} D^{*+}$,
- $B^0 \to D^- D_{s1}(2460)^+$,
- $B^0 \to D^{*-} D_{s1}(2460)^+$,
- $B_s^0 \to D^- D^+$,

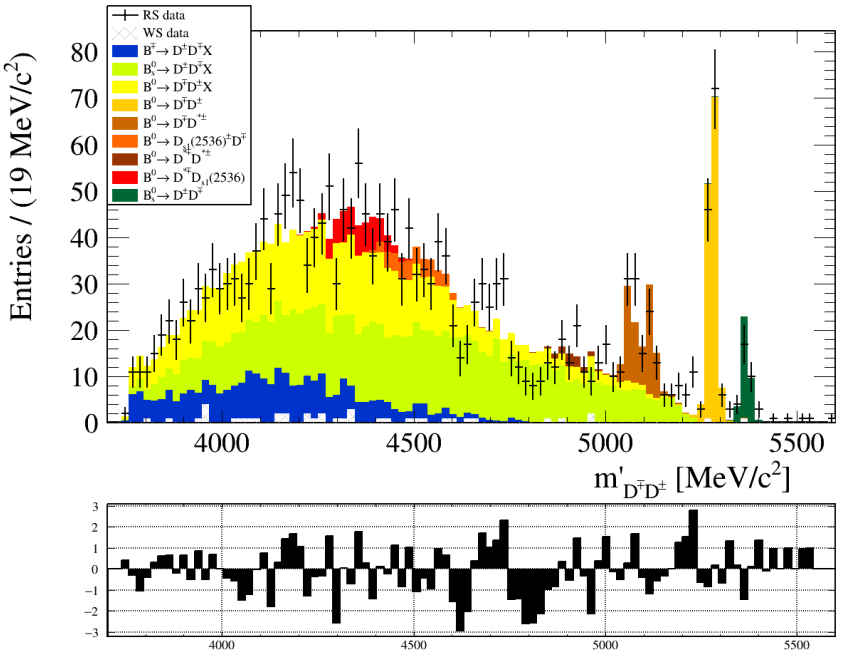

Figure 5.9: Invariant mass data and PDF of the $B \to D^- D^+(X)$ control sample subsample after fitting (top) and its pull (bottom).

- $B^- \to D^- D^+ X$, containing the decays originated from a B^- which are not included in the previous components,
- $B_s^0 \to D^- D^+ X$, containing the decays originated from a B_s^0 which are not included in the previous components,
- $B^0 \to D^- D^+ X$, containing the decays originated from a B^0 which are not included in the previous components,

The F parameters in this control sample are defined as

$$F_i \equiv \frac{N_i}{N_{B^- \to D^- D^+}}, \tag{5.27}$$

where N_i is the yield of the i-th component. The used PDF is

$$\mathrm{PDF}(m'_{D^- D^+}) = N_{\mathrm{WS}} \mathrm{PDF}_{\mathrm{WS}}(m'_{D^- D^+}) + \sum_i N_i \mathrm{PDF}_i(m'_{D^- D^+}), \tag{5.28}$$

where N_{WS} is the yield of the wrong-sign component, which is fixed to the value obtained from data. The free parameters of the fit are the total yield (N_{D^+}) and the F parameters of every component except the wrong-sign and $B^0 \to D^- D^+$ components. The results of this fit are shown in table 5.8 and in fig. 5.9

Parameter	Normalised	Fit result
N_{D^+}	2167	2168 ± 47
$F_{B^0 \to D^- D^{*+}}$	1.26723	0.60 ± 0.10
$F_{B^0 \to D^{*-} D^{*+}}$	0.321481	0.077 ± 0.076
$F_{B^0 \to D^- D_{s1}(2460)^+}$	0.23717	0.28 ± 0.20
$F_{B^0 \to D^{*-} D_{s1}(2460)^+}$	0.205645	0.41 ± 0.21
$F_{B_s^0 \to D^- D^+}$	0.719941	0.269 ± 0.051
$F_{B^- \to D^- D^+(X)}$	0.625	2.00 ± 0.96
$F_{B_s^0 \to D^- D^+(X)}$	5.27823	6.49 ± 0.98
$F_{B^0 \to D^- D^+(X)}$	11.2786	4.9 ± 1.8

Table 5.8: Free parameters of the $B \to D^- D^+(X)$ control sample fit, with their values before ("normalised") and after the fit ("fit result").

5.3 The $D_s^+ \to \pi^+\pi^-\pi^+(X)$ decay model

In the context of hadronic $R(D^{(*)})$ analyses, $D_s^+ \to \pi^+\pi^-\pi^+(X)$ decays are a significant source of uncertainty, and their modelling is specially important due to the large number of inclusive decays that contribute to this background. In the previous Run 1 analysis [30, 31], the model for these decays was determined by first creating a sample of $B \to D^{*-} D_s^+(X)$ decays, then fitting four distributions simultaneously: the minimum and maximum invariant mass of two opposite-charged pions ($\min[m(\pi^+\pi^-)]$ and $\max[m(\pi^+\pi^-)]$), the mass of the same-charge pions $m(\pi^+\pi^+)$, and the mass of the 3π system ($m(3\pi)$). The resulting fit model was constructed using a simulation sample that included both D_s^+ and non-D_s^+ components.

In this study, a different approach is used, with the goal of further reducing the systematic uncertainty due to these decays: several control samples are constructed by adding non-signal particles to the decay chain, and a fit is performed on these samples to obtain weights that can be used to correct the simulation sample.

The main $D_s^+ \to \pi^+\pi^-\pi^+(X)$ decays used in this study are listed in table 5.9. Note that some of these decays have not been measured but were included in the simulation. The following decays are also part of the simulation and will be referred to as "other D_s^+ decays": $D_s^+ \to K_S^0 K_S^0 \pi^+\pi^-\pi^+$, $D_s^+ \to K_L^0 \pi^+\pi^-\pi^-$, $D_s^+ \to K_L^0 K_L^0 \pi^+\pi^-\pi^-$, $D_s^+ \to K^-\pi^+\pi^-$, $D_s^+ \to \phi e^+\nu_e$, $D_s^+ \to \phi\mu^+\nu_\mu$, $D_s^+ \to \eta e^+\nu_e$, $D_s^+ \to \eta\mu^+\nu_\mu$, $D_s^+ \to \eta' e^+\nu_e$, $D_s^+ \to \eta'\mu^+\nu_\mu$, $D_s^+ \to f_0(980) e^+\nu_e$, $D_s^+ \to f_0(980)\mu^+\nu_\mu$.

Several of the mentioned resonances are also present in the signal $\tau^- \to \pi^-\pi^+\pi^-(\pi^0)\nu_\tau$ decays, so the proper description of data for these decays in the background components is of high importance for the performance of the signal fit (section 6.1.1).

Decay channel	Measured $\mathcal{B}$ (%)	$\mathcal{B}$ in simulation (%)
$D_s^+ \to \pi^+\pi^-\pi^+$	1.09 ± 0.05	1.09
$D_s^+ \to \pi^+\pi^-\pi^+\pi^0$	–	1.5
$D_s^+ \to \eta\pi^+$	1.70 ± 0.09	1.70
$D_s^+ \to \omega\pi^+$	0.24 ± 0.06	0.24
$D_s^+ \to \phi\pi^+$	4.5 ± 0.4	4.5
$D_s^+ \to \eta'\pi^+$	3.94 ± 0.25	3.94
$D_s^+ \to \eta\pi^+\pi^0$	9.2 ± 1.2	11.7
$D_s^+ \to \omega\pi^+\pi^0$	2.8 ± 0.7	2.8
$D_s^+ \to \phi\pi^+\pi^0$	$8.4^{+1.9}_{-2.3}$	9.2
$D_s^+ \to \eta'\pi^+\pi^0$	5.6 ± 0.8	6.9
$D_s^+ \to \pi^+\pi^-\pi^+\pi^-\pi^+$	0.80 ± 0.08	0.8
$D_s^+ \to \omega\pi^+\pi^-\pi^+$	1.6 ± 0.5	1.6
$D_s^+ \to \phi\pi^+\pi^-\pi^+$	1.21 ± 0.16	1.21
$D_s^+ \to \eta\pi^+\pi^-\pi^+$	3.12 ± 0.16	3.0
$D_s^+ \to \eta'\pi^+\pi^-\pi^+$	–	2.0
$D_s^+ \to K_S^0\pi^+\pi^-\pi^+$	0.30 ± 0.11	0.3
$D_s^+ \to \tau^+\nu_\tau$	5.48 ± 0.11	5.48

Table 5.9: Main D_s^+ decay modes considered in the model, with their corresponding measured branching fractions (all taken from [2] except $\mathcal{B}(D_s^+ \to \eta\pi^+\pi^-\pi^+)$, which is from a BES-III measurement [124]), along with the values used in the simulation. $D_s^+ \to \eta'\pi^+\pi^-\pi^+$ and non-resonant $D_s^+ \to \pi^+\pi^-\pi^+\pi^0$ decays have no measurements recorded in [2], but have been included in the simulation.

5.3.1 Preparation of the control samples

Events with $q^2 \in [3, 6.5]$ GeV$^2/c^4$ are selected to enrich the sample with D_s^+ decays, since this region is abundant in D_s^+ decays, while $B \to \overline{D}^0 D^0(X)$ and $B \to \overline{D}^0 D^+(X)$ events dominate in higher q^2 values. In addition to this requirement, charged (with the variables described in section 4.3.4) and neutral isolation requirements are used to select the additional tracks for each control sample.

Neutral π and η mesons are reconstructed with the $\gamma\gamma$ final state and a confidence level of CL > 0.2. They are also required to be within a ± 15 GeV$/c^2$ and ± 30 GeV$/c^2$ window around their known masses (from [2]), respectively.

Nine control samples are constructed using additional requirements and are sensitive to most of the main D_s^+ decay channels. A comprehensive list of these control samples is shown in table 5.10, along with their specific selection cuts.

The simulated samples are selected from the $B \to D^0 X_c X'$ simulation samples, which use the branching fractions listed in table 5.9, and are then normalised to their correspondent data using their q^2 distribution.

In addition, a re-weighting procedure is applied to some of the simulated control samples to account for unsimulated resonances that are present in data. The re-weighting is done through a Breit-Wigner distribution around the resonance mass peaks. The affected samples are the $D_s^+ \to \eta 3\pi$, to account for the $D_s^+ \to \eta\rho^0(\to \pi^+\pi^-)\pi^+$ contribution, and the $D_s^+ \to 2K3\pi$, to account for the $D_s^+ \to \phi a_1(\to \pi^+\pi^-\pi^+)$ contribution.

5.3.2 Fit procedure

To model the $D_s^+ \to \pi^+\pi^-\pi^+(X)$ decays, the simulation samples are split in 17 different components corresponding to the main decay channels shown in table 5.9. A weight w_i is assigned to each component of the fit. This weight is fixed to 1 for the components to which the fit is not sensitive. This is the case of $w_{D_s^+ \to \omega\pi^+\pi^0}$, $w_{D_s^+ \to \phi\pi^+\pi^0}$, and $w_{D_s^+ \to \tau^+\nu_\tau}$. The rest of the weights (14) are left free in the subsequent fit.

Two additional components are included in the fit (with fixed weights):

- "**Other D_s^+ decays**": the part of the simulation samples that is not included in any of the 17 main components and corresponds to D_s^+ decays. Includes the rarer D_s^+ decays not included in table 5.9.
- "**Not D_s^+ decays**": the part of the simulation samples that is not included in any of the 17 main components and corresponds to non-D_s^+ decays. Includes residual D^0 and D^+ decays that pass the selection criteria.

A simultaneous χ^2 template fit to data is performed with the nine control samples using the distributions in their respective invariant mass variables shown in table 5.10. The results of these fits are sown in table 5.11. Some of the invariant mass distributions after the fit are shown in fig. 5.10. The obtained weights are applied to the simulation samples containing D_s^+ decays that are used in the signal fit (section 6.1.1).

Control sample	Main decays	Relevant variable	Requirements
$D_s^+ \to 3\pi$	$D_s^+ \to \pi^+\pi^-\pi^+$	$m(3\pi)$	$\lvert m(3\pi) - m_{\rm PDG}(D_s^+)\rvert < 30$ MeV/c^2 $N_{\rm iso}(\tau) = 0$ $N_{\rm iso}(B) = 0$
$D_s^+ \to 5\pi$	$D_s^+ \to \pi^+\pi^-\pi^+\pi^-\pi^+$, $D_s^+ \to \omega(\to \pi^+\pi^-\pi^0)\pi^+\pi^-\pi^+$, $D_s^+ \to \eta(\to \pi^+\pi^-\pi^0)\pi^+\pi^-\pi^+$, $D_s^+ \to \eta'(\to \eta(\to \pi^+\pi^-\pi^0)\pi^+\pi^-)\pi^+$	$m(5\pi)$	$m(5\pi) \in [1.6, 2.1$ MeV/$c^2]$ extra pions' PID$_K < 0$ $N_{\rm iso}(\tau) = 2$ $N_{\rm iso}(\tau \vee B) = 2$
$D_s^+ \to 2K3\pi$	$D_s^+ \to \phi(\to K^+K^-)\pi^+\pi^-\pi^+$	$m(2K3\pi)$	extra kaons' PID$_K > 5$ $N_{\rm iso}(\tau) = 2$ $N_{\rm iso}(\tau \vee B) = 2$
$D_s^+ \to K_S^0 3\pi$	$D_s^+ \to K_S^0(\to \pi^+\pi^-)\pi^+\pi^-\pi^+$	$m(K_S^0 3\pi)$	$m(K_S^0 3\pi) \in [1.92, 2.0$ MeV/$c^2]$ extra pions' $\lvert m(\pi^+\pi^-) - m_{\rm PDG}(K_S^0)\rvert < 30$ MeV/c^2 $N_{\rm iso}(\tau) = 0$ $N_{\rm iso}(B) = 0$ K_S^0's $\chi^2_{\rm IP}(\tau) < 10$
$D_s^+ \to 3\pi\pi^0$	$D_s^+ \to \pi^+\pi^-\pi^+\pi^0$, $D_s^+ \to \omega(\to \pi^+\pi^-\pi^0)\pi^+$, $D_s^+ \to \eta(\to \pi^+\pi^-\pi^0)\pi^+$, $D_s^+ \to \phi(\to \pi^+\pi^-\pi^0)\pi^+$	$\min[m(\pi^+\pi^-\pi^0)]$	$\lvert m(3\pi\pi^0) - m_{\rm PDG}(D_s^+)\rvert < 30$ MeV/c^2 $N_{\rm iso}(\tau) = 0$ $N_{\rm iso}(B) = 0$ $\Delta R_{3\pi}(\pi^0) < 0.5$
$D_s^+ \to \eta\pi^+(\pi^0)$	$D_s^+ \to \eta(\to \pi^+\pi^-\pi^0)\pi^+(\pi^0)$	$m(3\pi\pi^0)$	$\lvert \min[m(\pi^+\pi^-\pi^0)] - m_{\rm PDG}(\eta)\rvert < 30$ MeV/c^2 $N_{\rm iso}(\tau) = 0$ $N_{\rm iso}(B) = 0$ $\Delta R_{3\pi}(\pi^0) < 0.5$
$D_s^+ \to \eta'\pi^+(\pi^0)$	$D_s^+ \to \eta'(\to \eta(\to \gamma\gamma)\pi^+\pi^-)\pi^+(\pi^0)$	$m(\eta 3\pi)$	$\lvert m(\eta\pi^+\pi^-) - m_{\rm PDG}(\eta')\rvert < 30$ MeV/c^2 $N_{\rm iso}(\tau) = 0$ $N_{\rm iso}(B) = 0$ $\Delta R_{3\pi}(\pi^0) < 0.5$
$D_s^+ \to \eta 3\pi$	$D_s^+ \to \eta(\to \gamma\gamma)\pi^+\pi^-\pi^+$	$m(\eta 3\pi)$	$\lvert m(\eta\pi^+\pi^-) - m_{\rm PDG}(\eta')\rvert > 50$ MeV/c^2 $m(\eta 3\pi) \in [1.9, 2.05$ GeV/$c^2]$ $N_{\rm iso}(\tau) = 0$ $N_{\rm iso}(B) = 0$
$D_s^+ \to 5\pi\gamma\gamma$	$D_s^+ \to \eta'(\to \eta(\to \gamma\gamma)\pi^+\pi^-)\pi^+\pi^-\pi^+$	$m(5\pi\gamma\gamma)$	$\lvert m(\eta\pi^+\pi^-) - m_{\rm PDG}(\eta')\rvert < 50$ MeV/c^2 $N_{\rm iso}(\tau) = 2$ $N_{\rm iso}(\tau \vee B) = 2$

Table 5.10: Control samples used to model $D_s^+ \to \pi^+\pi^-\pi^+(X)$ decays. The left-most column contains the names by which each control sample is referred to, "main decays" are the dominant decays in the control sample, "relevant variable" is the variable that is used in the simultaneous fit, and the last column contains the selection cuts imposed to each of the samples.

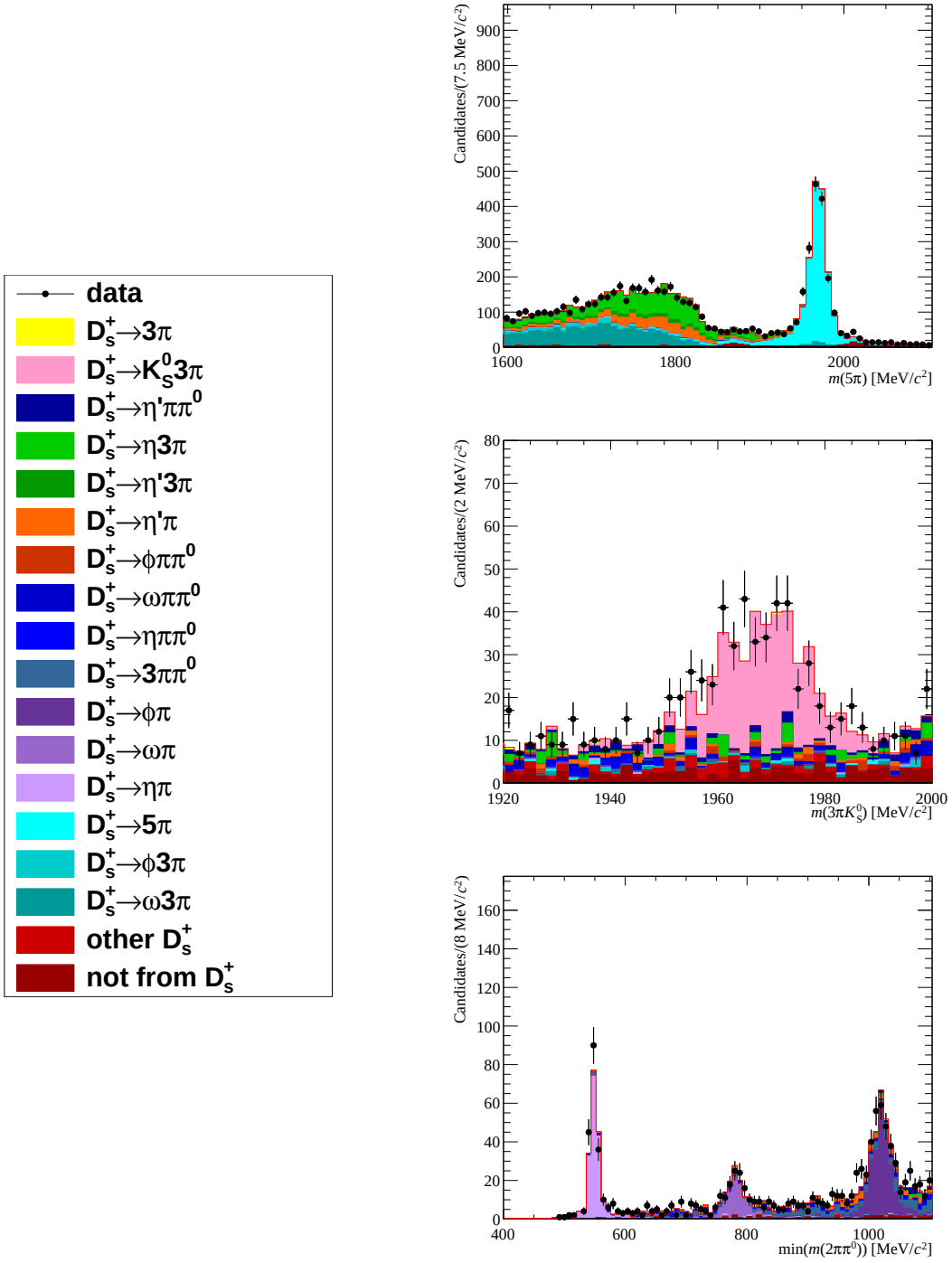

Figure 5.10: Left: legend for the plots. Right: Invariant mass distribution of the $D_s^+ \to 5\pi$ (top), $D_s^+ \to K_S^0 3\pi$ (middle), and $D_s^+ \to 3\pi\pi^0$ (bottom) control samples after the $D_s^+ \to \pi^+\pi^-\pi^+(X)$ model fit.

Fit component	Weight
$D_s^+ \to \pi^+\pi^-\pi^+$	1.004 ± 0.008
$D_s^+ \to \pi^+\pi^-\pi^+\pi^0$	0.99 ± 0.07
$D_s^+ \to \eta\pi^+$	0.78 ± 0.04
$D_s^+ \to \omega\pi^+$	0.7 ± 0.1
$D_s^+ \to \phi\pi^+$	0.73 ± 0.06
$D_s^+ \to \eta'\pi^+$	0.86 ± 0.05
$D_s^+ \to \eta\pi^+\pi^0$	0.96 ± 0.05
$D_s^+ \to \eta'\pi^+\pi^0$	0.94 ± 0.06
$D_s^+ \to 5\pi$	0.90 ± 0.02
$D_s^+ \to \omega 3\pi$	0.66 ± 0.04
$D_s^+ \to \phi 3\pi$	0.95 ± 0.04
$D_s^+ \to \eta 3\pi$	1.06 ± 0.04
$D_s^+ \to \eta' 3\pi$	0.25 ± 0.04
$D_s^+ \to K_S^0 3\pi$	0.79 ± 0.05

Table 5.11: Values of the weights of the $D_s^+ \to \pi^+\pi^-\pi^+(X)$ model, obtained from a simultaneous fit to the control samples.

6

Determination of the signal branching fractions, $R(D^0)$, and $R(D^{*0})$

Contents

This chapter contains the determination of the signal and normalisation yields, and the computation of preliminary results for the desired branching fractions and LFU ratios.

6.1 Signal yield

The $B^- \to D^{(*)0}\tau^-\overline{\nu}_\tau$ signal yields are extracted from a three-dimensional fit to the q^2, τ decay time, and BDT output distributions.

6.1.1 Fit model

The model uses a total of 24 components, which can be categorized as follows:

- **Signal components:** 4 components that correspond to the $B^- \to D^{(*)0}\tau^-\overline{\nu}_\tau$ channels (separated in $\tau^- \to \pi^-\pi^+\pi^-\nu_\tau$ and $\tau^- \to \pi^-\pi^+\pi^-\pi^0\nu_\tau$).
- $\overline{B}^0 \to D^{*+}\tau^-\overline{\nu}_\tau$ **components:** 2 components that correspond to the $\overline{B}^0 \to D^{*+}\tau^-\overline{\nu}_\tau$ channel (separated in $\tau^- \to \pi^-\pi^+\pi^-\nu_\tau$ and $\tau^- \to \pi^-\pi^+\pi^-\pi^0\nu_\tau$).
- D^{**} **component:** a single component corresponding to the $B \to D^{**}\tau^+\nu_\tau$ channels.
- **Prompt background**, a single component corresponding to the prompt $B \to D^0 3\pi$ channel.
- **Double-charm backgrounds:** components corresponding to the double-charm background channels. 1 component for $B \to \overline{D}^0 D^0(X)$, 1 for $B \to \overline{D}^0 D^+(X)$, and 12 for $B \to \overline{D}^0 D_s^+(X)$.
- **Combinatorial background:** a single component corresponding to the background created by wrong D^0–3π combinations.
- **"Not-D^0" background:** a single component corresponding to background contributions that pass the selection requirements but do not contain a D^0.

All of these components, except the not-D^0 background, use template PDFs extracted from their respective simulation samples, corrected as detailed in section 4.5 and —in the case of the prompt and double-charm backgrounds— also in chapter 5. The not-D^0 component is extracted from data by selecting the sidebands of the D^0 invariant mass distribution, with $|m(K\pi) - m_{\text{PDG}}(D^0)| \in (30, 40\ \text{MeV}/c^2)$.

The yields of these components, expressed in terms of the parameters of the fit, are detailed in table 6.1. The parameters used in the fit are:

- $N_{B^-\to D^0\tau^-\overline{\nu}_\tau}$ and $N_{B^-\to D^{*0}\tau^-\overline{\nu}_\tau}$: the number of signal events in the $B^- \to D^0\tau^-\overline{\nu}_\tau$ and $B^- \to D^{*0}\tau^-\overline{\nu}_\tau$ channels, respectively.
- $f_{D^{*+}/D^{*0}}$ and $f_{D^{**}/D^{*0}}$: the relative branching fraction of $\overline{B}^0 \to D^{*+}\tau^-\overline{\nu}_\tau$ and $B \to D^{**}\tau^+\nu_\tau$ decays, respectively, with respect to $B^- \to D^{*0}\tau^-\overline{\nu}_\tau$ decays. The $f_{D^{*+}/D^{*0}}$ value is fixed to the one obtained in table 4.11, and $f_{D^{**}/D^{*0}}$ is fixed to 0.043, as will be determined in section 6.1.2.

- $f_{3\pi}^{D^0}$, $f_{3\pi}^{D^{*0}}$, and $f_{3\pi}^{D^{*+}}$: the fraction of $\tau^- \to \pi^-\pi^+\pi^-\nu_\tau$ decays with respect to the sum of $\tau^- \to \pi^-\pi^+\pi^-\nu_\tau$ and $\tau^- \to \pi^-\pi^+\pi^-\pi^0\nu_\tau$ decays in the $B^- \to D^0\tau^-\overline{\nu}_\tau$, $B^- \to D^{*0}\tau^-\overline{\nu}_\tau$, and $\overline{B}^0 \to D^{*+}\tau^-\overline{\nu}_\tau$ channels, respectively. These values are fixed to the central values obtained in table 4.11.

- N_{D^0}, N_{D^+}, $N_{D_s^+}$, N_{prompt}, N_{comb}, and $N_{\text{not-}D^0}$: the number of events in their respective background components[1]. The N_{comb} and $N_{\text{not-}D^0}$ parameters are fixed to a value obtained from the data. The N_{D^0} parameter is constrained to a Gaussian distribution centered in the expected N_{D^0} value, computed from independent $D^0 \to K3\pi$ decays, and with a sigma equal to the 15% of that value.

- The ε_i, F_i, and F_i^* parameters, as defined in section 5.2.1. These parameters are chosen following the same logic as in the control-sample fit of section 5.2.1, but now constraining the free $F_i^{(*)}$ parameters to a Gaussian distribution with mean and σ set to the values obtained in that control sample's fit. The $F_i^{(*)}$ parameters corresponding to components with a D^{*+} are fixed to their central values[2].

The values of the fixed parameters (except N_{comb} and $N_{\text{not-}D^0}$) were determined according to efficiencies computed from the simulation samples and the known branching fractions from [2], with the exception of $f_{D^{**}/D^{*0}}$, whose computation is more complex and is explained in the following section.

In the case of N_{comb}, its simulation sample is scaled to match with the mass distribution from data above the B mass peak ($m(D^03\pi) \in (5400, 5600\ \text{MeV}/c^2)$), where all events are expected to be combinatorial background, and the resulting yield is taken as the fixed value. In the case of $N_{\text{not-}D^0}$, since the template is taken directly from data and is assumed to have a flat distribution in $m(K\pi)$, it is simply scaled by a factor of two, to account for the difference between the nominal selection ($|m(K\pi) - m_{\text{PDG}}(D^0)| < 20\ \text{MeV}/c^2$) and this template's selection ($|m(K\pi) - m_{\text{PDG}}(D^0)| \in (30, 40\ \text{MeV}/c^2)$).

Two non-physical parameters, $w_{\text{BDT}}^{(1)}$ and $w_{\text{BDT}}^{(2)}$, are added to the fit to correct the $B \to \overline{D}^0 D_s^+(X)$ components' shape in the BDT dimension. These parameters apply, respectively, a linear and a quadratic weight in the BDT axis, as

$$h_{\text{mod}} = \left(1 + w_{\text{BDT}}^{(1)}\left(\frac{\text{BDT} - \text{BDT}_{\text{min}}}{\text{BDT}_{\text{max}} - \text{BDT}_{\text{min}}} - \frac{1}{2}\right) + \right. \\ \left. + w_{\text{BDT}}^{(2)}\left(\frac{\text{BDT} - \text{BDT}_{\text{min}}}{\text{BDT}_{\text{max}} - \text{BDT}_{\text{min}}} - \frac{1}{2}\right)^2\right) h_0, \quad (6.1)$$

where h_{mod} is the modified template histogram, BDT is the BDT output value, with BDT_{min} and BDT_{max} being its minimum and maximum values (-0.4 and 1); and h_0 is

[1] N_{D^0, D^+, D_s^+} correspond to their respective $B \to \overline{D}^0 X_c(Y)$ double-charm backgrounds

[2] This choice is justified due to the data in the fit being selected not to contain D^* mesons, while the control-sample fit was done with a D^*-enriched sample.

Component	Yield
$B^- \to D^0\tau^-\overline{\nu}_\tau$, $\tau^- \to \pi^-\pi^+\pi^-\nu_\tau$	$N_{B^-\to D^0\tau^-\overline{\nu}_\tau} \times f_{3\pi}^{D^0}$
$B^- \to D^0\tau^-\overline{\nu}_\tau$, $\tau^- \to \pi^-\pi^+\pi^-\pi^0\nu_\tau$	$N_{B^-\to D^0\tau^-\overline{\nu}_\tau} \times (1 - f_{3\pi}^{D^0})$
$B^- \to D^{*0}\tau^-\overline{\nu}_\tau$, $\tau^- \to \pi^-\pi^+\pi^-\nu_\tau$	$N_{B^-\to D^{*0}\tau^-\overline{\nu}_\tau} \times f_{3\pi}^{D^{*0}}$
$B^- \to D^{*0}\tau^-\overline{\nu}_\tau$, $\tau^- \to \pi^-\pi^+\pi^-\pi^0\nu_\tau$	$N_{B^-\to D^{*0}\tau^-\overline{\nu}_\tau} \times (1 - f_{3\pi}^{D^{*0}})$
$\overline{B}^0 \to D^{*+}\tau^-\overline{\nu}_\tau$, $\tau^+ \to 3\pi\overline{\nu}_\tau$	$N_{B^-\to D^{*0}\tau^-\overline{\nu}_\tau} \times f_{D^{*-}/D^{*0}} \times f_{3\pi}^{D^{*-}}$
$\overline{B}^0 \to D^{*+}\tau^-\overline{\nu}_\tau$, $\tau^+ \to 3\pi\pi^0\overline{\nu}_\tau$	$N_{B^-\to D^{*0}\tau^-\overline{\nu}_\tau} \times f_{D^{*-}/D^{*0}} \times (1 - f_{3\pi}^{D^{*-}})$
$B \to D^{**}\tau^+\nu_\tau$	$N_{B^-\to D^{*0}\tau^-\overline{\nu}_\tau} \times f_{D^{**}/D^{*0}}$
$B \to D^0 3\pi(X)$	N_{prompt}
$B \to \overline{D}^0 D^0(X)$	N_{D^0}
$B \to \overline{D}^0 D^+(X)$	N_{D^+}
$B^+ \to \overline{D}^0 D_s^+$	$N_{D_s^+} \times \epsilon_{B^+\to\overline{D}^0 D_s^+} \times F^{(\overline{D}^0 D_s^+)}_{B^+\to\overline{D}^0 D_s^+} / \sum_i \epsilon_i F_i$
$B^+ \to \overline{D}^{*0} D_s^+$	$N_{D_s^+} \times \epsilon_{B^+\to\overline{D}^{*0} D_s^+} \times F^{(\overline{D}^0 D_s^+)}_{B^+\to\overline{D}^{*0} D_s^+} / \sum_i \epsilon_i F_i$
$B^+ \to \overline{D}^0 D_s^{*+}$	$N_{D_s^+} \times \epsilon_{B^+\to\overline{D}^0 D_s^{*+}} \times F^{(\overline{D}^0 D_s^+)}_{B^+\to\overline{D}^0 D_s^{*+}} / \sum_i \epsilon_i F_i$
$B^+ \to \overline{D}^{*0} D_s^{*+}$	$N_{D_s^+} \times \epsilon_{B^+\to\overline{D}^{*0} D_s^{*+}} \times F^{(\overline{D}^0 D_s^+)}_{B^+\to\overline{D}^{*0} D_s^{*+}} / \sum_i \epsilon_i F_i$
$B^+ \to \overline{D}^0 D_{s1}(2460)^+$	$N_{D_s^+} \times \epsilon_{B^+\to\overline{D}^0 D_{s1}(2460)^+} \times F^{(\overline{D}^0 D_s^+)}_{B^+\to\overline{D}^0 D_{s1}(2460)^+} / \sum_i \epsilon_i F_i$
$B^+ \to \overline{D}^{*0} D_{s1}(2460)^+$	$N_{D_s^+} \times \epsilon_{B^+\to\overline{D}^{*0} D_{s1}(2460)^+} \times F^{(\overline{D}^0 D_s^+)}_{B^+\to\overline{D}^{*0} D_{s1}(2460)^+} / \sum_i \epsilon_i F_i$
$B^+ \vert B_s^0 \to \overline{D}^0 D_s^+(X)$	$N_{D_s^+} \times \epsilon_{B^+\vert B_s^0\to\overline{D}^0 D_s^+(X)} \times F^{(\overline{D}^0 D_s^+)}_{B^+\vert B_s^0\to\overline{D}^0 D_s^+(X)} / \sum_i \epsilon_i F_i$
$B^0 \to \overline{D}^0 D_s^+ X$	$N_{D_s^+} \times \epsilon_{B^0\to\overline{D}^0 D_s^+ X} \times F^{(\overline{D}^0 D_s^+)}_{B^0\to\overline{D}^0 D_s^+ X} / \sum_i \epsilon_i F_i$
$B^0 \to D^{*-} D_s^+$	$N_{D_s^+} \times \epsilon_{B^0\to D^{*-} D_s^+} \times F^{(\overline{D}^0 D_s^+)}_{B^0\to D^{*-} D_s^+} / \sum_i \epsilon_i F_i$
$B^0 \to D^{*-} D_s^{*+}$	$N_{D_s^+} \times \epsilon_{B^0\to D^{*-} D_s^{*+}} \times F^{(\overline{D}^0 D_s^+)}_{B^0\to D^{*-} D_s^+} \times F^{*(D^{*-} D_s^+)}_{B^0\to D^{*-} D_s^{*+}} / \sum_i \epsilon_i F_i$
$B^0 \to D^{*-} D_{s0}^*(2317)^+$	$N_{D_s^+} \times \epsilon_{B^0\to D^{*-} D_{s0}^*(2317)^+} \times F^{(\overline{D}^0 D_s^+)}_{B^0\to D^{*-} D_s^+} \times F^{*(D^{*-} D_s^+)}_{B^0\to D^{*-} D_{s0}^*(2317)^+} / \sum_i \epsilon_i F_i$
$B^0 \to D^{*-} D_{s1}(2460)^+$	$N_{D_s^+} \times \epsilon_{B^0\to D^{*-} D_{s1}(2460)^+} \times F^{(\overline{D}^0 D_s^+)}_{B^0\to D^{*-} D_s^+} \times F^{*(D^{*-} D_s^+)}_{B^0\to D^{*-} D_{s1}(2460)^+} / \sum_i \epsilon_i F_i$
Comb. D^0–3π background	N_{comb}
Not-D^0 background	$N_{\text{not-}D^0}$

Table 6.1: Components of the signal fit and their yields, expressed in terms of the free parameters of the fit.

the original template histogram. All $B \to \overline{D}^0 D_s^+(X)$ components are modified equally by these two parameters. These parameters are introduced in order to compensate for the disagreement between the model and the data in the BDT dimension, which is expected to come mostly from the $B \to \overline{D}^0 D_s^+(X)$ component, since the BDT is trained in events with $m(3\pi) < 1600$ MeV/c^2 (below the τ mass), while the events used in the $B \to \overline{D}^0 D_s^+(X)$ control sample have $m(3\pi) \in (1938.35, 1998.35$ MeV/c^2). However, it is important to note that the presence of these parameters in the fit is not definitive: the sources of this discrepancy are being more carefully studied and the fit strategy will change accordingly before a final result is published. The systematic impact of this strategy will be studied in chapter 7.

This leaves a total of 15 free parameters in the fit: the 2 signal yields ($N_{B^-\to D^0\tau^-\overline{\nu}_\tau}$ and $N_{B^-\to D^{*0}\tau^-\overline{\nu}_\tau}$), 4 background yields ($N_{D^0}$, N_{D^+}, $N_{D_s^+}$, and N_{prompt}), 7 F_i parameters from the $B \to \overline{D}^0 D_s^+(X)$ model, and 2 w_{BDT} shape-correction parameters.

6.1.2 $B \to D^{**}\tau^+\nu_\tau$ feeddown

The feeddown from excited charmed mesons (D^{**}) to the signal channels is a sensitive matter in this analysis, since the individual branching fractions from $B \to D^{**}\tau^+\nu_\tau$ decays have not yet been determined. To account for this feeddown, the relative fraction of $B \to D^{**}\tau^+\nu_\tau$ decays present in the selected sample is estimated ($f_{D^{**}/D^{*0}}$). A total of ten of these decays are considered for this estimation:

- $B^- \to D_1(2420)^0\tau^-\overline{\nu}_\tau$,
- $B^- \to D_2^*(2460)^0\tau^-\overline{\nu}_\tau$,
- $B^- \to D_0^*(2300)^0\tau^-\overline{\nu}_\tau$,
- $B^- \to D_1'(2430)^0\tau^-\overline{\nu}_\tau$,
- $\overline{B}^0 \to D_1(2420)^+\tau^-\overline{\nu}_\tau$,
- $\overline{B}^0 \to D_2^*(2460)^+\tau^-\overline{\nu}_\tau$,
- $\overline{B}^0 \to D_0^*(2300)^+\tau^-\overline{\nu}_\tau$,
- $\overline{B}^0 \to D_1'(2430)^+\tau^-\overline{\nu}_\tau$,
- $\overline{B}_s^0 \to D_{s1}'(2536)^+\tau^-\overline{\nu}_\tau$, and
- $\overline{B}_s^0 \to D_{s2}^*(2573)^+\tau^-\overline{\nu}_\tau$.

Theoretical predictions of the LFU ratios [125]

$$R(D^{**}) = \frac{\mathcal{B}(B \to D^{**}\tau^+\nu_\tau)}{\mathcal{B}(B \to D^{**}\ell^+\nu_\ell)} \tag{6.2}$$

are used in addition to existing measurements of $\mathcal{B}(\overline{B} \to D^{**}\ell^+\nu_\ell)$ [2] and estimations of $\mathcal{B}(D^{**} \to X)$ based on isospin relations [126] in order to obtain the product of branching fractions $\mathcal{B}(B \to D^{**}\tau^+\nu_\tau) \times \mathcal{B}(D^{**} \to D^0X)$, where $\mathcal{B}(D^{**} \to D^0X)$ is the branching fraction of the corresponding excited meson to a final estate with a D^0 (since we are studying the feeddown to D^0). The results of this procedure are shown in table 6.2. As a cross-check, the total branching fractions $\mathcal{B}(B^- \to D^{**}\ell^-\bar{\nu}_\ell)$ and $\mathcal{B}(\overline{B}^0 \to D^{**}\ell^-\bar{\nu}_\ell)$ are compared, in table 6.3, to the experimental measurements from [2].

Once the branching fractions for $B \to D^{**}\tau^+\nu_\tau$ decays are obtained, it is possible to estimate their yields relative to the $B^- \to D^{*0}\tau^-\overline{\nu}_\tau$ signal,

$$f_{D^{**}/D^{*0}} = \frac{N_{B\to D^{**}\tau^+\nu_\tau}}{N_{B^-\to D^{*0}\tau^-\overline{\nu}_\tau}}, \tag{6.3}$$

in the signal-selection sample. This can be done through the expression

D^{**}	Decay recorded in [2]	$\mathcal{B}$ recorded in [2] (%)	Estimated $\mathcal{B}(\overline{B} \to D^{**}\ell\bar{\nu}_\ell)$ (%)	Estimated $\mathcal{B}(\overline{B} \to D^{**}\ell\bar{\nu}_\ell) \times \mathcal{B}(D^{**} \to D^0 X)$ (%)	$R(D^{**})$ from [125]	Estimated $\mathcal{B}(B \to D^{**}\tau^+\nu_\tau) \times \mathcal{B}(D^{**} \to D^0 X)$ (%)
D_1^0	$B^- \to D_1^0(\to D^{*+}\pi^-)\ell^-\bar{\nu}_\ell$	0.303 ± 0.020	0.721 ± 0.048	0.55 ± 0.04	0.10 ± 0.01	0.055 ± 0.007
D_2^{*0}	$B^- \to D_2^{*0}(\to D^{*+}\pi^-)\ell^-\bar{\nu}_\ell$ $B^- \to D_2^{*0}(\to D^{+}\pi^-)\ell^-\bar{\nu}_\ell$	0.101 ± 0.024 0.153 ± 0.016	0.385 ± 0.044	0.194 ± 0.022	0.07 ± 0.01	0.014 ± 0.002
$D_1'^0$	$B^- \to D_1'^0(\to D^{*+}\pi^-)\ell^-\bar{\nu}_\ell$	0.27 ± 0.06	0.403 ± 0.090	0.313 ± 0.070	0.06 ± 0.02	0.019 ± 0.008
D_0^{*0}	$B^- \to D_0^{*0}(\to D^{+}\pi^-)\ell^-\bar{\nu}_\ell$	0.25 ± 0.05	0.373 ± 0.075	0.123 ± 0.025	0.08 ± 0.03	0.010 ± 0.004
D_1^+	$\overline{B}^0 \to D_1^+(\to D^{*0}\pi^+)\ell^-\bar{\nu}_\ell$	0.280 ± 0.028	0.667 ± 0.067	0.525 ± 0.052	0.10 ± 0.01	0.052 ± 0.007
D_2^{*+}	$\overline{B}^0 \to D_2^{*+}(\to D^{*0}\pi^+)\ell^-\bar{\nu}_\ell$ $\overline{B}^0 \to D_2^{*+}(\to D^{0}\pi^+)\ell^-\bar{\nu}_\ell$	0.068 ± 0.012 0.121 ± 0.033	0.286 ± 0.053	0.214 ± 0.040	0.07 ± 0.01	0.015 ± 0.004
$D_1'^+$	$\overline{B}^0 \to D_1'^+(\to D^{*0}\pi^+)\ell^-\bar{\nu}_\ell$	0.31 ± 0.09	0.463 ± 0.134	0.412 ± 0.120	0.06 ± 0.02	0.025 ± 0.011
D_0^{*+}	$\overline{B}^0 \to D_0^{*+}(\to D^{0}\pi^+)\ell^-\bar{\nu}_\ell$	0.30 ± 0.12	0.448 ± 0.179	0.30 ± 0.12	0.08 ± 0.03	0.024 ± 0.013
$D_{s1}'^+$	$\overline{B}_s^0 \to D_{s1}'^+(\to D^{*0}K^+)\ell^-\bar{\nu}_\ell X$	0.44 ± 0.13	0.88 ± 0.26	0.73 ± 0.22	0.09 ± 0.02	0.066 ± 0.024
D_{s2}^+	$\overline{B}_s^0 \to D_{s2}^+(\to D^{0}K^+)\ell^-\bar{\nu}_\ell X$	0.27 ± 0.10	0.54 ± 0.20	0.27 ± 0.10	0.07 ± 0.01	0.019 ± 0.008

Table 6.2: Estimations of $\mathcal{B}(B \to D^{**}\tau^+\nu_\tau) \times \mathcal{B}(D^{**} \to D^0 X)$, along with some of the required input quantities for each meson. The total $\mathcal{B}(\overline{B} \to D^{**}\ell\bar{\nu}_l)$ is estimated by dividing the $\mathcal{B}$ from [2] by the estimated $\mathcal{B}$ of the D^{**} decay used in the measurement. Then, the total is multiplied by the corresponding $\mathcal{B}(D^{**})$, and multiplied by $R(D^{**})$ to obtain the desired quantity.

Parent	Estimated $\mathcal{B}(\overline{B} \to D^{**}\ell\nu)$ (%)	$\mathcal{B}(\overline{B} \to D^{(*)}n\pi\ell\nu)$ $(n \geq 1)$ from [2] (%)
B^-	1.88 ± 0.13	1.88 ± 0.25
$\overline{B}^0$	1.86 ± 0.24	2.3 ± 0.5

Table 6.3: Comparison between the estimated $\mathcal{B}(B^- \to D^{**}\ell^-\bar{\nu}_l)$ and $\mathcal{B}(\overline{B}^0 \to D^{**}\ell^-\bar{\nu}_l)$ branching fractions and the existing measurements from [2].

$$f_{D^{**}/D^{*0}} = \Bigg[\mathcal{B}(B^- \to D^{**}\tau^-\overline{\nu}_\tau) \times \frac{\varepsilon_{B^-\to D^{**}}}{\varepsilon_{B^-\to D^{*0}}} + \\ + \mathcal{B}(\overline{B}^0 \to D^{**}\tau^-\overline{\nu}_\tau) \times \frac{f_d}{f_u} \times \frac{\varepsilon_{\overline{B}^0\to D^{**}}}{\varepsilon_{B^-\to D^{*0}}} + \\ + \mathcal{B}(\overline{B}^0_s \to D^{**}\tau^-\overline{\nu}_\tau) \times \frac{f_s}{f_u} \times \frac{\varepsilon_{\overline{B}^0_s\to D^{**}}}{\varepsilon_{B^-\to D^{*0}}}\Bigg] \times \\ \times \frac{\mathcal{B}(D^{**} \to D^0 X)}{\mathcal{B}(B^- \to D^{*0}\tau^-\overline{\nu}_\tau) \times \mathcal{B}(D^{*0} \to D^0 X)}, \quad (6.4)$$

where $\varepsilon_{B^-\to D^{**}}/\varepsilon_{B^-\to D^{*0}}$, $\varepsilon_{\overline{B}^0\to D^{**}}/\varepsilon_{B^-\to D^{*0}}$ and $\varepsilon_{\overline{B}^0_s\to D^{**}}/\varepsilon_{B^-\to D^{*0}}$ are the relative efficiencies for $B^- \to D^{**}\tau^-\overline{\nu}_\tau$, $\overline{B}^0 \to D^{**}\tau^-\overline{\nu}_\tau$, and $\overline{B}^0_s \to D^{**}\tau^-\overline{\nu}_\tau$ decays with respect to signal $B^- \to D^{*0}\tau^-\overline{\nu}_\tau$ decays (computed from simulation); f_d/f_u and f_s/f_u are the ratios of fragmentation fractions, where $f_d/f_u = 1$ and f_s/f_u is taken from [127], and $\mathcal{B}(D^{*0} \to D^0 X)$ is taken to be 100%. This results in the value of $f_{D^{**}/D^{*0}} = 0.043$ which is fixed in the fit.

6.1.3 Blinding strategy

Since the analysis is not yet considered to be completed, its results must be blinded in order to avoid human biases during the development process. This is done by blinding the signal yields in the fit ($N_{B^-\to D^0\tau^-\overline{\nu}_\tau}$ and $N_{B^-\to D^{*0}\tau^-\overline{\nu}_\tau}$), adding to each one a random value drawn from a Gaussian distribution with mean zero and $\sigma = 20000$. Thus, the signal yield parameters currently being used in the fit are related to the actual values by

$$N_{\text{sig}} = N_{\text{sig}}^{(\text{blind})} + x_{\text{sig}}, \quad (6.5)$$

where x_{sig} is the random value being added. This approach allows the uncertainty of the signals to be monitored, while avoiding looking at the actual value of the parameters and their relative uncertainties.

In order to avoid inferring the added value of both signals, the main background yield, $N_{D_s^+}$, is also blinded with the same strategy as the signal, but with $\sigma = 40000$.

Finally, the visualisation of these blinded components in the fit results is also altered by normalising the PDF integral of the $B^- \to D^0\tau^-\overline{\nu}_\tau$ and $B^- \to D^{*0}\tau^-\overline{\nu}_\tau$ signal components to 9000 and 11000, respectively, and that of the $B \to \overline{D}^0 D_s^+(X)$ background component to 10000.

6.1.4 Result

The yields of the $B^- \to D^0\tau^-\overline{\nu}_\tau$ and $B^- \to D^{*0}\tau^-\overline{\nu}_\tau$ signal channels are obtained from a three-dimensional fit to the τ decay time, q^2, and BDT distributions using the

Parameter	Fit result	Constraint
$N_{B^- \to D^0 \tau^- \overline{\nu}_\tau}$	xxx $\pm$1655	—
$N_{B^- \to D^{*0} \tau^- \overline{\nu}_\tau}$	xxx $\pm$994	—
$N_{D_s^+}$	xxx $\pm$969	—
N_{D^0}	7996 ± 575	6655 ± 998
N_{D^+}	8578 ± 508	—
N_{prompt}	6261 ± 258	—
$N_{\text{not-}D^0}$	10902	10902
N_{comb}	3286	3286
$F^{(\overline{D}^0 D_s^+)}_{B^+ \to \overline{D}^{*0} D_s^+}$	0.949 ± 0.035	0.915 ± 0.054
$F^{(\overline{D}^0 D_s^+)}_{B^+ \to \overline{D}^0 D_s^{*+}}$	0.855 ± 0.041	0.935 ± 0.056
$F^{(\overline{D}^0 D_s^+)}_{B^+ \to \overline{D}^{*0} D_s^{*+}}$	1.847 ± 0.040	1.828 ± 0.047
$F^{(\overline{D}^0 D_s^+)}_{B^+ \to \overline{D}^0 D_{s1}(2460)^+}$	0.262 ± 0.032	0.332 ± 0.038
$F^{(\overline{D}^0 D_s^+)}_{B^+ \to \overline{D}^{*0} D_{s1}(2460)^+}$	0.816 ± 0.029	0.710 ± 0.040
$F^{(\overline{D}^0 D_s^+)}_{B^+ \mid B_s^0 \to \overline{D}^0 D_s^+(X)}$	0.778 ± 0.034	0.817 ± 0.037
$F^{(\overline{D}^0 D_s^+)}_{B^0 \to \overline{D}^0 D_s^+ X}$	0.1044 ± 0.0090	0.0990 ± 0.0092
$w^{(1)}_{\text{BDT}}$	0.143 ± 0.038	—
$w^{(2)}_{\text{BDT}}$	0.432 ± 0.183	—

Table 6.4: Results of the signal yield fit parameters along with their constraints.

previously explained fit model. The results of this fit are show in table 6.4, and its projections in fig. 6.1.

The resulting blinded signal yields are

$$\begin{aligned} N_{B^- \to D^0 \tau^- \overline{\nu}_\tau} &= \text{xxx} \pm 1655 \ , \\ N_{B^- \to D^{*0} \tau^- \overline{\nu}_\tau} &= \text{xxx} \pm 994 \ , \end{aligned} \tag{6.6}$$

with a correlation coefficient of -0.932 between the two parameters.

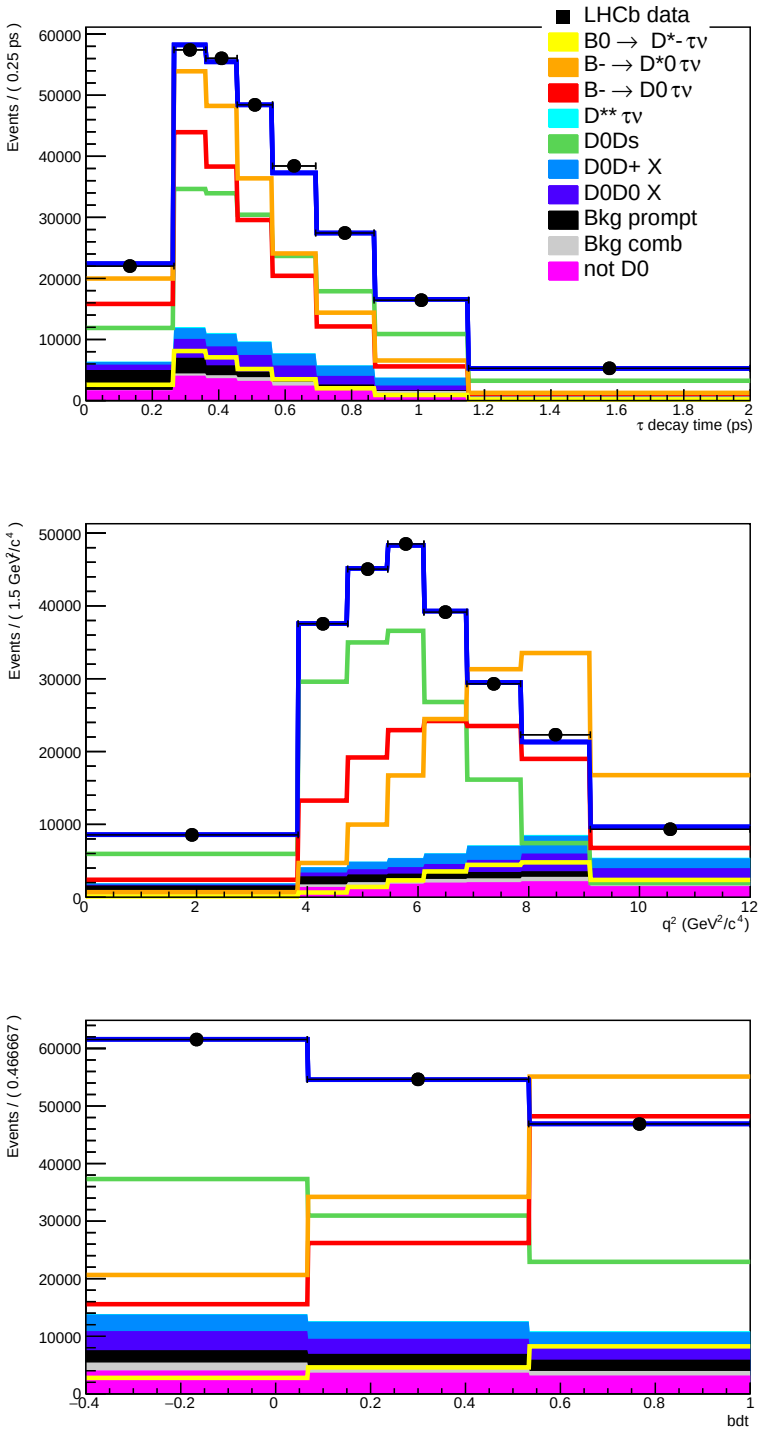

Figure 6.1: Projections of the (blinded) signal 3D fit on the τ decay time, q^2 and BDT distributions. The $B^- \to D^{(*)0}\tau^-\overline{\nu}_\tau$ (red and orange), $B^0 \to D^{*-}\tau^+\nu_\tau$ (yellow), and $B^+ \to \overline{D}^0 D_s^+$ (green) components are not represented according to their actual yield, as detailed in the blinding procedure (section 6.1.3). The dark blue line corresponds to the total PDF.

6.2 Normalisation yield

The $B^+ \to \overline{D}^0 D_s^+$ decay is used as normalisation channel. For this purpose, data and simulated events are required to pass the normalisation selection, described in section 4.3.5. The normalisation yield is obtained from a one-dimensional fit to the deconvoluted mass

$$m'_{\overline{D}^0 D_s^+} \equiv m_{\text{meas.}}(\overline{D}^0 D_s^+) - m_{\text{meas.}}(\overline{D}^0) - m_{\text{meas.}}(D_s^+) + m_{\text{PDG}}(\overline{D}^0) + m_{\text{PDG}}(D_s^+), \quad (6.7)$$

in a window of ± 60 MeV/c^2 around the known B^+ mass from [2].

In order to describe the shape of this mass distribution, a double-sided Crystal Ball (CB) function is used for the signal, and an exponential function for the background. The CB function is defined as

$$f_{\text{CB}}(m'_{\overline{D}^0 D_s^+}) \equiv \frac{N_{\text{norm}}}{C(\sigma, \alpha_i, n_i)} \cdot \begin{cases} A_L(B_L - \frac{\Delta m}{\sigma})^{-n_L}, & \text{for } m'_{\overline{D}^0 D_s^+} < \alpha_L \\ e^{-(\Delta m)^2/(2\sigma^2)}, & \text{for } \alpha_L \leq m'_{\overline{D}^0 D_s^+} \leq \alpha_R \\ A_R(B_R - \frac{\Delta m}{\sigma})^{-n_R}, & \text{for } m'_{\overline{D}^0 D_s^+} > \alpha_R \end{cases} \quad (6.8)$$

where

$$\begin{aligned} \Delta m &\equiv m'_{\overline{D}^0 D_s^+} - m_{\text{mean}}, \\ A_i &\equiv \left(\frac{n_i}{|\alpha_i|}\right)^{n_i} e^{-|\alpha_i|^2/2}, \\ B_i &\equiv \frac{n_i}{|\alpha_i|} - |\alpha_i|, \end{aligned} \quad (6.9)$$

$C(\sigma, \alpha_i, n_i)$ is a normalization factor such that N_{norm} is equal to the integral of the function, m_{mean} is the mean mass in which the CB function is centered, σ its standard deviation, and α_i and n_i are the so-called "tail parameters", with $i = \{L, R\}$, which modify the shape of the CB function on each side. m_{mean}, σ, and the tail parameters are the free parameters of the function.

First, a fit to the $B^+ \to \overline{D}^0 D_s^+$ simulation sample is performed using only the CB function (fig. 6.2). The result of this first fit is used to extract the tail parameters of the CB function. Then, a fit to the data sample is performed using the full model, with all parameters floating except the CB tail parameters, which are fixed to the result of the first fit.

The obtained yield is

$$N_{\text{norm}} = 3047 \pm 56 \ . \quad (6.10)$$

The fit results are shown in table 6.5 and in fig. 6.3.

Parameter	Fit result (sim.)	Fit result (data)
N_{norm}	162650 ± 400	3047 ± 56
m_{mean}	5279.455 ± 0.026	5278.87 ± 0.17
σ	8.288 ± 0.030	8.66 ± 0.14
α_R	-1.674 ± 0.031	-1.674 (fixed)
α_L	1.510 ± 0.023	1.510 (fixed)
n_R	44 ± 17	44 (fixed)
n_L	15.7 ± 2.0	15.7 (fixed)
N_{bkg}	-	27 ± 10
r_{bkg}	-	-0.0043 ± 0.0068

Table 6.5: Results of the normalisation fit procedure. The second column contains the results of the fit to the $B^+ \to \overline{D}^0 D_s^+$ simulation sample, while the last column shows the results of the fit to data. m_{mean}, σ, $\alpha_{R,L}$ and $n_{R,L}$ are the parameters of the Crystal Ball function, with N_{norm} being its integral, while N_{bkg} and r_{bkg} are the parameters of the exponential background model.

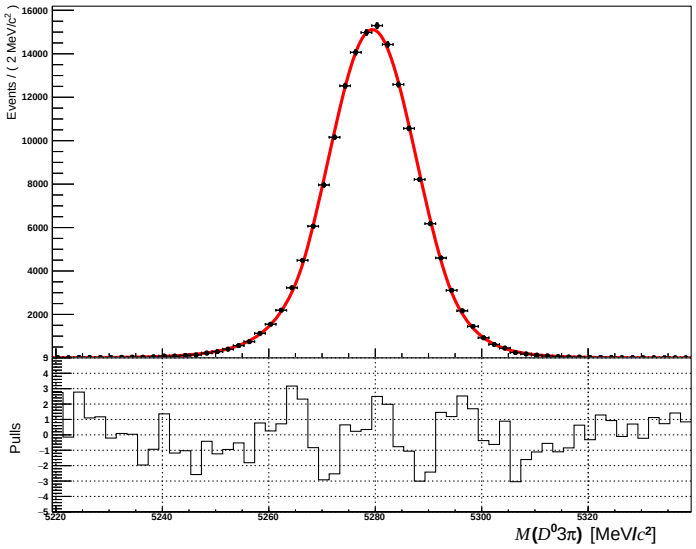

Figure 6.2: Fit to the $m'_{\overline{D}^0 D_s^+}$ distribution of simulated events passing the normalisation selection. The shape is described by a Crystal Ball function.

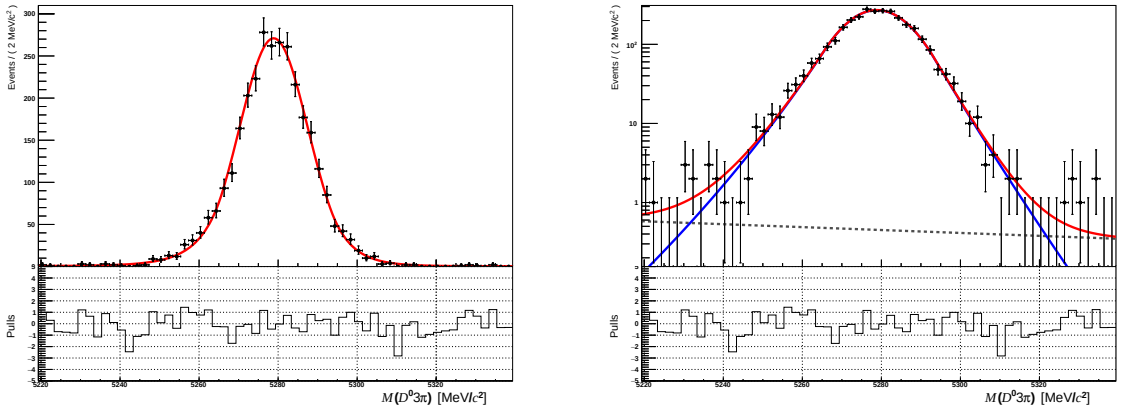

Figure 6.3: Fit to the $m'_{\overline{D}^0 D_s^+}$ distribution of real events passing the normalisation selection. The fit model (red line) is described by an exponential function and a Crystal Ball function, with its tail parameters fixed to those obtained in a fit to the simulation sample. In the right plot, the y axis is shown on a logarithmic scale, and the exponential function (dotted line) and Crystal Ball function (blue line) can be observed.

6.3 $B^- \to D^{(*)0}\tau^-\overline{\nu}_\tau$ branching fractions

The previously measured signal (section 6.1) and normalisation (section 6.2) yields are used to determine the $B^- \to D^0\tau^-\overline{\nu}_\tau$ and $B^- \to D^{*0}\tau^-\overline{\nu}_\tau$ branching fractions as

$$\begin{aligned}\mathcal{B}(B^- \to D^{(*)0}\tau^-\overline{\nu}_\tau) = \frac{N_{B^-\to D^{(*)0}\tau^-\overline{\nu}_\tau}}{N_{B^+\to\overline{D}^0 D_s^+}} \times \mathcal{B}(B^+ \to \overline{D}^0 D_s^+)\times \\ \times \frac{\varepsilon_{B^+\to\overline{D}^0 D_s^+}\mathcal{B}(D_s^+ \to \pi^+\pi^-\pi^+)}{\varepsilon^{\tau\to 3\pi\nu_\tau}_{B^-\to D^{(*)0}\tau^-\overline{\nu}_\tau}\mathcal{B}(\tau^- \to \pi^-\pi^+\pi^-\nu_\tau) + \varepsilon^{\tau\to 3\pi\pi^0\nu_\tau}_{B^-\to D^{(*)0}\tau^-\overline{\nu}_\tau}\mathcal{B}(\tau^- \to \pi^-\pi^+\pi^-\pi^0\nu_\tau)}\end{aligned} \tag{6.11}$$

where the efficiencies are computed from simulation (see section 4.6) and the branching fractions are external inputs, taken from [2] as

$$\begin{aligned}\mathcal{B}(B^+ \to \overline{D}^0 D_s^+) &= (9.0 \pm 0.9) \times 10^{-3}\ , \\ \mathcal{B}(D_s^+ \to \pi^+\pi^-\pi^+) &= (1.08 \pm 0.04) \times 10^{-2}\ , \\ \mathcal{B}(\tau^- \to \pi^-\pi^+\pi^-\nu_\tau) &= (9.02 \pm 0.05) \times 10^{-2}\ , \\ \mathcal{B}(\tau^- \to \pi^-\pi^+\pi^-\pi^0\nu_\tau) &= (4.49 \pm 0.05) \times 10^{-2}\ .\end{aligned} \tag{6.12}$$

Following this procedure, the measured blinded branching fractions are

$$\begin{aligned}\mathcal{B}(B^- \to D^0\tau^-\overline{\nu}_\tau) &= (\text{xxx} \pm 0.19\ (\text{stat.}) \pm 0.07\ (\text{ext.})) \times 10^{-2}\ , \\ \mathcal{B}(B^- \to D^{*0}\tau^-\overline{\nu}_\tau) &= (\text{xxx} \pm 0.14\ (\text{stat.}) \pm 0.15\ (\text{ext.})) \times 10^{-2}\ ,\end{aligned} \tag{6.13}$$

where the first uncertainties are due to the uncertainty provided by the signal and normalisation yield fits, and the second is due to the uncertainties of the external inputs. The correlation coefficient between the measured branching fractions is -0.301. Since the propagation of uncertainties requires the actual "unblinded" yield of the signals, these uncertainties are computed as if the signal yields were such that the resulting $R(D^{(*)})$ values match with the SM predictions. The actual uncertainties of the unblinded results are expected to be different but similar.

6.4 $R(D^0)$ and $R(D^{*0})$

With the signal branching fractions measured in section 6.3, the desired LFU quantities $R(D^0)$ and $R(D^{*0})$ can be computed as per their definition,

$$R(D^{(*)0}) = \frac{\mathcal{B}(B^- \to D^{(*)0}\tau^-\overline{\nu}_\tau)}{\mathcal{B}(B^- \to D^{(*)0}\ell^-\bar{\nu}_\ell)} \ , \tag{6.14}$$

where ℓ^- refers to either a μ^- or an e^- lepton, and $\mathcal{B}(B^- \to D^{(*)0}\ell^-\bar{\nu}_\ell)$ are external inputs taken from [2] as

$$\begin{aligned} \mathcal{B}(B^- \to D^0\ell^-\bar{\nu}_\ell) &= (2.30 \pm 0.09) \times 10^{-2} \ , \\ \mathcal{B}(B^- \to D^{*0}\ell^-\bar{\nu}_\ell) &= (5.58 \pm 0.22) \times 10^{-2} \ . \end{aligned} \tag{6.15}$$

The resulting blinded values for the two LFU ratios are

$$\begin{aligned} R(D^0) &= \text{xxx} \pm 0.084 \ (\text{stat.}) \pm 0.034 \ (\text{ext.}) \ , \\ R(D^{*0}) &= \text{xxx} \pm 0.025 \ (\text{stat.}) \pm 0.029 \ (\text{ext.}) \ , \end{aligned} \tag{6.16}$$

where the first uncertainties are due to the uncertainty from the signal and normalisation fits, while the second uncertainties are due to the uncertainties of the external inputs. The additional uncertainties due to systematic effects will be studied in chapter 7. The correlation coefficient between these two quantities is -0.288.

7

Study of systematic effects and uncertainties

Contents

In this chapter, an extensive study of the possible systematic effects and errors present in the analysis procedure is carried out, estimating the necessary corrections to the value and uncertainty of the final results.

7.1 Signal fit model

7.1.1 Fit model behaviour

In order to check if the fit model produces any biases or undesired effects, 1000 pseudo-experiments are generated and fitted. These pseudo-experiments consist of simulated "real data" samples, generated from the simulated distributions, and therefore they allow us to set the "true" value of the parameters that are being fit, with the purpose of comparing the fit results with their goal value. The "pull" distribution of each fit parameter is then checked for biases and other possible anomalies. All the resulting parameter pull distributions are compatible with a Gaussian distribution of mean zero and $\sigma = 1$, with all 100% of the fits converging successfully; therefore, no corrections or systematic uncertainties are applied. The pull distributions for the two signal yields are shown in fig. 7.1.

7.1.2 Signal model

The $f_{3\pi}^{X}$ and $f_{D^{*+}/D^{*0}}$ parameters are fixed in the signal fit, but these parameters have associated uncertainties, as shown in table 4.11, derived from the uncertainties in the computed efficiencies and in the external branching fractions, as seen in section 4.6. In order to estimate the systematic effects associated with the fixing of these four parameters, a fit is done by letting them float constrained to a Gaussian distribution centered at their central value and a sigma equal to their uncertainty. Then, a second fit is done by

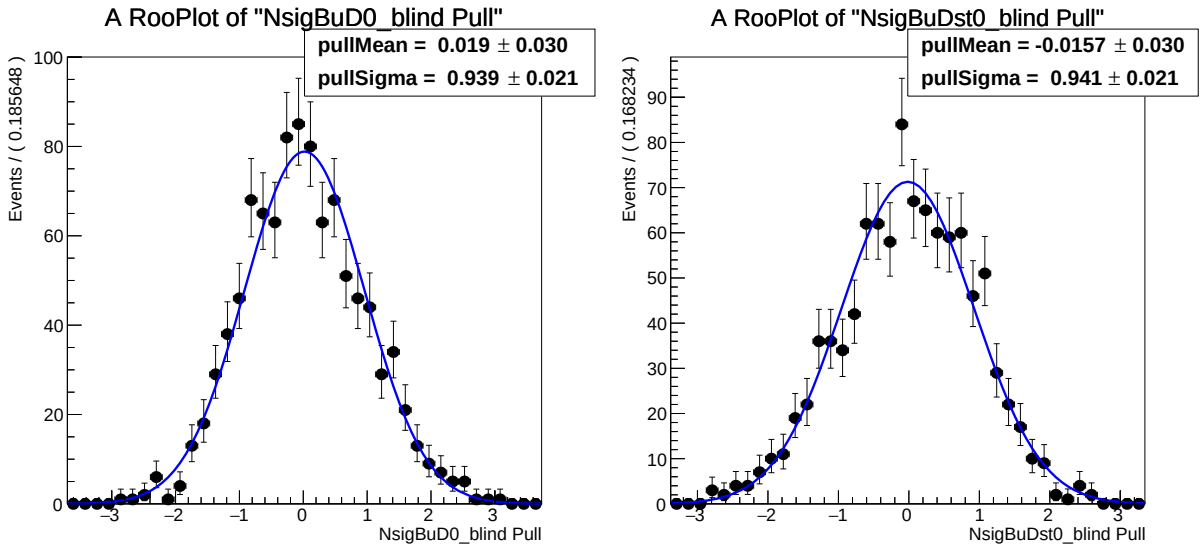

Figure 7.1: Pull distributions of the two signal yield fit parameters, obtained from 1000 pseudo-experiments.

fixing them to the results of the first fit. The quadratic difference between the parameter uncertainties of both fits is assigned as the systematic uncertainty due to this model, as

$$\sigma_f \approx \sqrt{\sigma^2_{\text{constr-}f} - \sigma^2_{\text{fixed-}f}}\ , \tag{7.1}$$

where σ_f is the systematic uncertainty assigned to the fixing of these f parameters in the signal fit, and $\sigma_{\text{constr-}f}$ and $\sigma_{\text{fixed-}f}$ are, respectively, the parameter uncertainties obtained from the fit done by constraining them to a Gaussian distribution and by fixing them to the previous fit's result.

The result obtained with this method is

$$\begin{aligned} \sigma_f(N_{B^-\to D^0\tau^-\overline{\nu}_\tau}) &\approx 87, \\ \sigma_f(N_{B^-\to D^{*0}\tau^-\overline{\nu}_\tau}) &\approx 50, \end{aligned} \tag{7.2}$$

with a correlation factor of -0.912 between the two.

7.1.3 Prompt background model

The prompt $B \to D^0 3\pi(X)$ background component is tuned using the weights obtained from its control-sample fit from section 5.1. These weights have their own uncertainties due to the limited statistics of the data and simulation samples used to compute them, which are not being taken into account in the signal fit. The potential effect of these uncertainties is estimated through an statistical study of the fit by repeating it 10000 times, each time varying the value of the weights by a random amount, given by a Gaussian distribution centered at zero and with a sigma equal to each weight's uncertainty.

Then, the systematic uncertainty due to the prompt weight uncertainties is estimated as

$$\sigma_{\text{prompt}}(N) \approx \sigma(N_{\text{rand.wg.}}), \tag{7.3}$$

where N is the yield parameter given by the nominal fit and $N_{\text{rand.wg.}}$ is the one given by these new fits with modified weights, $\sigma(N_{\text{rand.wg.}})$ denoting its standard deviation, which is extracted from a fit to a Gaussian distribution, shown in fig. 7.2.

By performing 10000 fits with "randomised" weights, the results with this method are

$$\begin{aligned} \sigma_{\text{prompt}}(N_{B^-\to D^0\tau^-\overline{\nu}_\tau}) &\approx 31, \\ \sigma_{\text{prompt}}(N_{B^-\to D^{*0}\tau^-\overline{\nu}_\tau}) &\approx 19, \end{aligned} \tag{7.4}$$

and a correlation between the two yields of -0.896.

7.1.4 Double-charm background models

Both the $B \to \overline{D}^0 D^0(X)$ and $B \to \overline{D}^0 D^+(X)$ background components are implemented in the fit in an analogous way: their shape is pre-tuned using an invariant mass fit in a dedicated control sample (section 5.2) and the total yield of the component is a free

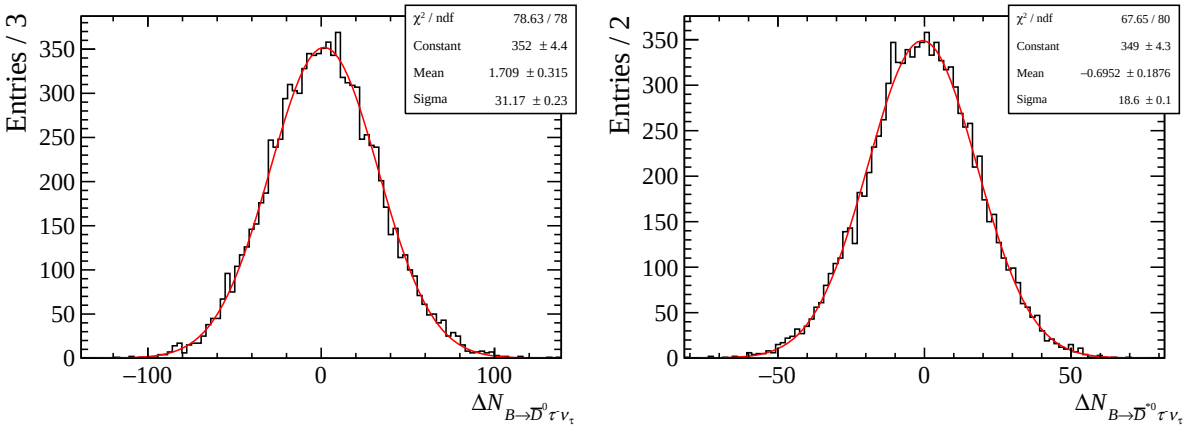

Figure 7.2: Distribution of the difference between the $B^- \to D^0\tau^-\overline{\nu}_\tau$ (left) and $B^- \to D^{*0}\tau^-\overline{\nu}_\tau$ (right) signal yields and their nominal fit results when performing 10000 fits with Gaussian-randomised prompt weights, fitted to a Gaussian distribution.

parameter in the signal fit. Since the q^2 and BDT distributions of these components may not be properly described just with the corrections derived from their control samples, an alternative approach is needed to study the systematic uncertainty of these models' description.

The used method is to introduce extra nuisance parameters in the signal fit which modify the shape of these components, in a similar way as was done with the w_{BDT} parameter used in the fit for the $B \to \overline{D}^0 D_s^+(X)$ components. These parameters are equivalent to a "linear weight" in each component and each dimension, modifying the template shapes as:

$$h_{\text{mod}}(x) = \left(1 + w_x \left(\frac{x - x_{\text{min}}}{x_{\text{max}} - x_{\text{min}}} - \frac{1}{2}\right)\right) h_0(x), \tag{7.5}$$

where $h_{\text{mod}}(x)$ is the new modified template histogram, x is its x-axis (in this case, either q^2 or the BDT output), with x_{min} and x_{max} being its minimum and maximum values; w_x is the nuisance parameter, and $h_0(x)$ is the original template histogram. In this way, w_x can also be viewed as an interpolation device between $h_0(x)$ and two limiting histograms at positive and negative w_x limiting values.

The procedure to estimate the systematic uncertainties due to the $B \to \overline{D}^0 D^0(X)$ and $B \to \overline{D}^0 D^+(X)$ background models can be summarised as follows:

1. Use the corresponding control sample to estimate the expected variance of w_x.

2. Perform many fits introducing the new w_{q^2} and w_{BDT} parameters as fixed values, with their values randomised on each iteration according to a Gaussian distribution with mean zero and variance set to the result of the previous step.

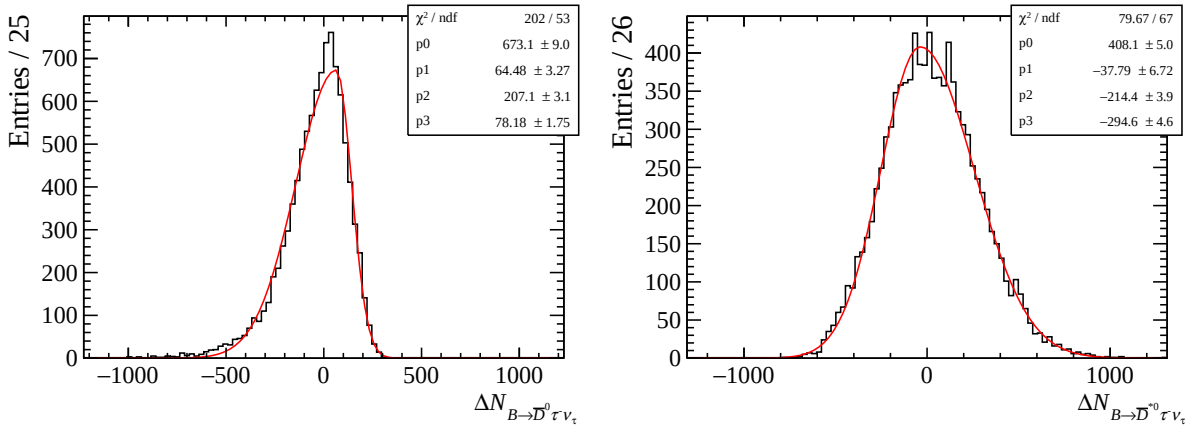

Figure 7.3: Distribution of the difference between the $B^- \to D^0\tau^-\overline{\nu}_\tau$ (left) and $B^- \to D^{*0}\tau^-\overline{\nu}_\tau$ (right) signal yields and their nominal fit results when performing 10000 fits with Gaussian-randomised q^2 and BDT linear weights in the $B \to \overline{D}^0 D^0(X)$ component, fitted to an asymmetrical Gaussian distribution.

3. Check the resulting distributions of the signal yields and extract their variance, which will be taken as the desired systematic uncertainty.

This will be done independently for each of the two components. The $B \to \overline{D}^0 D_s^+(X)$ background component will use a different procedure, as will be described later.

$B \to \overline{D}^0 D^0(X)$ background model

First, in order to estimate the expected variance of w_{q^2}, the ratio of the data and (corrected) simulation q^2 distributions of the $B \to \overline{D}^0 D^0(X)$ control sample is fitted to a function following eq. 7.5. The resulting value is $w_{q^2}^{(\text{control})} = -0.2 \pm 0.02$.

Since the BDT is trained in data with $m(3\pi) < 1600$ MeV/c^2, which is not the case of the control sample, we cannot estimate the value of w_{BDT} in the same way, since it would be unreliable. Instead, we assume that the discrepancies between data and simulation in the BDT distribution will be of the same magnitude as in the q^2 distribution.

Then, ten thousand signal fits are performed. On each one of them, w_{q^2} and w_{BDT} take a random value following a Gaussian distribution with mean zero and $\sigma = |w_{q^2}^{(\text{control})}| = 0.2$. The resulting distributions of the two signal yields are shown in fig. 7.3. Due to the asymmetrical nature of these distributions, they are fitted to asymmetrical Gaussian distributions, from where we extract the estimated systematic uncertainties:

$$\begin{aligned} \sigma_{B \to \overline{D}^0 D^0(X)}(N_{B^- \to D^0\tau^-\overline{\nu}_\tau}) &\approx {}^{+78}_{-207}, \\ \sigma_{B \to \overline{D}^0 D^0(X)}(N_{B^- \to D^{*0}\tau^-\overline{\nu}_\tau}) &\approx {}^{+295}_{-214}, \end{aligned} \tag{7.6}$$

and a correlation between the two yields of -0.359.

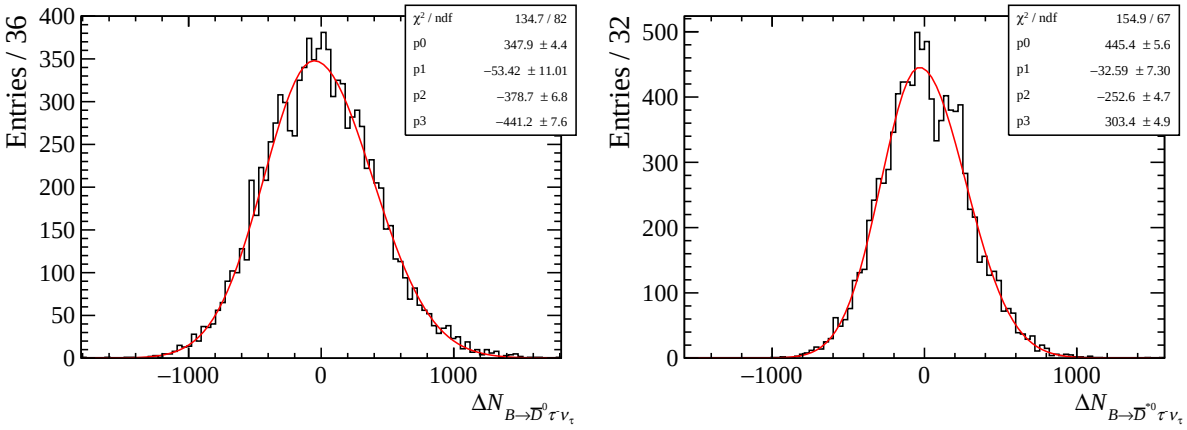

Figure 7.4: Distribution of the difference between the $B^- \to D^0\tau^-\overline{\nu}_\tau$ (left) and $B^- \to D^{*0}\tau^-\overline{\nu}_\tau$ (right) signal yields and their nominal fit results when performing 10000 fits with Gaussian-randomised q^2 and BDT linear weights in the $B \to \overline{D}^0 D^+(X)$ component, fitted to an asymmetrycal Gaussian distribution.

$B \to \overline{D}^0 D^+(X)$ background model

Following the same procedure as with the $B \to \overline{D}^0 D^0(X)$ component, the estimated parameter is $w_{q^2}^{(\text{control})} = -0.23 \pm 0.03$ in this control sample. Again, ten thousand signal fits are performed, setting the values of w_{q^2} and w_{BDT} to a random value following a Gaussian distribution with mean zero and $\sigma = |w_{q^2}^{(\text{control})}| = 0.23$. The resulting distributions of the two signal yields are shown in fig. 7.4. They are fitted to asymmetrical Gaussian distributions, from where we extract the estimated systematic uncertainties:

$$\begin{aligned} \sigma_{B \to \overline{D}^0 D^+(X)}(N_{B^- \to D^0\tau^-\overline{\nu}_\tau}) &\approx {}^{+441}_{-379}, \\ \sigma_{B \to \overline{D}^0 D^+(X)}(N_{B^- \to D^{*0}\tau^-\overline{\nu}_\tau}) &\approx {}^{+303}_{-253}, \end{aligned} \tag{7.7}$$

and a correlation between the two yields of -0.877.

$B \to \overline{D}^0 D_s^+(X)$ background model

The $B \to \overline{D}^0 D_s^+(X)$ background model is not implemented as a single component in the fit, and its multiple components are already allowed to float within the constraints determined in its control sample. This means that the possible discrepancies in q^2 between the control sample and the signal selection are already being taken into account in the signal fit, since the q^2 distribution shape will vary depending on the relative yields of each component. This is not the case of the $B \to D^{*-} D_s^+(X)$ components, though, which are fixed in the fit. To estimate the systematic uncertainty associated with fixing these components, the signal fit is performed by treating them in the same way as the other components (letting them float, but constrained to their control sample results), and then the fit is repeated by fixing them to the result of the first fit. The quadratic difference

between the uncertainties of the two fits is taken as the systematic uncertainty due to fixing these parameters, obtaining

$$\begin{aligned}\sigma_{B \to D^{*-} D_s^+(X)}(N_{B^- \to D^0 \tau^- \overline{\nu}_\tau}) &\approx 180, \\ \sigma_{B \to D^{*-} D_s^+(X)}(N_{B^- \to D^{*0} \tau^- \overline{\nu}_\tau}) &\approx 85,\end{aligned} \tag{7.8}$$

with a correlation factor of -0.983 between the two.

On the other hand, the shape of this component in the BDT dimension is already being modified in the signal fit by allowing the w_{BDT} and $w^{(2)}_{\mathrm{BDT}}$ parameters to float. In order to estimate the systematic uncertainty introduced by these parameters, the fit is repeated once more with their values fixed to the result of the first fit. The quadratic difference between the uncertainties of the two fits is taken as the systematic uncertainty associated with the BDT shape of this model, obtaining

$$\begin{aligned}\sigma_{w_{\mathrm{BDT}}}(N_{B^- \to D^0 \tau^- \overline{\nu}_\tau}) &\approx 1229, \\ \sigma_{w_{\mathrm{BDT}}}(N_{B^- \to D^{*0} \tau^- \overline{\nu}_\tau}) &\approx 611,\end{aligned} \tag{7.9}$$

with a correlation factor of -0.9998 between the two.

These later uncertainties are already part of the signal fit, and so they must be subtracted from the "statistical" part of the yield uncertainty presented in the previous chapter and added to the systematic part.

These two sources of systematic uncertainty are added to obtain the systematic uncertainties due to the $B \to \overline{D}^0 D_s^+(X)$ background model:

$$\begin{aligned}\sigma_{B \to \overline{D}^0 D_s^+(X)}(N_{B^- \to D^0 \tau^- \overline{\nu}_\tau}) &\approx 1242, \\ \sigma_{B \to \overline{D}^0 D_s^+(X)}(N_{B^- \to D^{*0} \tau^- \overline{\nu}_\tau}) &\approx 617.\end{aligned} \tag{7.10}$$

These are clearly dominated by the uncertainty introduced by the w_{BDT} parameters which, as noted in section 6.1.1, will likely be significantly reduced as the sources of discrepancy in the BDT output are being studied and the fit model will be improved accordingly. As such, this systematic uncertainty is expected to decrease considerably before a final result is published.

7.1.5 Template sample size

The limited size of the samples used as templates in the signal fit has proven –in previous analyses– to be one of the larger sources of systematic uncertainties for this kind of analyses. In this section, a statistical study of the fit is performed in order to estimate these effects, and the possible use of the Beeston-Barlow Lite method is analysed.

Statistical study of the fit

In order to estimate the systematic uncertainty due to the limited size of the template samples, we repeat many times the fit, each time varying the bin contents of the simulated

PDFs by a random amount. The new bin content corresponds to a Poisson distribution centered on the effective sample size of each bin, as it was in the original template. The statistical study of the results of these fits provides an estimation of how much the parameter values might change due to the limited size of our template samples. By assuming that the only differences between these parameter distributions and the corresponding result of the original signal fit are due to the template sample size, we can estimate the systematic uncertainty due to template statistics with

$$\sigma_{\text{templates}}(N) \approx \sigma(N_{\text{rand.}}), \tag{7.11}$$

where $\sigma_{\text{templates}}(N)$ is the total systematic uncertainty of the yield parameter due to limited template statistics, $N_{\text{rand.}}$ is the yield parameter given by these new fits performed with Poisson-randomised PDFs, and $\sigma(N_{\text{rand.}})$ denotes its standard deviation, extracted from a fit to a Gaussian distribution, as shown in fig. 7.5.

By performing 10000 of these "Poisson-randomised" fits, the results with this method are

$$\begin{aligned} \sigma_{\text{templates}}(N_{B^-\to D^0\tau^-\overline{\nu}_\tau}) &\approx 1372, \\ \sigma_{\text{templates}}(N_{B^-\to D^{*0}\tau^-\overline{\nu}_\tau}) &\approx 782, \end{aligned} \tag{7.12}$$

with a correlation factor between the two yields of -0.938 and being, as expected, the largest systematic uncertainty in this analysis.

The distributions of these yields are shown in fig. 7.5. Apart from the standard deviation, a bias in the yield value is also observed in both signals:

$$\begin{aligned} \langle \Delta N_{B^-\to D^0\tau^-\overline{\nu}_\tau} \rangle &\equiv \langle N_{\text{rand},B^-\to D^0\tau^-\overline{\nu}_\tau} - N_{B^-\to D^0\tau^-\overline{\nu}_\tau} \rangle \approx 1154, \\ \langle \Delta N_{B^-\to D^{*0}\tau^-\overline{\nu}_\tau} \rangle &\equiv \langle N_{\text{rand},B^-\to D^{*0}\tau^-\overline{\nu}_\tau} - N_{B^-\to D^{*0}\tau^-\overline{\nu}_\tau} \rangle \approx -501. \end{aligned} \tag{7.13}$$

These biases will be taken into account to correct the value of the final results.

Comparison of the fit results with and without the Beeston-Barlow method

The Beeston-Barlow [128] "lite" method (from now on, "BBLite") treats bin statistical uncertainties by introducing a single nuisance parameter per bin that accounts for the overall statistical uncertainty in each bin, so that the shape uncertainties due to the finite number of events in the template samples are included in the likelihood. This means that the total uncertainty provided by the fit already has this systematic uncertainty at least partially included.

As a test, the signal fit is performed using the BBLite method, and the uncertainties provided by this test are compared with those provided by the nominal fit.

First, we assume that the uncertainty of any parameter provided by this BBLite fit, σ_{fit}, can be expressed as

$$\sigma^2_{\text{fit}} = \sigma^2_{\text{BBLite}} + \sigma^2_{\text{rest}} \ , \tag{7.14}$$

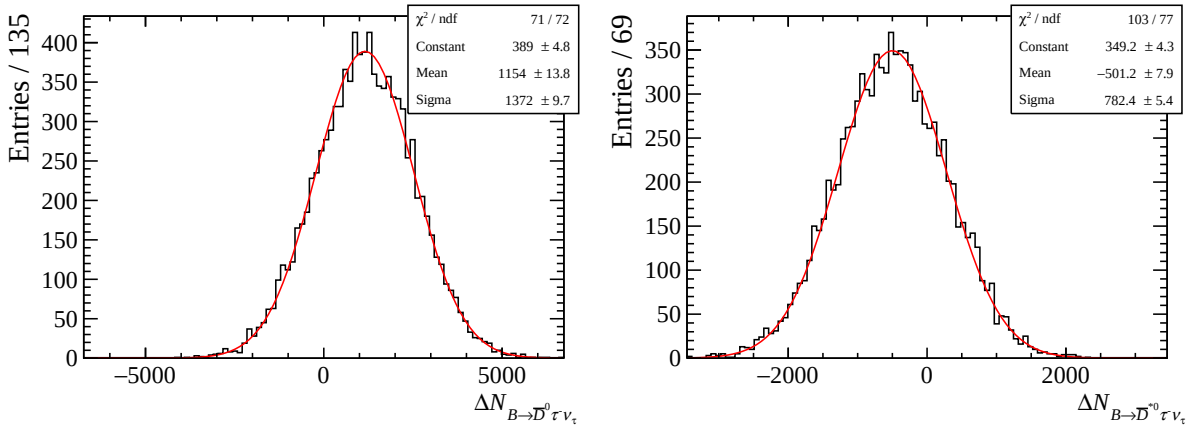

Figure 7.5: Distribution of the difference between the $B^- \to D^0\tau^-\overline{\nu}_\tau$ (left) and $B^- \to D^{*0}\tau^-\overline{\nu}_\tau$ (right) signal yields and their nominal fit results when performing 10000 fits with Poisson-randomised template PDFs, fitted to a Gaussian distribution.

where σ^2_{BBLite} is the variance introduced by the BBLite method due to the template sample size, and σ^2_{rest} is the variance due to all the other sources (which should match with the variance provided by the nominal fit).

After performing the fit with BBLite, the signal fit is run once more, but with the BBLite parameters fixed to the result of the first BBLite fit. Assuming that the parameter variance given by this second fit is a good approximation of the σ^2_{rest} in eq. 7.14, the systematic uncertainty due to template statistics that BBLite takes into account can be estimated as

$$\sigma_{\text{BBLite}} \approx \sqrt{\sigma^2_{\text{fit}} - \sigma^2_{\text{BB fixed}}}\ , \tag{7.15}$$

where $\sigma^2_{\text{BB fixed}}$ is the parameter variance given by this second fit.

In our fits, this provides the results

$$\begin{aligned} \sigma_{\text{BBLite}}(N_{B^-\to D^0\tau^-\overline{\nu}_\tau}) &\approx 820, \\ \sigma_{\text{BBLite}}(N_{B^-\to D^{*0}\tau^-\overline{\nu}_\tau}) &\approx 470. \end{aligned} \tag{7.16}$$

These results show that the systematic uncertainties provided by the BBLite method do not correspond with the full systematic uncertainty due to template statistics, shown in eq. 7.12. This may be due to using the Beeston-Barlow "Lite" method, instead of the full Beeston-Barlow method, which adds a nuisance parameter for each bin and for each template. Both the parameter values and uncertainties provided by this second fit show no noticeable shifts or improvements with respect to the result of the nominal signal fit. Thus, this comparison remains as a simple check, and the values taken as systematic uncertainties are those of eq. 7.12.

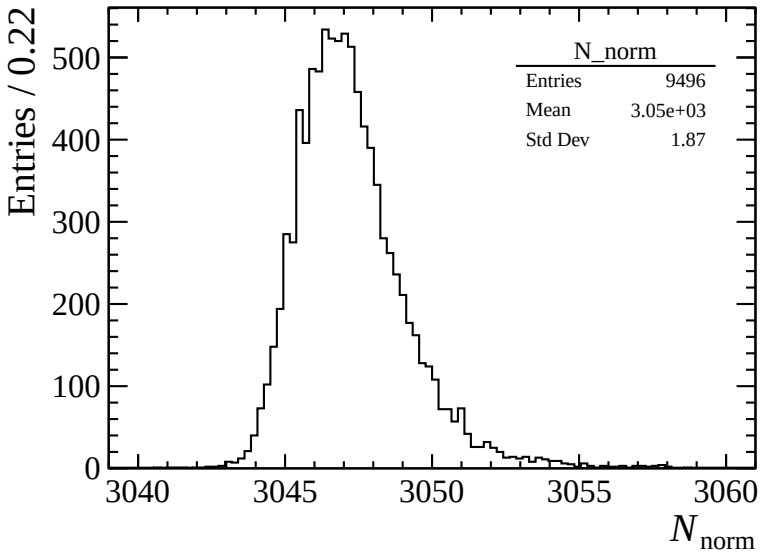

Figure 7.6: Distribution of the normalisation yield extracted from 9496 fits to data, each one with random fixed values for the Crystal Ball tail parameters, according to a Gaussian distribution with center and sigma set to the values and uncertainties extracted from the fit to simulated $B^+ \to \overline{D}^0 D_s^+$ events.

7.2 Normalisation fit model

The procedure for the extraction of the normalisation yield is shown in section 6.2. Some of the parameters of the fit model are fixed to the values obtained in a fit to simulated data. In order to determine the systematic uncertainty associated to this procedure, the fit to data is repeated 10000 times (of which 9496 converged), each time varying the values of the fixed parameters according to Gaussian distributions with center and sigma set to the values and uncertainties extracted from the fit to simulation (table 6.5). The results from these fits for the normalisation yield have a mean of 3047.3 and a standard deviation of 1.9, and their distribution is represented in figure 7.6. This standard deviation is taken as the systematic uncertainty due to the normalisation fit model.

7.3 Not-yet-studied systematic sources

Several possible sources of systematic uncertainties are still to be studied. These sources, explained below, are expected to be of the same magnitude as in similar past LHCb analyses [29, 31, 36], where their assigned uncertainties were all in the 0–3% range relative to the final $R(D^{(*)})$ result, and so they are expected to be almost negligible in comparison to the biggest sources of systematic uncertainty already shown in this chapter.

Selection

The PID variables used in the selection ($P_{\mathrm{NN}}(\pi)$, $P_{\mathrm{NN}}(K)$) have their own uncertainties and it must be studied how they affect the final results. The selection cut in the BDT output is also another possible source of systematic effects, as well as the stripping selection which is performed online during the data-taking process.

Form factors

In section 2.2.2, the construction of the BGL parameterisation for $B \to D^{(*)}\tau^-\overline{\nu}_\tau$ decays is shown. The use of this parameterisation and the limited knowledge of its parameter values must be taken into account to compute their potential systematic effect in the results of the analysis.

$B \to D^{**}\tau^+\nu_\tau$ feeddown

As detailed in section 6.1.2, the feeddown from $B \to D^{**}\tau^+\nu_\tau$ decays is estimated using approximate isospin conservation along with calculations based on experimental results. The used theoretical assumptions, experimental measurements, and selection requirements all should have an associated systematic uncertainty.

8

Results and conclusions

Contents

Following the method for determining the $B^- \to D^{(*)0}\tau^-\overline{\nu}_\tau$ branching fractions and the $R(D^{(*)0})$ ratios described in chapter 6, and applying the corrections obtained in chapter 7 to account for systematic effects and errors, the final results are presented in this chapter, along with the conclusions.

8.1 Results

Branching fractions

For the signal branching fractions, the (blinded) results, including systematic uncertainties and corrections, are

$$\begin{aligned} \mathcal{B}(B^- \to D^0\tau^-\overline{\nu}_\tau) &= (\text{xxx} \pm 0.13\ (\text{stat.}) \pm 0.22\ (\text{syst.}) \pm 0.07\ (\text{ext.})) \times 10^{-2}\ , \\ \mathcal{B}(B^- \to D^{*0}\tau^-\overline{\nu}_\tau) &= (\text{xxx} \pm 0.11\ (\text{stat.})\ ^{+0.15}_{-0.14}\ (\text{syst.}) \pm 0.15\ (\text{ext.})) \times 10^{-2}\ , \end{aligned} \tag{8.1}$$

with a correlation factor of -0.486 between the two quantities. The total uncertainties are 2.7×10^{-3} and 2.4×10^{-3}, respectively.

Systematic source	Relative uncertainty w.r.t. $R(D^0)_{\mathrm{SM}}$ (%)
Templates' sample size	23.09
Double-charm background models	$^{+22.22}_{-22.13}$
$B \to \overline{D}^0 D_s^+(X)$ background model	20.90
$B \to \overline{D}^0 D^+(X)$ background model	$^{+7.42}_{-6.38}$
$B \to \overline{D}^0 D^0(X)$ background model	$^{+1.31}_{-3.48}$
Prompt background model	0.52
Signal model	1.46
Efficiencies	0.59
Normalisation fit model	0.07
Total	$^{+32.09}_{-32.02}$

Table 8.1: Relative uncertainty for each systematic source with respect to the $R(D^0)_{\mathrm{SM}}$ theoretical prediction [34].

These results can be compared with the existing measurements found in [2],

$$\begin{aligned} \mathcal{B}(B^- \to D^0 \tau^- \overline{\nu}_\tau) &= (7.7 \pm 2.5) \times 10^{-3} \ , \\ \mathcal{B}(B^- \to D^{*0} \tau^- \overline{\nu}_\tau) &= (1.88 \pm 0.20) \times 10^{-2} \ , \end{aligned} \tag{8.2}$$

where it can be seen that the measurements done in this work are at the same level of precision as the existing measurements.

LFU ratios

For the desired LFU ratios, the (blinded) results, including systematic uncertainties and corrections, are

$$\begin{aligned} R(D^0) &= \mathrm{xxx} \pm 0.056 \ (\mathrm{stat.}) \pm 0.096 \ (\mathrm{syst.}) \pm 0.034 \ (\mathrm{ext.}) \ , \\ R(D^{*0}) &= \mathrm{xxx} \pm 0.020 \ (\mathrm{stat.}) \pm 0.026 \ (\mathrm{syst.}) \pm 0.029 \ (\mathrm{ext.}) \ , \end{aligned} \tag{8.3}$$

with a correlation factor of -0.471 between the two quantities. The total uncertainties are 0.12 and 0.044, respectively. A summary of all the sources of systematic uncertainty is shown in tables 8.1 and 8.2.

These results can be compared with the existing measurements shown in table 2.2, where it can be seen that the precision of $R(D^0)$ obtained in this work is slightly worse, but of similar magnitude, as the existing measurements; while the precision of $R(D^{*0})$ is very similar to the existing ones. A visual summary of this comparison is shown in fig. 8.1.

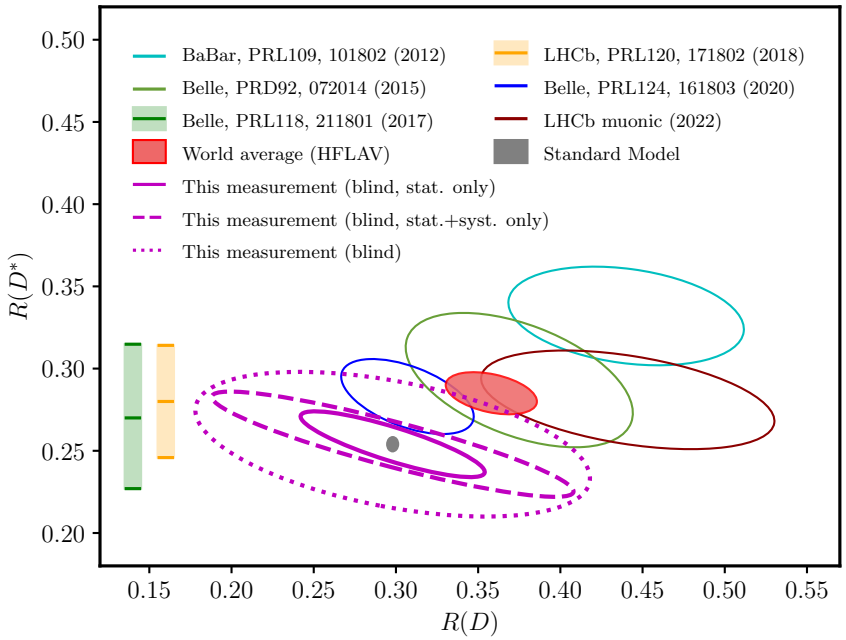

Figure 8.1: Current status of $R(D)$ and $R(D^*)$ measurements, with this measurement included for comparison. Each ellipse represents a combined $R(D^{(*)})$ measurement, with its contour representing its uncertainties and its tilt their correlation. The $R(D^{(*)0})$ measurement from this thesis is shown in purple (centered at the SM value because of the blinding), with the continuous line representing the measurement with only the statistical uncertainties, the dashed line representing the measurement with also systematic uncertainties, and the dotted line representing the full uncertainties. External uncertainties are expected to be reduced over the years, while the systematic uncertainties will also presumably reduce slightly before publication.

Systematic source	Relative uncertainty w.r.t. $R(D^{*0})_{\text{SM}}$ (%)
Templates' sample size	7.50
Double-charm background models	$^{+7.17}_{-6.71}$
$B \to \overline{D}^0 D_s^+(X)$ background model	5.91
$B \to \overline{D}^0 D^+(X)$ background model	$^{+2.91}_{-2.43}$
$B \to \overline{D}^0 D^0(X)$ background model	$^{+2.83}_{-2.05}$
Prompt background model	0.18
Signal model	0.48
Efficiencies	0.46
Normalisation fit model	0.06
Total	$^{+10.40}_{-10.09}$

Table 8.2: Relative uncertainty for each systematic source with respect to the $R(D^{*0})_{\text{SM}}$ theoretical prediction [34].

A more precise result can be obtained by adding the two signal channels together, taking advantage of their negative correlation. A new quantity, $R(D^0 \vee D^{*0})$, could be defined as

$$R(D^0 \vee D^{*0}) \equiv \frac{\mathcal{B}(B^- \to D^0 \tau^- \overline{\nu}_\tau) + \mathcal{B}(B^- \to D^{*0} \tau^- \overline{\nu}_\tau)}{\mathcal{B}(B \to D^0 \ell^- \overline{\nu}_\ell) + \mathcal{B}(B \to D^{*0} \ell^- \overline{\nu}_\ell)}, \tag{8.4}$$

where, again, ℓ^- refers to either a μ^- or an e^- lepton, and which, with our results (eq. 8.1) and the $B \to D^{(*)0} \ell^- \bar{\nu}_\ell$ branching fractions measured by [2] (eq. 6.15), takes the value

$$R(D^0 \vee D^{*0}) = \text{xxx} \pm 0.009 \text{ (stat.)} \pm 0.013 \text{ (syst.)} \pm 0.030 \text{ (ext.)}, \tag{8.5}$$

with a total uncertainty of 0.033. Using this quantity clearly reduces the statistical and systematic uncertainties, with the external uncertainty dominating over them.

8.2 Conclusions and prospects

In this thesis, data from proton-proton collisions at the LHC with a centre-of-mass energy of 13 TeV collected in the years 2016–2018 by the LHCb detector has been analysed in order to study $B \to D^{(*)} \tau^- \overline{\nu}_\tau$ decays, reconstructed in the $\tau^- \to \pi^- \pi^+ \pi^- (\pi^0) \nu_\tau$ channel, and their possible role in discovering physics beyond the Standard Model.

The analysis of these data is at a preliminary status, with the nominal value of the results still blinded to avoid human bias during the analysis.

The $B^- \to D^{(*)0} \tau^- \overline{\nu}_\tau$ branching fractions have been measured to be

$$\begin{aligned}\mathcal{B}(B^- \to D^0\tau^-\overline{\nu}_\tau) &= (\text{xxx} \pm 0.13\ (\text{stat.}) \pm 0.22\ (\text{syst.}) \pm 0.07\ (\text{ext.})) \times 10^{-2}\ , \\ \mathcal{B}(B^- \to D^{*0}\tau^-\overline{\nu}_\tau) &= (\text{xxx} \pm 0.11\ (\text{stat.})\ ^{+0.15}_{-0.14}\ (\text{syst.}) \pm 0.15\ (\text{ext.})) \times 10^{-2}\ ,\end{aligned} \tag{8.6}$$

with a correlation factor of -0.486 between the two quantities; while the $R(D^{(*)0})$ LFU ratios have been measured to be

$$\begin{aligned}R(D^0) &= \text{xxx} \pm 0.056\ (\text{stat.}) \pm 0.096\ (\text{syst.}) \pm 0.034\ (\text{ext.})\ , \\ R(D^{*0}) &= \text{xxx} \pm 0.020\ (\text{stat.}) \pm 0.026\ (\text{syst.}) \pm 0.029\ (\text{ext.})\ ,\end{aligned} \tag{8.7}$$

with a correlation factor of -0.471 between the two quantities.

At the time of writing this thesis, this $R(D^{(*)0})$ analysis is in its final steps before being submitted for group review within the LHCb collaboration, after which it will be "unblinded", revealing the nominal value of the obtained results, and eventually published.

The main contributions from this thesis to the analysis have been the corrections to simulation (section 4.5), the studies of the double-charm and prompt background channels and their resulting corrections (chapter 5), the optimisation of the signal fit, the normalisation fit, the computing of the results (chapter 6), and the study of systematic effects and uncertainties and their employment in the final results (chapter 7).

In the near future, before publication, the systematic uncertainty of the results is expected to be reduced by implementing improvements to the analysis strategy to account for discrepancies between the model and the real data. The work presented in this thesis has been essential to discover and analyse the impact of those discrepancies and therefore offer a chance to correct them. It should also be noted that, since the results are blinded, the uncertainties presented here were computed as if the results matched with the SM predictions, meaning that they are expected to vary slightly when computing them with the real unblinded values.

In the more distant future, the statistical uncertainty will be reduced in future analyses with more data, particularly with the large amounts of data expected from LHC's Run 3. The external uncertainty is also expected to improve over the years as newer and more precise measurements are performed by the particle physics community. The systematic uncertainty of future analyses will also presumably decrease as better and faster simulation techniques allow to produce larger samples and the understanding of the background contributions improves.

In parallel, some base work for a future $R(D^{(*)-})$ measurement is also presented within this thesis, namely the selection of data (section 4.3) and the study of control samples (chapter 5), along with all the methods developed for the $R(D^{(*)0})$ analysis that will set the basis for the ones that will be used in the $R(D^{(*)-})$ analysis, if not directly re-used. This second analysis is planned to be fully carried out after completing the $R(D^{(*)0})$ analysis, and it is expected to provide a similar level of precision.

Summarising, the analyses presented within this thesis will offer an important contribution to the long-standing anomalies in the $R(D^{(*)})$ LFU ratios, offering the first

measurement of $R(D)$ using hadronic τ decays by LHCb, and presumably improving the global state of searches for New Physics in the Lepton Flavour Universality sector.

A

Resumo da tese en galego

Contents

A.1 Fundamentos, motivación, e obxectivos

O Modelo Estándar é un marco teórico que describe as partículas fundamentais e as súas interaccións a través de tres forzas fundamentais: as forzas eletromagnética, nuclear feble, e nuclear forte. O Modelo Estándar foi extremadamente exitoso na predición e explicación dun amplo rango de resultados experimentais en física de partículas, incluíndo o descubrimento do bosón de Higgs en 2012 no Gran Colisionador de Hadróns (LHC), unha das validacións máis importantes e recentes do Modelo Estándar, que representou a culminación de décadas de traballo teórico e experimental. Con todo, sábese que o Modelo Estándar é incompleto, xa que non incorpora a gravidade nin ten en conta a materia escura, a cal se cre que compón unha parte significante da masa total do universo. Por iso, a investigación actual en física de partículas está centrada en poñer a proba as predicións do Modelo Estándar e explorar nova física máis aló del, co obxectivo de comprender mellor o universo nas escalas máis pequenas.

Esta tese contén o meu traballo en dúas análises actuais do experimento LHCb, que procuran esclarecer as recentes tensións entre o Modelo Estándar e os resultados experimentais sobre a propiedade chamada Universalidade Leptónica de Sabor (LFU, nas súas siglas en inglés). Múltiples experimentos, incluíndo BaBar e Belle xunto con LHCb, traballaron e están a traballar en probar a validez da Universalidade Leptónica e, na última década, a tensión entre experimentos e teoría mantívose aproximadamente ao redor de 2–3 desviacións estándar en varias das cantidades medidas, o que suxire a existencia de novos efectos físicos. Estas "anomalías" motivaron á comunidade de física de partículas a estudar de preto as súas posibles explicacións e a medilas con precisión, coa esperanza de atopar unha ruptura no Modelo Estándar.

As análises presentadas nesta tese son dúas da mesma natureza. A principal, a partir de agora referida como análise $R(D^{(*)0})$, ten como obxectivo medir simultaneamente as cantidades $R(D^0)$ e $R(D^{*0})$, cocientes de taxas de desintegración definidos como

$$R(D^{(*)0}) \equiv \frac{\mathcal{B}(B^- \to D^{(*)0}\tau^-\overline{\nu}_\tau)}{\mathcal{B}(B^- \to D^{(*)0}\ell^-\bar{\nu}_\ell)}, \tag{A.1}$$

onde ℓ^- representa ou un electrón ou un muón.

Esta medida faise no canal hadrónico $\tau^- \to \pi^-\pi^+\pi^-(\pi^0)\nu_\tau$, e sería a primeira medida de $R(D)$ no canal hadrónico polo experimento LHCb. A segunda análise é dos cocientes $R(D^{(*)-})$, definidos dun xeito análogo e co mesmo obxectivo, polo que ambas análises proporcionan resultados independentes e complementarios. Debido á inmensa semellanza entre as dúas análises, os algoritmos e métodos desenvolvidos para unha poden ser reutilizados para a outra, razón pola cal a segunda ($R(D^{(*)-})$) está nunha fase moito máis inicial e só se discute de forma breve e parcial nesta tese.

A.2 O experimento LHCb

O LHC é actualmente o acelerador de partículas máis grande e potente do mundo, localizado no CERN, preto de Xenebra, Suíza. O LHC é unha ferramenta clave no estudo da física de partículas e é central nos contínuos esforzos para probar e validar as predicións do Modelo Estándar, principalmente o comportamento das partículas e forzas fundamentais a moi altas enerxías e a procura de novas partículas máis aló do Modelo Estándar, incluída a procura de materia escura. Este colisionador é usado para acelerar dous feixes de protóns a altas enerxías para facelos colidir de fronte. Estas colisións producen unha ampla variedade de partículas subatómicas, as cales poden ser detectadas e analizadas por detectores sofisticados que rodean os puntos de colisión. O LHCb é un dos principais experimentos localizados no LHC e proporciona o marco experimental para esta tese.

O detector LHCb [94] é un espectrómetro cunha configuración "cara adiante", é dicir, detectando as partículas producidas a baixos ángulos con respecto ao raio de protóns do LHC. Esta configuración está deseñada para optimizar a medida de desintegracións de hadróns con quarks b.

O detector LHCb consiste nunha serie de subdetectores que cumpren diferentes funcións na toma de datos, estes poden dividirse segundo dúas funcionalidades principais: reconstrucción de trazas (os subdetectores que detectan as posicións e tempo nos que as partículas interactúan con eles, para así reconstruír a súa traxectoria) e identificación de partículas (os subdetectores que, segundo como as partículas interactúan con eles, identifican de que tipo se tratan). Ademais, un potente imán sitúase no medio do detector, deseñado para desviar a traxectoria das partículas segundo a súa relación carga-masa e así facilitar a súa identificación.

De forma complementaria a todo isto, cómpre mencionar dúas compoñentes adicionais: o seu sistema de *trigger*, unha combinación de *hardware* e de *software* que permite seleccionar só unha pequena porción dos datos medidos, descartando unha gran cantidade de eventos ordinarios non interesantes e permitindo aforrar espazo de almacenamento; e o seu sistema de simulación, o cal simula os eventos físicos que teñen lugar no detector e a resposta deste ás partículas xeradas neles, permitindo así contar con mostras simuladas das desintegracións máis importantes para a análise e comprender mellor os datos reais.

Durante o periodo de toma de datos usado no traballo desta tese (2016–2018), as colisións protón-protón tiñan unha enerxía no centro de masas de $\sqrt{s} = 13$ TeV, e recolectouse unha cantidade de datos correspondente a unha luminosidade integrada de 5.4 fb^{-1}.

A.3 Metodoloxía da análise de datos

Como se discutiu anteriormente, o principal obxectivo desta tese é a medida das cantidades $R(D^0)$ e $R(D^{*0})$ (ec. A.1) con datos tomados en LHCb en 2016–2018, e cas seguintes canles de desintegración:

$$\begin{aligned} D^{*0} &\to D^0\{\pi^0, \gamma\}, \\ D^0 &\to K^-\pi^+, \\ \tau^- &\to \pi^-\pi^+\pi^-(\pi^0)\nu_\tau. \end{aligned}$$

O denominador na ecuación A.1, $\mathcal{B}(B^- \to D^{(*)0}\ell^-\bar{\nu}_\ell)$, é tomado dunha fonte externa [2], mentres que o numerador, $\mathcal{B}(B^- \to D^{(*)0}\tau^-\overline{\nu}_\tau)$, é calculado a partir da nosa medida como

$$\begin{aligned} \mathcal{B}(B^- \to D^{(*)0}\tau^-\overline{\nu}_\tau) = \frac{N_{B^-\to D^{(*)0}\tau^-\overline{\nu}_\tau}}{N_{B^+\to\overline{D}^0 D_s^+}} \times \mathcal{B}(B^+ \to \overline{D}^0 D_s^+)\times \\ \times \frac{\varepsilon_{B^+\to\overline{D}^0 D_s^+}\mathcal{B}(D_s^+ \to \pi^+\pi^-\pi^+)}{\varepsilon^{\tau\to 3\pi\nu_\tau}_{B^-\to D^{(*)0}\tau^-\overline{\nu}_\tau}\mathcal{B}(\tau^- \to \pi^-\pi^+\pi^-\nu_\tau) + \varepsilon^{\tau\to 3\pi\pi^0\nu_\tau}_{B^-\to D^{(*)0}\tau^-\overline{\nu}_\tau}\mathcal{B}(\tau^- \to \pi^-\pi^+\pi^-\pi^0\nu_\tau)}, \end{aligned} \quad \text{(A.2)}$$

onde N son os números de eventos medidos en cada canle de desintegración e ε, as súas eficiencias. Os números de eventos son as cantidades reais que se miden nos datos, mentres que as eficiencias estímanse a partir das mostras simuladas. Todas as demais taxas de

desintegración son tomadas de fontes externas. Esta estratexia permite minimizar as incertezas sistemáticas medindo o cociente entre dúas canles de desintegración co mesmo estado final visible e mesma topoloxía ($B^- \to D^{(*)0}\tau^-\overline{\nu}_\tau$ con $\tau^- \to \pi^-\pi^+\pi^-(\pi^0)\nu_\tau$ e $B^+ \to \overline{D}^0 D_s^+$ con $D_s^+ \to \pi^+\pi^-\pi^+$). $B^+ \to \overline{D}^0 D_s^+$ foi escollido como canle de normalización debido á precisión coa que está medido [2] comparado con outros posibles candidatos como $B^- \to D^0\pi^-\pi^+\pi^-$.

A estratexia da análise de datos pode ser resumida nos seguintes pasos:

1. **Xeración de mostras de datos simulados**: prodúcense varias mostras simuladas que conteñen as principais canles de sinal e de ruído de fondo. Estas son usadas principalmente para calcular eficiencias e para estudar e optimizar a descrición das canles de fondo.

2. **Selección dos datos**: eventos inclusivos $B \to D^0\pi^-\pi^+\pi^-(X)$, con $D^0 \to K^-\pi^+$, son seleccionados dos datos dispoñibles de 2016–2018 e das mostras simuladas. Os diferentes requerimentos impostos na selección de datos ("cortes") poden resumirse nos seguintes pasos:

   - Primeiro, unha serie de cortes básicos son usados para limpar os datos de eventos indesexados. Estes inclúen requerir que os tres pións cargados formen un vértice compatible cun leptón τ, e que os tres pións e o mesón D^0 formen un vértice compatible cun mesón B.
   - Requérese que o vértice do B estea ben diferenciado do vértice dos tres pións (que forma o τ), para así descartar a maior parte dos eventos *prompt*, nos que os pións proceden directamente do B, sen partículas intermedias.
   - Requérese que non haxa máis trazas de partículas provintes dos vértices do B e do τ das que se espera que haxa nas canles de desintegración de sinal.
   - Sepáranse os datos en dúas mostras independentes, unha de sinal, optimizada para desintegracións $B^- \to D^{(*)0}\tau^-\overline{\nu}_\tau$, e outra de normalización, optimizada para $B^+ \to \overline{D}^0 D_s^+$.
   - Unha árbore de decisión (*Boosted Decision Tree*, BDT) é implementada para discriminar o sinal das principais canles de fondo restantes despois da selección, as cales son as chamadas *double-charm*, por conter dous mesóns D, sendo as principais as $B \to \overline{D}^0 D_s^+(X)$.

3. **Optimización das mostras simuladas**: unha serie de correccións é aplicada ás mostras simuladas para mellorar a súa descrición dos datos reais. Estas correccións son calculadas, principalmente, comparando as distribucións das mostras simuladas coas de datos reais nas variables que se sabe que non están correctamente descritas, e aplicando pesos nesas variables para facer que as distribucións coincidan cos datos reais. As correccións aplicadas resúmense en:

- A ferramenta `PIDCalib` [119] é usada para corrixir a simulación nas variables de identificación de partículas que son usadas na selección, facendo así que as súas distribucións coincidan coas dos datos reais.
- Unha serie de correccións é aplicada para conseguir a correcta descrición das variables Δz (distancia no eixo z entre os vértices de desintegración do mesón B e do τ) e δz (a anterior distancia dividida entre a súa incerteza). Esta última variable é usada na selección para separar os eventos de sinal dos eventos *prompt*. Para calcular estas correccións, compáranse as distribucións das incertezas na posición dos vértices con respecto ás súas respectivas masas invariantes, e realízase un axuste liñal para atopar as correccións precisas en función da masa. Unha corrección adicional é aplicada para os datos de 2016, no cal se sabe que a resolución dos vértices é distinta que nos outros anos de toma de datos: a distribución de δz é axustada aos datos usando unha distribución Gaussiana dobre.
- Outra nova serie de correccións é aplicada ás variables de multiplicidade (número de trazas e número de graos de liberdade do vértice primario), ás variables cinemáticas do B (momento transversal e pseudorapidez), e ás eficiencias do *trigger*. Estas correccións calcúlanse comparando directamente as distribucións nesas variables entre simulación e datos, atopando así os pesos que aplicar á simulación para facer que describa mellor os datos reais.
- Por último, a ferramenta HAMMER [120] é usada para corrixir os modelos teóricos usados na simulación, adaptando as mostras simuladas ao marco teórico usado na análise de datos.

4. **Cálculo das eficiencias**: as mostras de simulación son usadas para calcular a eficiencia de cada canle, é dicir, a porción de eventos que pasan todo o proceso de selección con respecto ao número de eventos producidos.

5. **Estudo de mostras de control**: unha serie de mostras de datos complementarias, seleccionadas para conter as principais canles de fondo, son usadas para describir correctamente as mostras simuladas nesas canles. Estas son:

   - As canles *double-charm* ($B \to \overline{D}^0 D_s^+(X)$, $B \to \overline{D}^0 D^+(X)$, e $B \to \overline{D}^0 D^0(X)$). Estas son as principais canles de fondo presentes na selección final. Selecciónanse mostras de control requerindo a reconstrución do mesón D correspondente a partir dos tres pións presentes na selección nominal ($D_s^+ \to 3\pi$, $D^+ \to K^- 2\pi^+$, ou $D^0 \to K3\pi$), e realízase un axuste á masa invariante do mesón B para obter as proporcións de cada unha das canles individuais que contribúen a estes fondos. Estas proporcións son logo usadas para mellorar o fit de sinal.
   - As canles *prompt* ($B \to D^0 3\pi(X)$). A segunda fonte principal de ruído. Selecciónase unha mostra de control requerindo que o vértice dos tres pións sexa

cercano ao vértice do mesón B, e calcúlanse pesos nas variables de q^2 e de BDT para facer que a mostra simulada coincida cos datos reais nesas variables.

- As canles de desintegración $D_s^+ \to 3\pi(X)$, as cales é importante ter ben descritas na simulación xa que o principal fondo provén das canles $B \to \overline{D}^0 D_s^+(X)$. Selecciónanse múltiples mostras complementarias enriquecidas con distintas canles resonantes e realízase un axuste simultáneo a todas elas, obtendo así as proporcións relativas de cada unha das canles, as cales son usadas para corrixir as mostras simuladas.

6. **Determinación do número de eventos de sinal**: un axuste tridimensional en q^2, tempo de desintegración do τ, e o valor dado pola BDT é usado para extraer o número de eventos das canles de sinal presentes na mostra de datos. Neste axuste, cada unha das principais canles de desintegración é modelada en base ás mostras de datos simulados corrixidos, obtendo un total de 24 compoñentes. Os fondos combinatorios (desintegracións que son incorrectamente reconstruídas e pasan a selección) son fixados baseándose nas súas distribucións en mostras de datos. Ademais, a relación entre algunhas das compoñentes é usada para reducir o número de graos de liberdade do fit ata 13. Dous parámetros adicionais son engadidos para permitir variar a forma das canles $B \to \overline{D}^0 D_s^+(X)$ na variable de BDT, a cal se sabe que non está ben descrita. A información obtida da mostra de control de $B \to \overline{D}^0 D_s^+(X)$ é usada para restrinxir os seus correspondentes parámetros. Desta forma obtéñense os números de eventos de cada unha das canles, incluíndo as de sinal que nos interesa medir: $B^- \to D^0 \tau^- \overline{\nu}_\tau$ e $B^- \to D^{*0} \tau^- \overline{\nu}_\tau$.

7. **Determinación do número de eventos de normalización** (section 6.2): un axuste unidimensional á masa invariante $m(\overline{D}^0 D_s^+)$ no pico de masa do mesón B é usado para extraer o número de eventos da canle de normalización ($B^+ \to \overline{D}^0 D_s^+$) presentes nos datos. Debido ao gran illamento desta canle, o modelo de axuste é relativamente simple, en comparación co axuste de sinal: unha distribución Crystal Ball para o pico de masas xunto a unha exponencial decrecente para o ruído de fondo.

8. **Estudo de efectos sistemáticos e incertezas**: as diferentes posibles fontes de erros e efectos sistemáticos son estudadas para determinar as correccións necesarias aos valores e incertezas dos resultados anteriores. Os principais efectos sistemáticos son:

   - A estadística limitada das mostras simuladas. Xa que o axuste de sinal se realiza con distribucións obtidas da simulación, o número limitado de eventos que se produciron é un factor limitante para a calidade desas distribucións. Estímase este efecto no resultado repetindo o axuste de sinal con distribucións alternativas variando as distribucións en base ao seu erro estadístico. Atópase

así que a incerteza sistemática introducida por este efecto está no 23% para $R(D^0)$ e no 7.5% para $R(D^{*0})$.

- O modelo das canles de fondo *double-charm*. A pesar de usar mostras de control dedicadas para describir estas canles, o seu modelo no axuste de sinal, e particularmente a súa distribución na variable de BDT, proba ser un dos efectos sistemáticos máis grandes. Estímase a súa magnitude facendo variar as distribucións destes modelos en base ás discrepancias atopadas nas mostras de control, e estudando o comportamento do axuste de sinal ao fixar os parámetros que afectan a estes modelos. Atópase así que a incerteza sistemática introducida por este efecto está no 22% para $R(D^0)$ e 7% para $R(D^{*0})$.

9. **Medida das taxas de desintegración $B^- \to D^{(*)0}\tau^-\overline{\nu}_\tau$ e dos cocientes $R(D^0)$ e $R(D^{*0})$**: finalmente, todos os resultados obtidos combínanse coas fontes externas para calcular as cantidades desexadas, tal e como se explicou anteriormente, e estas son corrixidas tendo en conta os efectos sistemáticos estudados no paso anterior.

Debido a que a análise aínda está en estado preliminar, pendente de ser revisada pola colaboración LHCb, os resultados obtidos son "cegados" durante todo o proceso, impedindo coñecer a súa magnitude e así evitando posibles sesgos no desenvolvemento da análise.

Ademais desta medida de $R(D^{(*)0})$, tamén está plantexada unha medida análoga de $R(D^{(*)-})$, a cal seguirá practicamente a mesma estratexia, coas únicas diferenzas procedendo das distintas canles de desintegración, sendo as canles de sinal $B^0 \to D^{(*)-}\tau^+\nu_\tau$ con

$$\begin{aligned} D^{*-} &\to D^-\{\pi^0, \gamma\}, \\ D^- &\to K^+\pi^-\pi^-, \\ \tau^+ &\to \pi^+\pi^-\pi^+(\pi^0)\overline{\nu}_\tau; \end{aligned}$$

precisando así unha selección de datos lixeiramente diferente.

Esta segunda análise deixouse nun segundo plano, coa intención de primeiro perfeccionar a medida de $R(D^{(*)0})$ e despois transferir directamente os algoritmos desenvolvidos e optimizados a esta nova medida, minimizando así o tempo e traballo requeridos.

A.4 Resultados e conclusións

Os resultados (cegados) obtidos para as taxas de desintegración foron

$$\begin{aligned} \mathcal{B}(B^- \to D^0\tau^-\overline{\nu}_\tau) &= (\text{xxx} \pm 0.13\ (\text{stad.}) \pm 0.22\ (\text{sist.}) \pm 0.07\ (\text{ext.})) \times 10^{-2}\ , \\ \mathcal{B}(B^- \to D^{*0}\tau^-\overline{\nu}_\tau) &= (\text{xxx} \pm 0.11\ (\text{stad.})\ ^{+0.15}_{-0.14}\ (\text{sist.}) \pm 0.15\ (\text{ext.})) \times 10^{-2}\ , \end{aligned} \tag{A.3}$$

onde as primeiras incertezas son estadísticas (debido á cantidade de datos), as segundas son debido a efectos sistemáticos, e as terceiras debido ás incertezas das medidas externas. Estas dúas cantidades teñen un factor de correlación de -0.486. As súas incertezas totais son, respectivamente, 2.7×10^{-3} e 2.4×10^{-3}. Estes resultados poden ser comparados coas medidas existentes recopiladas en [2],

$$\begin{aligned} \mathcal{B}(B^- \to D^0 \tau^- \overline{\nu}_\tau) &= (7.7 \pm 2.5) \times 10^{-3} \ , \\ \mathcal{B}(B^- \to D^{*0} \tau^- \overline{\nu}_\tau) &= (1.88 \pm 0.20) \times 10^{-2} \ , \end{aligned} \tag{A.4}$$

onde pode verse que as medidas realizadas nesta tese teñen o mesmo nivel de precisión que as xa existentes.

Para os cocientes de Universalidade Leptónica, os resultados obtidos son

$$\begin{aligned} R(D^0) &= \text{xxx} \pm 0.056 \ (\text{stat.}) \pm 0.096 \ (\text{syst.}) \pm 0.034 \ (\text{ext.}) \ , \\ R(D^{*0}) &= \text{xxx} \pm 0.020 \ (\text{stat.}) \pm 0.026 \ (\text{syst.}) \pm 0.029 \ (\text{ext.}) \ , \end{aligned} \tag{A.5}$$

cun factor de correlación de -0.471 entre as dúas cantidades. As súas incertezas totais son 0.12 and 0.044, respectivamente. Estes resultados son comparados coas medidas existentes na figura A.1, onde pode verse que a precisión obtida para $R(D^0)$ é lixeiramente peor, pero de magnitude similar, á das medidas existentes; mentres que a precisión obtida para $R(D^{*0})$ é parecida á das existentes.

No momento de escritura desta tese, esta análise de $R(D^{(*)0})$ atópase na súa fase final antes de ser revisada pola colaboración LHCb, despois do cal revelarase o seu resultado e será publicado.

No futuro próximo, antes de publicarse, a incerteza sistemática destes resultados será reducida implementando melloras á estratexia de análise para reducir a discrepancia entre o modelo e os datos reais. O traballo realizado para esta tese foi esencial para descubrir e analizar o impacto destas discrepancias, e así permitir corrixilas.

Nun futuro máis distante, as incertezas estadísticas poderán ser reducidas en futuras análises grazas ás grandes cantidades de datos que se esperan tomar nos próximos anos en LHC. As incertezas externas tamén mellorarán ao longo dos anos segundo novas medidas máis precisas sexan realizadas pola comunidade. As incertezas sistemáticas tamén se espera que melloren grazas a novas técnicas de simulación máis rápidas que permitan dispor de máis datos simulados e grazas a entender mellor as contribucións das canles de fondo.

En paralelo a esta medida de $R(D^{(*)0})$, algúns dos fundamentos para a futura medida de $R(D^{(*)-})$ tamén foron realizados durante o traballo desta tese, principalmente a selección de datos e o estudo de mostras de control das principais canles de fondo, así como todos os métodos e algoritmos desenvolvidos para a medida de $R(D^{(*)0})$ que poderán ser adaptados, senón reutilizados, para esta nova medida. A precisión esperada en $R(D^{(*)-})$ é similar á obtida para $R(D^{(*)0})$.

En conclusión, a análise de datos presentada nesta tese ofrece unha importante contribución ao estudo das anomalías en cocientes de Universalidade Leptónica $R(D^{(*)})$, e

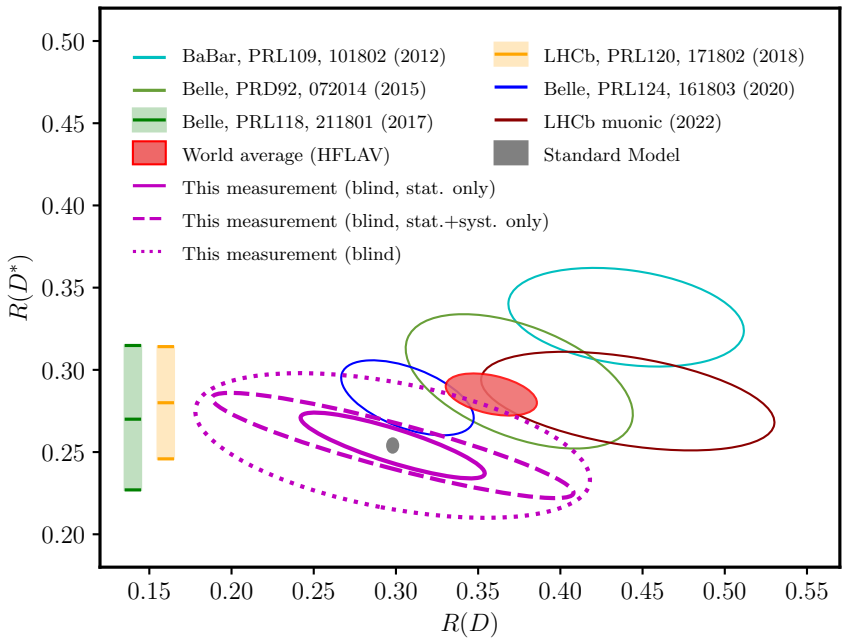

Figure A.1: Estado actual das medidas de $R(D)$ e $R(D^*)$, coa medida desta tese incluída. Cada elipse representa una medida combinada de $R(D^{(*)})$, co seu contorno representando as súas incertezas e a súa inclinación a súa correlación. A medida de $R(D^{(*)0})$ realizada nesta tese é representada en púrpura (centrada no valor teórico debido a estar cegada), coa liña contínua representando as incertezas estadísticas, a liña discontínua representándoa tamén coas incertezas sistemáticas, e a liña de puntos con todas as incertezas. As incertezas externas espérase que se reduzan ao longo dos anos, mentres que as sistemáticas tamén se reducirán lixeiramente antes da finalización da análise.

aporta a primeira medida de $R(D)$ usando a canle de desintegración hadrónica do leptón τ feita polo experimento LHCb, presumiblemente mellorando a situación global da procura de nova física fóra do Modelo Estándar no sector da Universalidade Leptónica.

Glossary of Terms

BBLite: Beeston-Barlow Lite. A fitting method that takes into account the limited sample size of template PDFs by introducing a nuisance parameter for each bin.

BDT: Boosted Decision Tree. A supervised machine learning algorithm.

$\mathcal{B}(X \to Y)$**:** Branching fraction of the $X \to Y$ decay.

CP: Charge-Parity. Usually used in the context of "CP-symmetry" (the symmetry of particles under the simultaneous inversion of charge and parity) or "CP violation" (the violation of such symmetry).

DIRA: Direction Angle. The angle between the line that connects a particle's primary vertex with its decay vertex and the direction of the sum of momenta of its decay products.

DOCA: Distance of Closest Approach. The shortest distance between two tracks.

DOF: Degrees of Freedom. Number of independent parameters.

ε**:** Efficiency. The fraction of events that passed certain requirements.

HLT: High Level Trigger. Defines the software-level trigger system of LHCb (see section 3.2.4).

LFU: Lepton Flavour Universality. See section 2.2.

LHC: Large Hadron Collider. See section 3.1.

L0: Level 0. Defines the hardware-level trigger system of LHCb (see section 3.2.4).

$N_{\mathbf{iso}}(X)$**:** Number of additional tracks with $p_T > 250$ MeV/c, $\chi^2_{\text{IP}}(\text{PV}) > 4$, and $\chi^2_{\text{IP}}(X) < 25$. A measurement of how many additional tracks a vertex X has, compared to the expected tracks from a signal decay (see section 4.3.4).

NP: New Physics. Any phenomenon that disagrees with the SM.

PDF: Probability Density Function. Function whose value at a given point represents the relative probability of a certain random variable being equal to that point.

PID: Particle Identification. See section 3.2.3.

PID_X**:** Log-likelihood difference between the X and pion hypotheses for a the identification of a certain particle ($\text{PID}_X = \log \mathcal{L}_X \log \mathcal{L}_\pi$).

$P_{\mathbf{NN}}(X)$**:** Bayesian posterior probability of a particle being of the type X. The "NN" refers to the Neural Networks used in the PID algorithm.

PV: Primary Vertex. The point in which the original collision happened (in this case, the proton-proton collision).

q^2**:** Squared transferred momentum. In a $h_0 \to h_1 W^{\pm}$ decay, $q^2 = (p_1 - p_0)^2$, which equals the invariant mass of the resulting particles from the subsequent $W^{\pm}$ decay.

RICH: Ring Imaging Cherenkov. A kind of detector that uses Cherenkov radiation to identify particles (see section 3.2.3).

SPD: Scintillator Pad Detector. See section 3.2.3.

SM: Standard Model. See section 2.1.

QCD: Quantum Chromodynamics. Theory that describes the strong interaction of quarks and gluons and is contained within the Standard Model.

VELO: Vertex Locator. Subdetector of LHCb (see section 3.2.2).

$\chi^2_{\mathbf{IP}}(X)$**:** Difference between the χ^2 of a vertex X built with and without the considered track (see section 4.3.4).

List of Figures

List of Tables

American Physical Society
Reuse and Permissions License

21-Mar-2023

This license agreement between the American Physical Society ("APS") and Julian Lomba Castro ("You") consists of your license details and the terms and conditions provided by the American Physical Society and SciPris.

Licensed Content Information

License Number:	**RNP/23/MAR/064417**
License date:	21-Mar-2023
DOI:	10.1103/RevModPhys.94.015003
Title:	Semitauonic b-hadron decays: A lepton flavor universality laboratory
Author:	Florian U. Bernlochner et al.
Publication:	Reviews of Modern Physics
Publisher:	American Physical Society
Cost:	USD $ 0.00

Request Details

Does your reuse require significant modifications: No

Specify intended distribution locations:	Worldwide
Reuse Category:	Reuse in a thesis/dissertation
Requestor Type:	Student
Items for Reuse:	Figures/Tables
Number of Figure/Tables:	1
Figure/Tables Details:	Figure 30
Format for Reuse:	Print and Electronic
Total number of print copies:	Up to 1000

Information about New Publication:

University/Publisher:	University of Santiago de Compostela
Title of dissertation/thesis:	Lepton Universality measurements in semileptonic decays of b-quark hadrons in the LHCb experiment at CERN
Author(s):	Julián Lomba Castro
Expected completion date:	Mar. 2023

License Requestor Information

Name:	Julian Lomba Castro
Affiliation:	Individual
Email Id:	julian.lomba.castro@cern.ch
Country:	Spain

Marketplace

Order Date	21-Mar-2023	**Type of Use**	Republish in a thesis/dissertation
Order License ID	1336693-1		
ISSN	1748-0221	**Publisher**	IOP Publishing
		Portion	Image/photo/illustration

LICENSED CONTENT

Publication Title	Journal of Instrumentation	**Country**	United Kingdom of Great Britain and Northern Ireland
Author/Editor	Institute of Physics (Great Britain), Institute of Physics Publishing., International School for Advanced Studies (Trieste, Italy)	**Rightsholder**	IOP Publishing, Ltd
		Publication Type	e-Journal
		URL	http://www.iop.org/EJ/jinst/
Date	01/01/2006		
Language	English		

REQUEST DETAILS

Portion Type	Image/photo/illustration	**Distribution**	Worldwide
Number of Images / Photos / Illustrations	5	**Translation**	Original language of publication
Format (select all that apply)	Print, Electronic	**Copies for the Disabled?**	No
		Minor Editing Privileges?	No
Who Will Republish the Content?	Publisher, not-for-profit	**Incidental Promotional Use?**	No
Duration of Use	Life of current edition	**Currency**	EUR
Lifetime Unit Quantity	Up to 499		
Rights Requested	Main product		

NEW WORK DETAILS

Title	Lepton Universality measurements in semileptonic decays of b-quark hadrons in the LHCb experiment at CERN	**Institution Name**	University of Santiago de Compostela
		Expected Presentation Date	2023-05-26
Instructor Name	Julian Lomba Castro		

ADDITIONAL DETAILS

Order Reference Number	N/A

The Requesting Person/Organization to Appear on the License	Julian Lomba Castro

REQUESTED CONTENT DETAILS

Title, Description or Numeric Reference of the Portion(s)	Figures 2.1, 4.2, 5.3, 5.4, and 10.1	**Title of the Article/Chapter the Portion Is From**	The LHCb Detector at the LHC
Editor of Portion(s)	LHCb collaboration	**Author of Portion(s)**	Institute of Physics (Great Britain); Institute of Physics Publishing.; International School for Advanced Studies (Trieste, Italy)
Volume of Serial or Monograph	3		
Page or Page Range of Portion	S08005	**Issue, if Republishing an Article From a Serial**	N/A
		Publication Date of Portion	2008-08-01

RIGHTSHOLDER TERMS AND CONDITIONS

These special terms and conditions are in addition to the standard terms and conditions for CCC's Republication Service and, together with those standard terms and conditions, govern the use of the Works. As the User you will make all reasonable efforts to contact the author(s) of the article which the Work is to be reused from, to seek consent for your intended use. Contacting one author who is acting expressly as authorised agent for their co-author(s) is acceptable. User will reproduce the following wording prominently alongside the Work: the source of the Work, including author, article title, title of journal, volume number, issue number (if relevant), page range (or first page if this is the only information available) and date of first publication; and a link back to the article (via DOI); and if practicable, and IN ALL CASES for new works published under any of the Creative Commons licences, the words "© IOP Publishing. Reproduced with permission. All rights reserved" Without the express permission of the author(s) and the Rightsholder of the article from which the Work is to be reused, User shall not use it in any way which, in the opinion of the Rightsholder, could: (i) distort or alter the author(s)' original intention(s) and meaning; (ii) be prejudicial to the honour or reputation of the author(s); and/or (iii) imply endorsement by the author(s) and/or the Rightsholder. This licence does not apply to any article which is credited to another source and which does not have the copyright line '© IOP Publishing Ltd'. User must check the copyright line of the article from which the Work is to be reused to check that IOP Publishing Ltd has all the necessary rights to be able to grant permission. User is solely responsible for identifying and obtaining separate licences and permissions from the copyright owner for reuse of any such third party material/figures which the Rightsholder is not the copyright owner of. The Rightsholder shall not reimburse any fees which User pays for a republication license for such third party content. This licence does not apply to any material/figure which is credited to another source in the Rightsholder's publication or has been obtained from a third party. User must check the Version of Record of the article from which the Work is to be reused, to check whether any of the material in the Work is third party material. Third party citations and/or copyright notices and/or permissions statements may not be included in any other version of the article from which the Work is to be reused and so cannot be relied upon by the User. User is solely responsible for identifying and obtaining separate licences and permissions from the copyright owner for reuse of any such third party material/figures where the Rightsholder is not the copyright owner. The Rightsholder shall not reimburse any fees which User pays for a republication license for such third party content. User and CCC acknowledge that the Rightsholder may, from time to time, make changes or additions to these special terms and conditions without express notification, provided that these shall not apply to permissions already secured and paid for by User prior to such change or addition. User acknowledges that the Rightsholder (which includes companies within its group and third parties for whom it publishes its titles) may make use of personal data collected through the service in the course of their business. If User is the author of the Work, User may automatically have the right to reuse it under the rights granted back when User transferred the copyright in the article to the Rightsholder. User should check the copyright form and the relevant author rights policy to check whether permission is required. If User is the author of the Work and does require permission for proposed reuse of the Work, User should select 'Author of requested content' as the Requestor Type. The Rightsholder shall not reimburse any fees which User pays for a republication license. If User is the author of the article which User wishes to reuse in User's thesis or dissertation, the republication licence covers the right to include the Version of Record of the article, provided it is not then shared or deposited online. User must include citation details. Where User wishes to share their thesis or dissertation online, they

should remove the Version of Record before uploading it. User may include a Preprint or the Accepted Manuscript (after the embargo period) in the online version of the thesis or dissertation, provided they do so in accordance with the Rightsholder's policies on sharing Preprints or Accepted Manuscripts. User may need to obtain separate permission for any third party content included within the article. User must check this with the copyright owner of such third party content. Any online or commercial use of User's thesis or dissertation containing the article, including publication via ProQuest, would need to be expressly notified in writing to the Rightsholder at the time of request and would require separate written permission from the Rightsholder. As well as CCC, the Rightsholder shall have the right to bring any legal action that it deems necessary to enforce its rights should it consider that the Work infringes those rights in any way. For content reuse requests that qualify for permission under the STM Permissions Guidelines, which may be updated from time to time, the STM Permissions Guidelines supplement the terms and conditions contained in this license.

Marketplace Permissions General Terms and Conditions

The following terms and conditions ("General Terms"), together with any applicable Publisher Terms and Conditions, govern User's use of Works pursuant to the Licenses granted by Copyright Clearance Center, Inc. ("CCC") on behalf of the applicable Rightsholders of such Works through CCC's applicable Marketplace transactional licensing services (each, a "Service").

1) **Definitions.** For purposes of these General Terms, the following definitions apply:

"License" is the licensed use the User obtains via the Marketplace platform in a particular licensing transaction, as set forth in the Order Confirmation.

"Order Confirmation" is the confirmation CCC provides to the User at the conclusion of each Marketplace transaction. "Order Confirmation Terms" are additional terms set forth on specific Order Confirmations not set forth in the General Terms that can include terms applicable to a particular CCC transactional licensing service and/or any Rightsholder-specific terms.

"Rightsholder(s)" are the holders of copyright rights in the Works for which a User obtains licenses via the Marketplace platform, which are displayed on specific Order Confirmations.

"Terms" means the terms and conditions set forth in these General Terms and any additional Order Confirmation Terms collectively.

"User" or "you" is the person or entity making the use granted under the relevant License. Where the person accepting the Terms on behalf of a User is a freelancer or other third party who the User authorized to accept the General Terms on the User's behalf, such person shall be deemed jointly a User for purposes of such Terms.

"Work(s)" are the copyright protected works described in relevant Order Confirmations.

2) **Description of Service.** CCC's Marketplace enables Users to obtain Licenses to use one or more Works in accordance with all relevant Terms. CCC grants Licenses as an agent on behalf of the copyright rightsholder identified in the relevant Order Confirmation.

3) **Applicability of Terms.** The Terms govern User's use of Works in connection with the relevant License. In the event of any conflict between General Terms and Order Confirmation Terms, the latter shall govern. User acknowledges that Rightsholders have complete discretion whether to grant any permission, and whether to place any limitations on any grant, and that CCC has no right to supersede or to modify any such discretionary act by a Rightsholder.

4) **Representations; Acceptance.** By using the Service, User represents and warrants that User has been duly authorized by the User to accept, and hereby does accept, all Terms.

5) **Scope of License; Limitations and Obligations.** All Works and all rights therein, including copyright rights, remain the sole and exclusive property of the Rightsholder. The License provides only those rights expressly set forth in the terms and conveys no other rights in any Works

6) **General Payment Terms.** User may pay at time of checkout by credit card or choose to be invoiced. If the User chooses to be invoiced, the User shall: (i) remit payments in the manner identified on specific invoices, (ii) unless otherwise specifically stated in an Order Confirmation or separate written agreement, Users shall remit payments upon receipt of the relevant invoice from CCC, either by delivery or notification of availability of the invoice via the Marketplace platform, and (iii) if the User does not pay the invoice within 30 days of receipt, the User may incur a service charge of 1.5% per month or the maximum rate allowed by applicable law, whichever is less. While User may exercise the rights in the License

immediately upon receiving the Order Confirmation, the License is automatically revoked and is null and void, as if it had never been issued, if CCC does not receive complete payment on a timely basis.

7) **General Limits on Use.** Unless otherwise provided in the Order Confirmation, any grant of rights to User (i) involves only the rights set forth in the Terms and does not include subsequent or additional uses, (ii) is non-exclusive and non-transferable, and (iii) is subject to any and all limitations and restrictions (such as, but not limited to, limitations on duration of use or circulation) included in the Terms. Upon completion of the licensed use as set forth in the Order Confirmation, User shall either secure a new permission for further use of the Work(s) or immediately cease any new use of the Work(s) and shall render inaccessible (such as by deleting or by removing or severing links or other locators) any further copies of the Work. User may only make alterations to the Work if and as expressly set forth in the Order Confirmation. No Work may be used in any way that is unlawful, including without limitation if such use would violate applicable sanctions laws or regulations, would be defamatory, violate the rights of third parties (including such third parties' rights of copyright, privacy, publicity, or other tangible or intangible property), or is otherwise illegal, sexually explicit, or obscene. In addition, User may not conjoin a Work with any other material that may result in damage to the reputation of the Rightsholder. Any unlawful use will render any licenses hereunder null and void. User agrees to inform CCC if it becomes aware of any infringement of any rights in a Work and to cooperate with any reasonable request of CCC or the Rightsholder in connection therewith.

8) **Third Party Materials.** In the event that the material for which a License is sought includes third party materials (such as photographs, illustrations, graphs, inserts and similar materials) that are identified in such material as having been used by permission (or a similar indicator), User is responsible for identifying, and seeking separate licenses (under this Service, if available, or otherwise) for any of such third party materials; without a separate license, User may not use such third party materials via the License.

9) **Copyright Notice.** Use of proper copyright notice for a Work is required as a condition of any License granted under the Service. Unless otherwise provided in the Order Confirmation, a proper copyright notice will read substantially as follows: "Used with permission of [Rightsholder's name], from [Work's title, author, volume, edition number and year of copyright]; permission conveyed through Copyright Clearance Center, Inc." Such notice must be provided in a reasonably legible font size and must be placed either on a cover page or in another location that any person, upon gaining access to the material which is the subject of a permission, shall see, or in the case of republication Licenses, immediately adjacent to the Work as used (for example, as part of a by-line or footnote) or in the place where substantially all other credits or notices for the new work containing the republished Work are located. Failure to include the required notice results in loss to the Rightsholder and CCC, and the User shall be liable to pay liquidated damages for each such failure equal to twice the use fee specified in the Order Confirmation, in addition to the use fee itself and any other fees and charges specified.

10) **Indemnity.** User hereby indemnifies and agrees to defend the Rightsholder and CCC, and their respective employees and directors, against all claims, liability, damages, costs, and expenses, including legal fees and expenses, arising out of any use of a Work beyond the scope of the rights granted herein and in the Order Confirmation, or any use of a Work which has been altered in any unauthorized way by User, including claims of defamation or infringement of rights of copyright, publicity, privacy, or other tangible or intangible property.

11) **Limitation of Liability.** UNDER NO CIRCUMSTANCES WILL CCC OR THE RIGHTSHOLDER BE LIABLE FOR ANY DIRECT, INDIRECT, CONSEQUENTIAL, OR INCIDENTAL DAMAGES (INCLUDING WITHOUT LIMITATION DAMAGES FOR LOSS OF BUSINESS PROFITS OR INFORMATION, OR FOR BUSINESS INTERRUPTION) ARISING OUT OF THE USE OR INABILITY TO USE A WORK, EVEN IF ONE OR BOTH OF THEM HAS BEEN ADVISED OF THE POSSIBILITY OF SUCH DAMAGES. In any event, the total liability of the Rightsholder and CCC (including their respective employees and directors) shall not exceed the total amount actually paid by User for the relevant License. User assumes full liability for the actions and omissions of its principals, employees, agents, affiliates, successors, and assigns.

12) **Limited Warranties.** THE WORK(S) AND RIGHT(S) ARE PROVIDED "AS IS." CCC HAS THE RIGHT TO GRANT TO USER THE RIGHTS GRANTED IN THE ORDER CONFIRMATION DOCUMENT. CCC AND THE RIGHTSHOLDER DISCLAIM ALL OTHER WARRANTIES RELATING TO THE WORK(S) AND RIGHT(S), EITHER EXPRESS OR IMPLIED, INCLUDING WITHOUT LIMITATION IMPLIED WARRANTIES OF MERCHANTABILITY OR FITNESS FOR A PARTICULAR PURPOSE. ADDITIONAL RIGHTS MAY BE REQUIRED TO USE ILLUSTRATIONS, GRAPHS, PHOTOGRAPHS, ABSTRACTS, INSERTS, OR OTHER PORTIONS OF THE WORK (AS OPPOSED TO THE ENTIRE WORK) IN A MANNER CONTEMPLATED BY USER; USER UNDERSTANDS AND AGREES THAT NEITHER CCC NOR THE RIGHTSHOLDER MAY HAVE SUCH ADDITIONAL RIGHTS TO GRANT.

13) **Effect of Breach.** Any failure by User to pay any amount when due, or any use by User of a Work beyond the scope of the License set forth in the Order Confirmation and/or the Terms, shall be a material breach of such License. Any breach not cured within 10 days of written notice thereof shall result in immediate termination of such License without further

notice. Any unauthorized (but licensable) use of a Work that is terminated immediately upon notice thereof may be liquidated by payment of the Rightsholder's ordinary license price therefor; any unauthorized (and unlicensable) use that is not terminated immediately for any reason (including, for example, because materials containing the Work cannot reasonably be recalled) will be subject to all remedies available at law or in equity, but in no event to a payment of less than three times the Rightsholder's ordinary license price for the most closely analogous licensable use plus Rightsholder's and/or CCC's costs and expenses incurred in collecting such payment.

14) **Additional Terms for Specific Products and Services.** If a User is making one of the uses described in this Section 14, the additional terms and conditions apply:

a) ***Print Uses of Academic Course Content and Materials (photocopies for academic coursepacks or classroom handouts).*** For photocopies for academic coursepacks or classroom handouts the following additional terms apply:

i) The copies and anthologies created under this License may be made and assembled by faculty members individually or at their request by on-campus bookstores or copy centers, or by off-campus copy shops and other similar entities.

ii) No License granted shall in any way: (i) include any right by User to create a substantively non-identical copy of the Work or to edit or in any other way modify the Work (except by means of deleting material immediately preceding or following the entire portion of the Work copied) (ii) permit "publishing ventures" where any particular anthology would be systematically marketed at multiple institutions.

iii) Subject to any Publisher Terms (and notwithstanding any apparent contradiction in the Order Confirmation arising from data provided by User), any use authorized under the academic pay-per-use service is limited as follows:

A) any License granted shall apply to only one class (bearing a unique identifier as assigned by the institution, and thereby including all sections or other subparts of the class) at one institution;

B) use is limited to not more than 25% of the text of a book or of the items in a published collection of essays, poems or articles;

C) use is limited to no more than the greater of (a) 25% of the text of an issue of a journal or other periodical or (b) two articles from such an issue;

D) no User may sell or distribute any particular anthology, whether photocopied or electronic, at more than one institution of learning;

E) in the case of a photocopy permission, no materials may be entered into electronic memory by User except in order to produce an identical copy of a Work before or during the academic term (or analogous period) as to which any particular permission is granted. In the event that User shall choose to retain materials that are the subject of a photocopy permission in electronic memory for purposes of producing identical copies more than one day after such retention (but still within the scope of any permission granted), User must notify CCC of such fact in the applicable permission request and such retention shall constitute one copy actually sold for purposes of calculating permission fees due; and

F) any permission granted shall expire at the end of the class. No permission granted shall in any way include any right by User to create a substantively non-identical copy of the Work or to edit or in any other way modify the Work (except by means of deleting material immediately preceding or following the entire portion of the Work copied).

iv) Books and Records; Right to Audit. As to each permission granted under the academic pay-per-use Service, User shall maintain for at least four full calendar years books and records sufficient for CCC to determine the numbers of copies made by User under such permission. CCC and any representatives it may designate shall have the right to audit such books and records at any time during User's ordinary business hours, upon two days' prior notice. If any such audit shall determine that User shall have underpaid for, or underreported, any photocopies sold or by three percent (3%) or more, then User shall bear all the costs of any such audit; otherwise, CCC shall bear the costs of any such audit. Any amount determined by such audit to have been underpaid by User shall immediately be paid to CCC by User, together with interest thereon at the rate of 10% per annum from the date such amount was originally due. The provisions of this paragraph shall survive the termination of this License for any reason.

b) ***Digital Pay-Per-Uses of Academic Course Content and Materials (e-coursepacks, electronic reserves, learning***

management systems, academic institution intranets). For uses in e-coursepacks, posts in electronic reserves, posts in learning management systems, or posts on academic institution intranets, the following additional terms apply:

i) The pay-per-uses subject to this Section 14(b) include:

A) **Posting e-reserves, course management systems, e-coursepacks for text-based content,** which grants authorizations to import requested material in electronic format, and allows electronic access to this material to members of a designated college or university class, under the direction of an instructor designated by the college or university, accessible only under appropriate electronic controls (e.g., password);

B) **Posting e-reserves, course management systems, e-coursepacks for material consisting of photographs or other still images not embedded in text,** which grants not only the authorizations described in Section 14(b)(i)(A) above, but also the following authorization: to include the requested material in course materials for use consistent with Section 14(b)(i)(A) above, including any necessary resizing, reformatting or modification of the resolution of such requested material (provided that such modification does not alter the underlying editorial content or meaning of the requested material, and provided that the resulting modified content is used solely within the scope of, and in a manner consistent with, the particular authorization described in the Order Confirmation and the Terms), but not including any other form of manipulation, alteration or editing of the requested material;

C) **Posting e-reserves, course management systems, e-coursepacks or other academic distribution for audiovisual content,** which grants not only the authorizations described in Section 14(b)(i)(A) above, but also the following authorizations: (i) to include the requested material in course materials for use consistent with Section 14(b)(i)(A) above; (ii) to display and perform the requested material to such members of such class in the physical classroom or remotely by means of streaming media or other video formats; and (iii) to "clip" or reformat the requested material for purposes of time or content management or ease of delivery, provided that such “clipping” or reformatting does not alter the underlying editorial content or meaning of the requested material and that the resulting material is used solely within the scope of, and in a manner consistent with, the particular authorization described in the Order Confirmation and the Terms. Unless expressly set forth in the relevant Order Conformation, the License does not authorize any other form of manipulation, alteration or editing of the requested material.

ii) Unless expressly set forth in the relevant Order Confirmation, no License granted shall in any way: (i) include any right by User to create a substantively non-identical copy of the Work or to edit or in any other way modify the Work (except by means of deleting material immediately preceding or following the entire portion of the Work copied or, in the case of Works subject to Sections 14(b)(1)(B) or (C) above, as described in such Sections) (ii) permit "publishing ventures" where any particular course materials would be systematically marketed at multiple institutions.

iii) Subject to any further limitations determined in the Rightsholder Terms (and notwithstanding any apparent contradiction in the Order Confirmation arising from data provided by User), any use authorized under the electronic course content pay-per-use service is limited as follows:

A) any License granted shall apply to only one class (bearing a unique identifier as assigned by the institution, and thereby including all sections or other subparts of the class) at one institution;

B) use is limited to not more than 25% of the text of a book or of the items in a published collection of essays, poems or articles;

C) use is limited to not more than the greater of (a) 25% of the text of an issue of a journal or other periodical or (b) two articles from such an issue;

D) no User may sell or distribute any particular materials, whether photocopied or electronic, at more than one institution of learning;

E) electronic access to material which is the subject of an electronic-use permission must be limited by means of electronic password, student identification or other control permitting access solely to students and instructors in the class;

F) User must ensure (through use of an electronic cover page or other appropriate means) that any person, upon gaining electronic access to the material, which is the subject of a permission, shall see:

- a proper copyright notice, identifying the Rightsholder in whose name CCC has granted permission,

- a statement to the effect that such copy was made pursuant to permission,
- a statement identifying the class to which the material applies and notifying the reader that the material has been made available electronically solely for use in the class, and
- a statement to the effect that the material may not be further distributed to any person outside the class, whether by copying or by transmission and whether electronically or in paper form, and User must also ensure that such cover page or other means will print out in the event that the person accessing the material chooses to print out the material or any part thereof.

G) any permission granted shall expire at the end of the class and, absent some other form of authorization, User is thereupon required to delete the applicable material from any electronic storage or to block electronic access to the applicable material.

iv) Uses of separate portions of a Work, even if they are to be included in the same course material or the same university or college class, require separate permissions under the electronic course content pay-per-use Service. Unless otherwise provided in the Order Confirmation, any grant of rights to User is limited to use completed no later than the end of the academic term (or analogous period) as to which any particular permission is granted.

v) Books and Records; Right to Audit. As to each permission granted under the electronic course content Service, User shall maintain for at least four full calendar years books and records sufficient for CCC to determine the numbers of copies made by User under such permission. CCC and any representatives it may designate shall have the right to audit such books and records at any time during User's ordinary business hours, upon two days' prior notice. If any such audit shall determine that User shall have underpaid for, or underreported, any electronic copies used by three percent (3%) or more, then User shall bear all the costs of any such audit; otherwise, CCC shall bear the costs of any such audit. Any amount determined by such audit to have been underpaid by User shall immediately be paid to CCC by User, together with interest thereon at the rate of 10% per annum from the date such amount was originally due. The provisions of this paragraph shall survive the termination of this license for any reason.

c) ***Pay-Per-Use Permissions for Certain Reproductions (Academic photocopies for library reserves and interlibrary loan reporting) (Non-academic internal/external business uses and commercial document delivery).*** The License expressly excludes the uses listed in Section (c)(i)-(v) below (which must be subject to separate license from the applicable Rightsholder) for: academic photocopies for library reserves and interlibrary loan reporting; and non-academic internal/external business uses and commercial document delivery.

i) electronic storage of any reproduction (whether in plain-text, PDF, or any other format) other than on a transitory basis;

ii) the input of Works or reproductions thereof into any computerized database;

iii) reproduction of an entire Work (cover-to-cover copying) except where the Work is a single article;

iv) reproduction for resale to anyone other than a specific customer of User;

v) republication in any different form. Please obtain authorizations for these uses through other CCC services or directly from the rightsholder.

Any license granted is further limited as set forth in any restrictions included in the Order Confirmation and/or in these Terms.

d) ***Electronic Reproductions in Online Environments (Non-Academic-email, intranet, internet and extranet).*** For "electronic reproductions", which generally includes e-mail use (including instant messaging or other electronic transmission to a defined group of recipients) or posting on an intranet, extranet or Intranet site (including any display or performance incidental thereto), the following additional terms apply:

i) Unless otherwise set forth in the Order Confirmation, the License is limited to use completed within 30 days for any use on the Internet, 60 days for any use on an intranet or extranet and one year for any other use, all as measured from the "republication date" as identified in the Order Confirmation, if any, and otherwise from the date of the Order Confirmation.

ii) User may not make or permit any alterations to the Work, unless expressly set forth in the Order Confirmation

(after request by User and approval by Rightsholder); provided, however, that a Work consisting of photographs or other still images not embedded in text may, if necessary, be resized, reformatted or have its resolution modified without additional express permission, and a Work consisting of audiovisual content may, if necessary, be "clipped" or reformatted for purposes of time or content management or ease of delivery (provided that any such resizing, reformatting, resolution modification or “clipping” does not alter the underlying editorial content or meaning of the Work used, and that the resulting material is used solely within the scope of, and in a manner consistent with, the particular License described in the Order Confirmation and the Terms.

15) **Miscellaneous.**

a) User acknowledges that CCC may, from time to time, make changes or additions to the Service or to the Terms, and that Rightsholder may make changes or additions to the Rightsholder Terms. Such updated Terms will replace the prior terms and conditions in the order workflow and shall be effective as to any subsequent Licenses but shall not apply to Licenses already granted and paid for under a prior set of terms.

b) Use of User-related information collected through the Service is governed by CCC's privacy policy, available online at www.copyright.com/about/privacy-policy/.

c) The License is personal to User. Therefore, User may not assign or transfer to any other person (whether a natural person or an organization of any kind) the License or any rights granted thereunder; provided, however, that, where applicable, User may assign such License in its entirety on written notice to CCC in the event of a transfer of all or substantially all of User's rights in any new material which includes the Work(s) licensed under this Service.

d) No amendment or waiver of any Terms is binding unless set forth in writing and signed by the appropriate parties, including, where applicable, the Rightsholder. The Rightsholder and CCC hereby object to any terms contained in any writing prepared by or on behalf of the User or its principals, employees, agents or affiliates and purporting to govern or otherwise relate to the License described in the Order Confirmation, which terms are in any way inconsistent with any Terms set forth in the Order Confirmation, and/or in CCC's standard operating procedures, whether such writing is prepared prior to, simultaneously with or subsequent to the Order Confirmation, and whether such writing appears on a copy of the Order Confirmation or in a separate instrument.

e) The License described in the Order Confirmation shall be governed by and construed under the law of the State of New York, USA, without regard to the principles thereof of conflicts of law. Any case, controversy, suit, action, or proceeding arising out of, in connection with, or related to such License shall be brought, at CCC's sole discretion, in any federal or state court located in the County of New York, State of New York, USA, or in any federal or state court whose geographical jurisdiction covers the location of the Rightsholder set forth in the Order Confirmation. The parties expressly submit to the personal jurisdiction and venue of each such federal or state court.

Last updated October 2022

REFERENCES

[1] G. Altarelli, *The standard model of particle physics*, 2005. doi: 10.48550/ARXIV.HEP-PH/0510281. (Cited on page 6.)

[2] Particle Data Group, R. L. Workman and Others, *Review of particle physics*, PTEP **2022** (2022) 083C01. (Cited on pages 6, 7, 8, 24, 54, 75, 80, 87, 88, 91, 98, 99, 105, 107, 108, 112, 114, 115, 130, 132, 137, 138, and 142.)

[3] ATLAS collaboration, G. Aad *et al.*, *Observation of a new particle in the search for the standard model higgs boson with the ATLAS detector at the LHC*, Physics Letters B **716** (2012) 1. (Cited on pages 7 and 28.)

[4] CMS collaboration, S. Chatrchyan *et al.*, *Observation of a new boson at a mass of 125 GeV with the CMS experiment at the LHC*, Physics Letters B **716** (2012) 30. (Cited on pages 7 and 28.)

[5] N. Cabibbo, *Unitary symmetry and leptonic decays*, Phys. Rev. Lett. **10** (1963) 531. (Cited on page 7.)

[6] M. Kobayashi and T. Maskawa, *CP-violation in the renormalizable theory of weak interaction*, Prog. Theor. Phys. **49** (1973) 652. (Cited on page 7.)

[7] B. Pontecorvo, *Inverse beta processes and nonconservation of lepton charge*, Zh. Eksp. Teor. Fiz. **34** (1957) 247. (Cited on page 7.)

[8] Z. Maki, M. Nakagawa, and S. Sakata, *Remarks on the Unified Model of Elementary Particles*, Progress of Theoretical Physics **28** (1962) 870, `arXiv:https://academic.oup.com/ptp/article-pdf/28/5/870/5258750/28-5-870.pdf`. (Cited on page 7.)

[9] S. Bifani, S. Descotes-Genon, A. R. Vidal, and M.-H. Schune, *Review of lepton universality tests in B decays*, Journal of Physics G: Nuclear and Particle Physics **46** (2018) 023001. (Cited on page 8.)

[10] D. Buttazzo, A. Greljo, G. Isidori, and D. Marzocca, *B-physics anomalies: a guide to combined explanations*, Journal of High Energy Physics **2017** (2017) . (Cited on page 8.)

[11] LHCb collaboration, R. Aaij *et al.*, *Measurement of CP-averaged observables in the $B^0 \to K^{*0}\mu^+\mu^-$ decay*, Phys. Rev. Lett. **125** (2020) 011802 LHCb-PAPER-2020-002 CERN-EP-2020-027, `arXiv:2003.04831`. (Cited on page 9.)

[12] LHCb collaboration, R. Aaij *et al.*, *Angular analysis of the $B^+ \to K^{*+}\mu^+\mu^-$ decay*, Phys. Rev. Lett. **126** (2021) 161802 LHCb-PAPER-2020-041,CERN-EP-2020-239, `arXiv:2012.13241`. (Cited on page 9.)

[13] LHCb collaboration, R. Aaij *et al.*, *Angular analysis of the rare decay* $B_s^0 \to \phi\mu^+\mu^-$, JHEP **11** (2021) 043 LHCb-PAPER-2021-022, CERN-EP-2021-138, arXiv:2107.13428. (Cited on page 9.)

[14] LHCb collaboration, R. Aaij *et al.*, *Differential branching fractions and isospin asymmetries of* $B \to K^{(*)}\mu^+\mu^-$ *decays*, JHEP **06** (2014) 133 LHCb-PAPER-2014-006 CERN-PH-EP-2014-055, arXiv:1403.8044. (Cited on page 9.)

[15] LHCb collaboration, R. Aaij *et al.*, *Measurements of the S-wave fraction in* $B^0 \to K^+\pi^-\mu^+\mu^-$ *decays and the* $B^0 \to K^*(892)^0\mu^+\mu^-$ *differential branching fraction*, JHEP **11** (2016) 047 LHCb-PAPER-2016-012 CERN-EP-2016-141, arXiv:1606.04731. (Cited on page 9.)

[16] LHCb collaboration, R. Aaij *et al.*, *Branching fraction measurements of the rare* $B_s^0 \to \phi\mu^+\mu^-$ *and* $B_s^0 \to f_2'(1525)\mu^+\mu^-$ *decays*, Phys. Rev. Lett. **127** (2021) 151801 LHCb-PAPER-2021-014, CERN-EP-2021-092, arXiv:2105.14007. (Cited on page 9.)

[17] M. Bordone, G. Isidori, and A. Pattori, *On the standard model predictions for* R_K *and* R_{K^*}, Eur. Phys. J. C **76** (2016) . (Cited on pages 9 and 11.)

[18] LHCb collaboration, R. Aaij *et al.*, *Test of lepton universality in beauty-quark decays*, arXiv:2103.11769 LHCb-PAPER-2021-004,CERN-EP-2021-042, arXiv:2103.11769, to appear in Nature Physics. (Cited on pages 9 and 11.)

[19] Belle collaboration, S. Choudhury *et al.*, *Test of lepton flavor universality and search for lepton flavor violation in* $B \to K\ell\ell$ *decays*, Journal of High Energy Physics **2021** (2021) . (Cited on pages 9 and 11.)

[20] BABAR collaboration, J. P. Lees *et al.*, *Measurement of branching fractions and rate asymmetries in the rare decays* $B \to K^{(*)}l^+l^-$, Physical Review D **86** (2012) . (Cited on pages 9 and 11.)

[21] LHCb collaboration, R. Aaij *et al.*, *Test of lepton universality with* $B^0 \to K^{*0}\ell^+\ell^-$ *decays*, JHEP **08** (2017) 055 LHCb-PAPER-2017-013 CERN-EP-2017-100, arXiv:1705.05802. (Cited on pages 9 and 11.)

[22] Belle collaboration, S. Wehle *et al.*, *Test of lepton-flavor universality in* $B \to K^*\ell^+\ell^-$ *decays at Belle*, Physical Review Letters **126** (2021) . (Cited on pages 9 and 11.)

[23] LHCb collaboration, R. Aaij *et al.*, *Tests of lepton universality using* $B^0 \to K^0_S\ell^+\ell^-$ *and* $B^+ \to K^{*+}\ell^+\ell^-$ *decays*, Phys. Rev. Lett. **128** (2022) 191802 LHCb-PAPER-2021-038, CERN-EP-2021-208, arXiv:2110.09501. (Cited on pages 9 and 11.)

[24] LHCb collaboration, R. Aaij *et al.*, *Test of lepton universality using $\Lambda_b^0 \to pK^-\ell^+\ell^-$ decays*, JHEP **05** (2020) 040 LHCb-PAPER-2019-040 CERN-EP-2019-272, arXiv:1912.08139. (Cited on pages 9 and 11.)

[25] LHCb Collaboration, *Measurement of lepton universality parameters in $b^+ \to k^+\ell^+\ell^-$ and $b^0 \to k^{*0}\ell^+\ell^-$ decays*, 2022. doi: 10.48550/ARXIV.2212.09153. (Cited on page 11.)

[26] BABAR collaboration, J. P. Lees *et al.*, *Evidence for an excess of $B \to D^{(*)}\tau^-\bar{\nu}_\tau$ decays*, Physical Review Letters **109** (2012) . (Cited on pages 9 and 11.)

[27] BABAR collaboration, J. P. Lees *et al.*, *Measurement of an excess of $B \to D^{(*)}\tau^-\bar{\nu}_\tau$ decays and implications for charged higgs bosons*, Physical Review D **88** (2013) . (Cited on pages 9 and 11.)

[28] Belle colaboration, G. Caria *et al.*, *Measurement of $\mathcal{R}(D)$ and $\mathcal{R}(D^*)$ with a semileptonic tagging method*, Physical Review Letters **124** (2020) . (Cited on pages 9 and 11.)

[29] LHCb collaboration, R. Aaij *et al.*, *Measurement of the ratio of branching fractions $\mathcal{B}(\overline{B}^0 \to D^{*+}\tau^-\overline{\nu}_\tau)/\mathcal{B}(\overline{B}^0 \to D^{*+}\mu^-\overline{\nu}_\mu)$*, Phys. Rev. Lett. **115** (2015) 111803 LHCb-PAPER-2015-025 CERN-PH-EP-2015-150, arXiv:1506.08614. (Cited on pages 9, 11, 21, and 126.)

[30] S. Fajfer, J. F. Kamenik, and I. Nišandžić, *$b \to D^*\tau\overline{\nu}_\tau$ sensitivity to new physics*, Phys. Rev. D **85** (2012) 094025. (Cited on pages 9, 11, 21, 24, and 97.)

[31] LHCb collaboration, R. Aaij *et al.*, *Measurement of the ratio of the $\mathcal{B}(B^0 \to D^{*-}\tau^+\nu_\tau)$ and $\mathcal{B}(B^0 \to D^{*-}\mu^+\nu_\mu)$ branching fractions using three-prong τ-lepton decays*, Phys. Rev. Lett. **120** (2018) 171802 LHCb-PAPER-2017-017 CERN-EP-2017-212, arXiv:1708.08856. (Cited on pages 9, 11, 21, 24, 51, 52, 56, 97, and 126.)

[32] LHCb collaboration, R. Aaij *et al.*, *Measurement of the ratio of branching fractions $\mathcal{B}(B_c^+ \to J/\psi\tau^+\nu_\tau)/\mathcal{B}(B_c^+ \to J/\psi\mu^+\nu_\mu)$*, Phys. Rev. Lett. **120** (2018) 121801 LHCb-PAPER-2017-035 CERN-EP-2017-275, arXiv:1711.05623. (Cited on pages 9 and 11.)

[33] LHCb collaboration, R. Aaij *et al.*, *Observation of the decay $\Lambda_b^0 \to \Lambda_c^+\tau^-\bar{\nu}_\tau$*, Phys. Rev. Lett. **128** (2021) 191803 LHCb-PAPER-2021-044,CERN-EP-2021-265, arXiv:2201.03497. (Cited on pages 9 and 11.)

[34] HFLAV collaboration, Y. Amhis *et al.*, *Averages of b-hadron, c-hadron, and τ-lepton properties as of 2021*, 2023. Updated results and plots available at https://hflav.web.cern.ch. (Cited on pages 10, 11, 13, 16, 130, 132, and 147.)

[35] F. U. Bernlochner, M. F. Sevilla, D. J. Robinson, and G. Wormser, *Semitauonic b-hadron decays: A lepton flavor universality laboratory*, Reviews of Modern Physics **94** (2022) . (Cited on pages 10, 22, 23, and 147.)

[36] LHCb Collaboration, *Measurement of the ratios of branching fractions $\mathcal{R}(D^*)$ and $\mathcal{R}(D^0)$*, 2023. doi: 10.48550/ARXIV.2302.02886. (Cited on pages 11 and 126.)

[37] A. Anisimov, I. Narodetskii, C. Semay, and B. Silvestre-Brac, *The bc meson lifetime in the light-front constituent quark model*, Physics Letters B **452** (1999), no. 1 129. (Cited on page 11.)

[38] V. V. Kiselev, *Exclusive decays and lifetime of B_c meson in QCD sum rules*, 2002. doi: 10.48550/ARXIV.HEP-PH/0211021. (Cited on page 11.)

[39] M. A. Ivanov, J. G. Körner, and P. Santorelli, *Exclusive semileptonic and nonleptonic decays of the B_c meson*, Phys. Rev. D **73** (2006) 054024. (Cited on page 11.)

[40] E. Hernández, J. Nieves, and J. M. Verde-Velasco, *Study of exclusive semileptonic and nonleptonic decays of B_c^- in a nonrelativistic quark model*, Phys. Rev. D **74** (2006) 074008. (Cited on page 11.)

[41] F. U. Bernlochner, Z. Ligeti, D. J. Robinson, and W. L. Sutcliffe, *Precise predictions for $\Lambda_b \to \Lambda_c$ semileptonic decays*, Phys. Rev. D **99** (2019) 055008. (Cited on page 11.)

[42] *Precision electroweak measurements on the Z resonance*, Physics Reports **427** (2006) 257. (Cited on page 10.)

[43] *Electroweak measurements in electron-positron collisions at W-boson-pair energies at LEP*, Physics Reports **532** (2013) 119. (Cited on page 10.)

[44] A. Pich, *Precision tau physics*, Progress in Particle and Nuclear Physics **75** (2014) 41. (Cited on page 10.)

[45] KEDR collaboration, V. Aulchenko *et al.*, *Measurement of the ratio of the lepton widths $\Gamma_{ee}/\Gamma_{\mu\mu}$ for the J/ψ meson*, Physics Letters B **731** (2014) 227. (Cited on page 10.)

[46] The NA62 Collaboration, *Precision measurement of the ratio of the charged kaon leptonic decay rates*, 2012. doi: 10.48550/ARXIV.1212.4012. (Cited on page 10.)

[47] BESIII Collaboration, M. Ablikim *et al.*, *Measurement of the branching fraction for the semileptonic decay $D^{0(+)} \to \pi^{-(0)}\mu^+\nu_\mu$ and test of lepton flavor universality*, Phys. Rev. Lett. **121** (2018) 171803. (Cited on page 10.)

[48] A. Celis, M. Jung, X.-Q. Li, and A. Pich, *Sensitivity to charged scalars in $B \to D^{(*)}\tau\nu_\tau$ and $B \to \tau\nu_\tau$ decays*, Journal of High Energy Physics **2013** (2013) . (Cited on pages 10 and 15.)

[49] C. G. Boyd, B. Grinstein, and R. F. Lebed, *Constraints on form factors for exclusive semileptonic heavy to light meson decays*, Phys. Rev. Lett. **74** (1995) 4603. (Cited on page 12.)

[50] C. G. Boyd, B. Grinstein, and R. F. Lebed, *Precision corrections to dispersive bounds on form factors*, Phys. Rev. D **56** (1997) 6895. (Cited on pages 12 and 13.)

[51] C. Glenn Boyd, B. Grinstein, and R. F. Lebed, *Model-independent determinations of $\bar{B} \to Dl\bar{\nu}$, $\bar{B} \to D^* l\bar{\nu}$ form factors*, Nuclear Physics B **461** (1996), no. 3 493. (Cited on pages 12 and 13.)

[52] Fermilab Lattice & MILC collaborations, J. A. Bailey *et al.*, *$B \to D\ell\nu$ form factors at nonzero recoil and $-V_{cb}-$ from 2+1-flavor lattice QCD*, Phys. Rev. D **92** (2015), no. 3 034506, arXiv:1503.07237. (Cited on page 14.)

[53] HPQCD collaboration, H. Na *et al.*, *$B \to Dl\nu$ form factors at nonzero recoil and extraction of $|V_{cb}|$*, Phys. Rev. D **92** (2015), no. 5 054510, arXiv:1505.03925, [Erratum: Phys.Rev.D 93, 119906 (2016)]. (Cited on page 14.)

[54] D. Bigi and P. Gambino, *Revisiting $B \to D\ell\nu$*, Phys. Rev. D **94** (2016), no. 9 094008, arXiv:1606.08030. (Cited on pages 14 and 72.)

[55] F. U. Bernlochner, Z. Ligeti, M. Papucci, and D. J. Robinson, *Combined analysis of semileptonic B decays to D and D^*: $R(D^{(*)})$, $|V_{cb}|$, and new physics*, Phys. Rev. D **95** (2017), no. 11 115008, arXiv:1703.05330, [Erratum: Phys.Rev.D 97, 059902 (2018)]. (Cited on page 14.)

[56] S. Jaiswal, S. Nandi, and S. K. Patra, *Extraction of $|V_{cb}|$ from $B \to D^{(*)}\ell\nu_\ell$ and the Standard Model predictions of $R(D^{(*)})$*, JHEP **12** (2017) 060, arXiv:1707.09977. (Cited on page 14.)

[57] D. Bigi, P. Gambino, and S. Schacht, *$R(D^*)$, $|V_{cb}|$, and the Heavy Quark Symmetry relations between form factors*, JHEP **11** (2017) 061, arXiv:1707.09509. (Cited on page 14.)

[58] P. Gambino, M. Jung, and S. Schacht, *The V_{cb} puzzle: An update*, Phys. Lett. B **795** (2019) 386, arXiv:1905.08209. (Cited on page 14.)

[59] BaBar collaboration, J. P. Lees *et al.*, *Extraction of form Factors from a Four-Dimensional Angular Analysis of $\overline{B} \to D^* \ell^- \overline{\nu}_\ell$*, Phys. Rev. Lett. **123** (2019), no. 9 091801, arXiv:1903.10002. (Cited on page 14.)

[60] M. Bordone, M. Jung, and D. van Dyk, *Theory determination of $\bar{B} \to D^{(*)}\ell^-\bar{\nu}$ form factors at $\mathcal{O}(1/m_c^2)$*, Eur. Phys. J. C **80** (2020), no. 2 74, arXiv:1908.09398. (Cited on page 14.)

[61] Fermilab Lattice & MILC collaborations, A. Bazavov *et al.*, *Semileptonic form factors for $B \to D^*\ell\nu$ at nonzero recoil from 2 + 1-flavor lattice QCD*, arXiv:2105.14019. (Cited on page 14.)

[62] G. Martinelli, S. Simula, and L. Vittorio, *$|V_{cb}|$ and $R(D)^{(*)}$ using lattice QCD and unitarity*, Phys. Rev. D **105** (2022), no. 3 034503, arXiv:2105.08674. (Cited on page 14.)

[63] A. J. Buras, *Weak hamiltonian, cp violation and rare decays*, 1998. (Cited on page 14.)

[64] J. D. Gómez, N. Quintero, and E. Rojas, *Charged current $b \to c\tau\bar{\nu}_\tau$ anomalies in a general W' boson scenario*, Physical Review D **100** (2019) . (Cited on page 14.)

[65] R. Mandal, C. Murgui, A. Peñuelas, and A. Pich, *The role of right-handed neutrinos in $b \to c\tau\bar{\nu}$ anomalies*, Journal of High Energy Physics **2020** (2020) . (Cited on page 14.)

[66] P. Asadi, M. R. Buckley, and D. Shih, *It's all right(-handed neutrinos): a new W' model for the $R_{D^{(*)}}$ anomaly*, Journal of High Energy Physics **2018** (2018) . (Cited on page 14.)

[67] A. Greljo, D. J. Robinson, B. Shakya, and J. Zupan, *$R(D^{(*)})$ from W' and right-handed neutrinos*, Journal of High Energy Physics **2018** (2018) . (Cited on page 14.)

[68] D. Robinson, B. Shakya, and J. Zupan, *Right-handed neutrinos and $R(D^{(*)})$*, Journal of High Energy Physics **2019** (2019) . (Cited on page 14.)

[69] K. S. Babu, B. Dutta, and R. N. Mohapatra, *A theory of $R(D^*, D)$ anomaly with right-handed currents*, Journal of High Energy Physics **2019** (2019) . (Cited on page 14.)

[70] V. Barger, J. L. Hewett, and R. J. N. Phillips, *New constraints on the charged higgs sector in two-higgs-doublet models*, Phys. Rev. D **41** (1990) 3421. (Cited on page 15.)

[71] J. F. Gunion and H. E. Haber, *Higgs bosons in supersymmetric models (i)*, Nuclear Physics B **272** (1986), no. 1 1. (Cited on page 15.)

[72] M. Wei and Y. Chong-Xing, *Charged higgs bosons from the 3-3-1 models and the $\mathcal{R}(D^{(*)})$ anomalies*, 2017. doi: 10.48550/ARXIV.1702.01255. (Cited on page 15.)

[73] C.-H. Chen and T. Nomura, *Charged-higgs on $R_{D^{(*)}}$, τ polarization, and FBA*, The European Physical Journal C **77** (2017) . (Cited on page 15.)

[74] J.-P. Lee, *$B \to D^{(*)}\tau\nu_\tau$ in the 2HDM with an anomalous τ coupling*, Physical Review D **96** (2017) . (Cited on page 15.)

[75] S. Iguro and K. Tobe, *$R(D^{(*)})$ in a general two higgs doublet model*, Nuclear Physics B **925** (2017) 560. (Cited on page 15.)

[76] A. Crivellin, C. Greub, and A. Kokulu, *Explaining $B \to D\tau\nu$ and $B \to \tau\nu$ in a 2HDM of type III*, Physical Review D **86** (2012) . (Cited on page 15.)

[77] Y. Sakaki, R. Watanabe, M. Tanaka, and A. Tayduganov, *Testing leptoquark models in $\bar{B} \to D^{(*)}\tau\bar{\nu}$*, Physical Review D **88** (2013) . (Cited on page 15.)

[78] X.-Q. Li, Y.-D. Yang, and X. Zhang, *Revisiting the one leptoquark solution to the $R(D^{(*)})$ anomalies and its phenomenological implications*, Journal of High Energy Physics **2016** (2016) . (Cited on page 15.)

[79] S. Bansal, R. M. Capdevilla, and C. Kolda, *Constraining the minimal flavor violating leptoquark explanation of the $R_{D^{(*)}}$ anomaly*, Physical Review D **99** (2019) . (Cited on page 15.)

[80] U. Aydemir, T. Mandal, and S. Mitra, *Addressing the $R_{D^{(*)}}$ anomalies with an S_1 leptoquark from SO(10) grand unification*, Physical Review D **101** (2020) . (Cited on page 15.)

[81] K. Cheung *et al.*, *Revisit to the $b \to c\tau\nu$ transition: In and beyond the SM*, Nuclear Physics B **965** (2021) 115354. (Cited on page 15.)

[82] M. P. ALTARELLI and F. TEUBERT, *B PHYSICS AT LHCb*, International Journal of Modern Physics A **23** (2008) 5117. (Cited on pages 18, 19, and 30.)

[83] LHCb collaboration, R. Aaij *et al.*, *Measurement of the inelastic pp cross-section at a centre-of-mass energy of $\sqrt{s}$ =13 TeV*, JHEP **06** (2018) 100 LHCb-PAPER-2018-003 CERN-EP-2018-044, `arXiv:1803.10974`. (Cited on page 18.)

[84] M. Deile, *Diffraction and total cross-section at the tevatron and the lhc*, 2006. doi: 10.48550/ARXIV.HEP-EX/0602021. (Cited on page 18.)

[85] S. Navin, *Diffraction in pythia*, 2010. doi: 10.48550/ARXIV.1005.3894. (Cited on pages 20 and 147.)

[86] LHCb collaboration, C. Elsässer, *$\bar{b}b$ production angle plots*, `https://lhcb.web.cern.ch/lhcb/speakersbureau/html/bb_ProductionAngles.html`. (Online; accessed 21-Sept-2022). (Cited on pages 20 and 147.)

[87] LHCb collaboration, R. Aaij *et al.*, *Measurement of the b-quark production cross-section in 7 and 13 TeV pp collisions*, Phys. Rev. Lett. **118** (2017) 052002 LHCb-PAPER-2016-031 CERN-EP-2016-201, arXiv:1612.05140. (Cited on page 19.)

[88] LHCb collaboration, I. Bediaga, M. C. Torres *et al.*, *Physics case for an LHCb upgrade II - opportunities in flavour physics, and beyond, in the HL-LHC era*, 2018. doi: 10.48550/ARXIV.1808.08865. (Cited on page 22.)

[89] L. Evans and P. Bryant, *LHC machine*, Journal of Instrumentation **3** (2008) S08001. (Cited on pages 27 and 32.)

[90] E. Lopienska, *The cern accelerator complex, layout in 2022*, https://cds.cern.ch/record/2800984. General Photo © 2022 CERN. (Cited on pages 29 and 147.)

[91] ALICE collaboration, K. Aamodt, A. A. Quintana *et al.*, *The ALICE experiment at the CERN LHC*, Journal of Instrumentation **3** (2008) S08002. (Cited on page 28.)

[92] ATLAS collaboration, G. Aad, E. Abat *et al.*, *The ATLAS experiment at the CERN large hadron collider*, Journal of Instrumentation **3** (2008) S08003. (Cited on page 28.)

[93] CMS collaboration, S. Chatrchyan, G. Hmayakyan *et al.*, *The CMS experiment at the CERN LHC*, Journal of Instrumentation **3** (2008) S08004. (Cited on page 28.)

[94] LHCb collaboration, A. A. Alves Jr. *et al.*, *The LHCb detector at the LHC*, JINST **3** (2008), no. LHCb-DP-2008-001 S08005. (Cited on pages 28, 30, 32, 34, 36, 38, 39, 136, and 147.)

[95] DELPHI collaboration, *The delphi detector at lep*, Nuclear Instruments and Methods in Physics Research Section A: Accelerators, Spectrometers, Detectors and Associated Equipment **303** (1991), no. 2 233. (Cited on page 30.)

[96] LHCb collaboration, R. Aaij *et al.*, *LHCb detector performance*, Int. J. Mod. Phys. **A30** (2015) 1530022 LHCB-DP-2014-002, CERN-PH-EP-2014-290, arXiv:1412.6352. (Cited on pages 30, 35, and 38.)

[97] LHCb collaboration, F. Alessio, R. Jacobsson, and R. L. Gac, *LHCb Operations Plots Webpage*, https://lbgroups.cern.ch/online/OperationsPlots/index.htm. (Online; accessed 30-Sept-2022). (Cited on pages 31 and 147.)

[98] LHCb collaboration, *LHCb reoptimized detector design and performance: Technical Design Report*, CERN-LHCC-2003-030. (Cited on pages 31 and 147.)

[99] LHCb collaboration, *Framework TDR for the LHCb Upgrade: Technical Design Report*, CERN-LHCC-2012-007. (Cited on page 31.)

[100] LHCb collaboration, *LHCb magnet: Technical Design Report*, CERN-LHCC-2000-007. (Cited on page 32.)

[101] LHCb collaboration, *LHCb VELO (VErtex LOcator): Technical Design Report*, CERN-LHCC-2001-011. (Cited on pages 33 and 147.)

[102] R. Aaij *et al.*, *Performance of the LHCb Vertex Locator*, JINST **9** (2014) P09007 LHCB-DP-2014-001, arXiv:1405.7808. (Cited on page 34.)

[103] J. Gassner, M. Needham, and O. Steinkamp, *Layout and Expected Performance of the LHCb TT Station*, tech. rep., CERN, Geneva, Apr, 2004. (Cited on page 34.)

[104] LHCb collaboration, *LHCb inner tracker: Technical Design Report*, CERN-LHCC-2002-029. (Cited on page 34.)

[105] LHCb collaboration, *LHCb outer tracker: Technical Design Report*, CERN-LHCC-2001-024. (Cited on page 35.)

[106] M. Adinolfi *et al.*, *Performance of the LHCb RICH detector at the LHC*, The European Physical Journal C **73** (2013) . (Cited on page 37.)

[107] LHCb collaboration, *LHCb calorimeters: Technical Design Report*, CERN-LHCC-2000-036. (Cited on page 37.)

[108] LHCb collaboration, *LHCb muon system: Technical Design Report*, CERN-LHCC-2001-010. (Cited on page 37.)

[109] LHCb collaboration, *LHCb trigger system: Technical Design Report*, CERN-LHCC-2003-031. (Cited on page 38.)

[110] M. Clemencic *et al.*, *The LHCb simulation application, gauss: Design, evolution and experience*, Journal of Physics: Conference Series **331** (2011) 032023. (Cited on page 40.)

[111] C. Bierlich *et al.*, *A comprehensive guide to the physics and usage of pythia 8.3*, 2022. doi: 10.48550/ARXIV.2203.11601. (Cited on page 40.)

[112] A. Ryd *et al.*, *EvtGen: A Monte Carlo Generator for B-Physics*, . (Cited on page 40.)

[113] S. Agostinelli, J. Allison *et al.*, *Geant4—a simulation toolkit*, Nuclear Instruments and Methods in Physics Research Section A: Accelerators, Spectrometers, Detectors and Associated Equipment **506** (2003), no. 3 250. (Cited on page 41.)

[114] LHCb collaboration, *LHCb computing: Technical Design Report*, CERN-LHCC-2005-019. (Cited on page 41.)

[115] D. Müller, M. Clemencic, G. Corti, and M. Gersabeck, *ReDecay: A novel approach to speed up the simulation at LHCb*, Eur. Phys. J. **C78** (2018) 1009 LHCb-DP-2018-004, arXiv:1810.10362. (Cited on pages 41 and 44.)

[116] M. Williams *et al.*, *The HLT2 Topological Lines*, . (Cited on page 46.)

[117] S. Tolk, J. Albrecht, F. Dettori, and A. Pellegrino, *Data driven trigger efficiency determination at LHCb*, LHCb-PUB-2014-039. (Cited on page 46.)

[118] H. Voss, A. Hoecker, J. Stelzer, and F. Tegenfeldt, *TMVA - Toolkit for Multivariate Data Analysis with ROOT*, PoS **ACAT** (2007) 040. (Cited on page 53.)

[119] L. Anderlini *et al.*, *The PIDCalib package*, tech. rep., CERN, Geneva, Jul, 2016. (Cited on pages 61 and 139.)

[120] F. U. Bernlochner *et al.*, *Das ist der HAMMER: Consistent new physics interpretations of semileptonic decays*, The European Physical Journal C **80** (2020) . (Cited on pages 72 and 139.)

[121] D. Bigi, P. Gambino, and S. Schacht, *A fresh look at the determination of $|V_{cb}|$ from $b \to d\ell\nu$*, Physics Letters B **769** (2017) 441. (Cited on page 73.)

[122] D. Bigi, P. Gambino, and S. Schacht, *R(d*), $|V_{cb}|$, and the heavy quark symmetry relations between form factors*, Journal of High Energy Physics **2017** (2017) . (Cited on page 73.)

[123] D. Scora and N. Isgur, *Semileptonic meson decays in the quark model: An update*, Physical Review D **52** (1995) 2783. (Cited on page 73.)

[124] BESIII, M. Ablikim *et al.*, *Study of the Decay $D_s^+ \to \pi^+\pi^+\pi^-\eta$ and Observation of the W-annihilation Decay $D_s^+ \to a_0(980)^+\rho^0$*, arXiv:2106.13536. (Cited on page 98.)

[125] F. U. Bernlochner and Z. Ligeti, *Semileptonic $B_{(s)}$ decays to excited charmed mesons with e, μ, τ and searching for new physics with $R(D^{**})$*, Phys. Rev. D **95** (2017), no. 1 014022, arXiv:1606.09300. (Cited on pages 107 and 108.)

[126] F. U. Bernlochner, M. F. Sevilla, D. J. Robinson, and G. Wormser, *Semitauonic b-hadron decays: A lepton flavor universality laboratory*, arXiv:2101.08326. (Cited on page 107.)

[127] LHCb, R. Aaij *et al.*, *Precise measurement of the f_s/f_d ratio of fragmentation fractions and of B_s^0 decay branching fractions*, Phys. Rev. D **104** (2021), no. 3 032005, arXiv:2103.06810. (Cited on page 109.)

[128] R. Barlow and C. Beeston, *Fitting using finite monte carlo samples*, Computer Physics Communications **77** (1993), no. 2 219. (Cited on page 124.)

In the Standard Model (SM), Lepton Flavour Universality (LFU) is a property that implies that the coupling between gauge bosons and the different leptons does not depend on the flavour of the lepton. In particular, the so-called LFU ratios such as R(D(*)0)=BF(B→D(*)0τν)/BF(B→D(*)0μν) are being thoroughly measured by different experiments, finding tensions with the SM predictions up to the 3 sigma range. In this thesis, a preliminary simultaneous measurement of the B→D(*)0τν branching fractions and the R(D(*)0) LFU ratios is reported, done with LHCb data from the years 2016–2018. The obtained results, with blinded values, are R(D0) = x ± 0.12 and R(D*0) = x ± 0.043.
In addition, the base work for a complementary and analogous measurement of the R(D(*)-) is laid out.